Climatic controls on drainage basin hydrology and topographic evolution

Shiuan-An Chen

A dissertation submitted to the University of Bristol in accordance with the requirements for award of the degree of Doctor of Philosophy in the Faculty of Science.

School of Geographical Sciences

March 2021

Word count: 26,276

Abstract

Climate is assumed to influence drainage basin evolution through interactions between rainfall, runoff, and erosion processes. Although former studies have extensively explored climatic controls on land surface processes and landforms, they were mainly targeted humid regions, owing to the lack of data in drylands and limited global databases. In addition, climatic controls tend to covary with other factors, such as vegetation and topography, complicating the detection of climatic signals on landforms. To explore the influences of climate on drainage basin topography across climate zones, this thesis meta-analysed hydrological regimes in the USA, and river longitudinal profile concavity and short- and long-term drainage basin erosion rates around the globe. The data were compiled from published literature and databases and classified by climate classifications. There is a spectrum of downstream changes in water discharge across basin aridity, reflecting different characteristics of rainfall–runoff links between climate zones. These various hydrological regimes control the shapes of river longitudinal profile, which are generally concave-up in all climate zones but systematically straighter with higher aridity. On the other hand, drainage basin erosion rates are influenced by various environmental controls between timescales. Long-term erosion rates are non-linearly related to climate, reflecting the balance between precipitation and vegetation cover. Long-term rates are also enhanced by past glaciation in mid- and high-latitude regions, and positively related to the topography of drainage basin. Short-term rates are dominated by anthropogenic activities and are more detectable in small basins with lower sediment buffering capacity. These results link climate with hydrology and land surface processes, improving our understanding on the influences of climate and climate change on drainage basin evolution.

Acknowledgements

Studying the PhD degree is an exciting yet challenging journey, especially studying abroad. I have faced many circumstances and made decisions that I had never done in the past. Fortunately, my supervisors, Dr Katerina Michaelides and Dr Michael Bliss Singer, are very kind, patient, and willing to spend time guiding students. They are not only teachers who taught me how to do research, but also friends who care about my thoughts, my life, and my future, and are always encouraging me. They made my life in Bristol much more comfortable than I would ever imagine. I also appreciate my supervisor, Dr David A. Richards, who taught me the principle of cosmogenic nuclides and helped me improve my study.

I thank Prof Rudy Slingerland for providing and modifying the LONGPRO model's code, and Dr Stuart W. D. Grieve for building the river long profile database and solving the following issues. I appreciate Prof Jim Freer, Prof Rachel Flecker, Dr Anita Ganesan, and Dr Gemma Coxon, who reviewed my works and gave me advices. I also appreciate my colleagues, Rosie Lane and Jeison Sosa, to provide me with ideas and helps for my study. Many thanks to Isaac Kipkemoi, Tamsin Lockwood, and Yinxue Liu. They are my colleagues and best friends who share lives with me, encourage me, and do our common hobbies together.

I thank my wife, Ya-Hsiu (Ashley) Chang, who paused her job in Taiwan and came to the UK for me. Without her support, I would not finish my study and would not gain as many experiences in the UK as I did. Huge thanks to my parents. They always support my hobbies and encourage me to study abroad. They did not give me pressure on my study or my life; therefore, I could conduct my research at my own pace and seek my career freely. Finally, I thank God who always create miracles in my life. No matter what challenges I face, what frustrations I have, He always solve my problem and give me more than I ask.

Author’s declaration

I declare that the work in this dissertation was carried out in accordance with the requirements of the University's *Regulations and Code of Practice for Research Degree Programmes* and that it has not been submitted for any other academic award. Except where indicated by specific reference in the text, the work is the candidate's own work. Work done in collaboration with, or with the assistance of, others, is indicated as such. Any views expressed in the dissertation are those of the author.

SIGNED: ..... DATE:.....

Table of contents

List of tables

List of figures

Glossary

A	Drainage area
AI	Aridity Index
DEM	Digital elevation model
E	Elevation
GLoPro	Global Longitudinal Profiles database
IQR	Interquartile range
K–G	Köppen–Geiger
K–S	Kolmogorov–Smirnov hypothesis test
K–W	Kruskal–Wallis hypothesis test
KDE	Kernel density estimation
L	Distance downstream
L_n	River length
LGM	Last glacial maximum
LiDAR	Light Detection and Ranging
Long profile	Longitudinal profile
MAE	Mean annual potential evapotranspiration
MAP	Mean annual precipitation
n	Number of data
NCI	Normalised Concavity Index
OCTOPUS	Open Cosmogenic Isotope and Luminescence database
Q	Water discharge
Q_n	Water discharge at the most downstream location
$R_{S/L}$	The ratio of short- to long-term median erosion rates
S	Slope gradient
SRTM	Shuttle Radar Topography Mission
α	The rate of downstream change of water discharge

1. General introduction

The topographic evolution of drainage basin reflects the balance between climate, hydrology, and tectonics, and is modified by land surface properties (Figure 1.1). Climate controls precipitation and temperature, and influence the hydrological regime of drainage basin (e.g. the runoff on the hillslope and streamflow in the river channel) (Dunne 1978; Knighton 1998). The hydrological processes erode land surface and transport sediments, which is assumed to shape the landform of drainage basin (Leopold and Maddock 1953; Wolman and Gerson 1978). On the other hand, tectonic uplift increases the elevation of land surface, which balances the denudation resulting from hydrological processes; however, tectonics also increase the slope gradient and weakening the bedrock, enhancing the erosive energy of land surface processes (Binnie et al. 2007; Knighton 1998; Whipple and Tucker 1999). Land surface properties modify the effectiveness of land surface processes, and thus, influencing the rate and pattern of landform change. The properties may be controlled by climate (e.g. vegetation type and density), hydrology (e.g. grain size), and geology of the basin (e.g. lithology) (Abrahams et al. 1988; Mishra et al. 2019; Olen et al. 2016; Singer and Michaelides 2014; Yatsu 1955), complicating the influences of land surface processes on landform developments. Besides the natural controls, human activity conducts an increasing power on landform change in the last few centuries, which is believed to outweigh natural controls in shaping the land surface (Kemp et al. 2020; Wilkinson and McElroy 2007).

Since the climate influences hydrological regime of drainage basin, and hydrological processes may shape the land surface, I am hypothesising that there is a link between climate–hydrology–erosion that is expressed in topographic metrics (e.g. basin shape, river network, channel steepness, and channel geometry). Previous studies explore the characteristics of drainage basin hydrology and topography, such as the rates, spatial patterns, and temporal variability of hydrological regime and topographic metrics, and identified the dominant controls (Bonnet and Crave 2003; Hack 1957; Leopold and Maddock 1953; Tucker and Slingerland 1997). Nevertheless, studies tend to focus on humid regions, with few data collections and analyses in drylands, defined as where the ratio of mean annual precipitation (MAP) to mean annual potential evapotranspiration (MAE) is lower than 0.5 by the Aridity Index (AI) classification (Trabucco and Zomer 2009). In addition, climatic controls on landform are hard to identify in certain regions because climate may covary with

various factors, such as the vegetation and topography (Bookhagen and Strecker 2012; Collins and Bras 2008; Olen et al. 2016; Roe et al. 2002). Therefore, climatic influences on landform are often unclear and debatable.

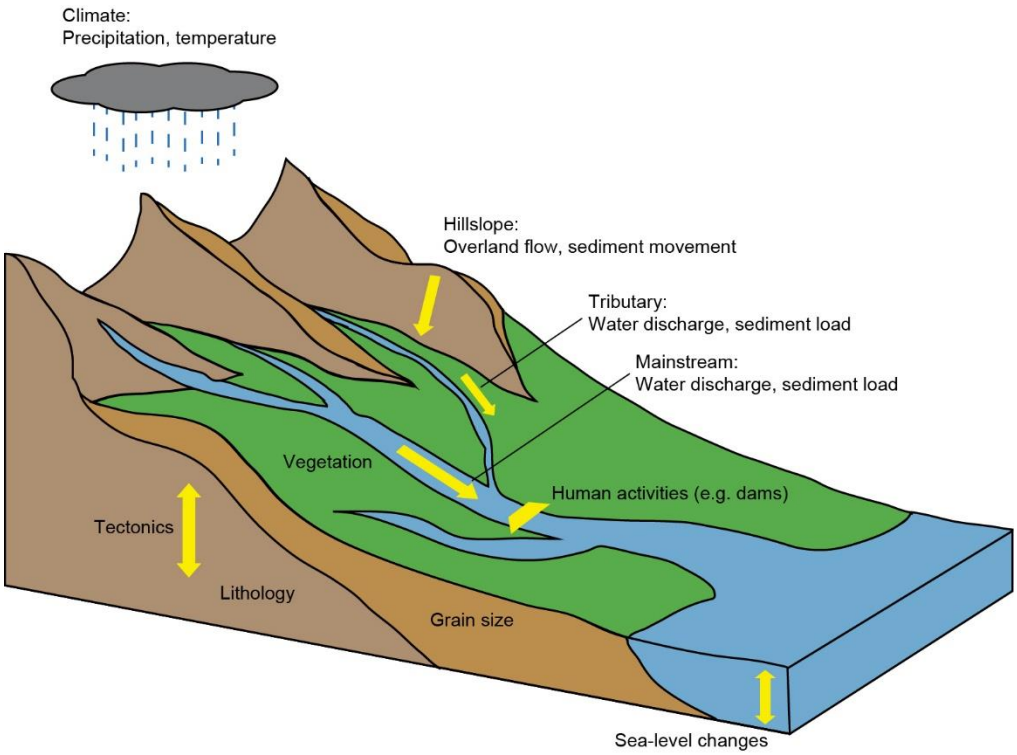

Figure 1.1 Environmental controls on drainage basin evolution. The controls include climatic factors (e.g. precipitation, temperature, vegetation, sea-level changes), hydrologic factors (e.g. water discharge, sediment load, grain size), geologic factors (e.g. tectonics, lithology), and human activity; however, the factors may interact with each other, so the categories are not exclusive.

To address the gap of climatic controls on drainage basin hydrology and topographic evolution, this thesis aimed to analyse the hydrological regime of basin and topographic metrics which can quantify landform characteristics between climate zones. One important factor in the determination of how basins evolve over time is the net balance between hillslope sediment supply to the river channel (via hillslope erosion) and channel sediment evacuation (via fluvial erosion) over time. Although climate affects both hillslope and channel erosional processes, the manifestation of climatic differences on each process domain may be different and hence the balance between sediment supply and evacuation may express differently. Therefore, I am hypothesising that the effects of climate on drainage basin evolution can be explored by studying two topographic metrics that encapsulate hillslope–

channel erosion balance: (1) the river longitudinal profile (long profile); and (2) the short- and long-term drainage basin erosion rates. River long profile (the elevation of river channel versus distance downstream) is controlled by the balance between sediment supply from hillslope to the river channel and sediment evacuation by streamflow (Michaelides et al. 2018; Sinha and Parker 1996; Snow and Slingerland 1987); therefore, its form should be diagnostic of the regional expression of climate, and reflects the history of drainage basin evolution. Basin-averaged erosion rate integrates erosion and sediment transportation on hillslope and in river channel, which has been proposed to be influenced by various environmental factors between timescales, including climate (Covault et al. 2013; Harel et al. 2016; Langbein and Schumm 1958; Milliman and Meade 1983; Summerfield and Hulton 1994; Wittmann et al. 2011).

To explore climatic controls on drainage basin evolution, I compiled data of streamflow, river long profile, short- and long-term drainage basin erosion rates, and relevant environmental factors at the continental and global scale. The data were then classified by climate classifications to analyse how climate influences hydrology, and whether there is detectable differences of river long profile shape and erosion rate between climate zones which can link climate–hydrology–erosion relationship.

2. Background and Motivation

Climate determines precipitation and temperature, which controls runoff and sediment-transport processes, and is assumed to affect sediment flux (Coulthard and Van de Wiel 2013) and drainage basin evolution (Seybold et al. 2017; Snow and Slingerland 1987). Climatic attributes include the rate, frequency, type of precipitation, and spatio-temporal distribution, which influence the generation and variability of runoff on the hillslope and streamflow in the river channel (Dunne 1978; Horton 1933; Knighton 1998). The runoff erodes bedrock and soil on the hillslope and transports the produced sediments into river channel; streamflow moves sediments further downstream, with some of them depositing on the riverbed and flood plain (Wittmann et al. 2011). The interplay between water and sediment within the basin should reflect the local climate and influence the topographic evolution of drainage basin.

Field observations show different precipitation characteristics between humid regions and drylands. Compared to humid regions, the rate and frequency of rainfall in drylands are low, and the variability is high (Nicholson 2011). These different precipitation characteristics between climate zones influence the hydrological regimes of drainage basins, producing frequent and high water discharge in humid regions, and highly variable streamflow in drylands (Molnar et al. 2006; Snelder et al. 2013; Yair et al. 1978), which may lead to distinct landform evolution. For example, the long profiles of graded rivers are assumed to have concave-up form (Hack 1957; Snow and Slingerland 1987), with fluctuations resulted from tectonic, lithologic, or anthropogenic influences (Hanks and Webb 2006; Kirby and Whipple 2001; Kirby and Whipple 2012; Pederson and Tressler 2012; Wang et al. 2008). However, several studies in drylands showed straight or convex-up river profiles (e.g. Singer and Michaelides 2014; Vogel 1989), which may result from the distinct hydrological regime in drylands, but the mechanism is lack systematic analysis. In addition, drainage basin erosion rate reflects sediment flux from hillslope to the river channel, and from river channel to the outlet of basin, which should reflect environmental controls on drainage basin. Studies found various environmental controls on erosion rate, such as the precipitation, glaciation, wildfire, topography, geology, and human activity (Dedkov and Mozzherin 1996; Kirchner et al. 2001; Langbein and Schumm 1958; Milliman and Meade 1983; Portenga and Bierman 2011). Nevertheless, the dominant control on erosion rate seems to depend on the study area and

analysed timescales. The global pattern of erosion rates and the link between climate and erosion between timescales still need to be explored in detail.

Although climate has long been assumed to influence topographic evolution of drainage basin, it is challenging to analyse its effects. Climate controls hydrology and glacial processes, which shape the land surface, yet they covary with other factors, such as topography (e.g. orographic precipitation), geology (e.g. weathering and erodibility of lithology), and vegetation (e.g. vegetation type and coverage) (Aalto et al. 2006; Bookhagen and Strecker 2012; Collins and Bras 2008; Li and Fang 2016; Mishra et al. 2019; Olen et al. 2016; Sorensen and Yanites 2019; Starke et al. 2020; Vandenberghe 2003; von Blanckenburg 2005). In some regions, climate change further complicates the detection of climatic influences between timescales (Bierman et al. 2005; Bookhagen and Strecker 2012; Bookhagen et al. 2005; Clapp et al. 2000). Therefore, climatic controls may not be detected in several locations (e.g. tectonic regions), at certain timescales (e.g. decadal year which is suffered from anthropogenic influences), or be considered as secondary control (e.g. von Blanckenburg 2005; Portenga and Bierman 2011).

The other challenge of analysing climatic control on the landform is the limited data in drylands. Previous geomorphologic studies mainly target humid regions, with few data collected in drylands (e.g. limited gauging stations were set in dryland rivers due to infrequent streamflow and low discharge). Therefore, there tends to be a bias towards humid regions, geomorphic data in drylands and the developments of global datasets are still limited. However, drylands account for approximately one-third of the global area with 14% of global population (Nicholson 2011). In addition, the dryland environment is fragile and changeable during rainfall events because of sparse vegetation, highly variable hydrological regime, growing human activities (e.g. agriculture and grazing), and potential impacts of climate change in the near future (Gellis et al. 2004; Michaelides et al. 2018; Molnar et al. 2006; Slater and Singer 2013; Wolman and Gerson 1978). Thus, it is needed to extend geomorphologic analyses to the basins with higher aridity.

Fortunately, global databases of topographic metrics and environmental data are becoming more comprehensive and openly accessible. There is potential for exploring climatic controls on hydrological regime and the hydrological influence on landform evolution. I aimed to compile streamflow, river long profile, erosion rates, and relevant environmental data from

published databases, and classified the data by two climate classifications for analysing climate–hydrology–erosion relationships at the continental or global scale.

The thesis is structured by the general introduction, background and motivation, methodology, and three sub-studies of hydrological regimes, river long profiles, and drainage basin erosion rates, respectively, followed by a synthesis and conclusions. Chapter 3 presents an overview of the methodological approach taken in the thesis, particularly the climate classifications, which were used in all three sub-studies (the details of other specific methods are explained within each following results chapter). Chapter 4 presents climatic controls on the downstream changes in discharge between flood events, to explore climate–hydrology connection. Because of the potential influence of hydrology on drainage basin landform, in the following results chapters, two topographic metrics, the river long profile and erosion rate, are explored, respectively. Chapters 5 presents river long profiles between climate zones, including numerical modelling (referred to the results from Chapter 4) for simulating hydrological influence on long profile evolution. Chapter 6 presents short- and long-term drainage basin erosion rate between climate zones and the controls of climate, topography, and anthropogenic factors on erosion. In Chapter 7, I synthesise the thesis's main findings and provide the direction for future works. Chapter 8 is the conclusions. The specific objectives of the thesis are:

(1) Hydrological regimes: compile streamflow data across the USA, analyse the downstream change in discharge of each flood event, and the relationship between drainage area and discharge.

(2) River long profiles: extract global river long profiles, calculate the concavity of profile, and conduct numerical modelling to explore the influence of streamflow on long profile evolution.

(3) Erosion rates: compile global short- and long-term erosion rates of drainage basin, collect the extent of environmental factors (e.g. precipitation rates, glacial regions, and agricultural regions), and identify the dominant controls of erosion rates between timescales.

3. Methodology overview

To quantify the role of climate on hydrological regimes, river long profiles, and drainage basin erosion rates, two climate classifications were used, the Köppen–Geiger (K–G) climate classification (Peel et al. 2007) and the quantitative Aridity Index (AI) (Trabucco and Zomer 2009), to classify the climate zones of analysed data. The streamflow data were compiled from USGS (National Water Information System, https://waterdata.usgs.gov/nwis) and United States Department of Agriculture, Agricultural Research Service (USDA–ARS; https://www.tucson.ars.ag.gov/dap) for analysing the differences of downstream change in discharge and the influence of spatial scale on discharge between climate zones. River long profiles were extracted manually from Google Earth for the preliminary test and then analysed from Global Longitudinal Profiles (GLoPro) database (Chen et al. 2019). To compare the characteristics of long profiles between climate zones, I developed the Normalised Concavity Index (NCI). Moreover, the numerical model, LONGPRO (Slingerland et al. 1994), were conducted to identify the dominant control of long profile concavity. To analyse drainage basin erosion rates, short- and long-term erosion rates were compiled from existing databases and published literature, including the Open Cosmogenic Isotope and Luminescence database (OCTOPUS) (Codilean et al. 2018) and USGS. To identify other environmental controls on erosion rates between climate zones and between timescales, various environmental data were also collected, including the MAP for the USA (calculated from CPC US Unified Precipitation data), ice extent at the last glacial maximum (LGM; Ray and Adams 2001), topography (mean slope gradient and total relief) of river channels (extracted and calculated from GLoPro; Chen et al. 2019), and agricultural regions (Foley et al. 2005) (Figure 3.1). Climate classifications and statistical tests used in all studies are described below; the specific methods for each study are explained in the corresponding chapter.

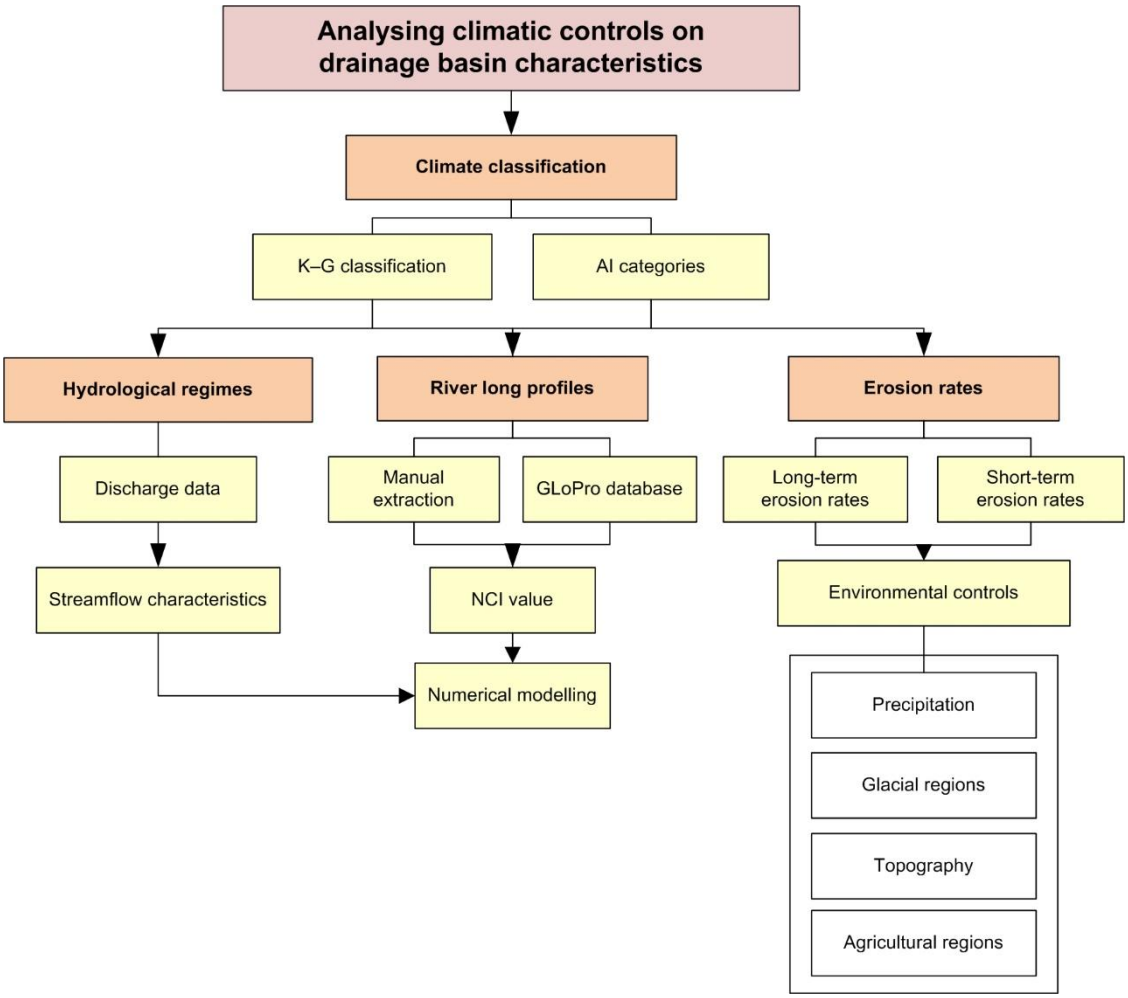

Figure 3.1 Flow chart of the overall methodology.

Climate zones were classified by K–G classification and AI. K–G classification is based on vegetation types, defined by temperature and precipitation thresholds. The extent of each climate zone was determined by Peel et al. (2007). The original classification includes five main climate zones (Tropical, Arid, Temperature, Cold, and Polar zones) and 29 sub-zones in the globe. However, several sub-zones of the Temperate and Cold zones are too small, even less than 1% of the global land area. To maximise the number of data in each climate zone, the 3rd categories of these two main zones were combined. Also, most of the lands in the Polar zone are permafrost, and the rivers are in the form of glaciers, making them subject to predominantly glacial processes rather than fluvial ones, and the public data collected in this zone are also limited. Therefore, I excluded the Polar zone and left four main zones and 13 sub-zones used in the analyses (Figure 3.2a).

The AI is a quantitative metric for representing water balance, which is calculated by dividing MAP by MAE, which declines with aridity. The spatial distribution of the AI was acquired from

the Global Aridity and PET Database (Trabucco and Zomer 2009). For ease of statistical comparison, a categorical approach was adopted and the following thresholds were used for the AI: Hyper-arid (< 0.03), Arid (0.03–0.2), Semi-arid (0.2–0.5), Dry sub-humid (0.5–0.65), and Humid (> 0.65) (Figure 3.2b). Both climate classifications were provided as raster files and converted into shapefiles by ArcGIS (version: 10.4.1). The compiled data were then overlapped to determine their K–G climate zones, AI values, and AI categories.

By this mean, I assume that the prevailing climate in any basin has not shifted at the analysed timescales. However, I opted to use climate metrics that can currently be measured on a global basis, since they represent the best available information for analyses of topographic processes. Having confirmation from two climatic indices, which are computed in distinct ways, gives me confidence that the climate influences on drainage basin evolution can be captured. Any basins with marked biome or climate shifts occurred during the analysed timescales should be shown as noise in the datasets.

Two statistical hypothesis testings were used for analysing whether the collected data are different between climate zones. Two-sample Kolmogorov–Smirnov (K–S) test is a nonparametric test for checking whether two continuous, one-dimensional data samples, X_1 and X_2, come from the same distribution. I used the built-in function, *kstest2*, in MATLAB (version: R2018a) to calculate the statistics and corresponding *P* values of data between climate zones. However, if the number of data is huge, this test gets extremely low *P* values. If the purpose was to determine the statistical difference by the prevailing *P* values threshold (0.05), the Kruskal–Wallis (K–W) test was used. K–W test is also a nonparametric test, which compares the median values of multiple samples to determine whether they are from the same distribution. I used the built-in function, *kruskalwallis*, in MATLAB to calculate the statistics and corresponding *P* values.

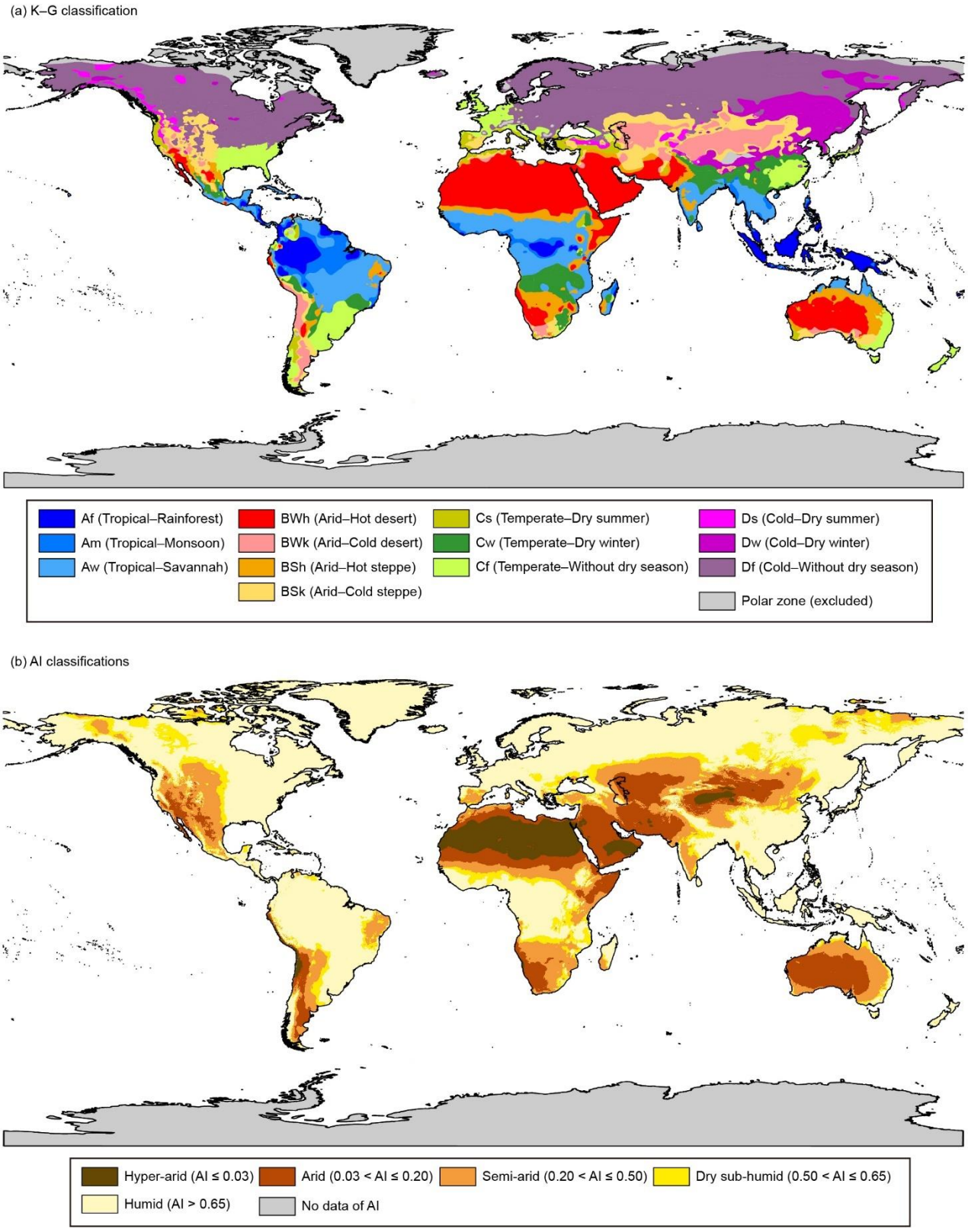

Figure 3.2 Köppen–Geiger (K–G) climate classification (a) and Aridity Index (AI) categories (b). The extent of K–G classification was collected from Peer et al. (2007), whilst AI values were from Trabucco and Zomer (2009). The coastline was from Natural Earth (https://www.naturalearthdata.com) in the Pseudo Plate Carree map projection in ArcGIS.

4. Links between climate and hydrological regime

4.1 Introduction

Climate determines the precipitation regime and influences the hydrological characteristics of a drainage basin. The precipitation controls the rate and frequency of water supply to the land surface, a proportion of which generates runoff over drainage basins, subject to losses by infiltration and evapotranspiration. Flow in rivers occurs when runoff reaches the channel, with notable baseflow contributions in humid regions from groundwater and subsurface drainage (Dunne 1978) and potential for prolonged periods of no flow in arid channels. Therefore, the climate influences the hydrological responses of river channel.

The characteristics of precipitation (e.g. the MAP, seasonality, intensity, duration, and spatial coverage of rainfall) between humid and arid regions are different. In humid regions, precipitation occurs during wet seasons or through out the year, and is relatively frequent and predictable (de Araújo and González Piedra 2009; Xue et al. 2017). Although various mechanisms can induce precipitation in humid regions (e.g. front, cyclone, and monsoon), the rainfall is typcially long-lived and covers a wide area, and the inter-event and interannual variability of rainfall in a drainage basin is normally small (Subramanya 2013). In contrast, rainfall events in drylands are infrequent. Rainfall is usually induced by convective storms during a brief period per year because of high temperature, low soil moisture, and spare vegetation, and is characterised with intense and short-duration precipitation with small spatial footprint (Belmonte and Beltrán 2001; Nicholson 2011; Renard 1970; Sharon et al. 2002; Stone et al. 2008). Because of the randomness of convective disturbances, the spatial distribution of rainfall depends on each event, and the annual rate and seasonality of precipitation are highly variable (sometimes the rainfall does not occur through out a year, and the MAP depends on few rainfall events) (Nicholson 2011; Thornes 2009). Although the spatial and temporal patterns of precipitation may be influenced by the environment of drainage basin, such as the moist wind direction and topography, the spatio-temperal variability of precipitation in drylands is higher than in humid regions (Belmonte and Beltrán 2001; Nicholson 2011; Renard 1970; Thornes 2009).

These different characteristics of precipitation between humid and arid regions influence the mechanisms of runoff generation and runoff characteristics on the hillslope. In humid regions, the land surface is often covered by well-developed soil layers and vegetation, with high infiltration capacity and the ability to disperse the raindrops; therefore, rainfall intensity seldom exceeds infiltration rate of the ground (Dunne 1978). Rainfall mostly infiltrates into the ground, raising groundwater level, producing return flow (saturation-excess runoff), and supply water (with subsurface stormflow) from underground into the river channel (Dunne 1978; Dunne 1991; Knighton 1998). In drylands, because of high rainfall intensity and sparse vegetation (lack of root system to promote interception of raindrops and percolation in the soil), the precipitation intensity often exceeds infiltration rate of the ground. In consequence, runoff is generated by infiltration-excess (Hortonian) overland flow (Horton 1933; Knighton 1998; Wilcox et al. 2003). The rate of runoff in drylands is controlled by the intensity and duration of precipitation and land surface characteristics; therefore, the runoff is characterised with infrequent, short-lived, and localised spatial coverage (Nicholson 2011; Thornes 2009; Wilcox et al. 2003). Since the runoff tends to occur in the region where the rainfall intensity is high, the areas producing runoff may not cover the entire drainage basin, leading to partial area runoff (Yair et al. 1978).

The different rainfall–runoff relationship between climate zones leads to various streamflow characteristics, such as the ephemerality (the percentage of time with no flow) and spatial distribution of streamflow. Rivers in humid regions are mainly perennial (i.e. with continuous streamflow all year round) because of high rate and frequency of rainfall, and a large amount of groundwater provides baseflow even during dry seasons. In contrast, dryland rivers tend to be ephemeral (i.e. with no flow in river channels during part of time every year) because of infrequent rainfall events, low groundwater table (enhances the infiltration rate of streamflow), and high temperature (increases the evaporation rate) (Fan et al. 2013; Hammond et al. 2020; Reynolds et al. 2015; Snelder et al. 2013; Wallace and Renard 1967).

In terms of the influence of spatial scale on streamflow, studies have long demonstrated a positive power-law relationship between drainage area (A) and discharge (Q): $Q \propto A^c$ (Hack 1957; Leopold and Maddock 1953). This relationship implies that larger basins have higher discharge, and the discharge increases downstream. This is expectable since larger basin areas accumulate higher water volume from rainfall and transfer into streamflow. Larger basins also have more tributaries to supply water into the mainstem river (Leopold et al.

1964). However, these studies mainly targeted humid rivers. In drylands, the discharge may not necessarily increase with drainage area becacuse of different hydrological regime from humid regions. First, partial area runoff results in a small proportion of basin tributaries contributing streamflow to the mainstem river for limited periods of time (Wickert 2018; Yair et al. 1978). Second, the high ephemerality of river channel and low groundwater table cause river to lose water through dry, porous beds (Fan et al. 2013; Jaeger et al. 2017; Keppel and Renard 1962; Quichimbo et al. 2020; Renard 1970; Wallace and Renard 1967). Finally, high temperature and low humidity enhance the evaporation of streamflow; although the evaporation may only accounts for minor influence on discharge because of short duration of streamflow (Ielpi et al. 2020; Lange 2005). In consequence, streamflow in drylands may subject to transmission loss when it transports downstream (Keppel and Renard 1962), which I am hypothesising to lead to different *Q*–*A* relationships from humid rivers. Observations in drylands have identified various environmental factors that influence the downstream distribution of streamflow, such as the location of storm, discharge of upstream reach and tributaries, characteristics of riverbed material, antecedent moisture of riverbed, geometry of river channel, and whether the water in the channel flows overbank (Abdulrazzak and Sorman 1994; Hughes and Sami 1992; Keppel and Renard 1962; Knighton and Nanson 1994; Lange 2005). Therefore, the influence of spatial scale on streamflow in drylands seems to be different from humid regions and more complex because all the rainfall, runoff, and land surface properties influence the *Q*–*A* relationship.

Since the rainfall–runoff relationships are different between humid and arid regions, and the dryland environments are understudied, it is crucial to investigate the characteristics of hydrological regimes across climate zones, especially in drylands with various aridity. Former studies on streamflow characteristics were mainly targeted humid rivers with positive *Q*–*A* relationship; those targeted dryland rivers were either focused on rivers with very high aridity and analysed limited number of flood events, or meta-analysed gauging stations across wider area but the stations may not be on the same rivers. There is lack of investigation of whether systematic patterns of downstream changes in discharge and *Q*–*A* relationships exist between humid and arid zones and between flood magnitudes. Therefore, the streamflow data were compiled and analysed between various flood magnitudes along the rivers across climate zones. The objectives are to explore climatic controls on the downstream distributions of discharge and the *Q*–*A* relationships.

4.2 Methodology

To investigate climatic controls on streamflow characteristics, the rivers were chosen within the USA spanning a range of river lengths, with at least two gauging stations along the same river, and excluded rivers with lakes, dams, or urban regions (ensuring from published databases; Google Earth Pro, version: 7.3.3.7786; Mulligan et al. 2020; Schneider et al. 2003) that could influence the downstream variation in discharge, and excluded rivers flow across the main K–G climate zone (Chapter 3). The simultaneous records of streamflow between gauging stations along the river were assumed to represent flow records of the same event at different downstream locations of the river channel. The simultaneous records of discharge of gauging stations were compiled from the USGS National Water Information System (https://waterdata.usgs.gov/nwis) and a detailed ephemeral flow dataset (Walnut Gulch) from USDA–ARS (https://www.tucson.ars.ag.gov/dap). Several hydrological metrics were computed for quantifying streamflow characteristics, including the ephemerality of streamflow, the discharge of various percentiles, and the downstream rate of change in discharge (α) (Figure 4.1). The latter was developed in this study, based on the power-law relationship between discharge and river length (described in detail below).

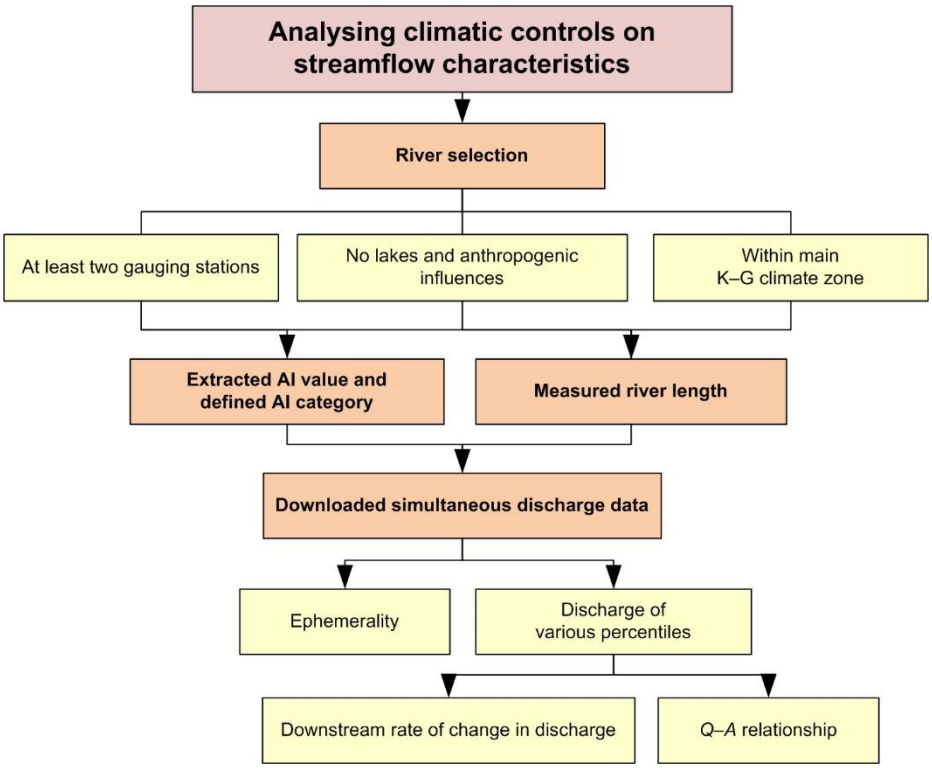

Figure 4.1 Flow chart of the methods of river selection and hydrological analyses.

Rivers in the USA were used because of high availability of open-accessed data in this nation. The selected rivers needed to fulfil the following criteria: (1) at least two gauging stations on the same river for calculating the downstream rate of change in discharge, and an overlap of gauging station records during a historical period longer than ten years; (2) no lakes and dams were shown on the river channel (Mulligan et al. 2020; digitised from Google Earth satellite imagery), and the river does not flow across urban areas (Schneider et al. 2003; derived from MODIS satellite data); and (3) no crossing between main K–G climate zones. The selected rivers distribute over different states with various river lengths (L_n). River length of each station was calculated by digitising river channel on Google Earth from the river head of the longest tributary to the location of station. The AI value of each river was sampled at the centre of river length between the river source and the most downstream gauging station (Figure 4.2). There were 24 rivers chosen across the USA (Table 4.1, Figure 4.3), including 65 gauging stations for analyses (Appendix A).

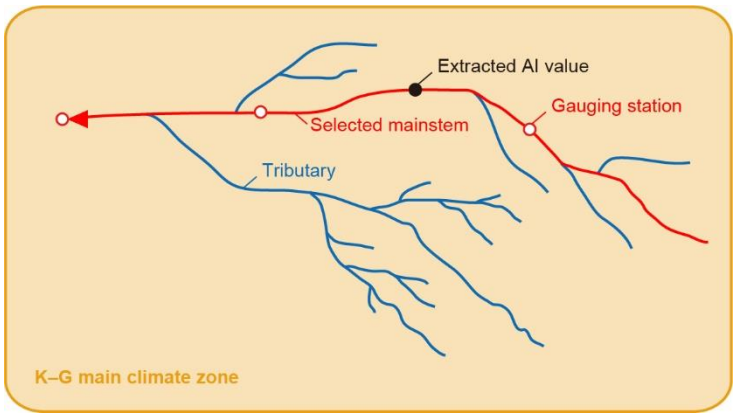

Figure 4.2 Schematic of river selection and climate classifications. The selected river (red line) is the longest river channel of the drainage basin which does not cross between main K–G climate zone, and with at least two gauging stations (white dot with red outline) with simultaneous streamflow records longer than ten years. I also ensured that there are no lakes, dams, and urban regions along the river channel (Mulligan et al. 2020; Schneider et al. 2003). The AI value of river was extracted at the centre (black dot) of river length.

Table 4.1 Climate categories and hydrological data of analysed rivers.

K–G climate zone	AI category (AI value)	River name	State	Drainage area (km²)	River length (km)	Ephe. (%)	Analysed period (yr)	Data source*
BWh	Arid (0.13)	Fortymile Wash	NV	818	75	99.7–99.8	15	1
BSk	Semi-Arid (0.22)	Walnut Gulch	AZ	149	31	90–98	53	2
BSk	Semi-Arid (0.27)	Limpia Creek	TX	588	52	23–83	13	1
BSk	Semi-Arid (0.38)	Dry Fork	UT	298	43	0–77	16	1
BSk	Arid (0.18)	Rio Puerco	NM	16,110	369	45–72	26	1
BSh	Semi-Arid (0.33)	Sycamore Creek	AZ	425	50	1–30	10	1
BSk	Semi-Arid (0.36)	Little Fountain Creek	CO	69	26	1–18	10	1
BWk	Semi-Arid (0.23)	Muddy Creek	WY	860	76	6–15	18	1
Cf	Humid (0.85)	Little River	GA	2,010	111	0–15	11	1
Aw	Humid (1.86)	Waikolu Stream	HI	10	6	0–7	35	1
Cf	Dry Sub-Humid (0.59)	Little Washita River	OK	601	56	0–2	29	1
Df	Humid (0.87)	Walnut Creek	IA	53	15	0–0.4	10	1
Af	Humid (1.02)	Waimea River	HI	217	23	0	22	1
Af	Humid (1.39)	Rio Tanama	PR	58	40	0	40	1
Af	Humid (2.45)	Waikamoi Stream	HI	10	11	0	10	1
Af	Humid (3.16)	Kapaula Gulch	HI	4	5	0	15	1
Cs	Humid (1.69)	South Fork Coquille River	OR	438	55	0	15	1
Cs	Humid (1.39)	Redwood Creek	CA	717	96	0	10	1
Ds	Humid (1.04)	East Fork Pine Creek	ID	190	14	0	15	1
Df	Humid (1.00)	Susitna River	AK	50,142	463	0	14	1
Df	Dry Sub-Humid (0.51)	Middle Loup River	NE	8,107	365	0	23	1
Df	Humid (1.17)	White River	VT	1,787	82	0	25	1
Df	Semi-Arid (0.37)	Little Snake River	CO	2,559	85	0	10	1
Df	Humid (0.87)	Salt River	MO	1,621	135	0	10	1

* Data sources: 1. USGS; 2. USDA–ARS.

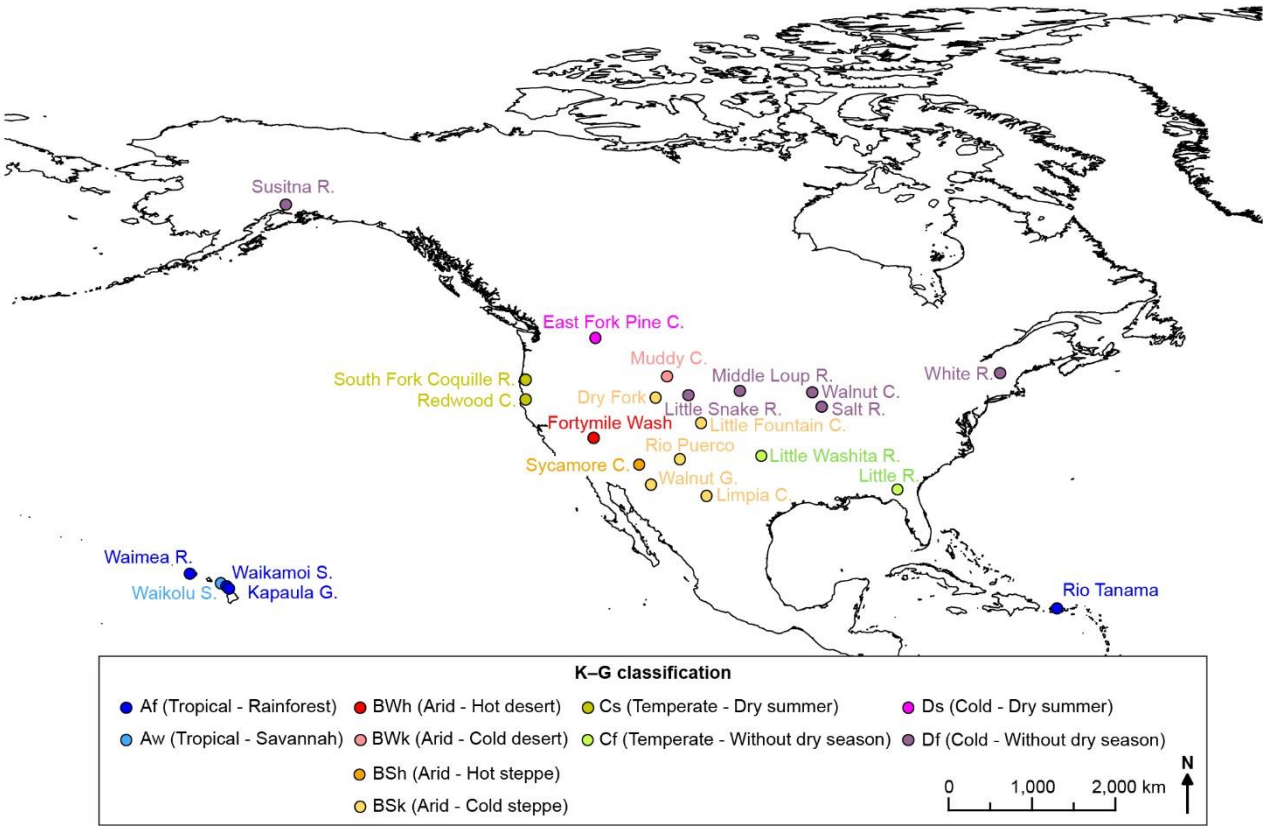

Figure 4.3 Locations of analysed rivers by K–G climate classification (C.: creek; G.; gulch: R.: river; S.: stream).

For rivers compiled from USGS, mean daily streamflow data were downloaded. For Walnut Gulch, runoff data of gauging stations of the mainstem were used, and converted runoff into discharge by multiplying by drainage area, and divided by the flow duration. The simultaneous records of gauging stations of each river were extracted. The ephemerality of streamflow is defined as the percentage of time with no flow during the simultaneous record:

$$\text{Ephemerality} = \frac{\text{Number of days with zero flow}}{\text{Number of days of simultaneous record}} \times 100\ \% \tag{4.1}$$

To compare characteristics of discharge between flood magnitudes, flood events were classified into four categories according to flood magnitudes: (1) extreme flood event; (2) large flood event; (3) moderate flood event; and (4) small flood event. Extreme flood events are defined as the top 10 events with the highest daily discharge of the station. The large events are those with peak daily discharge within the range of Q_{90}±30%, and the moderate and small events are within Q_{75}±30% and Q_{50}±30%, respectively. The analysed events were chosen with peak discharge above Q_{50} because there are rarely floods with peak discharge

below this percentile. The downstream rate of change in streamflow, α, was calculated based solely on the power-law relationship between discharge and river length, in order to relax the assumption of *Q*–*A* dependency, which is hypothesised to be weak in drylands:

$$Q_L = Q_n \left(\frac{L}{L_n}\right)^{\alpha} \tag{4.2}$$

where Q_L is the discharge at the distance downstream, L, Q_n is the discharge of the most downstream point. The α value is negative when the discharge decreases downstream, and positive if it increases downstream. For each flood event, I estimated a best-fit power-law trendline between discharge and distance downstream. Then the α value was extracted for each power-law fit using Equation 4.2.

4.3 Relationship between ephemerality and downstream distribution of streamflow

There were 24 rivers chosen which located over different states and with various drainage areas and lengths (Table 4.1, Figure 4.3). Twelve of them are ephemeral or partly ephemeral (i.e. with at least one station of each river recorded zero flow). They are mostly classified as Arid zone of K–G classification, and Arid or Semi-arid zone of AI categories, especially rivers recorded no flow in all stations along the rivers. The remainders are perennial, all located in the Tropical, Temperate, and Cold zones of K–G classification, and mainly in the Humid zone of AI categories.

Ephemeral and perennial rivers show different patterns of downstream distribution of discharge (Appendix B). I took three rivers, Walnut Gulch (ephemerality: 90–98%), Sycamore Creek (ephemerality: 1–30%), and East Fork Pine Creek (ephemerality: 0%), as examples for rivers with high ephemerality, low ephemerality, and perennial streamflow, respectively (Figure 4.4). These rivers were chosen because they contain more gauging stations along with them and have higher similarity of discharge patterns compared to rivers with similar ephemerality. In perennial rivers, the discharge increases along the entire river, and the increasing rate tends to be higher at the downstream reach (Figure 4.4i–l). In ephemeral rivers with low ephemerality, the discharge also increases from the river source to the downstream reach (Figure 4.4e–h). However, the increasing rate of discharge tends

to be constant for larger events (> Q_{90}; Figure 4.4e, f), but the rate decreases at the downstream reach for smaller events (< Q_{75}; Figure 4.4g, h). In ephemeral rivers with high ephemerality, the discharge tends to increase from the river source to a certain distance downstream and decreases further downstream (Figure 4.4b–d). Only for extreme flood events, the discharge increases again at the most downstream section (Figure 4.4a).

By calculating α values, the patterns of downstream distributions of discharge were quantified and can be compared between rivers. In perennial rivers, regardless of flood magnitudes, all median α values are higher than zero (the median of all α values is 1.31), and the ranges of α values between flood events are small (the interquartile range, IQR, of all α values is 0.91) (Figure 4.5b). The results show that discharge in perennial rivers increases downstream, and discharge patterns between flood events are similar. However, certain perennial rivers have more extensive ranges of α values (e.g. Waikamoi Stream, Kapaula Gulch), which may be due to small drainage areas (< 10 km^2) and short river lengths (< 11 km) of these rivers (Table 4.1). In ephemeral rivers with low ephemerality, median α values are also higher than zero (except Little Fountain Creek; the median α values is 1.28 for rivers with the highest ephemerality < 75%), but the ranges of α values are larger than perennial rivers (the IQR is 1.01) (Figure 4.5a). The results show that the discharge also tends to increase downstream, but the variation of discharge patterns between flood events is higher. In ephemeral rivers with high ephemerality, the α values tend to fluctuate between positive and negative values (i.e. discharge may increase or decrease downstream; the median α values is -0.14 for rivers with the highest ephemerality > 75%), and the ranges of α values are large (the IQR is 1.67) (Figure 4.5a). Generally, in highly-ephemeral rivers, the discharge tends to increase downstream only during extreme flood events and decrease in regular flow situations (i.e. < Q_{90}). Therefore, a positive relationship between flood magnitude and α value is shown in these rivers.

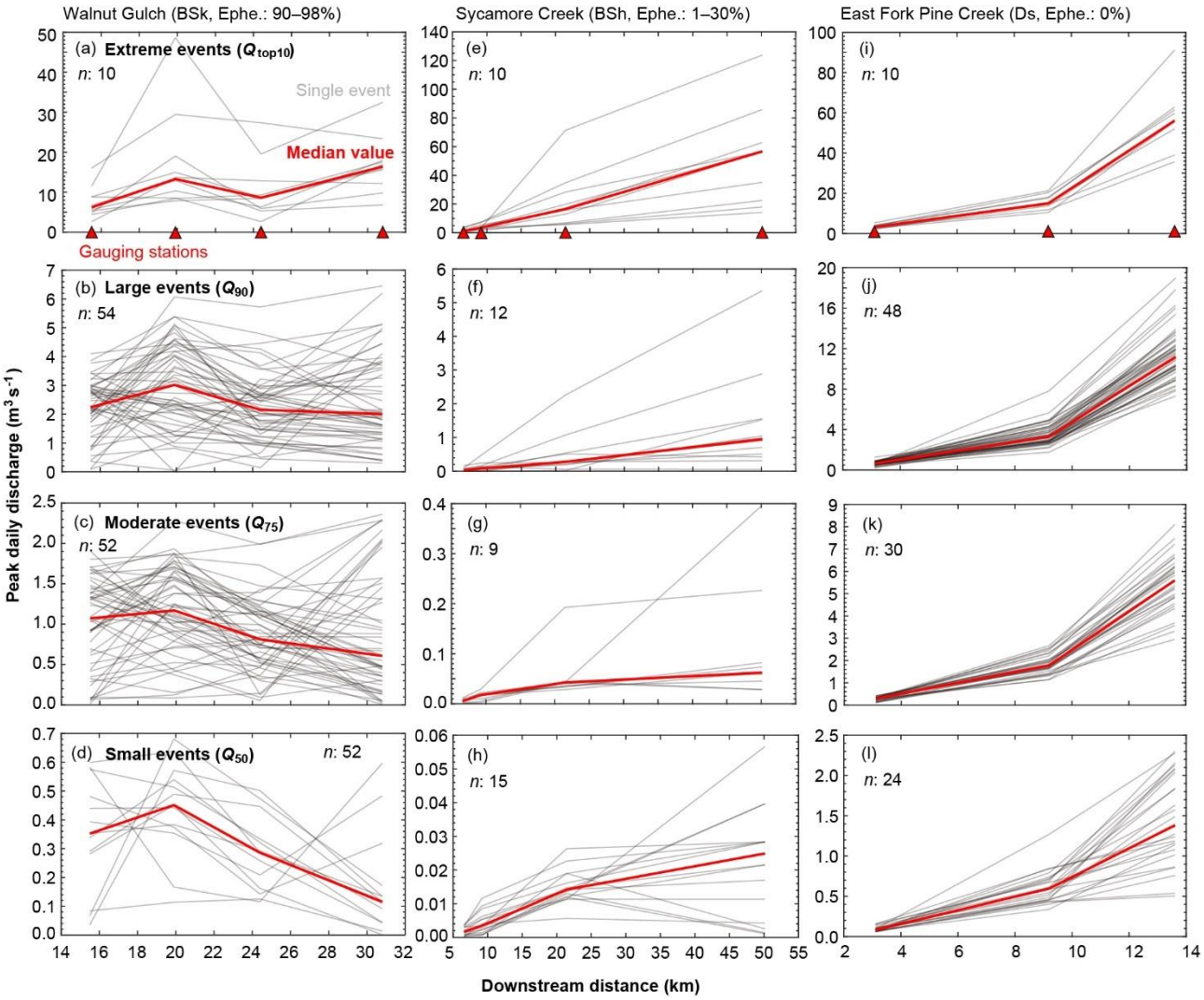

Figure 4.4 Three examples of rivers with various ephemerality for downstream distributions of discharge of compiled flood events: Walnut Gulch (a–d), Sycamore Creek (e–h), and East Fork Pine Creek (i–l). These rivers were chosen based on the number of stations along the rivers and the discharge patterns compared to rivers with similar ephemerality. The river name, K–G climate zone, and ephemerality of each river are listed on the top of each column. The grey line represents a single flood event, and the red line represents the median discharge of each flood category. The number (*n*) of compiled flood events of each flood category is listed in each plot. The red triangles on the x-axis on the first panel of each river represent the locations of gauging stations.

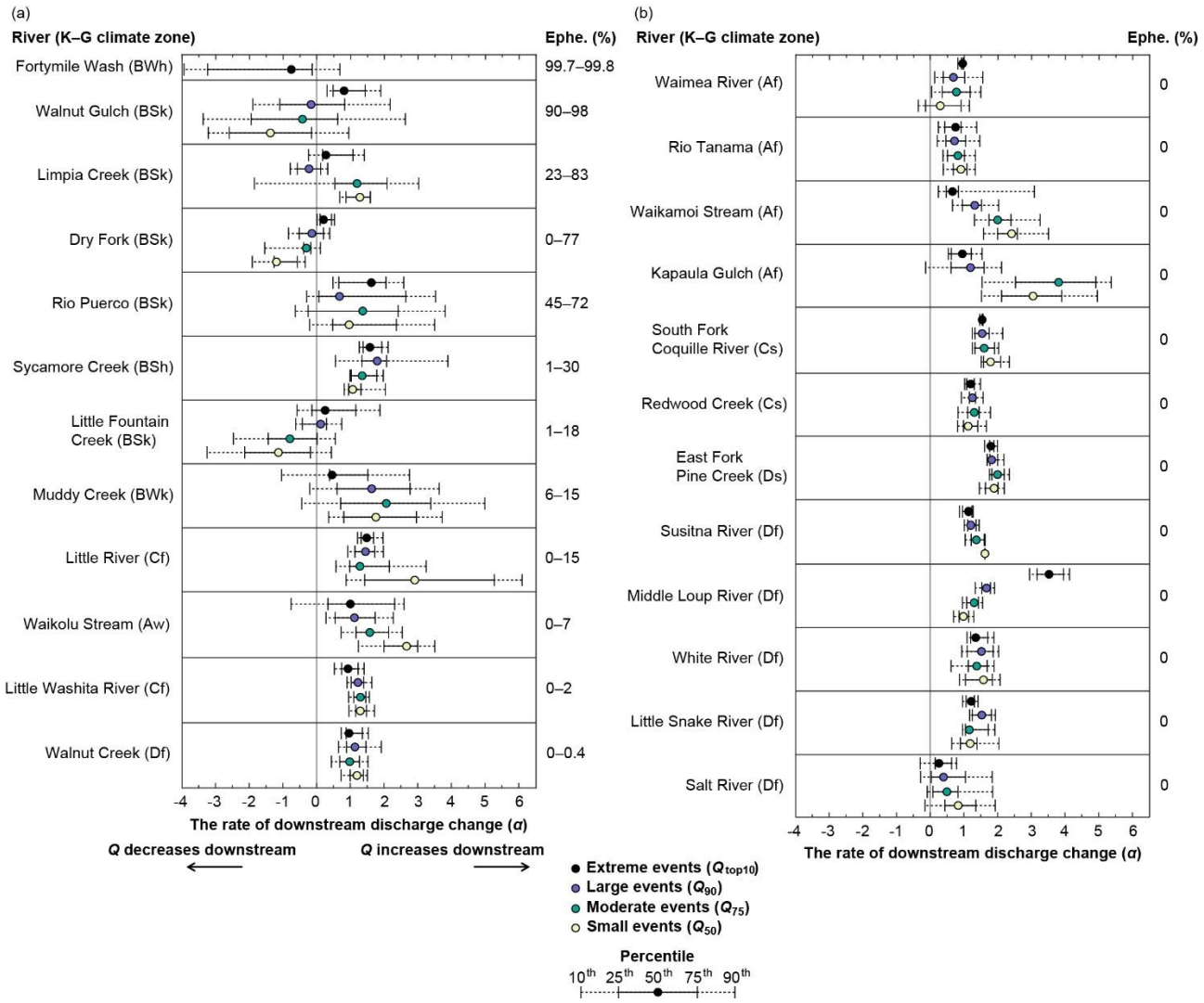

Figure 4.5 Downstream rate of change in discharge (α) of each flood category of ephemeral (a) and perennial rivers (b). The dot, colour-coded by flood category, indicates the median value of α of each flood category, and the boundaries from left to right indicate the 10th, 25th, 75th, and 90th percentiles, respectively. The grey line in each plot represents constant discharge distribution along the river (α equals zero). The order of rivers is consistent with the data in Table 4.1.

4.4 Relationship between drainage area and discharge

The *Q*–*A* relationships between discharge magnitudes of ephemeral and perennial gauging stations were analysed to explore how climate and flood magnitude control the influence of spatial scale on discharge. For perennial stations (i.e. stations have no zero flow records), positive power-law relationships are shown between drainage area and all discharge percentiles (i.e. Q_{90}, Q_{75}, Q_{50}, and Q_{25}; exponents of the power-law relationships: 0.73–0.85;

R^2: 0.67–0.87) (Figure 4.6). In contrast, the *Q*–*A* relationships are weaker for ephemeral stations (i.e. stations have recorded zero flow). There is still a positive relationship between area and Q_{90} (exponents: 0.41; R^2: 0.34). However, as the magnitude of discharge decreases, the exponent (slope) of the relationship becomes lower in ephemeral rivers, and the strength (R^2) becomes insignificant (exponents: 0.24–0.38, R^2: 0.07–0.24 for Q_{75}, Q_{50} and Q_{25}). Moreover, these relationships show that, for a given drainage area, the discharge of perennial station tend to be higher than ephemeral station. For example, for rivers with drainage area of 100 km^2, the Q_{90} of perennial station is about eight times higher than ephemeral station.

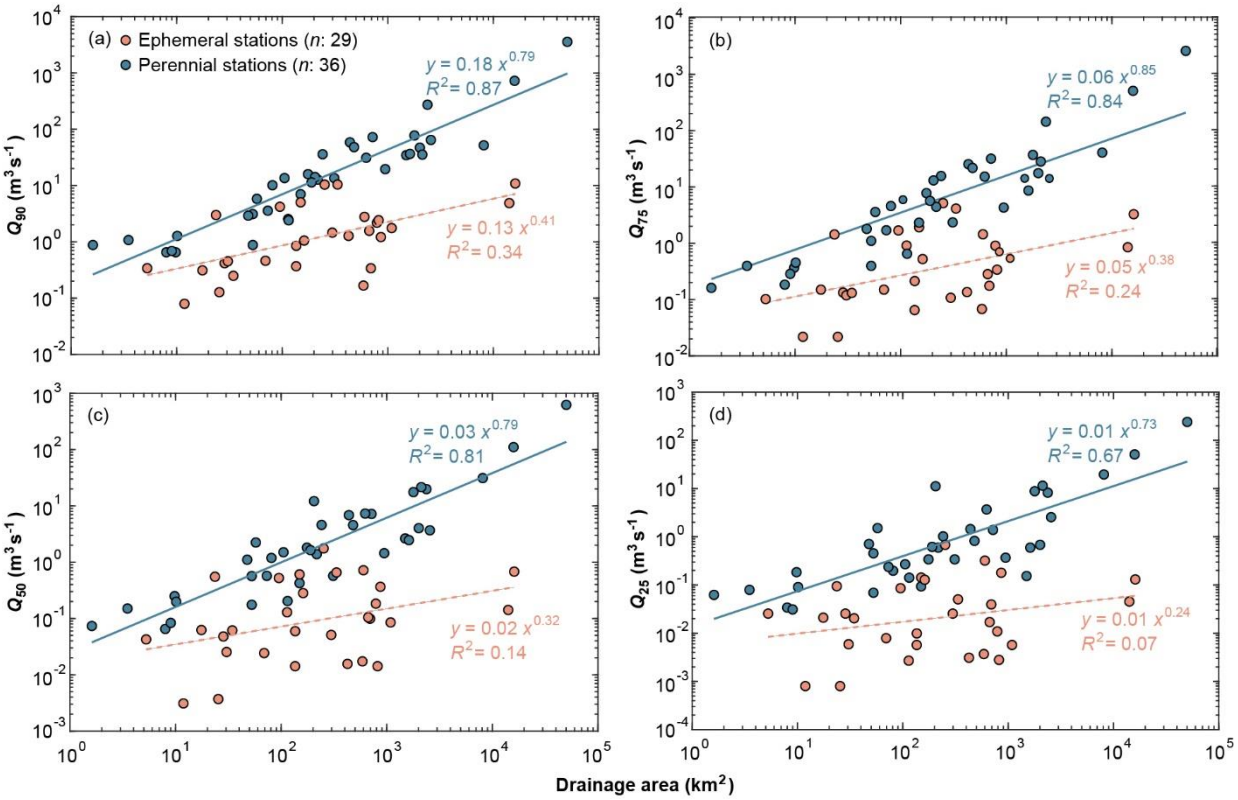

Figure 4.6 The relationships between drainage area and Q_{90} (a), Q_{75} (b), Q_{50} (c), and Q_{25} (d) for ephemeral and perennial stations. The data were calculated from all analysed records of all stations. Ephemeral stations are shown in orange, and perennial stations are in cyan. The trendlines of ephemeral stations are shown as dashed lines because the relationships for ephemeral stations are weak.

4.5 Climatic controls on streamflow characteristics

The climate of drainage basin controls its hydrological responses, such as the generation of runoff, and the rate, frequency, and spatial coverage of runoff and streamflow, reflecting climate–hydrology link within the basin (Dunne 1978; Horton 1933; Knighton 1998; Leopold et al. 1964). However, previous studies usually bias toward humid basins, with limited understanding on the climatic controls on streamflow characteristics in drylands. In this study, the streamflow data were compiled within the USA, and the downstream distributions of discharge and *Q*–*A* relationships were analysed between climate zones, especially drylands with various aridity. The key finding is a spectrum of prevailing downstream rates of change in discharge across the ephemerality of rivers (Figure 4.4, 4.5), reflecting the aridity of drainage basin (Table 4.1), and can be detected by different *Q*–*A* relationships (Figure 4.6).

During flood events, rivers with various ephemerality show different downstream distributions of discharge. In perennial rivers (mainly located in humid regions), the discharge increases downstream, and the increasing rate is higher toward downstream direction (i.e. $\alpha > 1$) (Figure 4.4i–l, 4.5b). This is due to high and frequent MAP (with long duration and high spatial footprint of rainfall) and water contributions from groundwater and tributaries (Figure 4.7a) (Dunne 1978; Knighton 1998; Leopold et al. 1964). In addition, the downstream distributions of discharge are similar between flood events and between floods magnitudes because of continuous flow in the river (for the former) and less variable peak discharge between flood events in humid regions (for the latter) (Molnar et al. 2006). These characteristics of discharge correspond with positive power-law *Q*–*A* relationship (with high slope of the equation and low variability between gauging stations), regardless of flood magnitudes (Figure 4.6), which is consistent with conventional theory (Leopold et al. 1964). The exception of low inter-event variability of discharge occurs in short rivers (Figure 4.5b), in which the streamflow lacks tributaries and flow distance to buffer the variability of rainfall and runoff through water inflow, infiltration, and flow overbank (the rivers are characterised with high topographic relief and V-shaped valley); therefore, showing higher variability of streamflow between flood events.

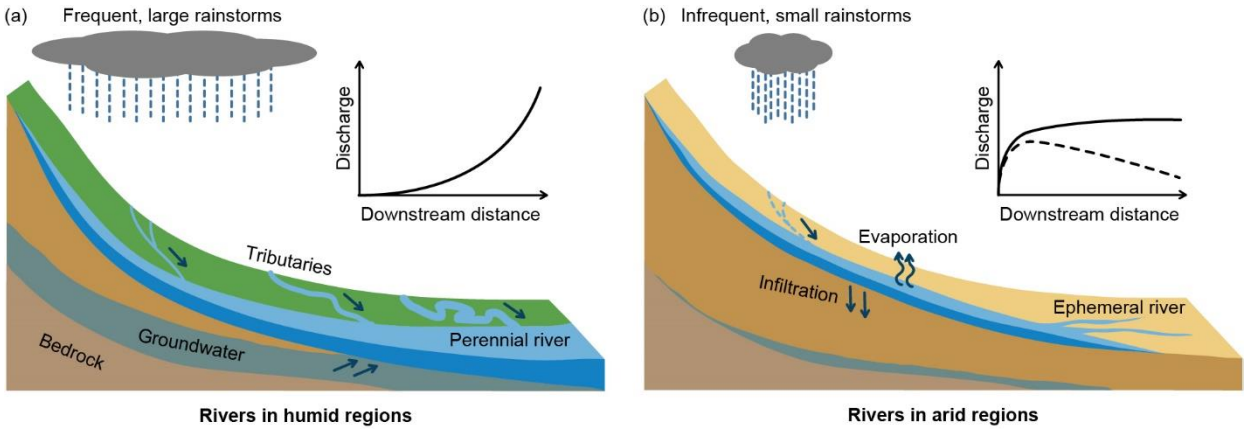

Figure 4.7 Downstream distribution of discharge and the causes in humid (a) and arid regions (b). Discharge in humid regions usually increases downstream (inserted plot) because of water supplies from groundwater and tributaries, and more extensive coverage and longer duration of precipitation. In drylands, the discharge tends to decrease downstream (dashed line of the inserted plot) except for extreme event (full line) because of high infiltration and evaporation rates, and infrequent and small covering area of precipitation.

In ephemeral rivers, the downstream distribution of discharge is more complicated, because it is controlled by the ephemerality of river (resulted from the aridity of basin), the magnitude of flood event, and the uniqueness of each event. In ephemeral rivers with lower ephemerality (located in both humid and arid regions), the discharge tends to increase downstream, similar to perennial rivers. However, the downstream-increasing rate is more constant (i.e. α ~ 1) for higher discharge (e.g. > Q_{90}) and the rate decreases toward downstream direction (i.e. α: 0–1) for small events (e.g. < Q_{75}), especially in rivers representing ephemerality along the entire channels (Figure 4.4e–h, 4.5a). In ephemeral rivers with higher ephemerality (in arid regions), the downstream-increasing rate of discharge decreases more significantly downstream, even causing the discharge at the downstream section lower than in the middle section (i.e. α < 0) for most flood events (e.g. < Q_{90}), except for extreme events which only occur several times for decades (Figure 4.4a–d, 4.5a). Generally, the downstream-increasing rate of discharge decreases more rapidly for dryland rivers with higher ephemerality and during smaller flood magnitude, and the variability of the rates between events is higher than humid rivers. These characteristics of discharge correspond to relatively stronger *Q*–*A* relationships for higher discharge (although the exponent and significance are both lower than perennial rivers), and the relationship is unclear for smaller discharge (Figure 4.6).

Former studies interpret the discharge characteristics in highly-ephemeral rives by the water contribution from tributaries within the coverage of storm, causing downstream-increasing discharge at the upstream section to a certain distance, and the transmission losses further downstream (resulted from partial area runoff and high infiltration and evaporation rates), leading to decreasing discharge downstream (Figure 4.7b) (Keppel and Renard 1962; Knighton and Nanson 1997; Tooth 2000; Wallace and Renard 1967; Yair et al. 1978). Several studies show that the amount of transmission loss is positively related to discharge because during large flood events, there may be higher water volume infiltrating into river bed by removing fine sediments on the land surface (which is not transportable during small events), and the possibility of river flowing overbanks in large events is higher (Abdulrazzak and Sorman 1994; Knighton and Nanson 1994; Lange 2005). However, there seems to be a threshold of transmission loss (as the soil moisture becoming saturated), and the proportion of water volume of transmission loss to the total streamflow is lower in large event (Hughes and Sami 1992; Keppel and Renard 1962). Therefore, there is still enough water to transport downstream for large event, leading to downstream-increasing discharge. In addition, the distributions of discharge in ephemeral rivers are highly variable between flood events due to the variable expression of climate in drylands. Precipitation in drylands is induced mainly by convective storms with high spatio-temporal variability between rainfall events (Belmonte and Beltrán 2001; Nicholson 2011; Renard 1970; Thornes 2009), and the rainfall characteristics influence the attributes of runoff and streamflow, causing the randomness of discharge patterns between flood events. The pattern of discharge in drylands is assumed to rely on the location, intensity, duration, and spatial coverage of rainfall/runoff, and the antecedent moisture of riverbed.

Previous studies rarely explore the characteristics of discharge in drylands with lower aridity. This study demonstrates that the patterns of streamflow in these regions fall in between perennial and highly-ephemeral rivers in terms of the ephemerality and downstream change of discharge. Based on previous studies, I speculate that the cause of the downstream-increasing discharge with more constant increasing rate is because relatively higher infiltration and evaporation rates, and less water contributions from tributaries and groundwater (compared to humid regions) hampering the rate increasing downstream, causing slightly lower α values than humid rivers. Nevertheless, the water volume transported from upstream section still exceeds the volume of transmission loss; therefore, the discharge increases downstream for all flood magnitudes.

Overall, this study shows various downstream distributions of discharge across the aridity of drainage basin, challenging the often-assumed downstream-increasing discharge and positive *Q*–*A* relationships. Because the water flow and the associated sediment-transport processes on the hillslopes and in the river channels are key drivers of landform changes, these findings imply distinct topographic evolutions of drainage basins between climate zones. For example, the discharge is in proportion to the stream power, and thus, the erosion rate of river channel (Lague 2014; Whipple and Tucker 1999); therefore, humid rivers with positive *Q*–*A* relationships tend to develop increasing channel width, depth, and cross-section area with drainage area by power-law relationships (Leopold and Maddock 1953). In contrast, studies show that the geometric parameters of dryland river channels tend to increase downstream until a drainage area threshold (~ 100km^2) and remain constant (Singer and Michaelides 2014; Tan et al. 2021; Wolman and Gerson 1978). This river landform in drylands may results from the distinct downstream distribution of discharge in arid rivers, since downstream-decreasing discharge (during small events) occurs more frequently but with less geomorphic effects, whilst downstream-increasing discharge (during large events) rarely happens but has higher power to shape the landscapes. In consequence, the long-term, integrated geomorphic work of arid river is hypothesised here to be constant downstream. If this is the case, I further hypothesise that in semi-arid or sub-humid regions, the channel geomotry in ephemeral rivers with low ephemerality tend to develop downstream-increaseing pattern, similar to humid rivers, but with less evident downstream trend. By exploring streamflow patterns between climate zones, this study enhances the understandings of climatic controls on the hydrological regime of drainage basin. The result implies potential influence of hydrology on the topographic evolution, addressing the climate–hydrology–erosion connections, and can be incorporated into future landscape evolution models.

4.6 Chapter summary

The streamflow data were compiled from public databases and used for analysing downstream rate of change in discharge and *Q*–*A* relationship between climate zones. The result shows various patterns of downstream distributions of discharge across the ephemerality of rivers, reflecting the local aridity of drainage basin. In perennial rivers, the discharge increases downstream because of water supply from tributaries and groundwater, and the inter-event variability of discharge patterns is low, except for short rivers. Therefore,

a positive *Q*–*A* relationship is shown for perennial rivers, regardless of flood magnitudes, and is consistent with conventional theory (Hack 1957; Leopold et al. 1964). In contrast, the downstream distribution of discharge is more complicated in ephemeral rivers since it is controlled by the ephemerality of river, the magnitude of flood event, and the characteristic of each storm. Because of transmission losses in ephemeral rivers, the discharge tends to decrease more rapidly downstream in rivers where the ephemerality is high and occur during smaller flood events. The variability of discharge patterns between events is high in ephemeral rivers because of the randomness of rainfall–runoff processes. These hydrological characteristics result in weak *Q*–*A* relationship. Although various environmental factors influence the hydrological regime of drainage basin (e.g. basin topography, organisation of channel network, and attribute of riverbed materials) (Abdulrazzak and Sorman 1994; Larned et al. 2011; Snelder et al. 2013), this study shows climatic controls on the hydrological regime and implies distinct topographic evolutions of drainage basins between climate zones.

5. Climatic controls on river long profiles globally

Parts of the following research chapter have been published under the following citation: Chen, S.-A., Michaelides, K., Grieve, S. W. D., Singer, M. B., 2019. Aridity is expressed in river topography globally. Nature, 573, 573–577.

5.1 Introduction

The long profile of a river is a plot of elevation with distance (from source area to the river mouth). As the bedrock on hillslope is weathered, the produced sediments will be detached and transported downslope by rainfall, runoff, or mass movement; as the sediments move into the river channel, the streamflow then transports them further downstream, which influence the shape of river long profile. Therefore, the shape of river long profile should reflect the net balance between sediment supply from the hillslope and evacuation from the river channel (Byun and Paik 2017; Michaelides et al. 2018; Sinha and Parker 1996; Snow and Slingerland 1987; Zaprowski et al. 2005), which may reflect the hydrological regime of drainage basin and the influence of climate.

5.1.1 The characteristics and controls of river long profile

In theory, if there is an equilibrium between sediment supply to a channel and the evacuation of the supplied sediment, a graded river profile is produced, characterised by a smooth, concave-up long profile (Sinha and Parker 1996; Snow and Slingerland 1987). The causes of concave-up long profiles are the limited ability of the river to erode bedrock in headwater areas and the general downstream increase in discharge and sediment deposition, and a decrease in sediment grain sizes on the riverbed (Charlton 2007; Ferrer-Boix et al. 2016; Hack 1957; Leopold et al. 1964; Snow and Slingerland 1987). According to stream power incision law (and the extension to transport-limited rivers), as water discharge increases downstream with drainage area due to the inflow of tributaries and groundwater (positive Q–A relationship, Section 4.1), the stream power of water also increases downstream, which erodes the riverbed and produces concave profile of river channel (Byun and Paik 2017; Charlton 2007; Whipple and Tucker 1999). Long profile shape is also controlled by sedimentary factors. If sediment load increases downstream due to contributions from

hillslopes and tributaries, the sediments will raise local bed elevation and flatten the long profile (Knighton 1998; Snow and Slingerland 1987), producing lower concavity of river profile. Moreover, the grain size of riverbed material is also seen as a dominant control of river long profile since it controls the mobility of particle and channel roughness (Blom et al. 2016; Hack 1957; Knighton 1998; Yatsu 1955). Where grain size decreases more rapidly due to higher abrasion on the sediments and grain size selective transportation, the profile is more concave because coarser grains at the upstream reach is harder to be transported and can maintain high gradient of profile, whilst finer grains at downstream section flatten the riverbed (Blom et al. 2016; Howard et al. 1994).

Because of the relationships between drainage area and discharge, river long profiles with knickpoints and other fluctuations (i.e. deviated from the smooth and concave form) are viewed as expressing the interactions of several independent variables, such as climate, geology, and human impacts (Hack 1957; Leopold et al. 1964; Phillips and Lutz 2008). In mountainous regions, because of prevailing orographic effect (i.e. precipitation is higher in headwater regions and decreases downstream), river profiles tend to be straighter compared to rivers with low topographic relief (Han et al. 2014; Roe et al. 2002). In basins with weak lithology of bedrock, rivers also tend to develop straighter profiles because of high supplements of coarse grains from the hillslope into the channel (Hanks and Webb 2006; Pederson and Tressler 2012). Within tectonically-active regions, the spatial distribution of tectonic uplift rate controls the concavity of river profile, which often develop knickpoints along the faults with higher uplifting rates (Kirby and Whipple 2001; Kirby and Whipple 2012). Human activities modify long profile through dam construction, water diversion (both decreasing its concavity because of enhanced sediment deposition) or dredging (increasing river incision and, therefore, increasing the concavity) (Wang et al. 2008). Since drainage basins often contain multiple environmental controls of river profiles, and the controls may interact with each other (Hanks and Webb 2006; Pederson and Tressler 2012), it is usually hard to detect the dominant control on the river long profile.

5.1.2 Indices of river long profile concavity

The shape of river long profile can be quantitatively expressed by the slope gradient or the overall degree of concavity (or curvature) along the profile. The slope gradient is defined as the change of elevation in the unit distance, whilst the concavity is the variation of the

gradient per unit distance. In other words, concavity is the second-order derivative of elevation with respect to distance. To quantify river profile concavity, studies have developed various concavity indices based on either the geometry of profile (e.g. the Curvature and Stream Concavity Index) or the relationships between hydraulic factors (e.g. the Concavity Index).

(1) Curvature (*C*) (Figure 5.1a) (Grieve et al. 2016):

The Curvature at the downstream distance *L*, C_L, is calculated as the second-order derivative of the change in elevation (ΔE) with respect to distance (ΔL) (Figure 5.1a):

$$C_L = -\frac{E_{L-\Delta L} - 2E_L + E_{L+\Delta L}}{(\Delta L)^2} \tag{5.1}$$

The median value of all Curvature values along the river can be used to represent the overall concavity of the river. A negative value of *C* implies a concave-up profile, whilst a positive value indicates a convex-up shape.

(2) Stream Concavity Index (SCI) (Figure 5.1b) (Snow and Slingerland 1987; Zaprowski et al. 2005):

The index is calculated by the ratio of two areas, the area between river long profile and the straight line connecting the profile endpoints (A_1), and the area of the triangle between the straight line and the axes connecting the profile (and the straight line) endpoints (A_2):

$$\mathrm{SCI} = \frac{A_1}{A_2} \tag{5.2}$$

If the profile is convex-up, the A_1 will be taken as a negative value. Suppose both axes are normalised by the length and total relief of the profile, respectively (Figure 5.1b). In that case, the A_2 will be 0.5, and the range of SCI will be between -1 (extremely convex profile) and 1 (extremely concave profile), appropriate for comparing profiles between rivers.

(3) Concavity Index (θ) (Figure 5.1c) (Flint 1974):

This index is based on the relationship between slope gradient (S) and drainage area (A) along the river channel since there is usually a negative power-law relationship between them (at least in humid regions) when the river is at a steady-state (i.e. the uplift rate equals to erosion rate):

$$S = k_s A^{-\theta} \tag{5.3}$$

where k_s is the Channel Steepness Index, and the exponent θ is the Concavity Index. A positive θ value implies a concave-up profile, whilst a negative value indicates a convex-up shape. This S–A relationship is consistent with (and can be converted from) stream power incision model, which describes the erosion rate (ε) of supply-limited bedrock river (Howard et al. 1994; Whipple and Tucker 1999):

$$\varepsilon = K A^m S^n \tag{5.4}$$

where K is the erodibility coefficient, and m and n are exponents. The drainage area represents the discharge based on the assumption of positive Q–A relationship. The θ in Equation 5.3 equals m/n, and k_s equals (ε/K)^1/n.

(4) Chi (χ) transformation (Figure 5.1d) (Royden et al. 2000):

Although the Concavity Index (Equation 5.3) is commonly used for quantifying river profile shape, it is sensitive to the noise and error of topographic data (Perron and Royden 2013; Royden et al. 2000). Therefore, an alternative method, Chi (χ) transformation, was proposed, which is based on the integration of Equation 5.3 in the upstream direction from the base level, yielding an equation for the elevation profile (Figure 5.1d) instead of gradient profile:

$$E_L = E_b + A_0^{-\theta} k_s \chi \tag{5.5}$$

where E_b is the elevation at the base level, and A_0 is the reference drainage area

(dimensionless). The longitudinal coordinate, χ (with the dimension of river length), is:

$$\chi = \int_{L_b}^{L} \left(\frac{A_0}{A_L}\right)^{\theta} dL \tag{5.6}$$

By this mean, the θ value can be estimated by the statistical test which best fit the profile data (Clubb et al. 2014; Mudd et al. 2018). Compared to analysing *S*–*A* relationship, the relation of elevation and χ can be used even if the river has not achieved steady-state, or with spatially variable uplift and erosion rates (Mudd et al. 2018; Perron and Royden 2013). Therefore, this method has increasing popularity for analysing the evolution of river long profile and its dominant control in the last decade.

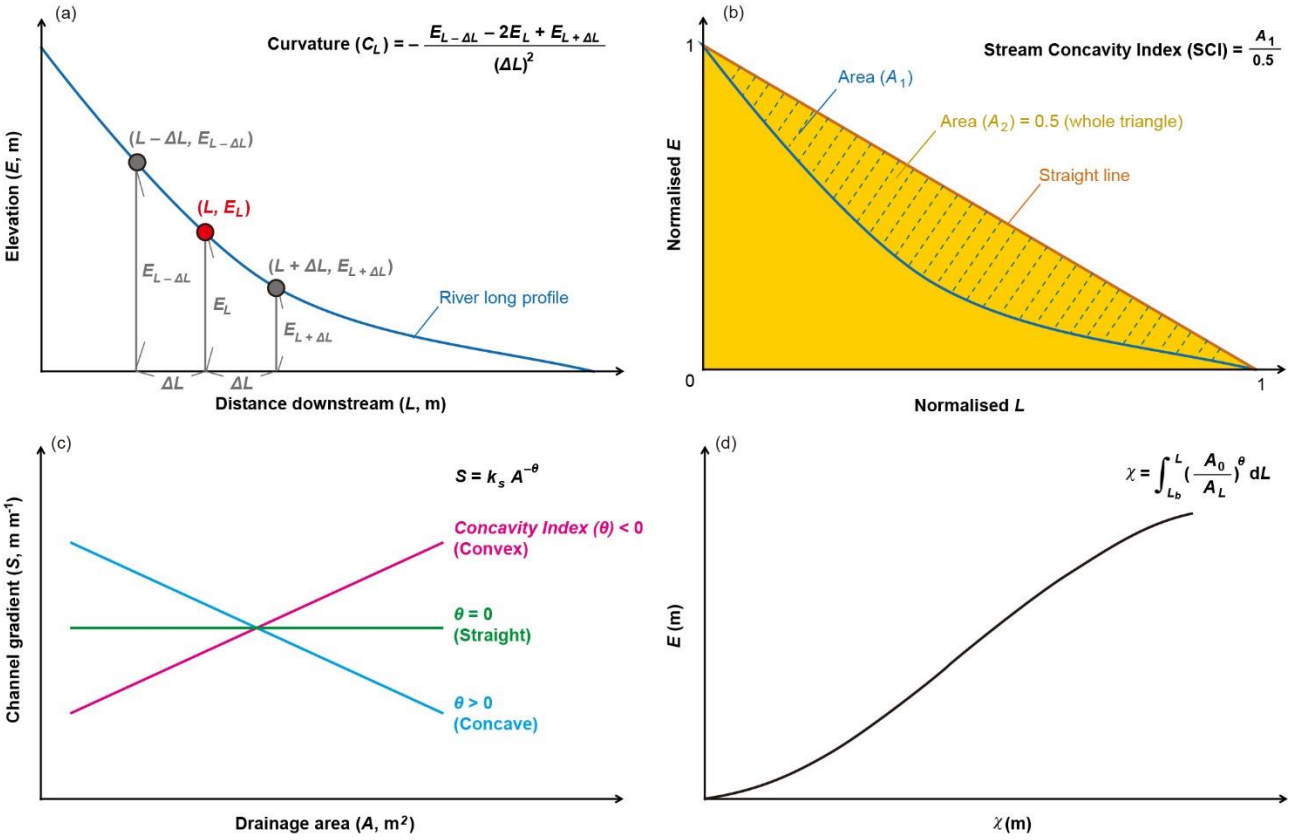

Figure 5.1 Schematic figures of indices of river long profile concavity, including the Curvature (*C*; a) (Grieve et al. 2016), the Stream Concavity Index (SCI; b) (Snow and Slingerland 1987; Zaprowski et al. 2005), the Concavity Index (θ; c) (Flint 1974), and the Chi (χ) plot (d) (Royden et al. 2000). The units in the plots are not exclusive but to show the dimensions of parameters.

5.1.3 Motivations and objectives

Although existing theory demonstrates concave-up long profile of graded river because of the influences of drainage area on water discharge and sediments, observations in dryland rivers show straighter profiles than humid rivers (Grenfell et al. 2014; Michaelides et al. 2018; Powell et al. 2012; Singer and Michaelides 2014; Sólyom and Tucker 2004; Vogel 1989). This inconsistency may result from different hydrological regimes between climate zones. As the analyses in Chapter 4 show, discharge in dryland rivers tends to decrease downstream except for extreme events, and the variability of streamflow patterns between events are high. Given that climate controls the transport of water and sediment on the hillslope and in the river channel, river long profile shapes in different climate zones may display systematic differences. However, the understanding of the global distribution of long profile concavities and their relation to climate is limited because there is lack of global database of river long profiles. In addition, modelling of long profile evolution tends to target bedrock rivers (e.g. stream power incision law), yet alluvial rivers dominate most of the cumulative global river channel length (Byun and Paik 2017). Therefore, I aimed to explore how climate influences river long profile concavity at the global scale, regardless of the type of riverbed. Although various indices of long profile concavity have been developed (Section 5.1.2), they are either sensitive to local variations along the profile (e.g. knickpoints) and require smoothing or applied to multiple segments along the same river trace, rather than to summarise the concavity of an entire profile. Some indices also assume Q–A and S–A relationships at steady-state, which are obscure in drylands (Section 4.4). Since my goal was to include conditions where these relationships are weak for complete river profiles, I opted for developing a new metric which does not rely on the relationship with drainage area, and can quantify the overall concavity of river long profile. The objectives of this study are to extract river long profiles around the globe, classify the river profiles by climate zones, develop a metric of river profile concavity, and compare the concavity between climates. I would expect to see different characteristic long profiles across various climate zones, including those which are distinct from the theoretical concave-up profile (e.g. straighter profiles in arid regions).

5.2 Methodology

To explore whether the characteristics of river long profiles are different between climate

zones, firstly, river profiles were extracted manually from Google Earth Pro (version: 7.1.8.3036) as a preliminary test. Then, I analysed river profiles automatically extracted from NASA's 30 m Shuttle Radar Topography Mission Digital Elevation Model (SRTM–DEM) (Farr et al. 2007), which was conducted by Dr Stuart Grieve (UCL) (Chen et al. 2019). Each profile was classified it by K–G and AI climate classifications (Chapter 3). The AI value was sampled at the centre of the river length. I then developed the new index of river long profile concavity, NCI, and computed NCI value of each river profile. The NCI is a metric computed solely on the basis of profile geometry that allows for standardised comparisons of river profile concavity across the globe. Finally, the LONGPRO numerical model was used to identify the dominant control on river long profile concavities between climate zones (Slingerland et al. 1994).

The manually-extracted rivers were selected across different K–G climate zones and distribute across various continents. The total number of extracted rivers was set as 100 initially, and the number of rivers in each climate zone depends on the area proportion of climate zone to the global land area. However, in some climate zones, the area proportions are less than 7%. To make the number of rivers with statistical significance, in those regions, the numbers were set as 7. Therefore, the total number of rivers digitised was 124 (Table 5.1). Rivers across the K–G climate sub zones and rivers with vegetation cover in the channel or obvious artificial impacts (e.g. reservoir, irrigation, tillage) were avoided. In each climate zone, rivers with different lengths were selected to minimise the influence of spatial scale on the long profile characteristics.

Each river was measured from the headwater to the lower reach, which is usually the estuary, the confluence of the mainstream or the point where the channel disappears. The interval of measurement was decided by the length and the mean gradient of each river. If one river is long and/or the landform is gentle, the measuring interval would be more extensive. Generally, the number of measured points for each river was between 100 to 300.

Although the resolutions and surveying periods of DEMs of Google Earth are not consistent globally, the analysed scales in this study, both spatially and temporally, are much larger than the data deviations in Google Earth. Moreover, a previous study shows that the extracted curvatures and network of rivers, and the length and relief of hillslope are not sensitive to the grid resolution of DEMs (Grieve et al. 2016). Therefore, the long profiles

acquired from Google Earth should be reliable.

Table 5.1 The land area proportion to the global land area of each K–G climate zone, and the number (*n*) of manually-extracted river long profiles.

K–G climate zone		Land area proportion (%)		*n* of extracted rivers	
Tropical		21.8		27	
	Af		4.7		7
	Am		3.9		7
	Aw		13.2		13
Arid		34.6		38	
	BWh		15.4		16
	BWk		5.3		7
	BSh		6.1		7
	BSk		7.8		8
Temperate		15.4		22	
	Cs		2.3		7
	Cw		5.3		7
	Cf		7.8		8
Cold		28.2		37	
	Ds		1.0		7
	Dw		3.9		7
	Df		23.3		23
Total		100	100	124	124

Dr Stuart Grieve extracted river long profiles from 30 m SRTM–DEM (Farr et al. 2007) using the software LSDTopoTools (Clubb et al. 2017) and build the GLoPro database (Chen et al. 2019). The rivers were extracted by a contributing area threshold method, which calculated river flow direction by the traditional D8 method, and decided the location of river head by a fixed threshold value of contributing area. The threshold value was set as 25,000 pixels, approximately to 22.5 km^2 at the equator. Only the mainstream (the longest river) of each drainage basin and/or its sub-basins which does not cross between K–G sub zone was selected. The extracted rivers are between 60°N and 56°S, since this is the extent covered by the SRTM–DEM.

NCI is defined as the median value of all vertical offsets between river long profile and the straight line fitted through the profile endpoints and normalised by topographic relief. I define the endpoints of the long profile (L_0, E_0) and (L_n, E_n) where L is distance downstream, E is elevation, and where the subscripts 0 and n indicate the most upstream and downstream points, respectively. To calculate NCI, a straight line is fitted through the endpoints of the

long profile described by the equation $Y_L = E_0 - aL$, where Y_L is the elevation on the line at each distance L, a is the gradient of the line, and E_0 is the y intercept. Then, at each measured point along the profile, the vertical offset between the river profile and the fitted straight line is calculated as $E_L - Y_L$. I then calculate the median value of all offsets, normalised by the total topographic relief along the profile ($E_0 - E_n$) to enable comparison across scales (Figure 5.2). Therefore, NCI is defined as follows:

$$\mathrm{NCI} = \mathrm{median}\left(\frac{E_L - Y_L}{E_0 - E_n}\right) \tag{5.7}$$

NCI is negative when the profile is concave, zero when the profile is straight, and positive if the profile is convex.

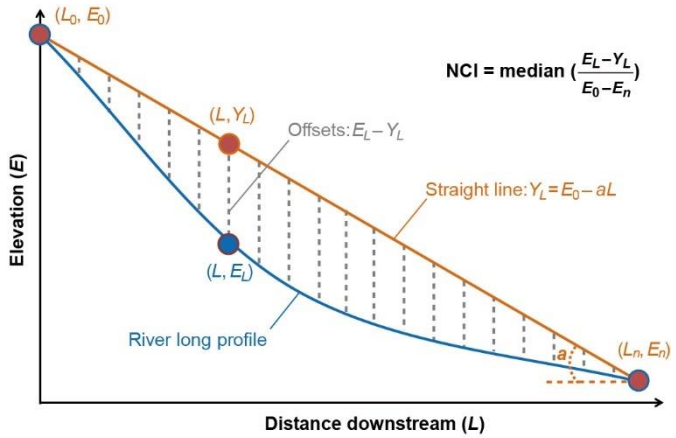

Figure 5.2 Schematic of NCI calculation. The blue line is a measured or modelled river long profile, and the orange line is the straight line fitted through the profile endpoints. The offset (E_L–Y_L) is the difference in elevations between the river long profile (E_L) and the straight line (Y_L) at each distance L. NCI is the median value of all offsets divided by topographic relief (E_0–E_n). NCI is negative when the profile is concave, zero when the profile is straight, and positive if the profile is convex.

Other concavity indices have been developed in the literature (Section 5.1.2). Compared to these metrics, the advantages of NCI are: (1) it calculates all offsets of measured points at the native resolution of the measurements (DEM, field survey, model output); (2) it does not require any smoothing along the profile; (3) it does not require any assumptions about the Q–A or S–A relationships; and (4) it can be used to quantify the concavity of a simulated profile (devoid of basin area). The calculation of all vertical offsets along the profile enables

the representation of local variations along the profile (for example, knickpoints), but the calculation of NCI is not sensitive to these variations (see Figure 5.3 and 5.4 for examples).

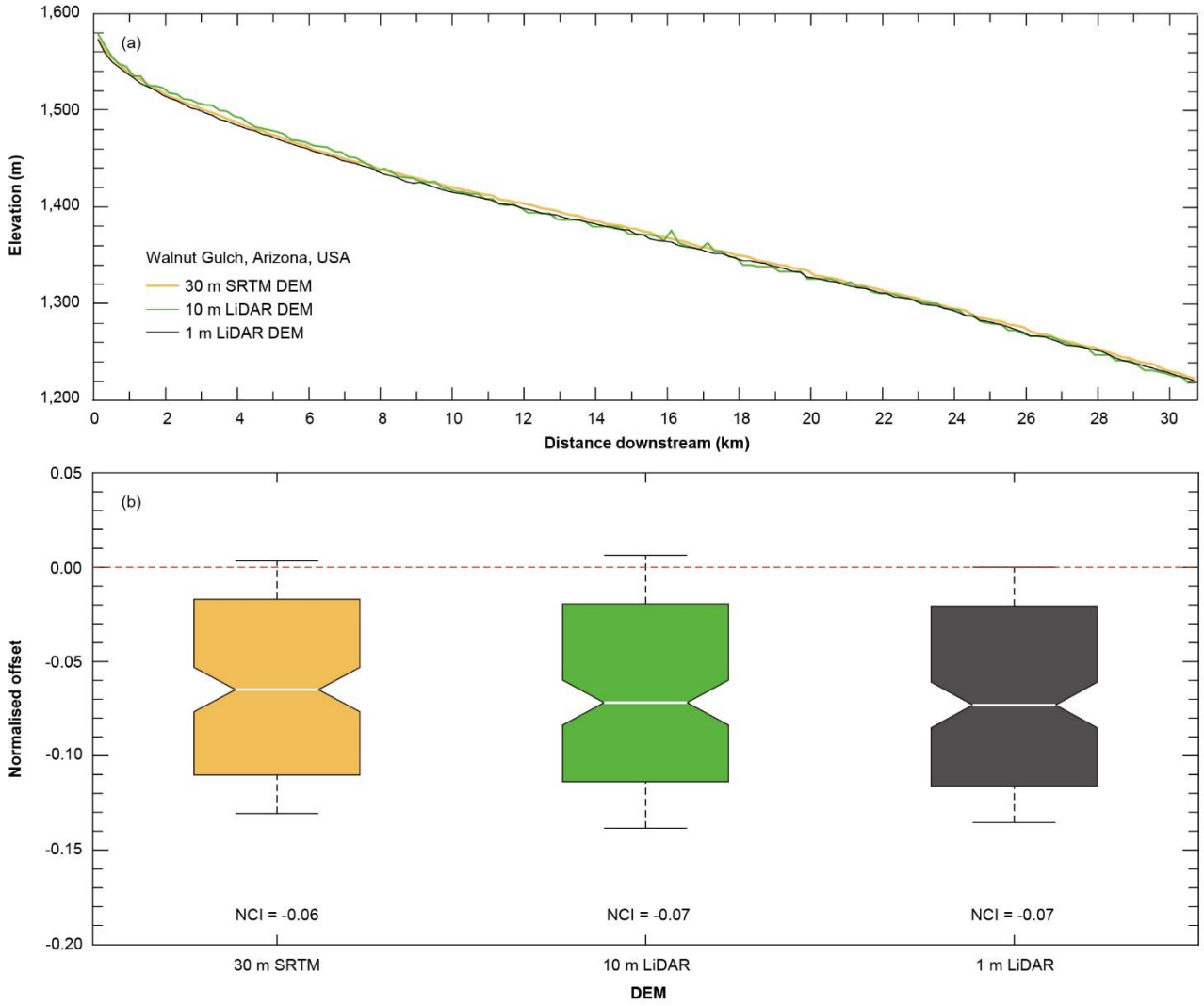

Figure 5.3 River long profiles (a) and NCI values (b) for Walnut Gulch extracted from digital elevation models (DEMs) of varying resolutions. The DEMs include Shuttle Radar Topography Mission (SRTM) and Light Detection and Ranging (LiDAR) DEMs. Normalised offsets in panel b are the offsets between river long profiles and the straight-line-fitted profile, divided by topographic relief. Positive offsets indicate that the elevation of the river long profile is higher than the straight line, whereas negative values mean the elevation of the long profile is lower than the straight line. The red dashed line indicates zero NCI (straight profiles). On each box, the central line indicates the median value, which is defined as the NCI value, and the bottom and top edges indicate the 25th and 75th percentiles, respectively. The notch represents the range of the median at the 5% significant level. These profiles show that DEM resolution has a minimal influence on NCI.

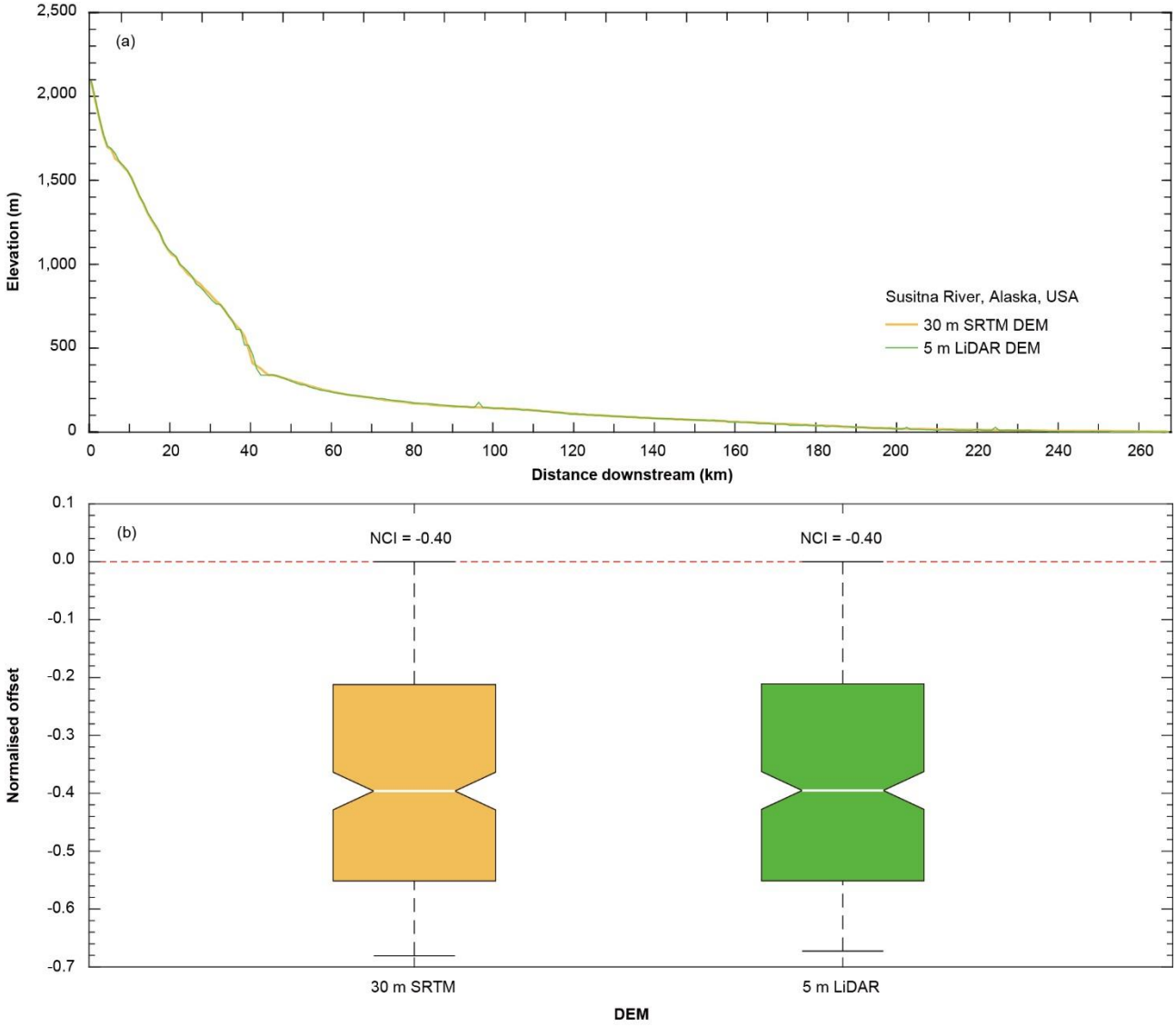

Figure 5.4 River long profiles (a) and NCI values (b) for Susitna River extracted from DEMs of varying resolutions. See the caption of Figure 5.3 for detailed explanation.

The river extraction methods and concavity calculation result in an internally consistent NCI dataset. The impact of the channel head location of GLoPro on NCI is minimal because only the longest river of each basin or sub-basin was analysed (not smaller tributaries). Therefore, I am confident in using NCI to compare rivers of different sizes and across climate zones.

Here I addressed the null hypothesis that there are no differences in NCI between climate zones. The river long profiles were not censored for any other natural or anthropogenic factors, and they include both bedrock and alluvial rivers. I did not make any assumptions about whether the profiles are steady-state (equilibrium) or transient, but assumed that climate categories in the K–G classification and the AI had not changed substantially over

the timescales of long profile development.

LONGPRO is a one-dimensional numerical model that simulates the dynamic evolution of the river long profile and can be used to explore responses to varying water discharge, sediment supply, riverbed grain size, tectonic uplift and base level (Slingerland et al. 1994). LONGPRO includes gradually varied flow, sediment transport by Yang's unit stream power equation (Yang 1973) and conservation of mass. I used LONGPRO to explore the relative controls on river long profile development. My goal was not to explore the parameter space of LONGPRO exhaustively, but rather to look at first-order effects of downstream discharge variation on the profile development for transport-limited conditions in a manner that is analogous to the supply-limited case generalised by stream power incision theory (Whipple and Tucker 1999).

Given the large variance in drainage basin properties across the globe, several parameters were fixed in LONGPRO in order to isolate the effects of the climate expression within discharge, and the corresponding impact on long profile evolution. I assumed no tectonic uplift and no base level change (but see Section 5.5 for sensitivity analysis of these and other factors). The river length was set to be 25 km, a value similar to the median value of all extracted rivers in GLoPro (26.7 km). The initial profile slope was set to 0.003, representing a linear decline from 75 m elevation at the upstream profile point (that is, E_0) to 0 m at the downstream point (E_n). Base level (the elevation of river water level above the riverbed at the most downstream point) was set at a constant value of 5 m. The maximum water discharge (Q_{max}) was set as 25 $m^3\ s^{-1}$. Sediment-related parameters in LONGPRO include sediment supply at the upstream boundary (MFEED), sediment concentration of lateral inflow to the mainstem (SEDCON), the median grain size of bed material (DIMID), and Manning's roughness coefficient (Manning's n). For these parameters, I set the following values as constants: MFEED to 10 kg s^{-1}, DIMID to 1 mm (uniform grain size along the profile), and Manning's n to 0.04. SEDCON was set to 0.00005 (the proportion of sediment concentration delivered by lateral tributary inputs), which follows the formula:

$$q_{s,\,L} = \text{SEDCON}\,(Q_L - Q_{L-1})(\Delta t) \tag{5.8}$$

where $q_{s,L}$ is the mass of lateral sediment supply at the distance downstream, L, which enters

over timestep Δt. For downstream decreasing discharge, the positions of Q_L and Q_{L-1} were exchanged in Equation 5.8, in order not to get a negative $q_{s,L}$ value. The distance between calculated nodes was set as 1 km, and the timestep Δt was set to 24 h. The models were run for 500 years of effective discharge, by which time the rate of change to the profile became relatively small. In fact, the model tended to adjust to near-steady-state conditions very rapidly, rendering the model results insensitive to the initial profile, as per the model's design (Slingerland et al. 1994). Since effective discharge tends to be expressed for much briefer periods (for example, bankfull discharge is often assumed to have a return period of about 1.5 years), the model simulation time actually represents a much longer period than 500 years of topographic adjustment.

I varied the downstream rate of change in discharge, α (Equation 4.2), to explore the effects of climatically driven discharge on long profile evolution in LONGPRO, and relaxed the assumption of Q–A dependency from stream power theory since this assumption breaks down in drylands (see Chapter 4). The original LONGPRO code can only simulate constant or linearly downstream-increasing discharge. To vary the downstream rate of change in discharge, the LONGPRO code was modified into Equation 4.2 to enable the power-law exponent α to vary from positive to negative values. For downstream-increasing discharge, Q_n (the discharge of the most downstream point) equals Q_{max} (25 m^3 s^{-1}). However, for downstream decreasing discharge, Q_{max} occurs at the most upstream point (Q_0), and Q_n is calculated from Equation 4.2 for the given α value. In this manner, I simulated variations in downstream discharge and their impact on long profile evolution. For each simulation, a long profile was generated for which I calculated the NCI.

5.3 Preliminary analyses of manually-extracted river long profiles

The manually-extracted rivers distribute across various continents all over the globe (Figure 5.5). The information of each river (e.g. K–G climate zone, region/country, river length, spatial interval of measurement, and the NCI value) are in Appendix C; the river long profiles are in Appendix D.

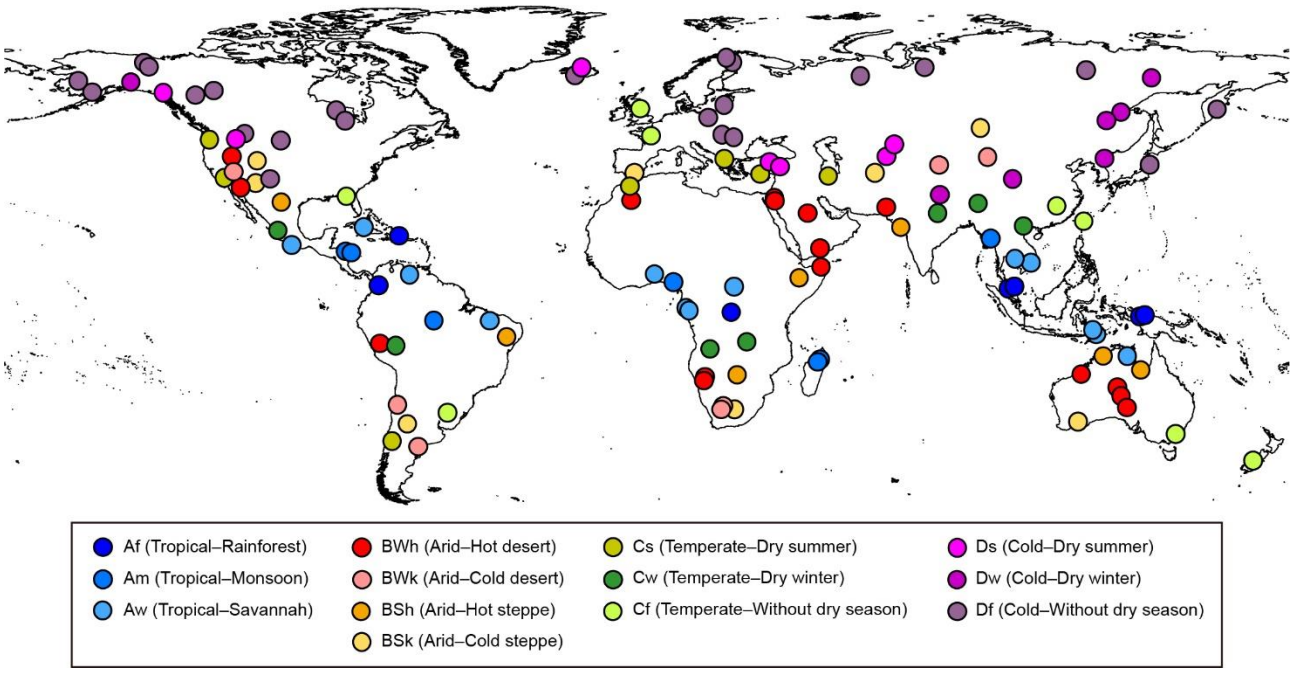

Figure 5.5 Global map of manually-extracted river long profile locations by K–G climate classification. River long profiles were extracted from Google Earth. The number of rivers is 124.

The distributions of NCI of river long profiles in all K–G climate zones tend to be negative, indicating that river profiles are concave (Figure 5.6). However, NCI values in the Arid zones are closer to zero compared to other humid zones, which shows that river profiles in the Arid zones are relatively straighter.

By conducting K–W test, there are significant differences between Af (Tropical–rainforest) and BWh (Arid–hot desert) zones (P = 0.01), Af and BSk (Arid–cold steppe) zones (P = 0.04), Am (Tropical–Monsoon) and BWh zones (P = 0.02), and Am and BSk zones (P = 0.05), but not between other comparisons (P > 0.05), which may due to limited number of rivers of other comparisons. Nevertheless, as I summed up the NCI from each climate sub zone into four main climate zones (i.e. the Tropical, Arid, Temperate, and Cold zones), there are significant differences between the Arid zone and other three main zones (P < 0.01), but not between the humid main zones (P > 0.05).

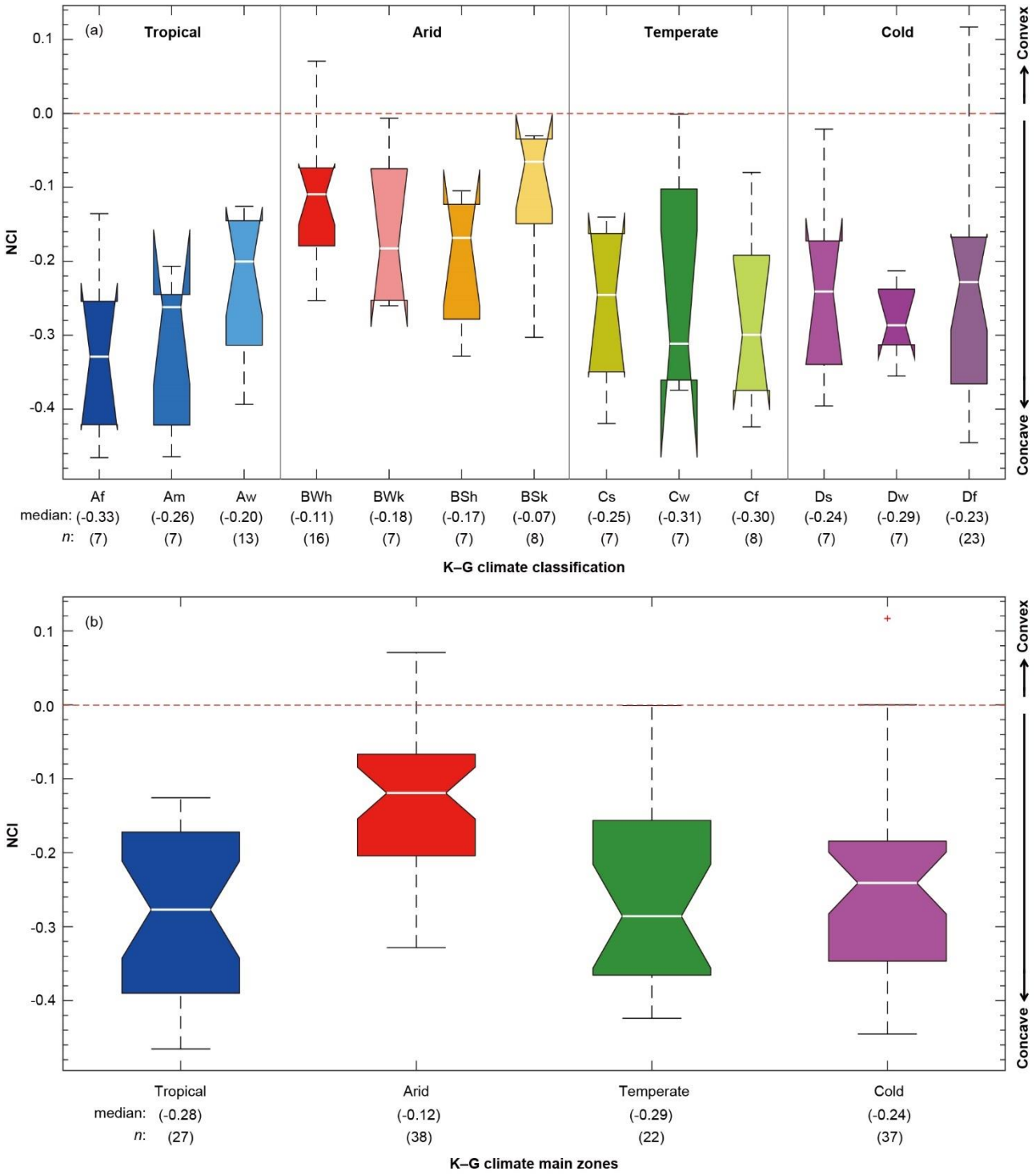

Figure 5.6 The boxplots of NCI distributions between K–G climate sub zones (a) and four main zones (b). The red dashed lines indicate straight profile. The median value and the number of data (*n*) of each boxplot are listed below each plot. This figure shows that arid regions have NCI distribution closer to zero, indicating straighter profiles compared to other humid regions.

The topographic parameters (river length, mean gradient, and relief) of selected rivers in the Arid zones are not different from other humid zones (Figure 5.7). Moreover, the relationships between NCI and these topographic parameters are not clear. These results indicate that the significant difference of long profile concavity in the Arid zone is not due to topographic factors, but may relate to the distinct hydrological controls on river landform.

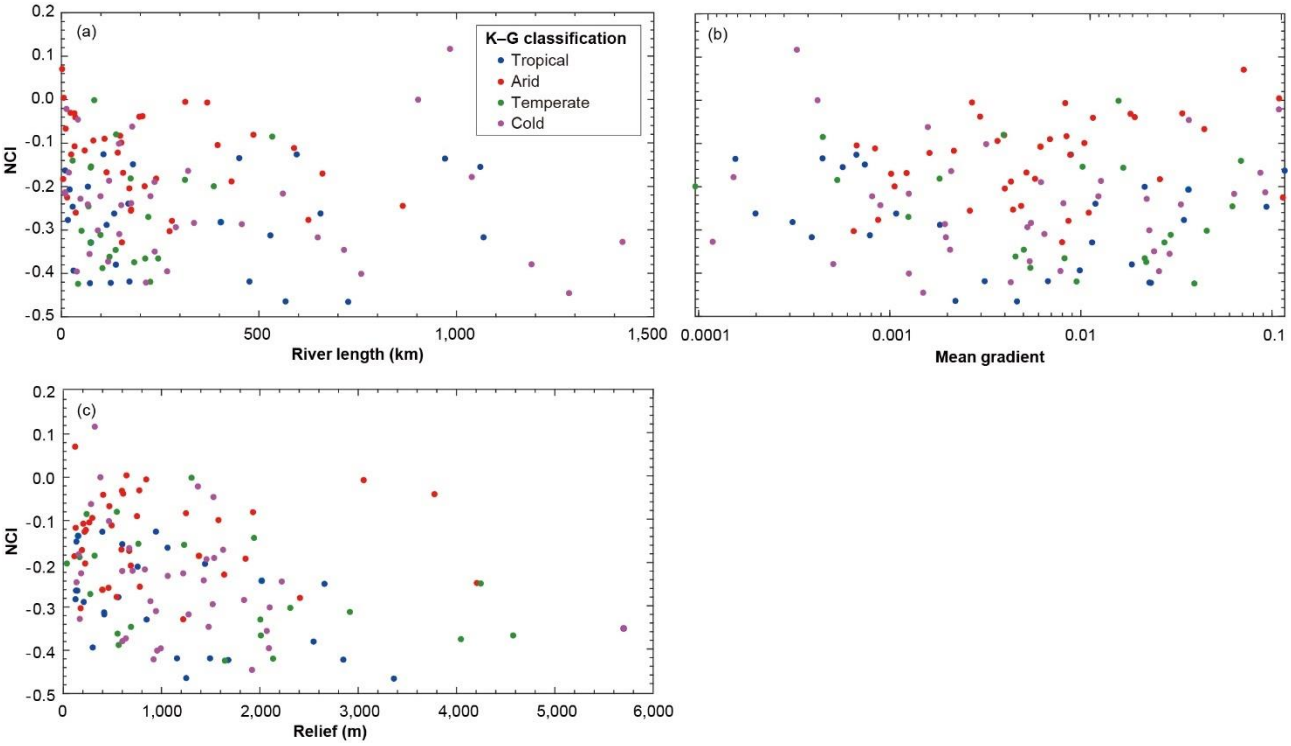

Figure 5.7 Relationships between NCI and topographic metrics, colour-coded by K–G main climate zones. The topographic metrics include the river length (a), mean gradient (b), and relief (c) of long profiles. This figure shows no clear relationship between NCI and any of these topographic metrics.

5.4 Global analyses of river long profile concavity

Preliminary analyses of manually-extracted rivers indicate that rivers in arid regions have less concave long profiles compared to humid regions. To confirm this characteristic and extend the database to include more rivers around the globe, I acquired rivers from GLoPro database (which includes 333,502 rivers), calculated the NCI of each river, and classified them not only by K–G climate classification, but also AI categories, to further investigate the influence of aridity on river long profile.

The global distribution of NCI values does not suggest any strong geographic biases, although there are clear concentrations of convex (southern Siberia), concave (southeast Asia), and nearly straight (Arabian peninsula) rivers (Figure 5.8). I present the NCI distributions of different climate categories based on Kernel density estimation (KDE). KDE is a nonparametric representation of the probability density function for the sample data. To show the distribution of NCI values of each climate zone, I used the built-in function, *ksdensity*, in MATLAB. NCI distributions of different climate classes (Figure 5.9a) overlap and display great breadth, reflecting the large sample size and the many interacting independent variables (climate, tectonics, lithology and human factors) that affect drainage basin development. Comparing the four main K–G climate zones, all NCI distributions are negatively skewed, revealing that river long profiles are generally concave-up. However, compared to the other three main climate zones (Tropical, Temperate and Cold), the NCI values for Arid zone rivers are notably closer to zero (straighter) with a narrower distribution (Table 5.2), consistent to the preliminary result from manually-extracted rivers. Within the Arid zone, the results of its four sub-zones also reveal that NCI distributions of BWh and BWk (Arid–desert) are skewed toward zero (profiles are straighter) compared to BSh and BSk (Arid–steppe) (Figure 5.9b), which further strengthen the finding.

To further explore this result, I investigated the relationship between NCI for the AI climate category. There is a systematic increase in NCI distribution medians from concave-up to straighter profiles as aridity increases (Figure 5.9c, d). Furthermore, there is a higher frequency of concave river profiles within humid regions (combining the Dry sub-humid and Humid categories of the AI) (Figure 5.9e), and a higher frequency of straighter profiles in drylands (combining the Hyper-arid, Arid and Semi-arid categories of the AI). Moreover, K–S test also suggests smaller *P* values when comparing NCI of arid zones to humid ones (Figure 5.10), even though all comparisons show statistical differences between NCI distributions (*P* values are between 1×10^{-250} and 1.48×10^{-22}).

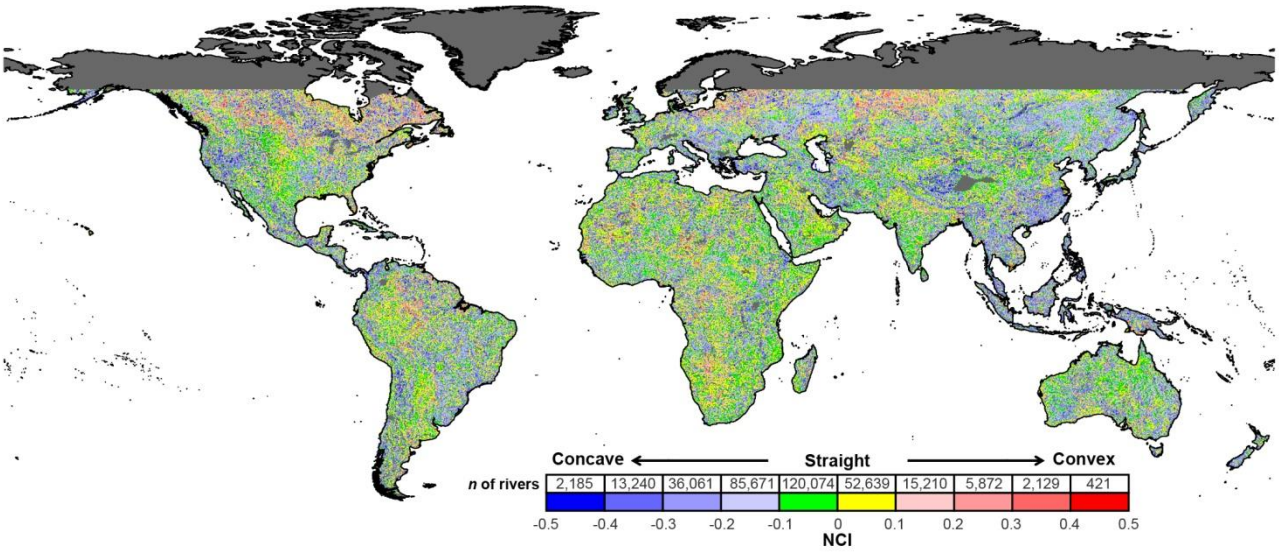

Figure 5.8 Global map of river long profiles acquired from GLoPro and classified by NCI values. Each dot identifies the most downstream point of each river profile, colour-coded by NCI value. The inset table shows the number of rivers in each NCI bin.

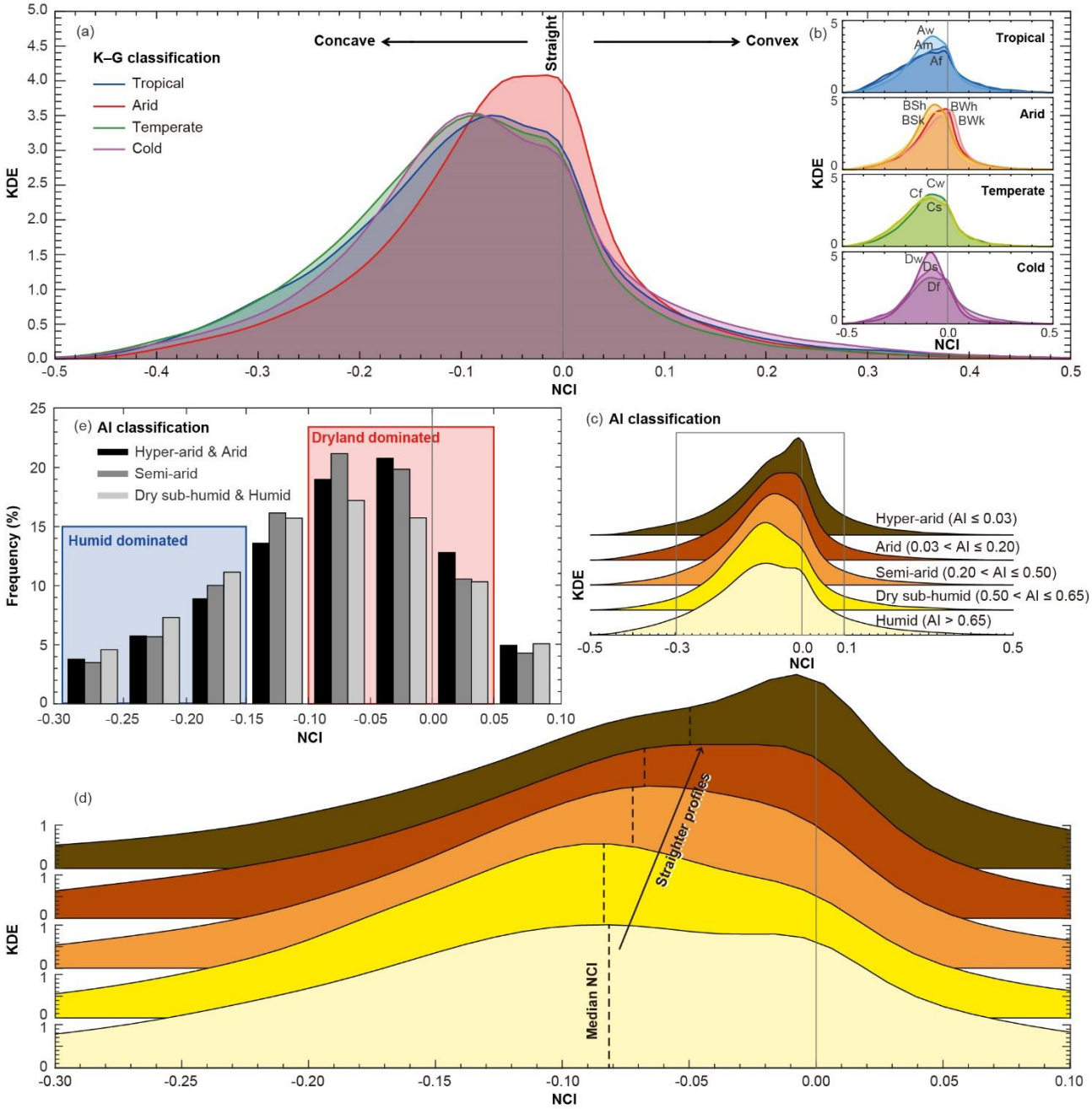

Figure 5.9 Effect of climate on NCI. Comparisons of Kernel density estimation (KDE) of NCI values for four main K–G climate zones (a) and the sub-zones (b) highlight the distinctiveness of Arid zone concavities. KDE values versus NCI values for AI climate categories (c) show variations in NCI distributions based on the AI (d is an enlargement of the rectangle in c, and the dashed lines represent the median NCI of each AI category). Frequencies of combined AI categories between NCI distributions (e) highlight dryland-dominated and humid-dominated bins of NCI values, where dryland includes the Hyper-arid, Arid and Semi-arid categories and humid include the Dry sub-humid and Humid categories. The grey vertical line on each plot represents straight profiles (NCI = 0).

Table 5.2 Information on the number of rivers and summary statistics of NCI by K–G and AI climate classifications.

K–G climate sub-zone	Af	Am	Aw	BWh	BWk	BSh	BSk	Cs	Cw	Cf	Ds	Dw	Df	All
n of rivers	13,319	10,020	35,950	50,760	17,697	18,775	26,132	6,983	16,654	25,002	3,476	20,213	88,521	333,502
K–G climate main zone	**Tropical**			**Arid**				**Temperate**			**Cold**			
n of rivers	59,289			113,364				48,639			112,210			
K–G climate sub-zone	**Af**	**Am**	**Aw**	**BWh**	**BWk**	**BSh**	**BSk**	**Cs**	**Cw**	**Cf**	**Ds**	**Dw**	**Df**	**All**
Median of NCI	-0.083	-0.073	-0.081	-0.058	-0.067	-0.063	-0.075	-0.106	-0.080	-0.098	-0.083	-0.105	-0.070	-0.076
K–G climate main zone	**Tropical**			**Arid**				**Temperate**			**Cold**			
Median of NCI	-0.080			-0.064				-0.093			-0.080			
K–G climate sub-zone	**Af**	**Am**	**Aw**	**BWh**	**BWk**	**BSh**	**BSk**	**Cs**	**Cw**	**Cf**	**Ds**	**Dw**	**Df**	**All**
IQR of NCI	0.188	0.176	0.141	0.130	0.147	0.120	0.141	0.161	0.150	0.157	0.142	0.110	0.158	0.150
K–G climate main zone	**Tropical**			**Arid**				**Temperate**			**Cold**			
IQR of NCI	0.159			0.135				0.157			0.154			

AI climate zone	Hyper-arid	Arid	Semi-arid	Dry sub-humid	Humid	All
n of rivers	21,070	56,571	63,925	33,499	156,759	331,824
Median of NCI	-0.050	-0.068	-0.073	-0.084	-0.082	-0.075
IQR of NCI	0.131	0.141	0.130	0.138	0.163	0.150

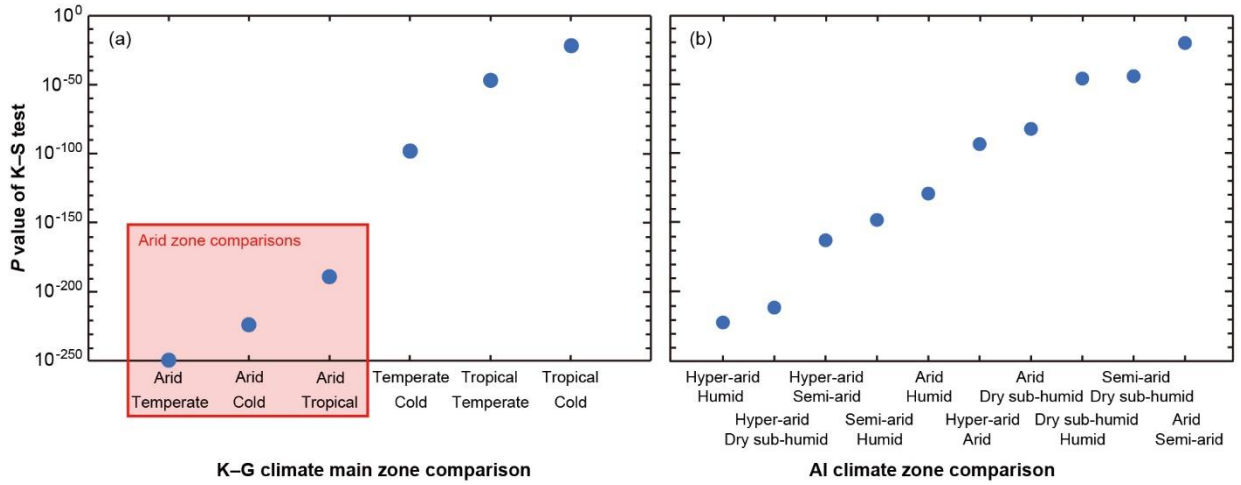

Figure 5.10 Statistical differences of NCI distributions between climate zones. Graphical results of two-sample Kolmogorov–Smirnov (K–S) tests, which include the *P* values of NCI comparisons within the main K–G climate zones (a) and within the AI climate categories (b). The red box in panel a shows the comparisons involving the Arid zone, which all have smaller *P* values than other comparisons.

Similar to the comparison between NCI and topographic parameters of manually-extracted rivers, the relationships between NCI of rivers acquired from GLoPro and their topographic metrics also suggest no clear relationship between them (Figure 5.11). This result indicates that NCI is not controlled by topographic controls, and the NCI is unbiased. In other words, the straightness of the long profile appears to be directly related to the water balance of a region, and by extension, so is its expression within hydrological regimes that erode riverbeds.

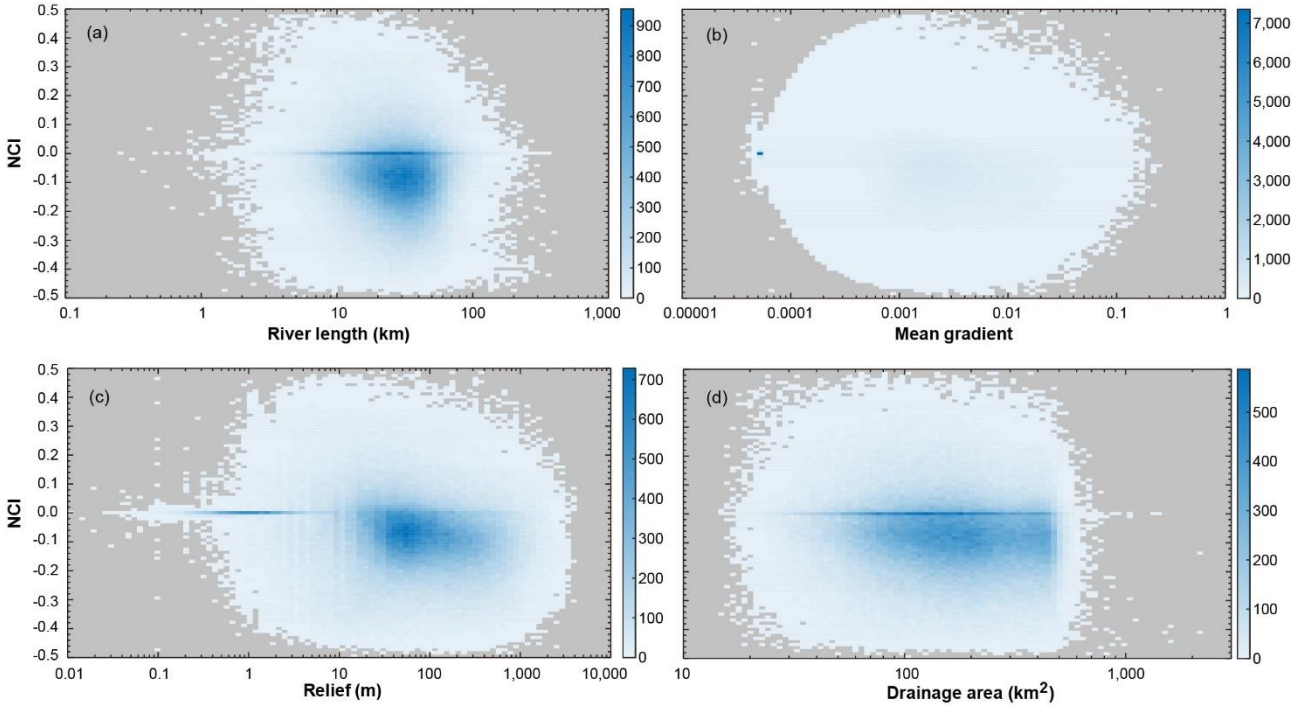

Figure 5.11 Relationships between NCI and topographic metrics. The topographic metrics include the river length (a), mean gradient (b), relief (c), and drainage area (d). The density of points (number of rivers represented by each pixel) in the scatter plot is shown in the colour scales to the right of each panel. The results show no apparent relationship between NCI and any of these topographic metrics, suggesting that NCI is unbiased.

5.5 Simulating the influences of hydrology on river long profile evolution

Why are arid river long profiles straighter than humid ones? Stream power theory indicates that the variation of discharge with drainage area influences long profile concavity for supply-limited channels (Whipple and Tucker 1999). I sought to relax this assumption of *Q*–*A* dependency and thus provides a more general mechanistic explanation of the results of long

profile concavity, and one that applies to transport-limited channels. Specifically, I used the LONGPRO model and simulated the evolution of river long profiles using six values of α that together represent a range of downstream decreasing and increasing discharge rates (α = -2, -1, -0.5, 0.5, 1, 2). All other model parameters were kept constant within established ranges for natural rivers.

The NCI in the simulated profiles is systematically influenced by α (Figure 5.12). The fastest downstream decreasing discharge (α = -2) produces convex-up profiles and profiles become progressively straighter and then concave-up with increasing α. In general, long profiles are straighter when α approaches zero (discharge does not vary downstream). These LONGPRO results provide definitive mechanistic support to my NCI results from manually-extracted rivers and rivers analysed from GLoPro, pointing to aridity and its influence on downstream discharge as a first-order control on long profile shape.

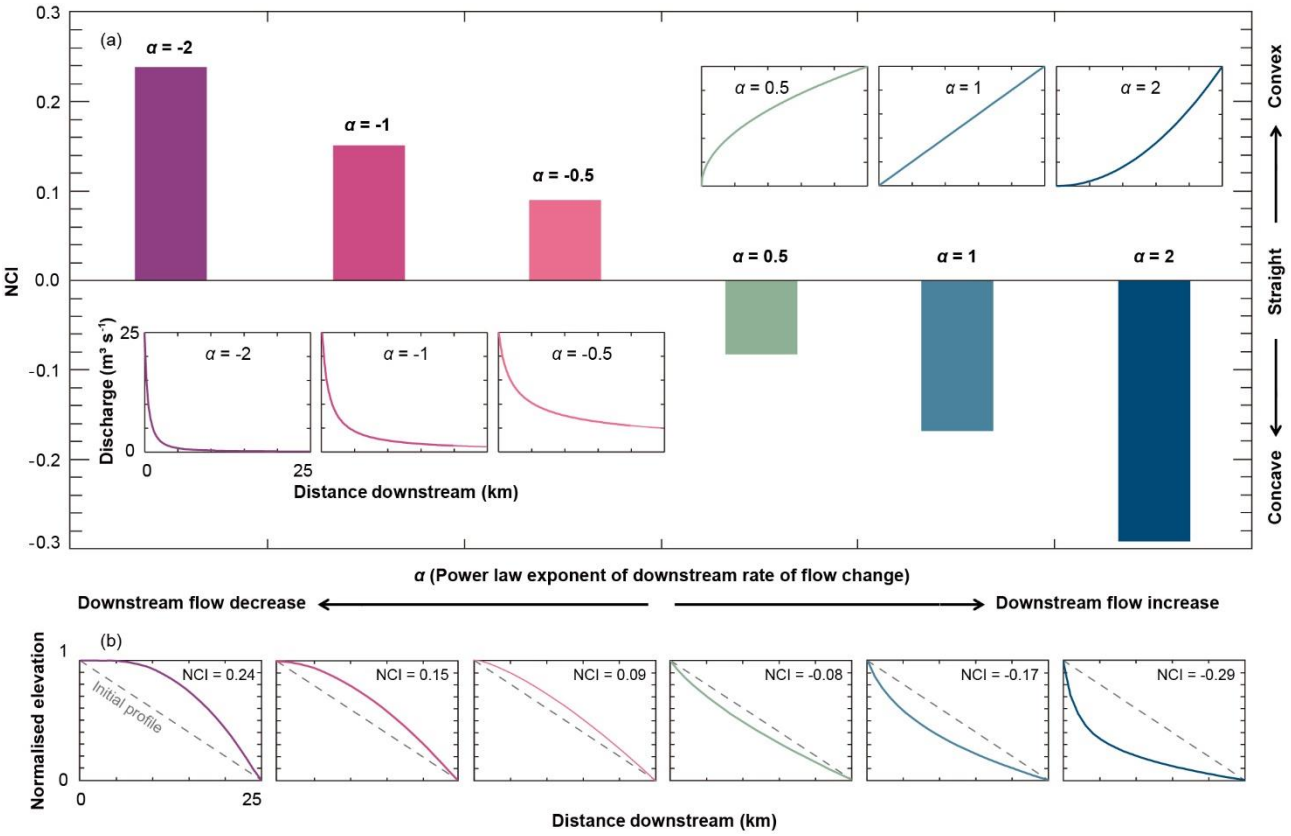

Figure 5.12 Modelling river long profiles with various downstream rates of flow change. NCI values for long profiles simulated with LONGPRO with a range of α (a). The inset panels show the corresponding downstream distributions of discharge for various α values used in the LONGPRO modelling. Simulated river long profiles for the corresponding values of α, normalised by total topographic relief (b).

Since other model parameters can also affect river long profile concavity, I conducted sensitivity analyses to discharge (Q_{max}), concentration of lateral sediment input (SEDCON), median grain size (DIMID), tectonic uplift, and base level change. To model tectonic uplift in LONGPRO, the maximum uplift rate was applied at the most upstream point (0.1 mm yr^{-1} and 1 mm yr^{-1}), and the rate decreased linearly downstream to zero at the most downstream point. To model base level change, LONGPRO uses a simple sine function to represent base level variation. I set the amplitude and period of the sine curve to represent continuous base level decline (10 mm yr^{-1} and 50 mm yr^{-1}). The results of these various sensitivity analyses show that α is the dominant control of long profile concavity, overprinting other factors (Figure 5.13). Moreover, the other exogenous factors that are often assumed to control long profile evolution have a lesser effect than the expression of downstream hydrology.

Combining the analyses of hydrological data in Chapter 4 with the model results enables interpretation of the global trends in long profile concavities with aridity, revealing three results: (1) The concave-up river profile can develop in all climate zones solely as a result of perennial flow conditions and downstream flow increase, consistent with stream power incision theory (Whipple and Tucker 1999); (2) Straighter long profiles concentrate in arid regions with rivers that flow infrequently and for which the median discharge is similar everywhere along the channel over the long term; (3) Convex long profiles can develop under a range of ephemeral or perennial conditions (e.g. humid regions with strong orographic effects; Roe et al. 2002; or arid regions with transmission losses), or where climate may not be the first-order control (e.g. tectonic regions). All of these profile shapes exist within manually-extracted rivers and GLoPro rivers (Figure 5.8, 5.9). This finding shows that the effect of downstream change of discharge in transport-limited rivers overprints other plausible controls on profile concavity on the global scale (Figure 5.13).

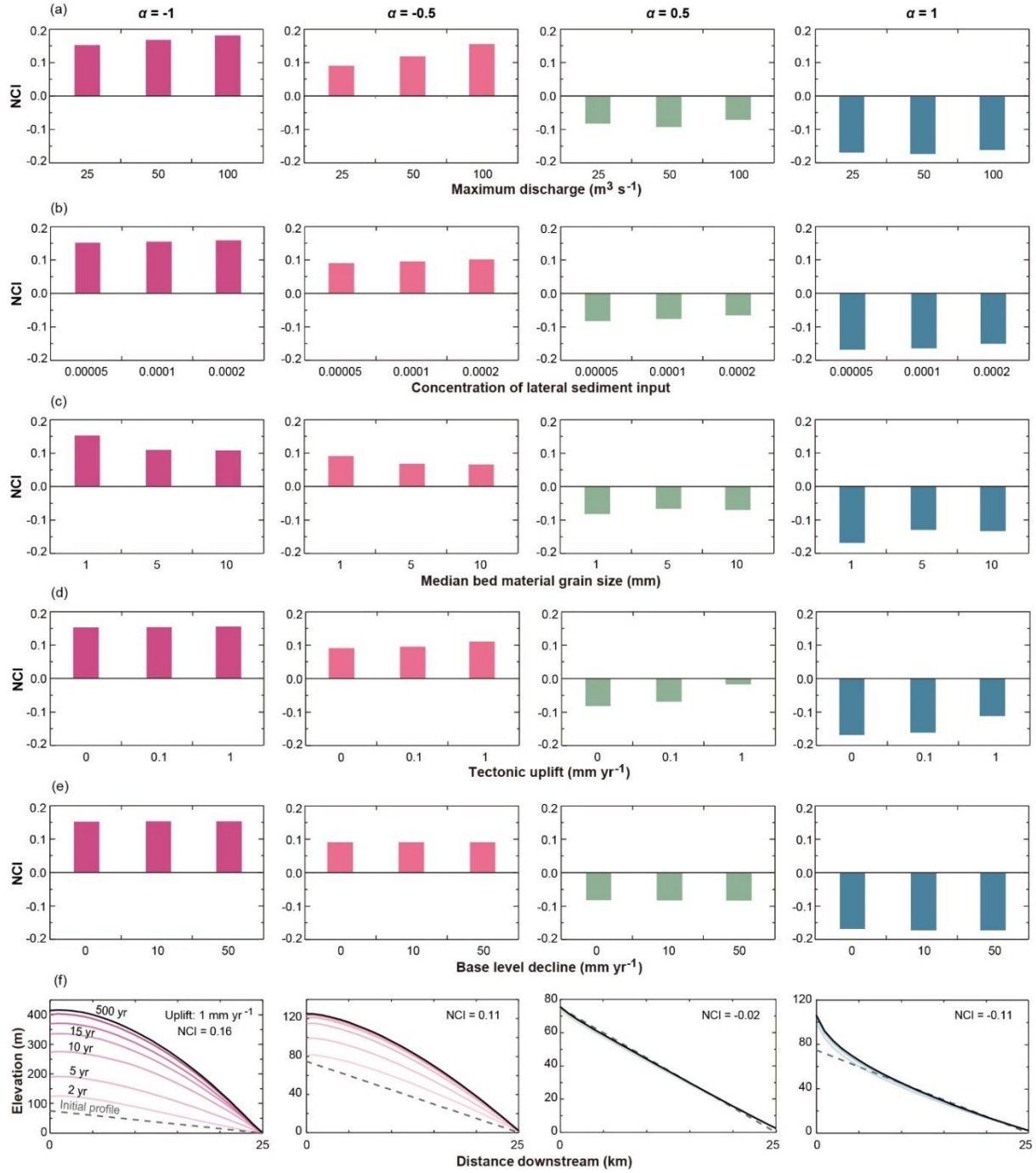

Figure 5.13 Sensitivity analyses of environmental controls on river long profile concavity simulated by LONGPRO. NCI values for long profiles with various values of maximum discharge (a), concentration of lateral sediment input (b), uniform median grain size (c), tectonic uplift rates of the headwater (d), and base level decline rates (e). All plots highlight the dominant effect of α on the river concavity. Long profile evolution with tectonic uplift (1 mm yr^{-1}), in which the profiles are shown for the initial profile (dashed line, the same for all simulations), 2 yr, 5 yr, 10 yr, 15 yr, 20 yr, 30 yr and 500 yr (f). The final simulated profile for each is indicated as a dark black line. Profiles evolve rapidly to near-steady-state conditions for all simulations.

5.6 Chapter summary

The long profile of a river is a key morphological attribute that reflects the history of drainage basin evolution, so its form should be diagnostic of the regional expression of climate and its interaction with the land surface. To explore the global distribution of river long profile shape and climatic controls on it, I developed a concavity index based on the geometry of river long profile, and used this index to analyse differences in overall profile concavity across climate zones from 124 manually-extracted rivers (as a preliminary test) and 333,502 rivers from the public database. Despite overlaps in the distributions of concavity, the river profiles are systematically straighter with increasing aridity. Through simple numerical modelling, I demonstrated that these global patterns in long profile shape could be explained by hydrological controls that reflect rainfall–runoff regimes in different climate zones. The most important of these is the downstream rate of change in discharge (Figure 5.14), independent of the area of the drainage basin. From the first global analysis of river long profiles, I demonstrated that climatic signals are etched into river profiles, irrespective of the variety of environmental conditions and other forcings across the globe.

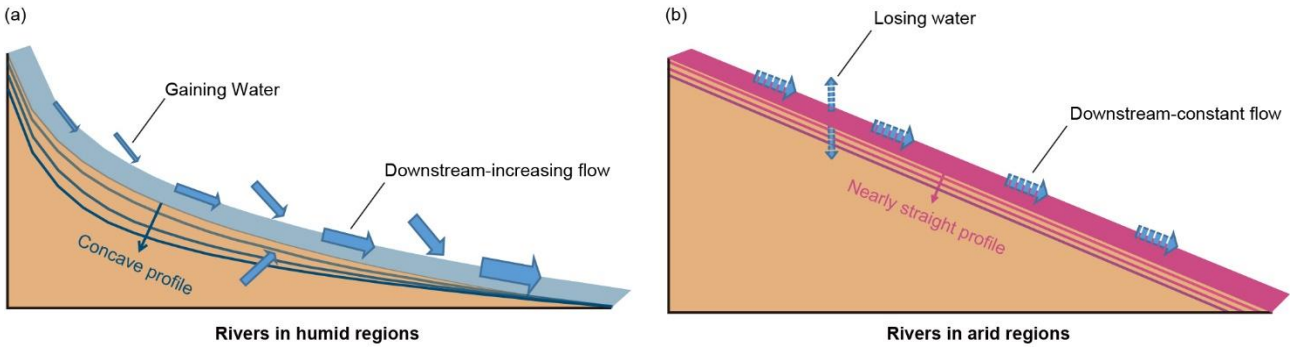

Figure 5.14 Schematic river long profiles between humid (a) and arid (b) regions and the first-order control of different hydrological regimes between these two climates.

6. Climatic controls on drainage basin erosion rates globally

The following research chapter has been submitted for publication under the following citation: Chen, S.-A., Michaelides, K., Singer, M. B., Richards, D. A., *in review*. Global analysis of short- versus long-term drainage basin erosion rates. Earth Surface Dynamics.

6.1 Introduction

Erosion is defined as the change of land surface elevation, resulting from sediment detachment and transport. The erosion rate of a drainage basin is an important geomorphic quantity because it reflects the net flux of sediment from source to sink in drainage basin and correspondingly, the rate and spatial pattern of landscape evolution. Therefore, measuring erosion rates, analysing their temporal variations, and exploring environmental controls are crucial in understanding the links between drainage basin environment, land surface processes, and landform development.

6.1.1 Representation of short-term erosion rates

'Short-term' erosion rate is referred here to the annual to decadal timescales in the recent past. Among various methods for measuring short-term erosion rate (e.g. depth of lacustrine sediments, plot experiment, and land surface measurement), suspended sediment flux record has been widely used, describe the history of fine sediment transport from uplands to lowlands within riverine flow (Milliman and Meade 1983).

Erosion rates based on suspended sediment yield are calculated by measuring the sediment concentration and discharge at a gauging station, and converting their product into mean annual sediment flux, then to sediment yield (t ha^{-1} yr^{-1}) normalised by upstream drainage area, and subsequently to erosion rate (mm yr^{-1}), assuming a basin-averaged soil bulk density. This method provides an averaged value of erosion rate for the upstream area that neglects the storage of sediment during transportation and assumes that eroded sediments are all transported as suspended load. This is a reasonable approximation because (1) storage of sediment can be considered to be negligible over longer timescales, and (2) suspended load dominates sediment flux (> 90%) for the majority of drainage basins, except

high relief or dryland catchments (Dedkov and Mozzherin 1996; Laronne 1993; Milliman and Meade 1983; Milliman and Syvitski 1992; Singer and Dunne 2004; Singer and Michaelides 2014). Suspended sediment records provide a record of recent and potentially transient responses within landscapes to climatic and/or anthropogenic forcing (Walling and Fang 2003; Walling and Webb 1996).

6.1.2 Representation of long-term erosion rates

'Long-term' erosion rate is often referred to the timescale longer than one thousand years, and can be estimated by stratigraphic analysis, thermochronology, and cosmogenic radionuclides. *In situ* cosmogenic radionuclide concentration within riverine sediment is a common tool for estimating erosion rates based on basin-averaged exposure age dating at timescales from 10^3 to 10^5 yr (Granger and Schaller 2014; von Blanckenburg and Willenbring 2014).

Cosmogenic radionuclides are high-energy particles generated from supernovas (composed primarily by protons) and transported as primary cosmic rays. As they reach the upper atmosphere of the Earth, hit the molecules and cause nuclear reactions, the secondary cosmic rays are produced (composed mainly by neutrons). These radionuclides then reach Earth surface and accumulate in the sediment, within the depth of about 0.6–1 m, as *in situ* cosmogenic radionuclides (von Blanckenburg 2005; von Blanckenburg and Willenbring 2014). Over time, the concentration of cosmogenic radionuclides near the surface increases until a balance is achieved between the production rate of the radionuclide, its radioactive decay rate, and erosion rate (or rate of surface stripping). Therefore, cosmogenic exposure age dates can be used for estimating drainage basin erosion rates (Brown et al. 1995; Granger et al. 1996; Granger et al. 2013; Granger and Schaller 2014; von Blanckenburg and Willenbring 2014).

This method, when applied to riverine sediments, also provides averaged erosion rate, assuming no sediment storage within the upstream basin. Furthermore, this method assumes that: erosion rate is faster than the radioactive decay rate (for beryllium-10, ^{10}Be, erosion rate should be faster than 0.3 mm kyr^{-1}); radionuclide concentration has achieved the balance between production, erosion and decay rates (the landscape is in a state of equilibrium); the nuclide concentration has no dependency on grain size (a narrow range of

grain sizes is typically used for analysis); there is no erosion–deposition cycle in the drainage basin; and quartz exists in sediments throughout the entire basin (Brown et al. 1995; Dosseto and Schaller 2016; Granger et al. 2013; Struck et al. 2018). Erosion rates estimated using cosmogenic nuclides represent longer timescales than suspended sediment records (10^3–10^5 yr versus 10^0–10^1 yr), and are therefore suitable for analysing the influences of climate and tectonics, and insensitive to the influences of anthropogenic activities or recent stochastic events (Brown et al. 1995; Dosseto and Schaller 2016; Granger et al. 2013; Granger and Schaller 2014; von Blanckenburg 2005).

Although multiple cosmogenic radionuclides used for estimating erosion rates, ^{10}Be is the most common one. This is because ^{10}Be does not exist in the mineral before exposed under the cosmogenic ray, and can be produced in quartz (which is chemically stable, solid, and extensively distributed on the land surface), and the knowledge of its production rates has been well-developed (Wittmann and von Blanckenburg 2012).

6.1.3 The characteristics and controls of erosion rate

At both regional and global scales, suspended sediment yields and cosmogenic nuclides have been widely used for analysing short- and long-term erosion rates, respectively. Suspended sediment analysis has been employed for many decades, initiated by major investment in a nationwide monitoring programmes (e.g. USGS) and subsequently replicated in many other countries. Exploration of the valuable data provided by programmes has revealed insights into the relationships between climatic and anthropogenic drivers and sediment yields. For example, Langbein and Schumm (1958) used a limited dataset on sediment yields to identify a non-linear relationship between sediment yields and effective MAP across various biomes in the USA, with a peak in the semi-arid rainfall regimes. They considered both precipitation and vegetation cover to play important roles. Specifically, they suggested that at low MAP, there is also little vegetation, so erosion increases commensurately with rainfall via Hortonian overland flow. However, with sufficient rainfall, vegetation cover may increase and slow erosion rate because of increased interception, higher infiltration, and correspondingly higher evapotranspiration or subsurface storm flow (Dunne and Leopold 1978). Thus, humid regions have lower sediment yields than semi-arid landscapes. Subsequently, Walling and Kleo (1979) extended this analysis to include data from around the globe and therefore including regions with higher MAP than the USA. Their

results show that for basins smaller than 10,000 km^2, sediment yield peaks in semi-arid regions, but also in Mediterranean and tropical monsoon climate zones, with a strong seasonal rainfall pattern and intense precipitation that can exceed the protection capacity of vegetation cover. In addition to climatic controls, land surface processes are strongly influenced by anthropogenic activities through construction, mining, timber harvesting, and conversion of natural vegetation to agriculture (crop and pasture), the last of which is the most dominant in terms of area (Hooke 2000). Global analyses of short-term erosion rates from suspended sediment records suggest that a change to agricultural land cover has enhanced erosion rates by one to two orders of magnitude (Dedkov and Mozzherin 1996; Kemp et al. 2020; Montgomery 2007; Wilkinson and McElroy 2007).

Regarding long-term erosion rates, a non-linear relationship between MAP and erosion rate was developed by Mishra et al. (2019) on the basis of a global compilation of ^{10}Be measurements (n = 1,790). Whilst significant scatter is observed in the data, they identify a general increase in erosion rate to a local maximum MAP at ~ 1,000 mm, followed by a slight reduction up to MAP of ~ 2,200 mm and then return to increasing values for higher MAP. The relationship is explained by the interrelated influences of precipitation and vegetation cover as suggested for short-term studies (e.g. Langbein and Schumm 1958), although their pattern of erosion rate change with MAP is quite different.

In addition to these climate/vegetation controls, glaciers and wildfires exert important influences on long-term erosion rates. Glaciers shape the land surface directly through the stripping of rock underneath basal ice, and through freeze–thaw and weathering processes on the margins of ice (Cook et al. 2020; Harel et al. 2016). Glacial erosion, for example, has been shown to increase long-term erosion rates in temperate and cold regions, especially within mid- and high-latitudes (Gabet et al. 2008; Harel et al. 2016; Portenga and Bierman 2011). Wildfires, on the other hand, are more prevalent during dry periods and the occurrence is modified by variation of temperature and wind regimes (Han et al. 2020; Pierce et al. 2004). Wildfires burn the vegetation cover and deposit loose material on the hillslope, destroy root system underground, decrease the infiltration rate, and provide the material for transportation (Cannon et al. 1998; Pierce et al. 2004). Burned areas are more susceptible to debris flow and landslides, which transports sediments from hillslopes to river channels, and increase the erosion rate of drainage basins over longer timescales (Cannon et al. 1998; Meyer et al. 2001).

Topography, tectonics, and lithology also influence erosion rates. For example, erosion rates tend to be positively related to total basin relief and slope gradient, tectonic uplift rates, and the erodibility of lithology, for short-term (Aalto et al. 2006; Milliman and Farnsworth 2011; Milliman and Meade 1983; Milliman and Syvitski 1992; Summerfield and Hulton 1994; Syvitski and Milliman 2007; Yizhou et al. 2014) and long-term erosion rates (Bierman and Caffee 2001; Binnie et al. 2007; Codilean et al. 2014; Covault et al. 2013; DiBiase et al. 2010; Granger et al. 1996; Grin et al. 2018; Harel et al. 2016; Hilley et al. 2019; Portenga and Bierman 2011; Schaller et al. 2001; Schmidt et al. 2016; Struck et al. 2018; Tofelde et al. 2018; von Blanckenburg 2005; Wittmann et al. 2011). However, many of these physiographic controls are not independent and hamper efforts to deconvolve their relative influence (Milliman and Farnsworth 2011). For example, a basin with rapid tectonic uplift tends to have both higher relief and gradients and lower rock strength due to the high density of faults and joints (Binnie et al. 2007; Grin et al. 2018). Furthermore, rapidly uplifting mountain ranges are subject to significant orographic precipitation (e.g. Himalayas, Taiwan), making it challenging to distinguish between the tectonics or climate forcing of erosion rates.

6.1.4 Temporal variations and causes of erosion rate

To investigate temporal variations of erosion rates at the basin scale and to distinguish their respective drivers, several studies have compared short- and long-term erosion rates, but the results are inconclusive. In some regions, short-term erosion rates are higher than long-term rates because of recent human activities (Clapp et al. 2000; Gellis et al. 2004; Kemp et al. 2020; von Blanckenburg 2005) or climatic changes, which leads to higher precipitation rates (Bierman et al. 2005; Clapp et al. 2000; Gellis et al. 2004; Wittmann et al. 2011). In contrast, other regions show higher long-term erosion rates, which were interpreted to be a result of incorporating more high-magnitude, low-frequency, natural events (e.g. wildfires, landslides), that increase mean erosion rates over a longer timescale but are not detectable within short erosion records (Covault et al. 2013; Kirchner et al. 2001; Schaller et al. 2001). Higher long-term rates compared to short-term rates may also result from natural climatic changes, which might have promoted higher vegetation cover or less precipitation more recently (Bookhagen and Strecker 2012; Bookhagen et al. 2005; Dosseto and Schaller 2016). Also, less active glacial processes and chemical weathering due to climate changes might have decreased the erosion energy of flowing ice and available materials (Cook et al. 2020; Dosseto and Schaller 2016; Gabet et al. 2008; Portenga and Bierman 2011; Schaller

et al. 2001). Signals are further complicated by spatial variations of erosion rates within basins that may not be detected at the basin outlet due to the buffering capacity associated with sediment sequestration along channels and behind dams, which is more common in large basins (Milliman and Syvitski 1992; Walling and Fang 2003; Wilkinson and McElroy 2007; Wittmann et al. 2011).

6.1.5 Motivations and objectives

Former studies have analysed long- and short-term erosion rates for drainage basins across the globe. These studies investigated spatial and temporal changes in erosion in response to climatic and tectonic forcing (Clapp et al. 2001; Pan et al. 2010; Wittmann et al. 2011; Yizhou et al. 2014) and to compared erosions rates between basins (Dedkov and Mozzherin 1996; Harel et al. 2016; Milliman and Meade 1983; Milliman and Syvitski 1992; Portenga and Bierman 2011; Summerfield and Hulton 1994). The combination of long- and short-term erosion rates enables the investigation of potential drivers of erosion and consideration of the role of time averaging on erosion rates (Covault et al. 2013; Kirchner et al. 2001; Schaller et al. 2001).

Despite impressive and increasing collections of long- and short-term erosion rates for drainage basins across the globe, it remains equivocal whether there are identifiable patterns in these erosion rates that reflect the prevailing climatic regime and/or anthropogenic activities within basins. Therefore, I aimed to understand the geographic expression of long- and short-term erosion rates around the globe and explore the climatic and other potential controls on erosion rates across spatial and temporal scales. The following questions were specifically addressed: (1) What is the overall pattern of long- and short-term erosion rates across climate regimes? (2) To what extent do long-term erosion rates reflect glacial processes in mid- and high-latitude regions? (3) Is the previously observed non-linear relationship between precipitation and erosion rate applicable to both short and long timescales? (4) Do human activities outweigh other controls over short-term erosion rates? (5) How do basin topography and topology affect erosion rates?

To answer these questions, the drainage basin erosion rates were compiled based on *in situ* ^{10}Be data (long-term) and suspended sediment yields from gauging stations (short-term). The erosion rates were then stratified using K–G and AI climate classifications (Chapter 3),

and analysed the relationships between erosion rates and potential controls, including climate, topography, and anthropogenic activity. I compared erosion rates around the globe with and without these controls to quantitatively assess their influence on erosion rates between timescales.

6.2 Methodology

I compiled long- and short-term drainage basin erosion rates from existing databases and published literature. All erosion rate data were stratified by the K–G and AI climate classifications (Chapter 3). I also assembled the ice coverage at the LGM (Ray and Adams 2001), MAP (calculated from CPC US Unified Precipitation data), topographic parameters (extracted and calculated from GLoPro database; Chen et al., 2019), and global agricultural regions (Foley et al. 2005).

Long-term erosion rates were obtained from OCTOPUS database, which includes basin-averaged erosion rates derived from cosmogenic nuclides (^{10}Be and ^{26}Al) and luminescence measurements in fluvial sediments (Codilean et al. 2018). This database classifies data based on the methods, regions, and degree of completeness. To gain the highest reliability and consistency, I only included ^{10}Be-derived erosion rates of CRN (cosmogenic radionuclide) International and CRN Australia categories from the database, resulting in a total of 3,074 data points (Figure 6.1). For each data point, I extracted the erosion rate, coordinates, and drainage basin area.

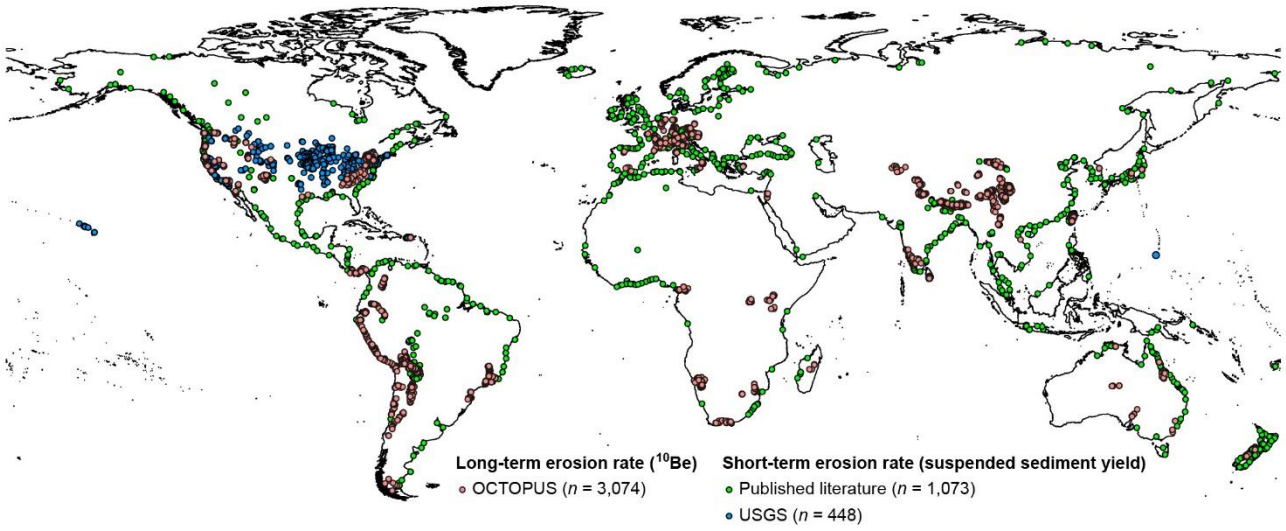

Figure 6.1 Global map of drainage basin erosion rate locations. Long-term erosion rates were obtained from OCTOPUS, estimated by ^{10}Be in the fluvial sediments. Short-term erosion rates were compiled from published literature (green) and USGS (blue), determined by suspended sediment yield of gauging stations.

Short-term erosion rates were compiled from the published literature and the USGS, based on estimations from suspended sediment yields at gauging stations. From the published literature, I compiled sediment yields (t ha^{-1} y^{-1}) or erosion rates (mm ky^{-1}) at each data point. To convert erosion rates from sediment yields, the sediment density was assumed to be 1.6 g cm^{-3} (= 1.6 t m^{-3}). Using this density, sediments with the depth of 0.1 mm across 1 ha area weight 1.6 t. A sediment yield of 1 t ha^{-1} y^{-1}, for example, is equivalent to an erosion rate of 0.0625 mm y^{-1} (= 62.5 mm ky^{-1}). If the coordinates of the gauging stations were not provided, the point coordinates were acquired from Google Maps. If data from the same gauging station were reported in multiple literature sources, I only included the erosion rate with the most recent data record. For USGS data, two criteria were set for choosing gauging station data: (1) the monitoring time period needed to be > 5 years, and (2) the basin area < 2,500 km^2 (to avoid basins representing more than one climate zone). Note that some of the gauging stations meeting these criteria may be on the same river. I extracted the daily sediment discharge (t d^{-1}), converted this into sediment yield (t ha^{-1} y^{-1}) by summing the daily data and dividing by the number of years and basin area. The sediment yield was then converted into an erosion rate. In total, I obtained 1,521 short-term erosion rates; 1,073 from the published literature and 448 from USGS (Figure 6.1), with corresponding station coordinates and drainage basin areas (Appendix E).

There are numerous environmental controls on erosion rates around the globe, among them glacial processes during the ice ages (Harel et al. 2016; Portenga and Bierman 2011), topography (e.g. Portenga and Bierman 2011), and human activities (e.g. Covault et al. 2013). To explore the influence on erosion rates of these three broad drivers, I considered the extent of ice coverage at the LGM, the slope gradient and relief of river channels, and the spatial pattern of agricultural regions. Previous studies typically used MAP to examine climatic controls on erosion rates (e.g. Langbein and Schumm 1958; Walling and Kleo 1979). Thus, in addition to classifying erosion rates by climate classifications, the MAP across the continental USA was also used for further analysis.

The extent of glacial processes at the ice ages was determined from Ray and Adams (2001), which provides the global vegetation map at the LGM (25,000–15,000 BP) based on fossil and sedimentary information, and expert consultation. Since the timescale of ^{10}Be-derived erosion rates is in the range of 10^3–10^5 years, the data cover several ice ages. However, I used coverage of the last ice age as the most reliable estimate of glacial influences. The glacial regions at the LGM were defined as the following five categories in the data source: Tundra, Steppe-tundra, Polar and alpine desert, Alpine tundra, and Ice sheet and other permanent ice.

The topographic parameters used here include the mean slope gradient and total relief of river long profiles extracted from the GLoPro database (Chen et al. 2019). The recorded topographic data in GLoPro include the NCI value, elevation, flow distance, and drainage area of each river profile. To extract river profiles from the database for comparing topographic parameters with erosion rates, I chose a subjective distance threshold as 150 m between river profiles and erosion rate sampling points (i.e. selecting river profiles which are within 150 m to the closest erosion rate points), and calculated the mean slope gradient and total relief of river long profiles.

Anthropogenically-impacted regions were determined from Foley et al. (2005), which provides global maps of ‘croplands’, and ‘pastures and rangelands’ classified by the relative percentages of areas within these land uses. These maps were modified from previous studies (Asner et al. 2004; Ramankutty and Foley 1999), in which they classified land use types from satellite images using GIS analysis. I conservatively defined anthropogenic regions with higher than 50% area of croplands or pastures and rangelands.

MAP across the continental USA was obtained from CPC US Unified Precipitation data produced by National Oceanic and Atmospheric Administration Physical Sciences Laboratory (NOAA PSL). The data is in raster format with 0.25-degree resolution (~ 28 km at the equator), including daily precipitation rates from 1948 to 2006 (59 years). I summed the daily data of each grid in each year to convert daily data into yearly data and calculated the precipitation rates for all erosion rate locations.

6.3 Global patterns of long- and short-term erosion rates

6.3.1 Climatic influences on long- and short-term erosion rates

Using both K–G and AI climate classifications, short-term erosion rates are significantly higher ($P < 0.05$) than long-term rates in all climate zones, except for the Cold K–G zone (Figure 6.2, Table 6.1a). Within the AI categories, there is a general pattern of an increasing difference between long- and short-term erosion rates with higher aridity. However, these differences are only significant for the Arid and Semi-arid categories ($P < 0.05$, Figure 6.2b, Table 6.1b).

For the long-term erosion rates, Tropical and Arid K–G zones have significantly ($P < 0.01$) lower erosion rates (medians = 29.7 and 32.2 mm kyr^{-1}, respectively) than Temperate and Cold zones (medians = 92.9 and 92.5 mm kyr^{-1}, respectively, Figure 6.2a, Table 6.1a). Within the AI categories, long-term erosion rates are significantly lower in the dryland regions (i.e. Hyper-arid, Arid, and Semi-arid group of categories) compared to the non-dryland regions (i.e. Dry sub-humid and Humid group of categories, $P < 0.01$) (Figure 6.2b), and there are no differences within them ($P > 0.05$, Table 6.1b). The maximum long-term erosion rates are exhibited in the Temperate and Cold K–G categories and in the Dry sub-humid AI category.

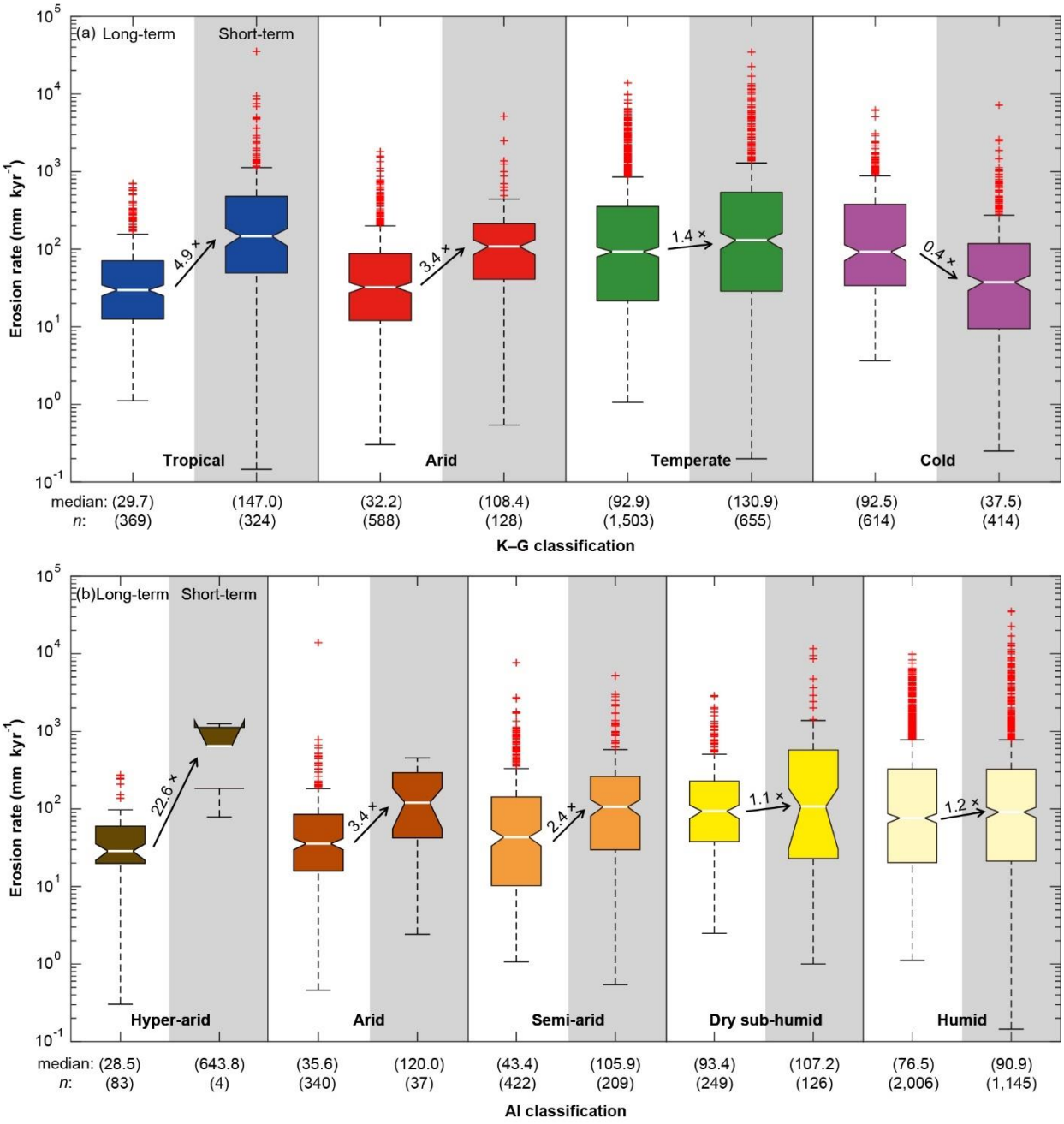

Figure 6.2 Long- and short-term erosion rates for climate zones of K–G climate classification (a) and AI classification (b). Boxplots with white backgrounds are the long-term rates, whilst the grey backgrounds are the short-term rates. The arrow and number between boxplots in each climate zone indicate the trend and ratio of median values of short- to long-term rates ($R_{S/L}$). Median value and the number of data for each distribution are listed below.

Table 6.1 The *P* values of K–W hypothesis testing of long-term (*n* = 3,074) and short-term (*n* = 1,521) erosion rates between climate zones of K–G climate classification (a) and AI classification (b), and between long- and short-term erosion rates of each climate zone. Bold numbers indicate *P* values < 0.05. The number of data points for each climate zone is listed in Figure 6.2.

(a)

Long-term rates comparison

	Arid	Temperate	Cold
Tropical	0.88	**<0.001**	**<0.001**
Arid		**<0.001**	**<0.001**
Temperate			0.54

Short-term rates comparison

	Arid	Temperate	Cold
Tropical	0.42	0.95	**<0.001**
Arid		0.82	**<0.001**
Temperate			**<0.001**

Long- and short-term rates comparison

Tropical	**<0.001**
Arid	**<0.001**
Temperate	**0.02**
Cold	**<0.001**

(b)

Long-term rates comparison

	Arid	Semi-arid	Dry sub-humid	Humid
Hyper-arid	0.97	0.40	**<0.001**	**<0.001**
Arid		0.75	**<0.001**	**<0.001**
Semi-arid			**<0.001**	**<0.001**
Dry sub-humid				0.53

Short-term rates comparison

	Arid	Semi-arid	Dry sub-humid	Humid
Hyper-arid	0.88	0.79	0.88	0.73
Arid		1	1	1
Semi-arid			1	1
Dry sub-humid				0.95

Long- and short-term rates comparison

Hyper-arid	0.07
Arid	**0.02**
Semi-arid	**<0.001**
Dry sub-humid	1
Humid	1

To make my analysis comparable to other studies, I also analysed long-term erosion rates against MAP for all data points within the continental USA. The result shows a similar pattern of erosion rates as those analysed by AI, with the highest erosion rates exhibited in the Dry sub-humid category (MAP ~ 600 mm, Figure 6.3a) but also followed by a dip around 1,250 mm and a subsequent increase again in erosion rates in extremely humid regions, where MAP is higher than 1,300 mm.

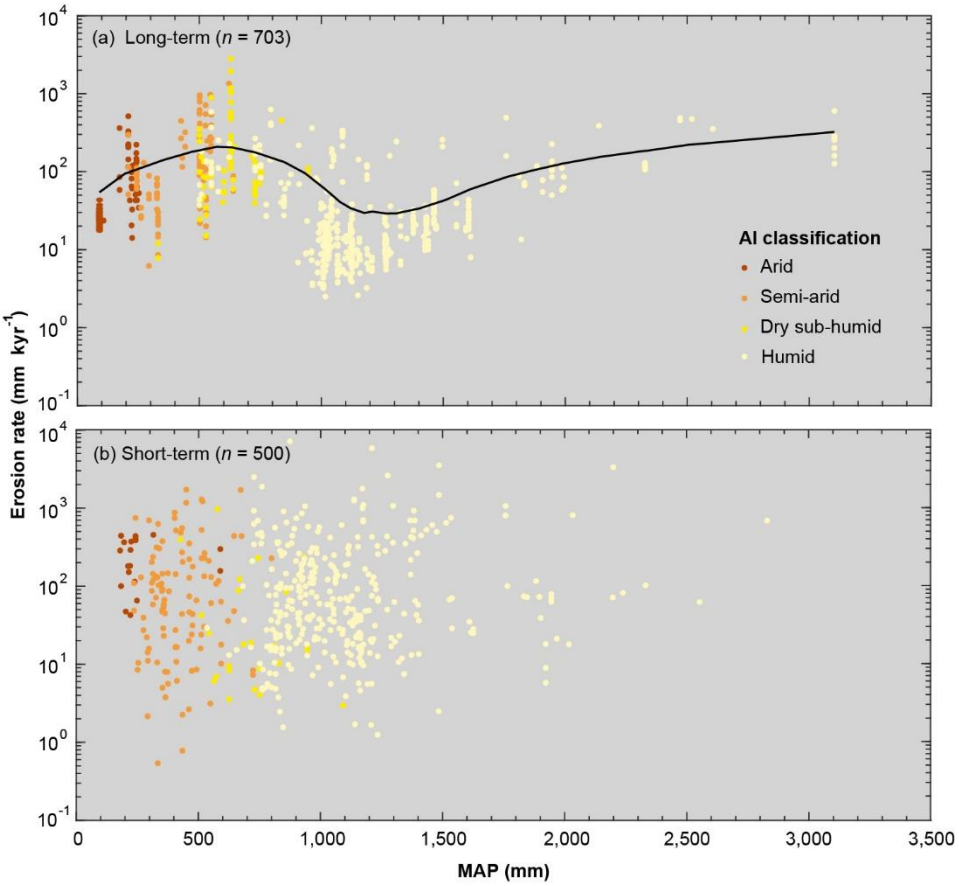

Figure 6.3 The relationships between MAP and long- (a) and short-term (b) erosion rates in the USA. The precipitation data were acquired from CPC US Unified Precipitation data. Points are colour coded by AI categories. Black curve in panel a is LOWESS regression, showing that long-term erosion rates peak at regions with precipitation about 600 mm and more than 1,300 mm. In contrast, no clear pattern is indicated for short-term erosion rates.

Within the short-term erosion rates, there is no dependency on climate according to either climate classifications ($P > 0.05$), except in the Cold zone of K–G classification, where there were significantly lower erosion rates compared to other climate zones ($P < 0.01$, Figure 6.2, Table 6.1). The medians of short-term erosion rates in all climates are generally between 90 and 150 mm kyr^{-1}, whereas the Cold K–G zone is only 37.5 mm kyr^{-1}, and the Hyper-arid AI category is as high as 643.8 mm kyr^{-1} (note that the result of Hyper-arid category may not be robust because of limited available data). Similarly, there is no apparent relationship between short-term erosion rates and MAP across the continental USA (Figure 6.3b).

6.3.2 Influences of glaciation on long-term erosion rates

To explore the influence of past glaciations on long-term erosion rates, I compared data for those locations that are currently in the Temperate K–G zone and were previously in glacial and pro-glacial zones during the Pleistocene (e.g. north-western Europe, part of the Andes, the Himalayas, and New Zealand) against the Temperate sites that were not glaciated (Figure 6.4). I found that long-term erosion rates for formerly-glaciated regions of the Temperature zone are approximately 5 times higher than in non-glaciated regions (medians = 202.3 and 41.4 mm kyr^{-1}, respectively, $P < 0.01$). This result accentuates the role of glaciers in stripping surfaces across the landscape resulting in higher long-term erosion rates.

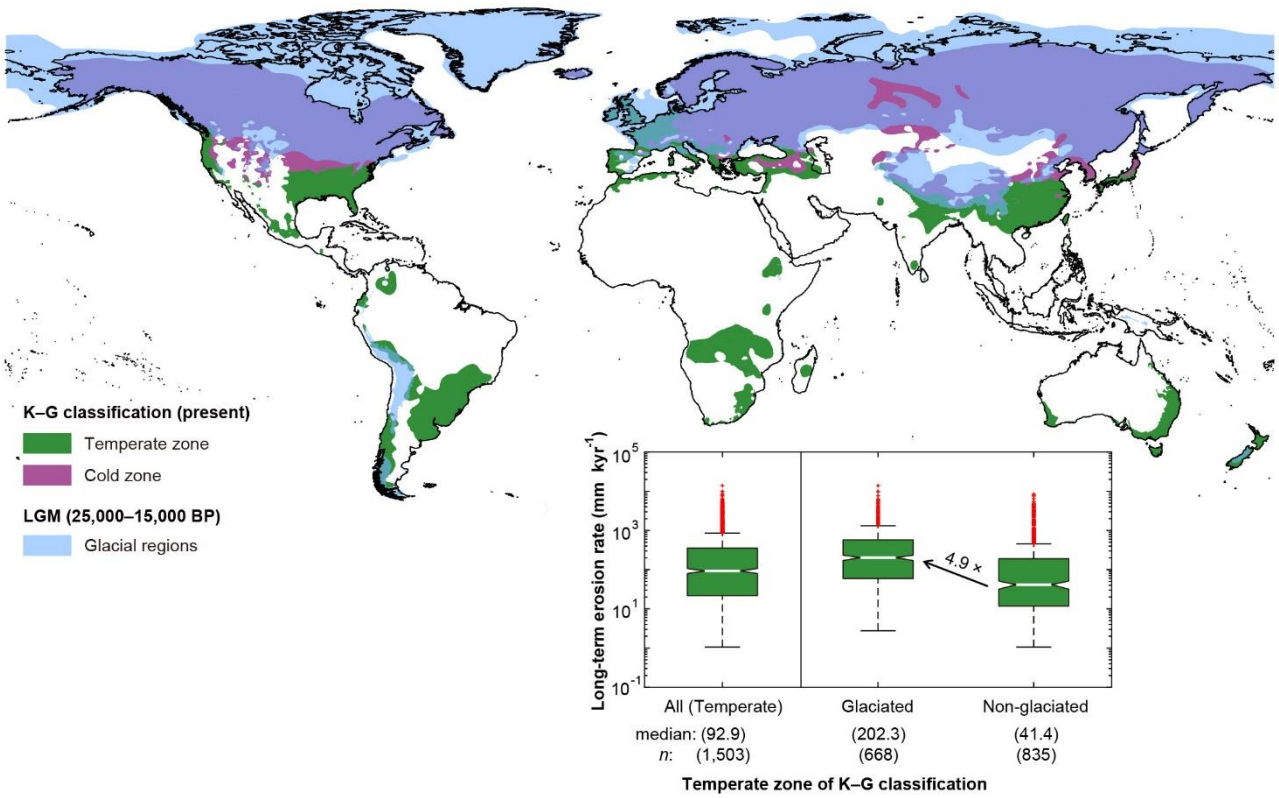

Figure 6.4 The extent of glacial regions at the LGM and the area of Temperate and Cold zones of K–G climate classification in the present. The glacial regions were drawn from Ray and Adams (2001). The inserted figure compares long-term erosion rates in the Temperate zone with and without glacial influences at the LGM. The figure shows 4.9 times higher median erosion rates in formerly-glaciated regions compared to non-glacial regions.

6.3.3 Anthropogenic influences on short-term erosion rates

To examine the anthropogenic influences on short-term erosion rates, I compared the erosion rates in 'croplands', and 'pastures and rangelands', with erosion rates in regions with no such evidence of anthropogenic disturbance. Short-term erosion rates in 'croplands', and 'pastures and rangelands' are 1.4 times higher than regions without these influences (78.3 mm kyr^{-1}, $P < 0.05$, Figure 6.5). However, there was no significant difference in erosion rates between these anthropogenically impacted land use types (104.2 and 114.0 mm kyr^{-1}, respectively, $P > 0.05$).

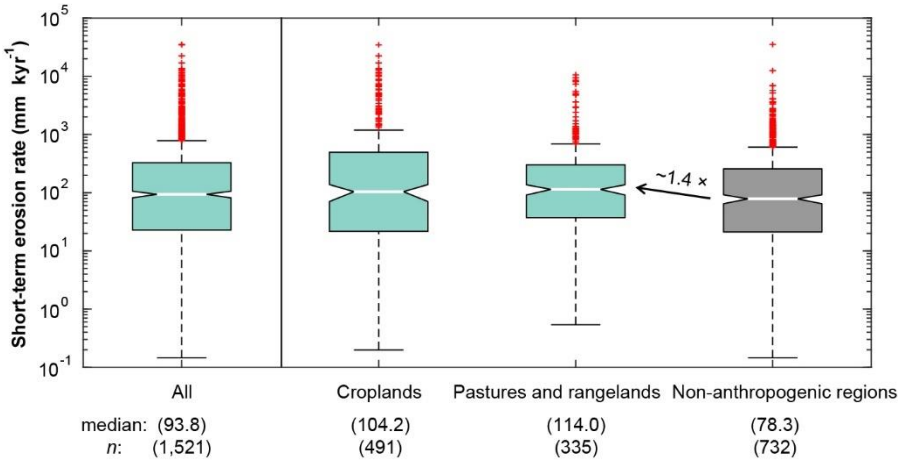

Figure 6.5 The comparison of global short-term erosion rates with and without anthropogenic influences. The extent of 'croplands' and 'pastures and rangelands' were digitised from Foley et al. (2005). The figures show that short-term erosion rates with anthropogenic influences are about 1.4 times higher than in non-anthropogenic regions.

6.3.4 Influences of basin characteristics

Finally, I explored the influences of spatial scale and topography on erosion rates. Across the whole datasets, for both long- and short-term erosion rates, there is no clear relationship with basin area (Figure 6.6). To investigate this further, the erosion rates were grouped in three bins of basin area, < 500 km^2, 500–2,500 km^2, and ≥ 2,500 km^2. The area thresholds were chosen to achieve a similar number of observations within each bin and climate category. I then calculated the ratio of short- to long-term median erosion rates ($R_{S/L}$). There

is a negative relationship between $R_{S/L}$ and basin area for each K–G climate zone, except the Cold zone (Figure 6.7). Generally, short-term erosion rates are several times higher than long-term rates in small basins, whilst in large basins, long-term rates tend to be more similar or even higher than short-term rates.

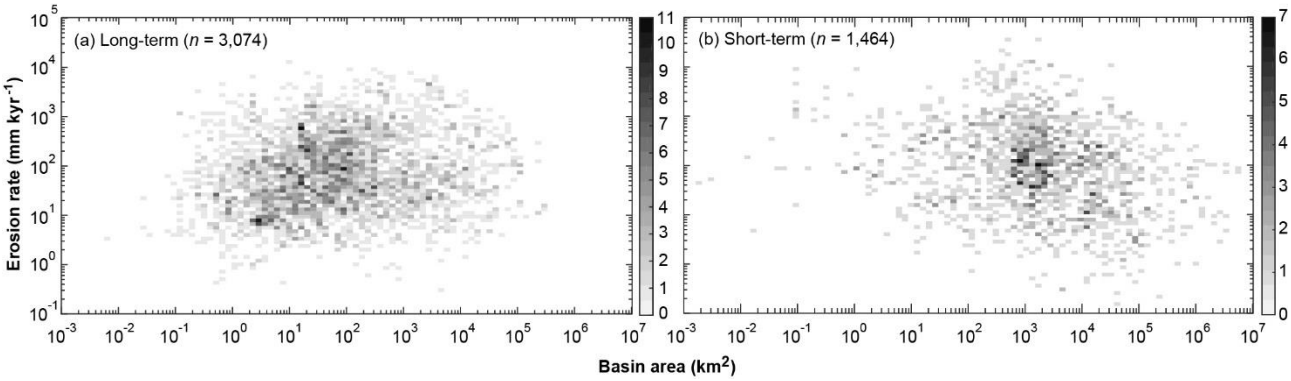

Figure 6.6 The relationships between the drainage basin area and long- (a) and short-term (b) erosion rates. The figures indicate no apparent connection between basin area and either long- or short-term erosion rates.

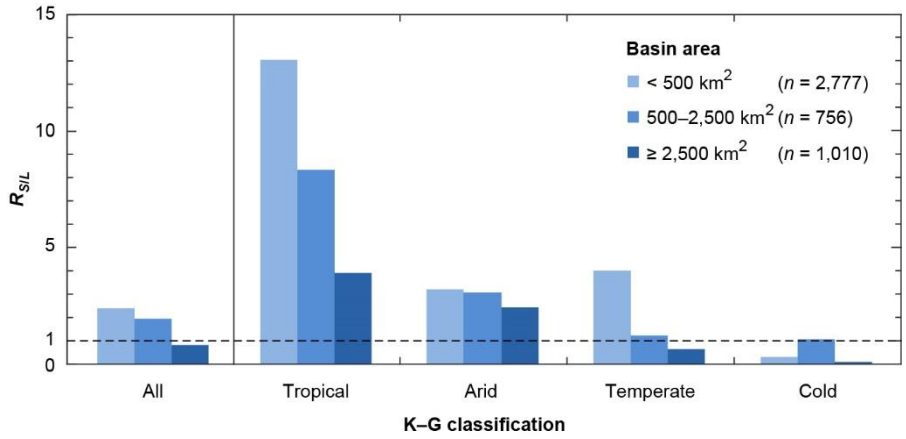

Figure 6.7 The ratio of short- to long-term erosion rates of each basin area bin between climate zones of K–G climate classification. Each ratio was calculated by the medians of short- and long-term erosion rates of each area bin in each climate zone. The numbers of data of each basin area bin (short-term plus long-term erosion rates) are listed in the legend. The dotted lines indicate the same value of short- and long-term rates. Generally, in smaller basins, short-term erosion rates tend to be higher than long-term rates compared to larger basins.

In addition, long-term erosion rates are positively related to the slope gradient and total relief of the river channels (R^2 = 0.29 and 0.24, respectively), whilst for short-term erosion rates,

the influences of these topographic parameters are unclear (Figure 6.8).

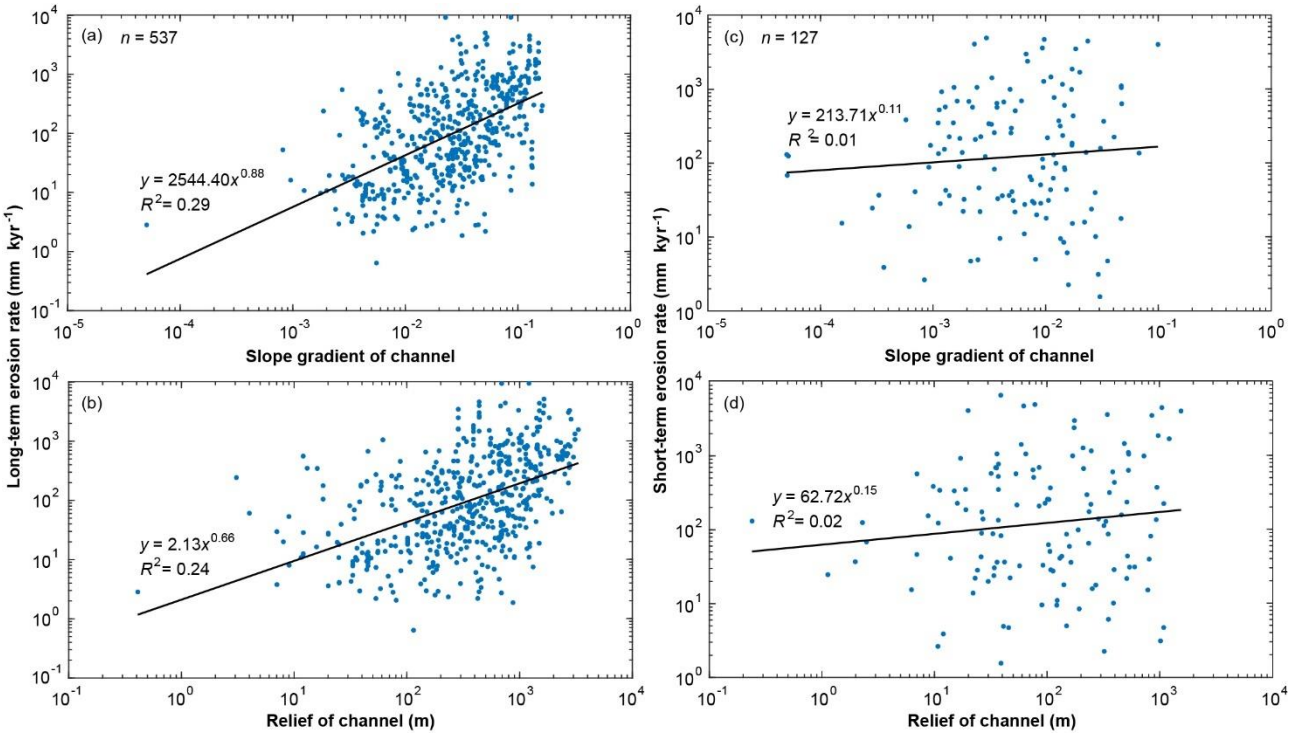

Figure 6.8 The relationships between topographic parameters of river long profiles and long- (a, b) and short-term (c, d) erosion rates. River profiles were extracted from GLoPro database (Chen et al. 2019) within 150 m of the erosion rate sampling locations. There are positive relationships between long-term erosion rates and channel gradient and relief, whilst the relationships with short-term rates are obscured.

6.4 Influence of climate on long-term erosion rates

Drainage basin erosion influences landscape evolution and has been studied widely to estimate its spatial and temporal changes and identify its environmental controls. The dominant controls on erosion rates between locations and over different timescales may vary and climate influence on erosion rates is complex and hard to isolate (Aalto et al. 2006; Li and Fang 2016; von Blanckenburg 2005). Here I compiled long- and short-term drainage basin erosion rates around the globe and analysed the relationships between erosion rates and potential climatic and environmental controls. I demonstrated that precipitation, former glacial processes, and topography influence long-term erosion rates, whilst anthropogenic activities dominate short-term erosion rates. In addition, drainage basin area influences the

difference between short- and long-term erosion rates, as does aridity.

A key finding from this meta-analysis using a large, globally distributed dataset, is that there is a non-linear relationship between long-term erosion rates and climate (Figure 6.3a) which broadly corroborates early theoretical work on short-term erosion rates (Figure 6.9; Langbein and Schumm 1958; Walling and Kleo 1979) and subsequent modelling work (Collins and Bras 2008). My result is based on a robust scatterplot smoothing method (LOWESS). Based on a small number of data points, Langbein and Schumm (1958) proposed that sediment yields (as a proxy for erosion rates) in the USA peak in semi-arid regions due to the combination of rainfall (high enough) and vegetation cover (low enough) that results in optimum conditions for erosion (Figure 6.9). Following their work, Walling and Kleo (1979) analysed sediment yields from around the globe and in regions with higher humidity. Their result shows that in addition to semi-arid regions, there are also peaks in sediment yield in humid climates, where the precipitation is subject to highly seasonal variability (Figure 6.9). These previous studies can be considered useful theoretical frameworks for interpreting erosion–climate relationships as the data points are limited and the curves fitted are subjective. Mishra et al. (2019), broadly corroborated this result with compiled global ^{10}Be data by showing a non-linear relationship between long-term erosion rate and precipitation which, however, differs in its peaks and dips relative to the others (Figure 6.9).

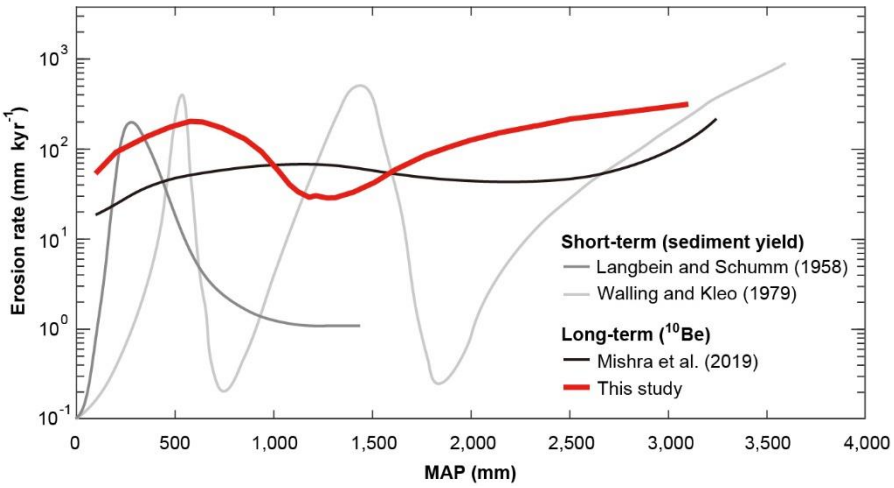

Figure 6.9 Synthesis of studies showing non-linear relationships between MAP and short-term erosion rates (Langbein and Schumm 1958, and Walling and Kleo 1979), and between MAP and long-term erosion rate (Mishra et al. 2019) and this study. See main text for the detailed explanation.

Using 3,074 data points, my study shows that there is a relationship between climate and erosion rates that likely results from the interplay between rainfall and vegetation cover (Langbein and Schumm 1958; Mishra et al. 2019; Walling and Kleo 1979). My results show a peak in erosion rates in the Dry sub-humid regions (MAP ~ 600 mm), a dip in the humid regions (MAP ~ 1,250 mm) and then an increase in erosion rates again in the very humid regions (MAP > 1,300 mm). The patterns in Figure 6.3a support with an extensive dataset the idea that the interplay between rainfall and vegetation represent an important expression of climate that controls erosion rates globally. In arid regions, rainfall is too low to induce any significant erosion despite the lack of vegetation cover (Molnar et al. 2006). In dry sub-humid regions, the rainfall is high enough and the vegetation cover low enough to result in high erosion rates. In humid regions, the substantive vegetation cover hinders the effectiveness of high precipitation, but as rainfall continues to increase, the highly erosive energy of precipitation exceeds the protective capability of vegetation and results in higher erosion rates again (Collins and Bras 2008). One major finding of my study is that the systematic relationship between erosion and climate only holds for long-term erosion rates (Figure 6.3a), and not for short-term rates (Figure 6.3b). I propose that this difference is due to the overwhelming influence of anthropogenic activities on the land surface that masks the inherent climatic influence.

6.5 Influence of glaciation on long-term erosion rates

Prior studies argued that in mid- and high-latitude regions, long-term erosion rates tend to be higher than low-latitude regions because glacial processes during ice ages stripped away the underlying land surface and increased physical weathering through freeze–thaw processes (Cook et al. 2020; Gabet et al. 2008; Harel et al. 2016; Portenga and Bierman 2011; Schaller et al. 2002). These processes would yield young exposure ages directly after glacial retreat, after which the rates might not be expected to change much in the absence of glacial processes. Since cosmogenic radionuclide-derived erosion rates span the period of glaciation up to the present, they average over the relatively fast and high erosion by glaciers and the subsequent low erosion period. I quantified the role of glaciers in producing such high long-term erosion rates through my comparison of formerly-glaciated versus non-glaciated areas within temperate regions (Figure 6.4). This analysis showed five times higher erosion rates for the formerly-glaciated locations within the same Temperate K–G climate zone, which is consistent with previous studies (Harel et al. 2016; Portenga and

Bierman 2011; Schaller et al. 2002). This result is consistent with the relatively low ratio of short- to long-term erosion for the Humid AI category (Figure 6.2b), which likely arises in part because the Humid class includes 46% of the total number of formerly-glaciated sites included in my analysis. Overall, my results suggest that post-glacial erosion rates within temperate areas were much lower due to widespread vegetation cover and thick soils, and the long-term average mostly reflects the result of glacial erosion.

6.6 Anthropogenic influences on short-term erosion rates

Human activities have increased short-term erosion rates by an estimated one to two orders of magnitude (Dedkov and Mozzherin 1996; Kemp et al. 2020; Milliman and Syvitski 1992; Montgomery 2007; Wilkinson and McElroy 2007), suggesting that human influences on sediment yields outweigh natural processes (Hooke 2000; Kemp et al. 2020; Wilkinson and McElroy 2007). Among the many human activities expressed on surface erosion around the globe, agriculture has one of the highest impacts on the land surface because it directly alters both vegetation through replacement of forest canopies with low-interception coverage crops, and soils through replacement of natural profiles containing developed organic layers with homogenised profiles that undergo cycles of tillage and surface compaction (Hooke 2000). This anthropogenic disruption of vegetation and soils should create higher susceptibility to erosion by rainsplash, runoff, and wind (Dedkov and Mozzherin 1996; Kemp et al. 2020; Wilkinson and McElroy 2007). The eroded material would then contribute to stream channels, where it would be measured as elevated sediment flux compared to pre-historic levels.

My analysis showed that short-term erosion rates are higher than the long-term rates in all climate categories, except for the K–G Cold zone (Figure 6.2). The short-term erosion rates within this zone, mainly concentrated in Canada, Eastern Europe, and Russia, are significantly lower than other climate zones (Figure 6.2a, Table 6.1), which I suggest is because most of these regions are covered by contiguous boreal forest that protects the land surface from erosion. Moreover, once the short-term erosion rates were classified by land-use categories, I found that erosion in ‘croplands’ and ‘pastures and rangelands’ is similar, but these rates are significantly higher than erosion rates for classes without anthropogenic influences (Figure 6.5). These results demonstrate that human activities significantly increase short-term erosion rates, that they are consistently detectable around

the globe, and that these influences outweigh natural controls including climate and topography (Figure 6.2, 6.3b, 6.8c, d, Table 6.1). I note that short-term erosion rates are likely to change in the future due to both changes in human land use and due to the regional expression of climate change. For example, milder winters and less snow cover in higher latitudes may promote more land management activities such as forestry, agriculture, and road building, all of which could rapidly increase short-term erosion rates (Serreze et al. 2000). Even though the prevailing agriculture types between climate zones are different and may have different impacts on erosion, my results strongly point to the overwhelming impact of agriculture and related activities on short-term erosion rates, corroborating previous work (Dedkov and Mozzherin 1996; Kemp et al. 2020; Montgomery 2007; Wilkinson and McElroy 2007).

However, it is worth noting that the difference in short-term erosion rates between anthropogenic and non-anthropogenic regions shown here is smaller than was shown in previous studies (Dedkov and Mozzherin 1996; Kemp et al. 2020; Montgomery 2007; Wilkinson and McElroy 2007). For example, Dedkov and Mozzherin (1996) estimated that anthropogenic activities increase sediment yields by a factor of 3.5 in large rivers and 8 in small rivers. I speculate that one of the main reasons for this discrepancy is that here the amount of area that is influenced by anthropogenic activity may be underestimated, based on the defined threshold of > 50% agricultural area. Another possibility is that my analysis may be including more short-term erosion rates sampled in anthropogenically impacted regions, where substantial soil and water conservation efforts in upstream basins, as well as engineering structures (e.g. dams) that trap sediment may result in artificially lower sediment yields (Hooke 2000; Singer and Aalto 2009; Singer and Dunne 2006; Syvitski et al. 2005; Walling and Fang 2003; Walling and Webb 1996; Wilkinson and McElroy 2007).

6.7 Physiographic controls on basin-averaged erosion rates

Although drainage basin area is commonly-used (in combination with slope) as a proxy for erosion (i.e. stream power incision law), I found no clear relationship between basin area and long-term or short-term erosion rates within my compiled global dataset (Figure 6.6), consistent with other studies (e.g. DiBiase et al. 2010; Kirchner et al. 2001; Summerfield and Hulton 1994). There are several factors that potentially obscure any systematic relationship between basin area and erosion including sampling location within the basin,

tectonic setting, and underlying lithology. Cosmogenic radionuclide-derived erosion rates assume a uniform average erosion rate within the upstream contributing area, so sampling location matters. Samples taken in lower order streams (upper parts of basins) reflect more hillslope and debris flow erosion (Stock and Dietrich 2003), whereas downstream samples reflect more fluvial erosion, but may be biased by floodplain storage of sediment, violating the supply-limited assumption within area–erosion relationships (Whipple et al. 1999). Tectonic setting controls the topographic relief of the basin, where active margins have higher relief and steepness than passive margins, promoting higher erosion rates and lower deposition (Ahnert 1984; Milliman and Meade 1983; Walling and Webb 1996; Whipple et al. 1999). Underlying lithology also affects erosion rates, yielding lower exhumation for basins with harder basement rocks for the same drainage area (Hurst et al. 2013). Finally, climate influences the development of soils and vegetation cover, as well as orographic gradients, all of which in turn affect erosion, irrespective of basin area (Collins and Bras 2010; Dedkov and Mozzherin 1996; Milliman and Farnsworth 2011; Olen et al. 2016; Walling and Webb 1996; Willett 1999).

When I classified erosion rates by basin area, a negative relationship between $R_{S/L}$ value and basin area is shown for each of the K–G climate zones, except the Cold zone (Figure 6.7). Studies have shown that in large basins (e.g. Amazon River), the differences between long- and short-term erosion rates are less discernible compared to small basins, due to the sediment buffering capacity of large drainage basins (Covault et al. 2013; Wittmann et al. 2011). Buffering capacity, or the degree of sediment transport delay from the source area to the basin outlet in response to the variations of environmental controls, is determined by the balance between sediment supply (affected by erosion rate and river transport capacity) and the accommodation of deposition, such as riverbed or flood plain (Covault et al. 2013; Wittmann et al. 2011). Large basins usually have higher buffering capacity, since they tend to have longer river channels and larger flood plains; therefore, short-term variations of sediment supply from the uplands may be diluted within the basin (i.e. the increased sediments may deposit temporarily when transported along the river channel), and harder to be detected at the downstream sections (Jerolmack and Paola 2010).

The $R_{S/L}$ values are insensitive to basin area within Arid catchments (Figure 6.7). I argue that this is because arid regions have a distinctive hydrological regime, such as partial area runoff (Yair et al. 1978) and transmission loss (Keppel and Renard 1962; Wallace and

Renard 1967), which was discussed in Chapter 4. These characteristic features of arid zone hydrology reduce the influence of basin area on hydrological processes, including sediment transportation, leading to weaker influence of buffering capacity of drainage basins in arid regions. In the Temperature and Cold zones, the $R_{S/L}$ values are generally lower than the other two categories (i.e. long-term erosion rates are more similar to short-term rates, or even higher) because glacial processes during past ice ages led to increased long-term rates (Section 6.5). In addition to glacial processes, wildfires, landslides and volcanic events that exhibit high magnitude and low frequency, may also lead to higher long-term erosion rates in humid climate zones (Covault et al. 2013; Kirchner et al. 2001; Schaller et al. 2001) as the higher soil coverage can generate large amounts of sediment. The rarity of these large magnitude events means that they are not usually captured in short-term records. The increased timescale of ^{10}Be-derived erosion rates provides a higher probability that extreme erosion events are included in the data record.

Drainage basin steepness is considered a critical control on erosion rates (e.g. Granger et al. 1996; Portenga and Bierman 2011; Summerfield and Hulton 1994), which is also fundamental to the stream power incision law. Drainage basins with higher steepness tend to produce higher velocity of runoff because of the downslope vector of potential energy, which increase the shear stress of water flow and thus produce higher erosion that shapes land surface and transports sediments downstream (Knighton 1998; Whipple and Tucker 1999). In addition, steep drainage basins are often located in tectonically-active regions, with low strength of bedrock (because of joints and faults developments), high frequency of landslides (Binnie et al. 2007; Grin et al. 2018), and high precipitation rates caused by orographic effects (Roe et al. 2002; Willett 1999), all of which would tend to increase erosion rates. My analyses show positive relationships between slope gradient and total relief of river channels and long-term erosion rates (Figure 6.8a, b), suggesting that both climatic and topographic factors control long-term erosion rates despite no clear relationship between short-term erosion rates and these topographic controls (Figure 6.8c, d). Short-term erosion rates are dominated by anthropogenic activities. Agriculture, a key anthropogenic influence on erosion, tends to cluster in downstream parts of drainage basins with gentler slopes (Wilkinson and McElroy 2007). In upstream sections of drainage basins, anthropogenic activities that accelerate erosion (e.g. deforestation) may be ameliorated (from a sediment yield perspective) by soil and water conservation efforts (Montgomery 2007), and/or by the trapping of sediment within reservoirs (Syvitski et al. 2005; Walling and

Fang 2003; Walling and Webb 1996). Thus, sediment yields may differ substantially from upstream to downstream within the same basin, depending on the locations of these anthropogenic activities within the landscape. Therefore, human-induced sediment yields may generate unclear relationships between short-term erosion rates and steepness of drainage basins.

6.8 Chapter summary

By compiling and analysing erosion rates from globally distributed sites, I demonstrate a few key differences in long- and short-term rates and their dominant controls: (1) short-term erosion rates are significantly higher than long-term erosion rates in all climate zones except in the K–G Cold zone; (2) long-term erosion rates are higher in mid- and high-latitude regions (and in K–G Cold zone), which were enhanced by glacial processes during past ice ages; (3) only long-term erosion rates are strongly related to climate and topography, while short-term rates do not exhibit any relationship to climatic or topographic factors; (4) short-term rates seem to be dominated by human activities which mask natural controls; (5) a key finding is that a non-linear relationship exists between long-term erosion rates and climate, reflecting the balance between precipitation and vegetation cover; however, this relationship does not hold for the short-term erosion rates as proposed by former studies (Langbein and Schumm 1958; Walling and Kleo 1979); (6) short-term erosion rates are generally several times higher than long-term rates in small basins, showing that human-induced erosion is more detectable in small basins with lower sediment buffering capacity; (7) on the contrary, long-term erosion rates tend to be similar or even higher than short-term rates in large basins. The latter can be explained by former glacial processes and high-magnitude, low frequency natural events such as wildfires, mass movements, and volcanic activity (Covault et al. 2013; Kirchner et al. 2001; Schaller et al. 2001). Based on these findings, I suggest that erosion rates around the world, regardless of climate zone, are likely to change in the future in response to both climate change and anthropogenic influences, which are growing in prevalence globally.

7. Synthesis

7.1 Climatic controls on drainage basin evolution

In the field of geomorphology, scientists have long been studying the characteristics of landform in the drainage basin, and analysing the processes and controls shaping the landform. The drainage basin, including the hillslope and river channel parts, is a topographic unit receiving water supply from precipitation and drainage the land surface through runoff and streamflow. When water flows downslope, the gravitational energy from the slope may cause the water to shape the land surface by eroding the bedrock and transporting produced sediments into the river channel, which then be transported downstream by streamflow. Various topographic metrics have been proposed for analysing the landform. Some of them related to the vertical aspect of basin (e.g. slope gradient/topographic relief, river long profile, and erosion rate) (e.g. Hack 1957; Lague 2005; Langbein and Schumm 1958), others focus on the planar organisation (e.g. drainage density, river network, drainage divide location, and basin shape) (e.g. Bonnet 2009; Rinaldo et al. 1995; Seybold et al. 2017; Singer et al. 2018).

Through field observations, experiments, and numerical modelling, the environmental factors that have been identified to control land surface processes and topographic features including the climate, tectonics, topography, lithology, grain size, vegetation, and human activities (Figure 1.1). Climate controls the precipitation and temperature, influencing the type, rate and spatio-temporal distribution of precipitation (Bookhagen and Strecker 2012; Murphy et al. 2016; Nicholson 2011); tectonics controls the topography (e.g. the relief and slope gradient) of basin, influencing the gravitational energy of land surface processes, and may decrease the strength of bedrock through developing joints and faults (Portenga and Bierman 2011; Yizhou et al. 2014); lithology controls the landform directly by its erodibility and indirectly by the amount and grain size of weathered and produced sediments (Pederson and Tressler 2012; Yatsu 1955); sediment grain size represent the roughness of land surface, and influence the transportability by water flow (Blom et al. 2016; Hack 1957); vegetation intercepts the raindrop by the leaves, hamper the erosion by the root system, but the root may also enhance the weathering rate of bedrock (Collins and Bras 2008; Langbein and Schumm 1958; Mishra et al. 2019; Starke et al. 2020); and finally, human activities

change the land surface by altering the vegetation cover, tilling, and construction, which tend to increase erosion rate significantly (Dedkov and Mozzherin 1996; Montgomery 2007; Wilkinson and McElroy 2007).

In order to identify the dominant control on landform, studies have measured topographic metrics across various basins, but the identified control often depends on the environmental characteristics of studied areas. For example, Ferrier et al. (2013) studied river incision rate in Kaua'I island, where the rainfall gradient is steep. They found a positive relationship between MAP and river incision rate. The incision rate cannot be explained only by the slope gradient and drainage area, but it needs to incorporate the influence of precipitation. On the other hand, Pan et al. (2010) and Yizhou et al. (2014) studied erosion rates in Qilian Shan Mountains, China, and showed that the erosion rates are mainly controlled by the slope gradient and topographic relief, whilst the influence of climate is minor. To explore the pattern of drainage basin topography across a wider area, several studies aimed at global analyses. Some of them found that the topography and tectonics are dominant controls on landform, and the influence of precipitation can only be detected at a smaller spatial scale (Harel et al. 2016; Portenga and Bierman 2011).

Given that climatic influences on land surface processes seem to be logical, which should also control landform development, it is surprising that the link between climate and topographic evolution is still debatable (Aalto et al. 2006; Balco and Stone 2005; Harel et al. 2016; Portenga and Bierman 2011). The possible reasons for the obscure climatic influences on the landform are (1) land surface processes are controlled by several environmental factors in addition to climate (e.g. topography, tectonics), and their relative importance may differ between drainage basins and spatio-temporal scales (Aalto et al. 2006; Portenga and Bierman 2011); (2) climate tends to covary with several factors (e.g. vegetation, topography) (Li and Fang 2016; Olen et al. 2016; Vandenberghe 2003); (3) climatic controls on landform may be non-linear (e.g. the relationship between MAP and erosion rate is influenced by vegetation density, leading to a non-linear relationship) (Langbein and Schumm 1958); (4) climate may shift during landform development, making the climatic signals hard to be detected at specific timescales (Bookhagen et al. 2005).

Since the climate is assumed to influence drainage basin landform, but the climatic signal is challenging to identify, especially at the global scale, in this thesis, the global data of

topographic metrics were compiled for analysing whether there are differences between climate zones, and whether these differences can be linked to drainage basin hydrology. The river long profile and drainage basin erosion rate were chosen because these metrics relate to the vertical change of land surface elevation, which is hypothesised to reveal the balance between water and sediment transportation within the basin and may reflect climatic influences.

As an early analysis on river long profile shape, Hack (1957) measured river profiles and relevant environmental data in Virginia and Maryland, USA, and found that the slope gradient of river channel is proportional to the grain size of riverbed materials and inversely proportional to drainage area (represents the discharge). Similarly, Snow and Slingerland (1987) conducted numerical modelling on river long profile evolution and found that the graded river profile concavity is controlled by the downstream distribution of water discharge, the sediment flux, grain size of sediment, and channel width. Because discharge tends to increase while sediment concentration and grain size decrease from the river head toward downstream direction, the slope gradient is gentler with downstream distance, developing a concave form of river long profile. The long profile shape of bedrock river can be described by stream power incision law (Equation 5.4), which shows that river incision rate has a positive power-law relationship with drainage area and slope gradient. Because a river generally performs positive *Q*–*A* and negative *S*–*A* relationships, the maximum stream power (and incision rate) occurs at the middle section of river channel, forming a concave long profile (Flint 1974; Howard et al. 1994; Knighton 1999; Whipple and Tucker 1999).

Although conventional theory predicts river long profile has concave form, several studies found that precipitation influence river profile concavity. For example, if the MAP is subjected to orographic rainfall, leading to lower increasing rates of downstream variations in discharge and river incision rate, the river tends to develop a straighter long profile (Han et al. 2014; Roe et al. 2002; Zaprowski et al. 2005). Also, studies in drylands showed that river profiles are straighter (or even convex) compared to humid rivers, which may relate to different hydrological regimes in drylands (Grenfell et al. 2014; Michaelides et al. 2018; Powell et al. 2012; Singer and Michaelides 2014; Sólyom and Tucker 2004; Vogel 1989). However, there is yet a global analysis of river long profiles; therefore, the overall pattern of river long profile concavity around the globe and whether there is a link between climate and river long profile are still unknown.

Studies have measured drainage basin erosion rate extensively and analysed them between drainage basins and between timescales. Various environmental factors influence erosion rates as described above (i.e. climate, tectonics, land surface properties, and human activity), depending on the local environments of drainage basins and the analysed timescale. For climatic factors, studies generally show a positive relationship between MAP and erosion rate because of limited and infrequent water supply in drylands and high precipitation in humid regions, influencing the raindrop erosion, chemical weathering, possibility of landslide on the hillslope, and river incision in the channel (Bookhagen and Strecker 2012; Burbank et al. 2003; Gabet et al. 2008; Harel et al. 2016; Thiede et al. 2004; von Blanckenburg 2005). Nevertheless, vegetation may complicate the influence of precipitation on erosion. Langbein and Schumm (1958) analysed sediment yield with MAP and found a non-linear relationship between them. This is because in drylands, the vegetation is sparse, erosion rate increases with precipitation. In contrast, in humid regions, dense vegetation cover hampers the erosion, causing erosion rate decreases with higher precipitation. Therefore, the maximum erosion rate appears in semi-arid regions where enough water can cause erosion, but the vegetation is too sparse to protect the land surface. This non-linear relationship, reflecting the balance between MAP and vegetation cover, is also revealed by later field measurements for both short-term (Walling and Kleo 1979) and long-term erosion rates (Mishra et al. 2019; Starke et al. 2020), and modelling works (Collins and Bras 2008). In addition, the climate can influence erosion rate by glacial processes and wildfire. The glaciation is assumed to increase long-term erosion rate within mid- and high-latitudes because of higher erosion from glaciers and freeze–thaw processes at ice ages (Gabet et al. 2008; Harel et al. 2016; Portenga and Bierman 2011; Schaller et al. 2002). Wildfires are more prevalent during dry periods (Han et al. 2020; Pierce et al. 2004) and tend to increase erosion rate by destroying vegetation and increasing mass movement possibility (Cannon et al. 1998; Meyer et al. 2001; Pierce et al. 2004). Although studies have analysed erosion rates over the decades, the dominant controls vary between drainage basins and timescales. It remains unclear the global pattern of erosion rates, and whether climatic signals can be detected worldwide between timescales.

In this thesis, I demonstrated various downstream distributions of discharge between climate zones, reflecting the aridity of drainage basin (Chapter 4). Specifically, rivers in humid regions are mainly perennial (Table 4.1) and exhibit downstream-increasing discharge (Figure 4.4i–l, 4.5b), which is due to high and frequent precipitation and water contributions

from tributaries and groundwater, resulting in a positive power-law *Q*–*A* relationship (Figure 4.6), and is consistent with previous theory (Leopold and Maddock 1953; Whipple and Tucker 1999). However, as the aridity increases, the streamflow becomes ephemeral (Table 4.1), and the downstream-increasing rate of discharge becomes constant toward downstream direction (Figure 4.4e–h, 4.5a) or even negative (Figure 4.4a–d, 4.5a), especially during small flood events. This is because in drylands, the precipitation is low, infrequent, and with highly spatio-temporal variability (due to the nature of convective storms), which leads to partial area runoff, supplying water into river channel in a limited proportion of land area (Yair et al. 1978) and during limited time period. As water flows into the channel, the streamflow is subjected to transmission loss because of high infiltration and evaporation rates (Fan et al. 2013; Jaeger et al. 2017; Keppel and Renard 1962; Thornes 2009). Therefore, the discharge tends to be constant or decrease downstream, and the often-assumed *Q*–*A* relationship is not applicable for in drylands (Figure 4.6). These various streamflow patterns not only reflect climatic controls but also influence drainage basin topography, such as the river long profile (Chapter 5). River profiles are generally concave in all climate zones (Figure 5.6, 5.9), consistent with existing theory (Hack 1957; Sinha and Parker 1996; Snow and Slingerland 1987); nevertheless, they are systematic straighter with higher aridity. Through numerical modelling, the mechanism of straighter profiles in drylands is shown to result from constant downstream distribution of discharge (Figure 5.12). In drylands, ephemerality accentuates transmission losses that reduce downstream flow and also gives more weight to each extreme flood event; that is, smaller floods that exhibit downstream-decreasing discharge are more frequent yet less geomorphically effective than large ones that increase downstream. Thus, the discharge may increase and decrease downstream for each flood, resulting in a distributional median value close to zero, and generate straighter river long profile.

In terms of climatic influences on the erosion rate, a non-linear relationship is shown between long-term erosion rate and aridity/MAP (Figure 6.2b, 6.3a), reflecting the balance between precipitation and vegetation cover. This non-linear relationship is similar to the patterns proposed by Langbeian and Schumm (1958) and Walling and Kleo (1979), except that the data here show increasing erosion rates from humid to extremely humid regions. However, this non-linear relationship only exists for long-term erosion rates but not for short-term rates since the latter is dominated by anthropogenic factors (Figure 6.5). In addition, long-term erosion rates are higher in mid- and high-latitude regions because of past

glaciation (Figure 6.2a, 6.4), confirming previous assumption (Harel et al. 2016; Portenga and Bierman 2011; Schaller et al. 2002).

Overall, this thesis shows that the aridity of drainage basin controls the hydrological regime, influencing river long profile shape and long-term erosion rate. River long profile can be explained mainly by the hydrological control, whilst erosion rate is also influenced by vegetation cove (which is positively related to precipitation; Mishra et al. 2019), therefore, showing a non-linear relationship with climate. However, long-term erosion rates in temperate and cold regions are also enhanced by past glaciations when the temperature was lower, showing the influences of climate change and timescale on landform evolution.

Since drainage basin erosion rate integrates erosion processes on the hillslope and in the river channel, and river long profile reflects the balance between sediment supply from the hillslope and sediment evacuation by the streamflow, I expect to find a connection between erosion rate and river profile concavity between climate zones. For example, where the erosion rate on the hillslope is higher than river incision rate, the river channel is assumed to aggrade and develop convex long profile; in contrast, where the erosion rate is lower than incision rate, the channel should degrade and produce concave form (Michaelides et al. 2018; Snow and Slingerland 1987). However, according to the results, long-term erosion rates tend to increase from arid to sub-humid regions and decrease from sub-humid to humid regions (Figure 6.2b, 6.3a), whilst river long profiles are more concave with higher humidity (Figure 5.9c–e). Therefore, there seems no clear link between these two metrics. This may partly due to the basin-averaged erosion rate integrates processes on the hillslope, and in the channel; the difference of processes between these two parts of basin cannot be distinguished. To understand the connection between erosion rate and river long profile, the interplay of water and sedimentary processes between the hillslope and river channel need to be investigated in the future. The specific questions include: What is the relative importance of long-term erosion rate on the hillslope and river incision rate in the channel? Whether sediment supply from the hillslope exceed/below sediment-transport capacity of streamflow? Whether the proportion of bedrock river to alluvial rivers differ between climate zones?

Although this thesis classified hydrologic and topographic metrics between climate zones and detected climatic signals, other environmental factors may also influence the metrics

but were not censored and excluded (except several factors were considered for the sensitivity analyses of river long profile evolution and the analyses of erosion rate). For example, long-term erosion rates are positively related to the topography (Figure 6.8a, b). According to previous studies, erosion rates are also enhanced in regions with tectonic uplift, weak lithology, small grain size of sediments on the land surface, and high frequency of landslides (Binnie et al. 2007; Codilean et al. 2014; Grin et al. 2018; Schaller et al. 2001; Struck et al. 2018; Wittmann et al. 2011). Even though river long profile concavity is not clearly influenced by topography (Figure 5.11b, c), the profile tends to be more concave with higher downstream-decreasing rates in grain size (relating to the spatial distributions of discharge and lithological erodibility), sediment supply (influenced by landslide location, tributary organisation, and land uses along the river), and tectonic uplifting (Blom et al. 2016; Hanks and Webb 2006; Kirby and Whipple 2001; Kirby and Whipple 2012; Pederson and Tressler 2012; Yatsu 1955). Even for hydrological analyses, the grain size of riverbed materials (influencing infiltration rate), tributaries organisation, and channel geometry (determining whether the water flows overbank during flood events) influence the downstream rate of change in discharge (Abdulrazzak and Sorman 1994; Belmonte and Beltrán 2001; Knighton and Nanson 1994; Lange 2005; Snelder et al. 2013; Tan et al. 2021). Some of the environmental controls are indirectly influenced by the climate (e.g. landslide, grain size, tributary organisation), whilst others do not have clear relationship with climate (e.g. tectonics, lithology) and may hamper the detection of climatic signals with these environmental variabilities.

In addition to the variability of environments around the globe, there are few assumptions made for the analyses, including the inconsistency of timescales between data and the methods used for estimating drainage basin erosion rate. Using K–G and AI climate classifications (based on current climatic conditions), the climate is assumed to remain constant over the landform development periods. This assumption is feasible for analysing the hydrological regime and short-term erosion rate since these data were measured during decadal timescales, consistent with the climate classifications. However, river long profiles have been developing over longer timescale, and the long-term erosion rates are with timescale from 10^3 to 10^5 yr (Granger and Schaller 2014; von Blanckenburg and Willenbring 2014). Therefore, these analyses assumed that the climate had not changed dramatically during longer time period, and the river profiles have reached the steady-state under current climate. The former assumption should be reasonable in most regions (note that for long-

term erosion rates, the influences of past glaciation were considered); however, the latter may cause bias in basins with high tectonic activities and where large-magnitude events (e.g. landslides) happen frequently.

Compared to the hydrological and river long profile data which were based on direct measurements, drainage basin erosion rates were estimated indirectly by sediment flux (for short-term) and cosmogenic radionuclide concentration (for long-term), which include assumptions that may affect the interpretation of landform evolution. Both methods provide the averaged value of erosion rate for the upstream area, which neglects sediment storage during transportation. The former can be influenced by spatially variable erosion rates within the basin; for example, large-magnitude landslides or various erosion rates result from non-climatic factors (e.g. different lithologic, tectonic, and topographic conditions) may overestimate basin-averaged erosion rates and bias the interpretation of climatic controls. The neglect of sediment storage is an issue mainly for short-term erosion rates estimated in large basins since large basins have higher buffering capacity (Figure 6.7; Covault et al. 2013; Wittmann et al. 2011). Short-term enhancement of sediments in large basin may deposit temporally in the riverbed or flood plain and are not detectable at the outlet of basin. Erosion rate estimated from sediment flux also assume a spatially constant soil density worldwide and assume that sediments are all transported as suspended load. However, soil density is influenced by lithology, soil texture and moisture. Moreover, the eroded sediment from hillslope may come from bedrock (with higher density) rather than soil, and the sediments may transport as bed load. Both situations are more common in drylands and mountainous regions with less developed soil layers, and less sorting and abrasion processes in river channels during sediment transportation (Milliman and Syvitski 1992; Singer and Dunne 2004; Singer and Michaelides 2014).

Erosion rate estimated by cosmogenic radionuclides also assume that the erosion rate is faster than radioactive decay rate; radionuclide concentration has achieved the balance between production, erosion and decay rates; the nuclide concentration has no dependency on grain size; there is no erosion–deposition cycle in the drainage basin; and quartz exists in sediments throughout the entire basin (Brown et al. 1995; Dosseto and Schaller 2016; Granger et al. 2013; Struck et al. 2018). The first two assumptions may not influence the results significantly because erosion rates are mostly high enough (> 0.3 mm kyr^{-1} for ^{10}Be; Granger et al. 2013; Figure 6.2), and the landscapes should be old enough for estimating

by radionuclides (> 10^4 yr when the erosion rate is 100 mm kyr^{-1}; Brown et al. 1995). However, the influences of the rest of assumptions depending on the choice of basin and are harder to assess. For example, whether the drainage basin experiences erosion–deposition cycle during the analysed timescale depending on the variations of climate, hydrology, and land use (Clapp et al. 2000; Dethier et al. 1988; Grenfell et al. 2014); and the universality of sand-sized quartz within the basin depends on the lithology and land surface processes (Singleton et al. 2017; Tofelde et al. 2018). Several recent studies found a negative relationship between the concentration of cosmogenic radionuclide and grain size. This is because coarser sediments tend to situate at deeper soil layer and have received lower amount of radionuclide. If sediments of a basin are mainly produced by deep erosional processes (e.g. landslide), the grain size of sediments are likely to be high; and because the radionuclide concentration is usually measured only from sand-sized grain, the erosion rate may be underestimated (van Dongen et al. 2019; Tofelde et al. 2018).

Since global compilations of hydrologic and topographic data contain large variability of environmental conditions, and many environmental factors are not directly related to climate, the compiled data display large scatters even within each climate zone. Moreover, several assumptions of methodology may be inapplicable in certain regions. Nevertheless, by meta-analysing global data classified by climate zones, I hypothesised that the influences of this variability can be diluted; although by further excluding these factors, the climatic signals on basin landform should be revealed more clearly. The results demonstrate that the climate influences hydrological regime of basin, which can be linked to topographic evolution. Moreover, the conventional assumptions of spatial influences on hydrologic parameters (e.g. Q–A and S–A relationships) and the stream power incision law are not universally applicable. Although in humid regions, these theories have been investigated and validated across various locations (e.g. Harel et al. 2016; Kirby and Whipple 2001; Knighton 1999), they are weaker with higher aridity. These findings enhance the understanding of topographic response to climate and climate change, and can improve the accuracy and comprehension of landscape evolution models in the future.

7.2 Suggestions for future work

Based on the assumptions and findings of this thesis, the following research questions/objectives are suggested for future works:

(1) Given that drainage basin evolution is controlled by numerous factors other than climate (e.g. tectonics, lithology, and topography), and climate tends to covary with some of them (Aalto et al. 2006; Bookhagen and Strecker 2012; Li and Fang 2016; von Blanckenburg 2005), it is worth to consider other environmental controls and explore whether patterns of hydrology and topographic metrics between climate zones are more obvious without the influences of other environmental factors, and what are the relative importance on landform developments between climate and these factors.

(2) River long profile is influenced by both runoff and sedimentary factors (Hack 1957; Michaelides et al. 2018; Snow and Slingerland 1987); therefore, I would expect that erosion rate of hillslope (controlling sediment supply from the hillslope to the river channel) influences river long profile shape. However, the modelling results show that the downstream distribution of discharge dominates rive profile concavity. Therefore, it is unclear how does the interplay between runoff and sediment-transport on the hillslope and in the river channel controls river long profile, and what is the relative importance on river long profile between hillslope erosion and river incision rates.

(3) A non-linear relationship between climate and long-term erosion rate is shown in this study. In extremely humid regions, the erosion rates increase with precipitation, which I proposed to be the result of high erosive power of rainfall. However, some other studies suggest that the higher erosion rate may also result from high weathering rate of bedrock, high nutrients in soil, and high frequency of landslides in these regions (Mishra et al. 2019; Starke et al. 2020), which is lack of definite evidence. Therefore, the mechanisms of high erosion rate in extreme humid regions need to be studied further.

(4) The classification of K–G climate zone and AI category used in this study are based on vegetation types and the balance between MAP and MAE, respectively. These classifications do not link directly to hydrologic factors, such as streamflow pattern. A recent hydrology-based classification categorises the climate zones by three indices, the aridity, aridity seasonality, and proportion of precipitation as snow (Knoben et al. 2018), which may be able to show the links of climate–hydrology–erosion more clearly and may reveal more details of climatic controls on topographic evolution.

(5) This study assumes that the climate remains constant during past drainage basin evolution, and the results imply the response of landform change to future climate change. Considering that human-induced climate change is an ongoing phenomenon, resulting in shifts of aridity and temperature of drainage basins (Serreze et al. 2000), I suggest that future work can analyses co-evolution of drainage basin topography with climate change by conducting experiments or modellings.

(6) In addition to river long profile and drainage basin erosion rate, climate may also influence other topographic metrics of drainage basin, such as the bedrock erosion rate, drainage density, channel steepness, and basin shape. Global analyses of climatic controls on other topographic metrics can improve our understanding on different aspects landform responses to climate change.

8. Conclusions

I compiled streamflow data in the USA, and river long profiles, short- and long-term erosion rates worldwide from literature and open-accessed databases. These data were classified by K–G climate classification and AI categories, and analysed with relevant environmental data, to explore climatic controls on drainage basin hydrology and topographic evolution. Two parameters were also developed for quantifying the hydrological regime and river long profile shape, including the rate of downstream change in discharge (α) and the Normalised Concavity Index (NCI) of river long profile.

The aridity of drainage basin controls the ephemerality of streamflow and downstream change in discharge. In humid rivers, the streamflow is mainly perennial, with downstream-increasing discharge contributing from tributaries and groundwater, showing a positive *Q*–*A* relationship. As the aridity of drainage basin increases, the streamflow tends to be ephemeral, with constant discharge (for low ephemeral rivers) or decreasing discharge downstream (for high ephemeral rivers, except during extreme flood events), owing to infrequent and highly variable rainfall and transmission losses in drylands. Therefore, the *Q*–*A* relationship is obscure in dryland rivers, especially with high aridity and during small events.

The river long profiles are generally concave-up across all climate zones; however, the profiles are systematically straighter with higher aridity. Through numerical modelling, I demonstrated that these patterns in long profile shape are dominated by the downstream change in discharge. In humid regions, downstream-increasing discharge develops concave profiles, as described by the conventional theory; whilst in arid regions, the downstream distribution of median discharge tends to be constant over longer timescale, leading to straighter river profiles. This hydrologic control on profile reflects different rainfall–runoff regimes between climate zones, which overrides other environmental controls.

For drainage basin erosion rates, a non-linear relationship between climate and long-term erosion rates is shown, reflecting the balance between precipitation and vegetation cover. In addition, glacial processes during ice ages enhance long-term erosion rates in mid- and high-latitude regions. However, long-term rates are also positively related to the steepness

of drainage basins, meaning that climate and topography are the common factors. In contrast, short-term erosion rates are dominated by human activities, which mask the influences of natural controls and are more detectable in small basins due to lower sediment buffering capacity of smaller basins.

The study demonstrates the spectrums of downstream changes in discharge and river long profile concavity across the aridity of drainage basins and identifies the patterns and complex environmental interplays with erosion rates between timescales. The results confirm several arguments from previous studies but also challenge the conventional theory of positive *Q*–*A* relationship and concave river long profile around the globe. Despite various environmental conditions around the globe, this thesis links climatic controls to the hydrological regime and landform evolution, which can improve our understanding on climate–hydrology–erosion relationships.

References

Aalto, R., Dunne, T., Guyot, J. L., 2006. Geomorphic controls on Andean denudation rates. The Journal of Geology, 114, 85–99.

Abdulrazzak, M. J., Sorman, A. U., 1994. Transmission losses from ephemeral stream in arid region. Journal of Irrigation and Drainage Engineering, 120, 669–675.

Abrahams, A. D., Parsons, A. J., Luk, S.-H., 1988. Hydrologic and sediment responses to simulated rainfall on desert hillslopes in southern Arizona. Catena, 15, 103–117.

Ahnert, F., 1984. Local relief and the height limits of mountain ranges. American Journal of Science, 284, 1035–1055.

Asner, G. P., Elmore, A. J., Olander, L. P., Martin, R. E., Harris, A. T., 2004. Grazing systems, ecosystem responses, and global change. Annual Review of Environment and Resources, 29, 261–299.

Balco, G., Stone, J. O. H., 2005. Measuring middle Pleistocene erosion rates with cosmic-ray-produced nuclides in buried alluvial sediment, Fisher Valley, southeastern Utah. Earth Surface Processes and Landforms, 30, 1051–1067.

Belmonte, A. M. C., Beltrán, F. S., 2001. Flood events in Mediterranean ephemeral streams (ramblas) in Valencia region. Spain. Catena, 45, 229–249.

Bierman, P. R., Caffee, M., 2001. Slow rates of rock surface erosion and sediment production across the Namib Desert and escarpment, southern Africa. American Journal of Science, 301, 326–358.

Bierman, P. R., Reuter, J. M., Pavich, M., Gellis, A. C., Caffee, M. W., Larsen, J., 2005. Using cosmogenic nuclides to contrast rates of erosion and sediment yield in a semi-arid, arroyo-dominated landscape, Rio Puerco Basin, New Mexico. Earth Surface Processes and Landforms, 30, 935–953.

Binnie, S. A., Phillips, W. M., Summerfield, M. A., Fifield, L. K., 2007. Tectonic uplift, threshold hillslopes, and denudation rates in a developing mountain range. Geology, 35, 743–746.

Blom, A., Viparelli, E., Chavarrías, V., 2016. The graded alluvial river: profile concavity and downstream fining. Geophysical Research Letters, 43, 6285–6293.

Bonnet, S., 2009. Shrinking and splitting of drainage basins in orogenic landscapes from the migration of the main drainage divide. Nature Geoscience, 2, 766–771.

Bonnet, S., Crave, A., 2003. Landscape response to climate change: insights from experimental modeling and implications for tectonic versus climatic uplift of topography.

Geology, 31, 123–126.

Bookhagen, B., Strecker, M. R., 2012. Spatiotemporal trends in erosion rates across a pronounced rainfall gradient: Examples from the southern Central Andes. Earth and Planetary Science Letters, 327, 97–110.

Bookhagen, B., Thiede, R. C., Strecker, M. R., 2005. Late Quaternary intensified monsoon phases control landscape evolution in the northwest Himalaya. Geology, 33, 149–152.

Brown, E. T., Stallard, R. F., Larsen, M. C., Raisbeck, G. M., Yiou, F., 1995. Denudation rates determined from the accumulation of in situ-produced ^{10}Be in the Luquillo Experimental Forest, Puerto Rico. Earth and Planetary Science Letters, 129, 193–202.

Burbank, D. W., Blythe, A. E., Putkonen, J., Pratt-Sitaula, B., Gabet, E., Oskin, M., Barros, A., Ojha, T. P., 2003. Decoupling of erosion and precipitation in the Himalayas. Nature, 426, 652–655.

Byun, J., Paik, K., 2017. Small profile concavity of a fine-bed alluvial channel. Geology, 45, 627–630.

Cannon, S. H., Powers, P. S., Savage, W. Z., 1998. Fire-related hyperconcentrated and debris flows on Storm King Mountain, Glenwood Springs, Colorado, USA. Environmental Geology, 35, 210–218.

Charlton, R., 2007. Fundamentals of Fluvial Geomorphology. Routledge, Oxon.

Chen, S.-A., Michaelides, K., Grieve, S. W. D., Singer, M. B., 2019. Aridity is expressed in river topography globally. Nature, 573, 573–577.

Clapp, E. M., Bierman, P. R., Nichols, K. K., Pavich, M., Caffee, M., 2001. Rates of sediment supply to arroyos from upland erosion determined using in situ produced cosmogenic ^{10}Be and ^{26}Al. Quaternary Research, 55, 235–245.

Clapp, E. M., Bierman, P. R., Schick, A. P., Lekach, J., Enzel, Y., Caffee, M., 2000. Sediment yield exceeds sediment production in arid region drainage basins. Geology, 28, 995–998.

Clubb, F. J., Mudd, S. M., Milodowski, D. T., Grieve, S. W. D., Hurst, M. D., 2017. LSDChannelExtraction Version v1.0. Zenodo, https://doi.org/10.5281/zenodo.824198.

Clubb, F. J., Mudd, S. M., Milodowski, D. T., Hurst, M. D., Slater, L. J., 2014. Objective extraction of channel heads from high-resolution topographic data. Water Resources Research, 50, 4283–4304.

Codilean, A. T., Fenton, C. R., Fabel, D., Bishop, P., Xu, S., 2014. Discordance between cosmogenic nuclide concentrations in amalgamated sands and individual fluvial pebbles in an arid zone catchment. Quaternary Geochronology, 19, 173–180.

Codilean, A. T., Munack, H., Cohen, T. J., Saktura, W. M., Gray, A. G., Mudd, S. M., 2018. OCTOPUS: An open cosmogenic isotope and luminescence database. Earth System Science Data, 10, 2123–2139.

Collins, D. B. G., Bras, R. L., 2008. Climatic control of sediment yield in dry lands following climate and land cover change. Water Resources Research, 44, W10405.

Collins, D. B. G., Bras, R. L., 2010. Climatic and ecological controls of equilibrium drainage density, relief, and channel concavity in dry lands. Water Resources Research, 46, W04508.

Cook, S. J., Swift, D. A., Kirkbride, M. P., Knight, P. G., Waller, R. I., 2020. The empirical basis for modelling glacial erosion rates. Nature Communications, 11, 759.

Coulthard, T. J., Van de Wiel, M. J., 2013. Climate, tectonics or morphology: what signals can we see in drainage basin sediment yields? Earth Surface Dynamics, 1, 13–27.

Covault, J. A., Craddock, W. H., Romans, B. W., Fildani, A., Gosai, M., 2013. Spatial and temporal variations in landscape evolution: historic and longer-term sediment flux through global catchments. The Journal of Geology, 121, 35–56.

de Araújo, J. C., González Piedra, J. I., 2009. Comparative hydrology: analysis of a semiarid and a humid tropical watershed. Hydrological Processes, 23, 1169–1178.

Dedkov, A. P., Mozzherin, V. I., 1996. Erosion and sediment yield on the Earth. In Erosion and Sediment Yield: Global and Regional Perspectives, IAHS Publications, Wallingford, Oxfordshire, 236, 29–36.

Dethier, D. P., Harrington, C. D., Aldrich, M. J., 1988. Late Cenozoic rates of erosion in the western Española basin, New Mexico: Evidence from geologic dating of erosion surfaces. Geological Society of America Bulletin, 100, 928–937.

DiBiase, R. A., Whipple, K. X., Heimsath, A. M., Ouimet, W. B., 2010. Landscape form and millennial erosion rates in the San Gabriel Mountains, CA. Earth and Planetary Science Letters, 289, 134–144.

Dosseto, A., Schaller, M., 2016. The erosion response to Quaternary climate change quantified using uranium isotopes and in situ-produced cosmogenic nuclides. Earth-Science Reviews, 155, 60–81.

Dunne, T., 1978. Field studies of hillsope flow processes. In Hillslope Hydrology, John Wiley & Sons, Chichester, 227–293.

Dunne, T., 1991. Stochastic aspects of the relations between climate, hydrology and landform evolution. Transactions, Japanese Geomorphological Union, 12, 1–24.

Dunne, T., Leopold, L. B., 1978. Water in Environmental Planning. Freeman, New York.

Fan, Y., Li, H., Miguez-Macho, G., 2013. Global patterns of groundwater table depth. Science, 339, 940–943.

Farr, T. G., Rosen, P. A., Caro, E., Crippen, R., Duren, R., Hensley, S., Kobrick, M., Paller, M., Rodriguez, E., Roth, L., Seal, D., Shaffer, S., Shimada, J., Umland, J., Werner, M., Oskin, M., Burbank, D., Alsdorf, D., 2007. The shuttle radar topography mission. Reviews of Geophysics, 45, RG2004.

Ferrer-Boix, C., Chartrand, S. M., Hassan, M. A., Martín-Vide, J. P., Parker, G., 2016. On how spatial variations of channel width influence river profile curvature. Geophysical Research Letters, 43, 6313–6323.

Ferrier, K. L., Huppert, K. L., Perron, J. T., 2013. Climatic control of bedrock river incision. Nature, 496, 206–209.

Flint, J. J., 1974. Stream gradient as a function of order, magnitude, and discharge. Water Resources Research, 10, 969–973.

Foley, J. A., DeFries, R., Asner, G. P., Barford, C., Bonan, G., Carpenter, S. R., Chapin, F. S., Coe, M. T., Daily, G. C., Gibbs, H. K., 2005. Global consequences of land use. Science, 309, 570–574.

Gabet, E. J., Burbank, D. W., Pratt-Sitaula, B., Putkonen, J., Bookhagen, B., 2008. Modern erosion rates in the High Himalayas of Nepal. Earth and Planetary Science Letters, 267, 482–494.

Gellis, A. C., Pavich, M. J., Bierman, P. R., Clapp, E. M., Ellevein, A., Aby, S., 2004. Modern sediment yield compared to geologic rates of sediment production in a semi-arid basin, New Mexico: assessing the human impact. Earth Surface Processes and Landforms, 29, 1359–1372.

Granger, D. E., Kirchner, J. W., Finkel, R., 1996. Spatially averaged long-term erosion rates measured from in situ-produced cosmogenic nuclides in alluvial sediment. The Journal of Geology, 104, 249–257.

Granger, D. E., Lifton, N. A., Willenbring, J. K., 2013. A cosmic trip: 25 years of cosmogenic nuclides in geology. GSA Bulletin, 125, 1379–1402.

Granger, D. E., Schaller, M., 2014. Cosmogenic nuclides and erosion at the watershed scale. Elements, 10, 369–373.

Grenfell, S. E., Grenfell, M. C., Rowntree, K. M., Ellery, W. N., 2014. Fluvial connectivity and climate: a comparison of channel pattern and process in two climatically contrasting fluvial sedimentary systems in South Africa. Geomorphology, 205, 142–154.

Grieve, S. W., Mudd, S. M., Milodowski, D. T., Clubb, F. J., Furbish, D. J., 2016. How does

grid-resolution modulate the topographic expression of geomorphic processes? Earth Surface Dynamics, 4, 627–653.

Grin, E., Schaller, M., Ehlers, T. A., 2018. Spatial distribution of cosmogenic ^{10}Be derived denudation rates between the Western Tian Shan and Northern Pamir, Tajikistan. Geomorphology, 321, 1–15.

Hack, J. T., 1957. Studies of Longitudinal Stream Profiles in Virginia and Maryland. Report 294B, US Government Printing Office.

Hammond, J. C., Zimmer, M., Shanafield, M., Kaiser, K., Godsey, S. E., Mims, M. C., Zipper, S. C., Burrows, R. M., Kampf, S. K., Dodds, W., Jones, C. N., Krabbenhoft, C. A., Boersma, K. S., Datry, T., Olden, J. D., Allen, G. H., Price, A. N., Costigan, K., Hale, R., Ward, A. S., Allen, D. C., 2020. Spatial patterns and drivers of non-perennial flow regimes in the contiguous U.S. Geophysical Research Letters, 48, e2020GL090794.

Han, J., Gasparini, N. M., Johnson, J. P., Murphy, B. P., 2014. Modeling the influence of rainfall gradients on discharge, bedrock erodibility, and river profile evolution, with application to the Big Island, Hawai'i. Journal of Geophysical Research: Earth Surface, 119, 1418–1440.

Han, Y., An, Z., Marlon, J. R., Bradley, R. S., Zhan, C., Arimoto, R., Sun, Y., Zhou, W., Wu, F., Wang, Q., Burr, G. S., Cao, J., 2020. Asian inland wildfires driven by glacial–interglacial climate change. Proceedings of the National Academy of Sciences, 117, 5184–5189.

Hanks, T. C., Webb, R. H., 2006. Effects of tributary debris on the longitudinal profile of the Colorado River in Grand Canyon. Journal of Geophysical Research: Earth Surface, 111, F02020.

Harel, M.-A., Mudd, S., Attal, M., 2016. Global analysis of the stream power law parameters based on worldwide ^{10}Be denudation rates. Geomorphology, 268, 184–196.

Hilley, G. E., Porder, S., Aron, F., Baden, C. W., Johnstone, S. A., Liu, F., Sare, R., Steelquist, A., Young, H. H., 2019. Earth's topographic relief potentially limited by an upper bound on channel steepness. Nature Geoscience, 12, 828–832.

Hooke, R. L., 2000. On the history of humans as geomorphic agents. Geology, 28, 843–846.

Horton, R. E., 1933. The role of infiltration in the hydrologic cycle. Eos, Transactions American Geophysical Union, 14, 446–460.

Howard, A. D., Dietrich, W. E., Seidl, M. A., 1994. Modeling fluvial erosion on regional to continental scales. Journal of Geophysical Research: Solid Earth, 99, 13971–13986.

Hughes, D. A., Sami, K., 1992. Transmission losses to alluvium and associated moisture

dynamics in a semiarid ephemeral channel system in Southern Africa. Hydrological Processes, 6, 45–53.

Hurst, M. D., Mudd, S. M., Yoo, K., Attal, M., Walcott, R., 2013. Influence of lithology on hillslope morphology and response to tectonic forcing in the northern Sierra Nevada of California. Journal of Geophysical Research: Earth Surface, 118, 832–851.

Ielpi, A., Lapôtre, M. G. A., Finotello, A., Ghinassi, M., D'Alpaos, A., 2020. Channel mobility drives a diverse stratigraphic architecture in the dryland Mojave River (California, USA). Earth Surface Processes and Landforms, 45, 1717–1731.

Jaeger, K. L., Sutfin, N. A., Tooth, S., Michaelides, K., Singer, M., 2017. Geomorphology and sediment regimes of intermittent rivers and ephemeral streams. In Intermittent Rivers and Ephemeral Streams, Elsevier, 21–49.

Jerolmack, D. J., Paola, C., 2010. Shredding of environmental signals by sediment transport. Geophysical Research Letters, 37, L19401.

Kemp, D. B., Sadler, P. M., Vanacker, V., 2020. The human impact on North American erosion, sediment transfer, and storage in a geologic context. Nature Communications, 11, 6012.

Keppel, R. V., Renard, K. G., 1962. Transmission losses in ephemeral stream beds. Journal of the Hydraulics Division, 88, 59–68.

Kirby, E., Whipple, K., 2001. Quantifying differential rock-uplift rates via stream profile analysis. Geology, 29, 415–418.

Kirby, E., Whipple, K. X., 2012. Expression of active tectonics in erosional landscapes. Journal of Structural Geology, 44, 54–75.

Kirchner, J. W., Finkel, R. C., Riebe, C. S., Granger, D. E., Clayton, J. L., King, J. G., Megahan, W. F., 2001. Mountain erosion over 10 yr, 10 k.y., and 10 m.y. time scales. Geology, 29, 591–594.

Knighton, A., Nanson, G., 1997. Distinctiveness, diversity and uniqueness in arid zone river systems. In Arid Zone Geomorphology: Process, Form and Change in Drylands, 2nd Edition, John Wiley & Sons, Chichester, 185–203.

Knighton, A. D., 1999. Downstream variation in stream power, Geomorphology, 29, 293–306.

Knighton, A. D., Nanson, G. C., 1994. Flow transmission along an arid zone anastomosing river, Cooper Creek, Australia. Hydrological Processes, 8, 137–154.

Knighton, D., 1998. Fluvial Forms and Processes: A New Perspective. Edward Arnold, London.

Knoben, W. J. M., Woods, R. A., Freer, J. E., 2018. A quantitative hydrological climate classification evaluated with independent streamflow data. Water Resources Research, 54, 5088–5109.

Lague, D., Hovius, N., Davy, P., 2005. Discharge, discharge variability, and the bedrock channel profile. Journal of Geophysical Research: Earth Surface, 110, F04006.

Lague, D., 2014. The stream power river incision model: evidence, theory and beyond. Earth Surface Processes and Landforms, 39, 38–61.

Langbein, W. B., Schumm, S. A., 1958. Yield of sediment in relation to mean annual precipitation. Eos, Transactions American Geophysical Union, 39, 1076–1084.

Lange, J., 2005. Dynamics of transmission losses in a large arid stream channel. Journal of Hydrology, 306, 112–126.

Larned, S. T., Schmidt, J., Datry, T., Konrad, C. P., Dumas, J. K., Diettrich, J. C., 2011. Longitudinal river ecohydrology: flow variation down the lengths of alluvial rivers. Ecohydrology, 4, 532–548.

Laronne, J. B., 1993. Very high rates of bedload sediment transport by ephemeral desert rivers. Nature, 366, 148–150.

Leopold, L. B., Maddock, T., 1953. The Hydraulic Geometry of Stream Channels and Some Physiographic Implications. Vol. 252, US Government Printing Office.

Leopold, L. B., Wolman, M. G., Miller, J. P., 1964. Fluvial Processes in Geomorphology. Freeman, San Francisco.

Li, Z., Fang, H., 2016. Impacts of climate change on water erosion: a review. Earth-Science Reviews, 163, 94–117.

Meyer, G. A., Pierce, J. L., Wood, S. H., Jull, A. J. T., 2001. Fire, storms, and erosional events in the Idaho batholith. Hydrological Processes, 15, 3025–3038.

Michaelides, K., Hollings, R., Singer, M. B., Nichols, M. H., Nearing, M. A., 2018. Spatial and temporal analysis of hillslope–channel coupling and implications for the longitudinal profile in a dryland basin. Earth Surface Processes and Landforms, 43, 1608–1621.

Milliman, J. D., Farnsworth, K. L., 2011. River Discharge to the Coastal Ocean: A Global Synthesis. Cambridge University Press, Cambridge.

Milliman, J. D., Meade, R. H., 1983. World-wide delivery of river sediment to the oceans. The Journal of Geology, 91, 1–21.

Milliman, J. D., Syvitski, J. P. M., 1992. Geomorphic/tectonic control of sediment discharge to the ocean: The importance of small mountainous rivers. The journal of Geology, 100, 525–544.

Mishra, A. K., Placzek, C., Jones, R., 2019. Coupled influence of precipitation and vegetation on millennial-scale erosion rates derived from ^{10}Be. PloS One, 14, e0211325.

Molnar, P., Anderson, R. S., Kier, G., Rose, J., 2006. Relationships among probability distributions of stream discharges in floods, climate, bed load transport, and river incision. Journal of Geophysical Research: Earth Surface, 111, F02001.

Montgomery, D. R., 2007. Soil erosion and agricultural sustainability. Proceedings of the National Academy of Sciences, 104, 13268–13272.

Mudd, S. M., Clubb, F. J., Gailleton, B., Hurst, M. D., 2018. How concave are river channels? Earth Surface Dynamics, 6, 505–523.

Mulligan, M., van Soesbergen, A., Sáenz, L., 2020. GOODD, a global dataset of more than 38,000 georeferenced dams. Scientific Data, 7, 31.

Murphy, B. P., Johnson, J. P. L., Gasparini, N. M., Sklar, L. S., 2016. Chemical weathering as a mechanism for the climatic control of bedrock river incision. Nature, 532, 223–227.

Natural Earth, Free vector and raster map data, https://www.naturalearthdata.com (last access: 11 March 2021)

Nicholson, S. E., 2011. Dryland Climatology. Cambridge University Press, Cambridge.

NOAA PSL, Boulder, Colorado, CPC US Unified Precipitation data, https://psl.noaa.gov (last access: 13 January 2020).

Olen, S. M., Bookhagen, B., Strecker, M. R., 2016. Role of climate and vegetation density in modulating denudation rates in the Himalaya. Earth and Planetary Science Letters, 445, 57–67.

Pan, B.-T., Geng, H.-P., Hu, X.-F., Sun, R.-H., Wang, C., 2010. The topographic controls on the decadal-scale erosion rates in Qilian Shan Mountains, N.W. China. Earth and Planetary Science Letters, 292, 148–157.

Pederson, J. L., Tressler, C., 2012. Colorado River long-profile metrics, knickzones and their meaning. Earth and Planetary Science Letters, 345–348, 171–179.

Peel, M. C., Finlayson, B. L., McMahon, T. A., 2007. Updated world map of the Köppen–Geiger climate classification. Hydrology and Earth System Sciences Discussions, 4, 439–473.

Perron, J. T., Royden, L., 2013. An integral approach to bedrock river profile analysis. Earth Surface Processes and Landforms, 38, 570–576.

Phillips, J. D., Lutz, J. D., 2008. Profile convexities in bedrock and alluvial streams. Geomorphology, 102, 554–566.

Pierce, J. L., Meyer, G. A., Jull, A. J. T., 2004. Fire-induced erosion and millennial-scale

climate change in northern ponderosa pine forests. Nature, 432, 87–90.

Portenga, E. W., Bierman, P. R., 2011. Understanding Earth's eroding surface with ^{10}Be. GSA today, 21, 4–10.

Powell, D. M., Laronne, J. B., Reid, I., Barzilai, R., 2012. The bed morphology of upland single-thread channels in semi-arid environments: evidence of repeating bedforms and their wider implications for gravel-bed rivers. Earth Surface Processes and Landforms, 37, 741–753.

Quichimbo, E. A., Singer, M. B., Cuthbert, M. O., 2020. Characterising groundwater–surface water interactions in idealised ephemeral stream systems. Hydrological Processes, 34, 3792–3806.

Ramankutty, N., Foley, J. A., 1999. Estimating historical changes in global land cover: croplands from 1700 to 1992. Global Biogeochemical Cycles, 13, 997–1027.

Ray, N., Adams, J., 2001. A GIS-based vegetation map of the world at the Last Glacial Maximum (25,000–15,000 BP). Internet Archaeology, 11, https://archive-ouverte.unige.ch/unige:17817.

Renard, K. G., 1970. The Hydrology of Semiarid Rangeland Watersheds. Agricultural Research Service, United States Department of Agriculture.

Reynolds, L. V., Shafroth, P. B., Poff, N. L., 2015. Modeled intermittency risk for small streams in the Upper Colorado River Basin under climate change. Journal of Hydrology, 523, 768–780.

Rinaldo, A., Dietrich, W. E., Rigon, R., Vogel, G. K., Rodrlguez-Lturbe, I., 1995. Geomorphological signatures of varying climate. Nature, 374, 632–635.

Roe, G. H., Montgomery, D. R., Hallet, B., 2002. Effects of orographic precipitation variations on the concavity of steady-state river profiles. Geology, 30, 143–146.

Royden, L. H., Clark, M. K., Whipple, K. X., 2000. Evolution of river elevation profiles by bedrock incision: analytical solutions for transient river profiles related to changing uplift and precipitation rates. Eos, Transactions American Geophysical Union, 81, Fall Meeting Supplement Abstract T62F-09.

Schaller, M., von Blanckenburg, F., Hovius, N., Kubik, P. W., 2001. Large-scale erosion rates from in situ-produced cosmogenic nuclides in European river sediments. Earth and Planetary Science Letters, 188, 441–458.

Schaller, M., von Blanckenburg, F., Veldkamp, A., Tebbens, L., Hovius, N., Kubik, P., 2002. A 30 000 yr record of erosion rates from cosmogenic ^{10}Be in Middle European river terraces. Earth and Planetary Science Letters, 204, 307–320.

Schmidt, A. H., Neilson, T. B., Bierman, P. R., Rood, D. H., Ouimet, W. B., Gonzalez, V. S., 2016. Influence of topography and human activity on apparent in situ ^{10}Be-derived erosion rates in Yunnan, SW China. Earth Surface Dynamics, 4, 819–830.

Schneider, A., Friedl, M. A., McIver, D. K., Woodcock, C. E., 2003. Mapping urban areas by fusing multiple sources of coarse resolution remotely sensed data. Photogrammetric Engineering & Remote Sensing, 69, 1377–1386.

Serreze, M. C., Walsh, J. E., Chapin III, F. S., Osterkamp, T., Dyurgerov, M., Romanovsky, V., Oechel, W. C., Morison, J., Zhang, T., Barry, R. G., 2000. Observational evidence of recent change in the northern high-latitude environment. Climatic Change, 46, 159–207.

Seybold, H., Rothman, D. H., Kirchner, J. W., 2017. Climate's watermark in the geometry of stream networks. Geophysical Research Letters, 44, 2272–2280.

Sharon, D., Margalit, A., Berkowicz, S. M., 2002. Locally modified surface winds on linear dunes as derived from directional raingauges. Earth Surface Processes and Landforms, 27, 867–889.

Singer, M. B., Aalto, R., 2009. Floodplain development in an engineered setting. Earth Surface Processes and Landforms, 34, 291–304.

Singer, M. B., Dunne, T., 2004. Modeling decadal bed material sediment flux based on stochastic hydrology. Water Resources Research, 40, W03302.

Singer, M. B., Dunne, T., 2006. Modeling the influence of river rehabilitation scenarios on bed material sediment flux in a large river over decadal timescales. Water Resources Research, 42, W12415.

Singer, M. B., Grieve, S. W. D., Chen, S.-A., Michaelides, K., 2018. Climatic signatures within the world's rivers. In AGU Fall Meeting Abstract EP52B-04, Washington, D.C.

Singer, M. B., Michaelides, K., 2014. How is topographic simplicity maintained in ephemeral dryland channels? Geology, 42, 1091–1094.

Singleton, A. A., Schmidt, A. H., Bierman, P. R., Rood, D. H., Neilson, T. B., Greene, E. S., Bower, J. A., Perdrial, N., 2017. Effects of grain size, mineralogy, and acid-extractable grain coatings on the distribution of the fallout radionuclides ^{7}Be, ^{10}Be, ^{137}Cs, and ^{210}Pb in river sediment. Geochimica et Cosmochimica Acta, 197, 71–86.

Sinha, S. K., Parker, G., 1996. Causes of concavity in longitudinal profiles of rivers. Water Resources Research, 32, 1417–1428.

Slater, L. J., Singer, M. B., 2013. Imprint of climate and climate change in alluvial riverbeds: continental United States, 1950–2011. Geology, 41, 595–598.

Slingerland, R., Harbaugh, J. W., Furlong, K., 1994. Building depositional systems. In

Simulation Clastic Sedimentary Basins: Physical Fundamentals and Computer Programs for Creating Dynamic Systems. Prentice Hall, 173–211.

Snelder, T. H., Datry, T., Lamouroux, N., Larned, S. T., Sauquet, E., Pella, H., Catalogne, C., 2013. Regionalization of patterns of flow intermittence from gauging station records. Hydrology and Earth System Sciences, 17, 2685–2699.

Snow, R. S., Slingerland, R. L., 1987. Mathematical modeling of graded river profiles. The Journal of Geology, 95, 15–33.

Sorensen, C. S., Yanites, B. J., 2019. Latitudinal trends in modern fluvial erosional efficiency along the Andes. Geomorphology, 329, 170–183.

Starke, J., Ehlers, T. A., Schaller, M., 2020. Latitudinal effect of vegetation on erosion rates identified along western South America. Science, 367, 1358–1361.

Stock, J., Dietrich, W. E., 2003. Valley incision by debris flows: evidence of a topographic signature. Water Resources Research, 39, 1089.

Stone, J. J., Nichols, M. H., Goodrich, D. C., Buono, J., 2008. Long-term runoff database, Walnut Gulch Experimental Watershed, Arizona, United States. Water Resources Research, 44, W05S05.

Struck, M., Jansen, J. D., Fujioka, T., Codilean, A. T., Fink, D., Fülöp, R.-H., Wilcken, K. M., Price, D. M., Kotevski, S., Fifield, L. K., 2018. Tracking the ^{10}Be–^{26}Al source-area signal in sediment-routing systems of arid central Australia. Earth Surface Dynamics, 6, 329–349.

Subramanya, K., 2013. Engineering Hydrology (4th Edition). McGraw Hill Education, New Delhi.

Summerfield, M. A., Hulton, N. J., 1994. Natural controls of fluvial denudation rates in major world drainage basins. Journal of Geophysical Research: Solid Earth, 99, 13871–13883.

Syvitski, J. P., Milliman, J. D., 2007. Geology, geography, and humans battle for dominance over the delivery of fluvial sediment to the coastal ocean. The Journal of Geology, 115, 1–19.

Syvitski, J. P., Vörösmarty, C. J., Kettner, A. J., Green, P., 2005. Impact of humans on the flux of terrestrial sediment to the global coastal ocean. Science, 308, 376–380.

Sólyom, P. B., Tucker, G. E., 2004. Effect of limited storm duration on landscape evolution, drainage basin geometry, and hydrograph shapes. Journal of Geophysical Research: Earth Surface, 109, F03012.

Tan, C., Feng, S., Zhao, X., Shan, X., Feng, S., 2021. Longitudinal variations in channel morphology of an ephemeral stream from upland to lowland, Daihai Lake basin, North

China. Geomorphology, 372,107450.

Thiede, R. C., Bookhagen, B., Arrowsmith, J. R., Sobel, E. R., Strecker, M. R., 2004. Climatic control on rapid exhumation along the Southern Himalayan Front. Earth and Planetary Science Letters, 222, 791–806.

Thornes, J. B., 2009. Catchment and channel hydrology. In Geomorphology of Desert Environments. Springer, Dordrecht, 303–332.

Tofelde, S., Duesing, W., Schildgen, T. F., Wickert, A. D., Wittmann, H., Alonso, R. N., Strecker, M., 2018. Effects of deep-seated versus shallow hillslope processes on cosmogenic ^{10}Be concentrations in fluvial sand and gravel. Earth Surface Processes and Landforms, 43, 3086–3098.

Tooth, S., 2000. Downstream changes in dryland river channels: the Northern Plains of arid central Australia. Geomorphology, 34, 33–54.

Trabucco, A., Zomer, R. J., 2009. Global Aridity and PET Database. CGIAR Consortium for Spatial Information, https://cgiarcsi.community/data/global-aridity-and-pet-database (last access: 11 May 2018).

Tucker, G. E., Slingerland, R., 1997. Drainage basin responses to climate change. Water Resources Research, 33, 2031–2047.

USDA–ARS, Southwest Watershed Research Center, https://www.tucson.ars.ag.gov/dap (last access: 5 June 2020).

U.S. Geological Survey, National Water Information System data available on the World Wide Web (USGS Water Data for the Nation), 2016, https://waterdata.usgs.gov/nwis (last access: 2 December 2020).

van Dongen, R., Scherler, D., Wittmann, H., von Blanckenburg, F., 2019. Cosmogenic ^{10}Be in river sediment: where grain size matters and why. Earth Surface Dynamics, 7, 393–410.

Vandenberghe, J., 2003. Climate forcing of fluvial system development: an evolution of ideas. Quaternary Science Reviews, 22, 2053–2060.

Vogel, J., 1989. Evidence of past climatic change in the Namib Desert. Palaeogeography, Palaeoclimatology, Palaeoecology, 70, 355–366.

von Blanckenburg, F., 2005. The control mechanisms of erosion and weathering at basin scale from cosmogenic nuclides in river sediment. Earth and Planetary Science Letters, 237, 462–479.

von Blanckenburg, F., Willenbring, J. K., 2014. Cosmogenic nuclides: dates and rates of Earth-surface change. Elements, 10, 341–346.

Wallace, D. E., Renard, K. G., 1967. Contribution to regional water table from transmission losses of ephemeral streambeds. Transaction of the American Society of Agricultural Engineers, 10, 786–789.

Walling, D., Fang, D., 2003. Recent trends in the suspended sediment loads of the world's rivers. Global and Planetary Change, 39, 111–126.

Walling, D., Webb, B., 1996. Erosion and sediment yield: a global overview. In Erosion and Sediment Yield: Global and Regional Perspectives, IAHS Publications, Wallingford, Oxfordshire, 236, 3–20.

Walling, D. E., Kleo, A. H. A., 1979. Sediment yields of rivers in areas of low precipitation: a global view. In The Hydrology of Areas of Low Precipitation. IAHS Publications, Wallingford, Oxfordshire, 128, 479–493.

Wang, Z., Wang, Z., de Vriend, H. J., 2008. Impact of water diversion on the morphological development of the Lower Yellow River. International Journal of Sediment Research, 23, 13–27.

Whipple, K. X., Kirby, E., Brocklehurst, S. H., 1999. Geomorphic limits to climate-induced increases in topographic relief. Nature, 401, 39–43.

Whipple, K. X., Tucker, G. E., 1999. Dynamics of the stream-power river incision model: implications for height limits of mountain ranges, landscape response timescales, and research needs. Journal of Geophysical Research: Solid Earth, 104, 17661–17674.

Wickert, A. D., 2018. How should we estimate river discharge from drainage area? In AGU Fall Meeting Abstract EP21D-2294, Washington, D.C.

Wilcox, B. P., Breshears, D. D., Allen, C. D., 2003. Ecohydrology of a resource-conserving semiarid woodland: Effects of scale and disturbance. Ecological Monographs, 73, 223–239.

Wilkinson, B. H., McElroy, B. J., 2007. The impact of humans on continental erosion and sedimentation. GSA Bulletin, 119, 140–156.

Willett, S. D., 1999. Orogeny and orography: the effects of erosion on the structure of mountain belts. Journal of Geophysical Research: Solid Earth, 104, 28957–28981.

Wittmann, H., von Blanckenburg, F., 2012. The geological significance of cosmogenic nuclides in sediment of large lowland basins, In EGU General Assembly Conference Abstracts, p. 12721, Vienna.

Wittmann, H., von Blanckenburg, F., Maurice, L., Guyot, J.-L., Filizola, N., Kubik, P. W., 2011. Sediment production and delivery in the Amazon River basin quantified by in situ-produced cosmogenic nuclides and recent river loads. Bulletin, 123, 934–950.

Wolman, M. G., Gerson, R., 1978. Relative scales of time and effectiveness of climate in watershed geomorphology. Earth Surface Processes, 3, 189–208.

Xue, L., Zhu, B., Yang, C., Wei, G., Meng, X., Long, A., Yang, G., 2017. Study on the characteristics of future precipitation in response to external changes over arid and humid basins. Scientific Reports, 7, 15148.

Yair, A., Sharon, D., Lavee, H., 1978. An instrumented watershed for the study of partial area contribution of runoff in the arid zone. Zeitschrift für Geomorphologie. Supplementband Stuttgart, 29, 71–82.

Yang, C. T., 1973. Incipient motion and sediment transport. Journal of the Hydraulics Division, 99, 1679–1704.

Yatsu, E., 1955. On the longitudinal profile of the graded river. Eos, Transactions American Geophysical Union, 36, 655–663.

Yizhou, W., Huiping, Z., Dewen, Z., Wenjun, Z., Zhuqi, Z., Weitao, W., Jingxing, Y., 2014. Controls on decadal erosion rates in Qilian Shan: re-evaluation and new insights into landscape evolution in north-east Tibet. Geomorphology, 223, 117–128.

Zaprowski, B. J., Pazzaglia, F. J., Evenson, E. B., 2005. Climatic influences on profile concavity and river incision. Journal of Geophysical Research: Earth Surface, 110, F03004.

Appendices

Appendix A. Information of gauging stations for hydrology analyses

K–G climate zone	AI category (AI value)	River name	State	Station ID	Drainage area (km^2)	River length (km)	Ephe. (%)
BWh	Arid (0.13)	Fortymile Wash	NV	10251250	667	48	99.8
				10251255	788	58	99.7
				10251258	818	75	99.8
BSk	Semi-Arid (0.22)	Walnut Gulch	AZ	FL009	24	16	98
				FL006	95	20	97
				FL002	114	24	90
				FL001	149	31	97
BSk	Semi-Arid (0.27)	Limpia Creek	TX	08431700	136	20	83
				08431800	588	52	23
BSk	Semi-Arid (0.38)	Dry Fork	UT	09268000	115	21	0
				09270000	252	34	77
				09270500	298	43	4
BSk	Arid (0.18)	Rio Puerco	NM	08334000	1088	113	47
				08352500	14141	289	45
				08353000	16110	369	72
BSh	Semi-Arid (0.33)	Sycamore Creek	AZ	09510070	12	7	30
				09510080	25	9	21
				09510150	135	21	1
				09510200	425	50	6
BSk	Semi-Arid (0.36)	Little Fountain Creek	CO	07105920	28	12	1
				07105928	31	12	16
				07105940	69	26	18
BWk	Semi-Arid (0.23)	Muddy Creek	WY	06257500	692	44	15
				06258000	860	76	6
Cf	Humid (0.85)	Little River	GA	02317797	334	40	15
				02318000	1494	80	0
				02318380	2010	111	0
Aw	Humid (1.86)	Waikolu Stream	HI	16405500	5	3	7
				16408000	10	6	0
Cf	Dry Sub-Humid (0.59)	Little Washita River	OK	07327442	34	7	2
				07327447	161	21	0.6
				07327550	601	56	0.3
Df	Humid (0.87)	Walnut Creek	IA	05487540	18	5	0.4
				05487550	53	15	0

K–G climate zone	AI category (AI value)	River name	State	Station ID	Drainage area (km^2)	River length (km)	Ephe. (%)
Af	Humid (1.02)	Waimea River	HI	16016000	53	6	0
				16031000	149	21	0
				16031001	217	23	0
Af	Humid (1.39)	Rio Tanama	PR	50028000	48	19	0
				50028400	58	40	0
Af	Humid (2.45)	Waikamoi Stream	HI	16554000	8	7	0
				16555000	10	11	0
Af	Humid (3.16)	Kapaula Gulch	HI	16511000	2	4	0
				16510000	4	5	0
Cs	Humid (1.69)	South Fork Coquille River	OR	14324600	81	17	0
				14324700	105	23	0
				14324900	241	37	0
				14325000	438	55	0
Cs	Humid (1.39)	Redwood Creek	CA	11481500	175	30	0
				11482200	479	73	0
				11482500	717	96	0
Ds	Humid (1.04)	East Fork Pine Creek	ID	12413360	9	3	0
				12413370	73	9	0
				12413445	190	14	0
Df	Humid (1.00)	Susitna River	AK	15291000	2375	70	0
				15292000	15877	301	0
				15294350	50142	463	0
Df	Dry Sub-Humid (0.51)	Middle Loup River	NE	06775500	205	165	0
				06779000	2124	292	0
				06785000	8107	365	0
Df	Humid (1.17)	White River	VT	01142000	624	50	0
				01144000	1787	82	0
Df	Semi-Arid (0.37)	Little Snake River	CO	09251500	311	28	0
				09257000	2559	85	0
Df	Humid (0.87)	Salt River	MO	05502300	945	80	0
				05503500	1621	135	0

Appendix B. Downstream distributions of discharge of selected rivers

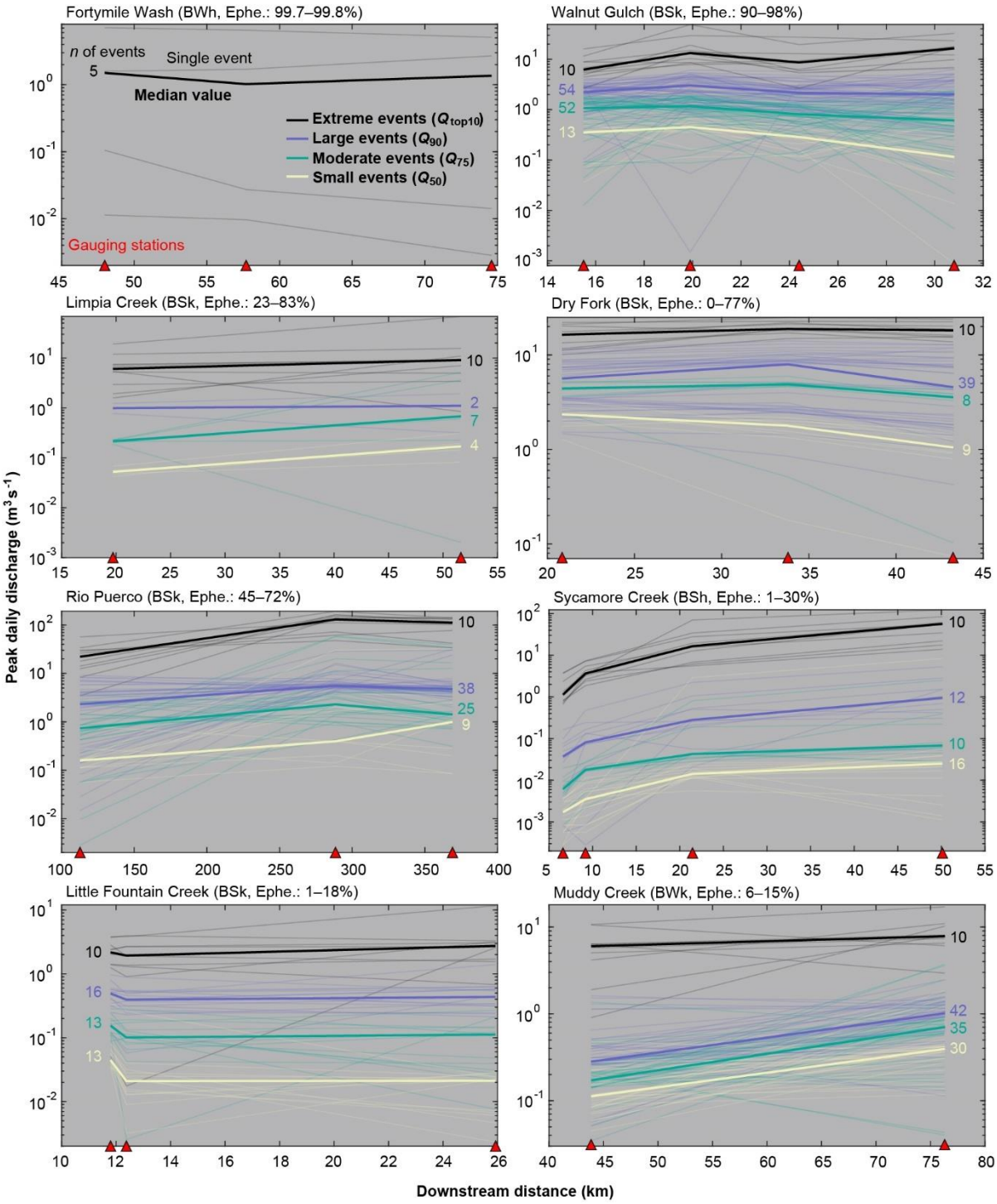

Downstream distributions of discharge of compiled flood events of selected rivers. The thin line represents single flood event, and thick line represents the median discharge of each flood category. The lines are colour coded by flood category. The number of compiled flood events of each flood category is listed in the plot. The red triangles on the x-axis represent the locations of gauging stations. Note that the y-axis is in log scale.

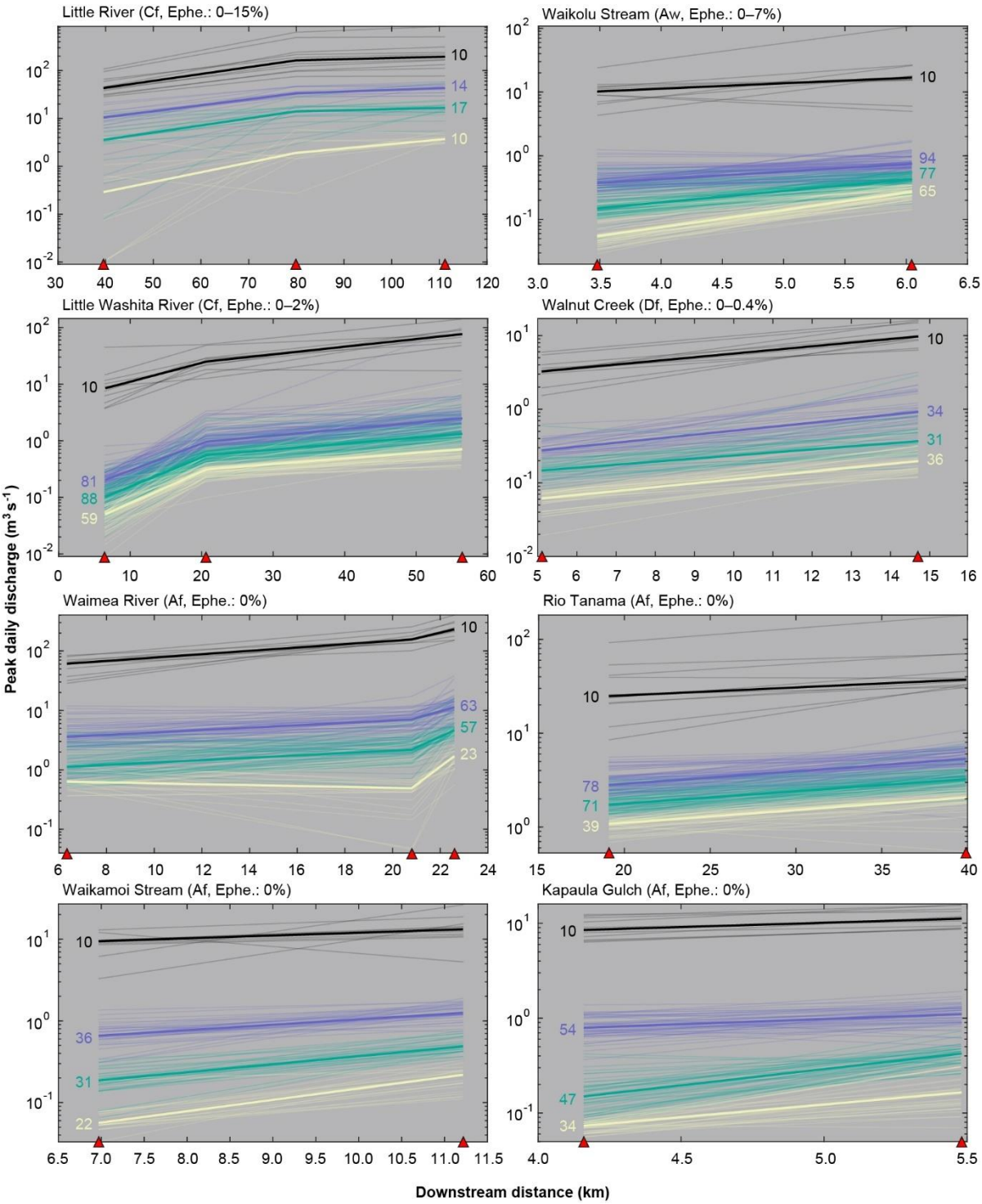
Little River (Cf, Ephe.: 0–15%)
10
14
17
10
Waikolu Stream (Aw, Ephe.: 0–7%)
10
94
77
65
Little Washita River (Cf, Ephe.: 0–2%)
10
81
88
59
Walnut Creek (Df, Ephe.: 0–0.4%)
10
34
31
36
Waimea River (Af, Ephe.: 0%)
10
63
57
23
Rio Tanama (Af, Ephe.: 0%)
10
78
71
39
Waikamoi Stream (Af, Ephe.: 0%)
10
36
31
22
Kapaula Gulch (Af, Ephe.: 0%)
10
54
47
34
Peak daily discharge (m3 s-1)
Downstream distance (km)

Continued.

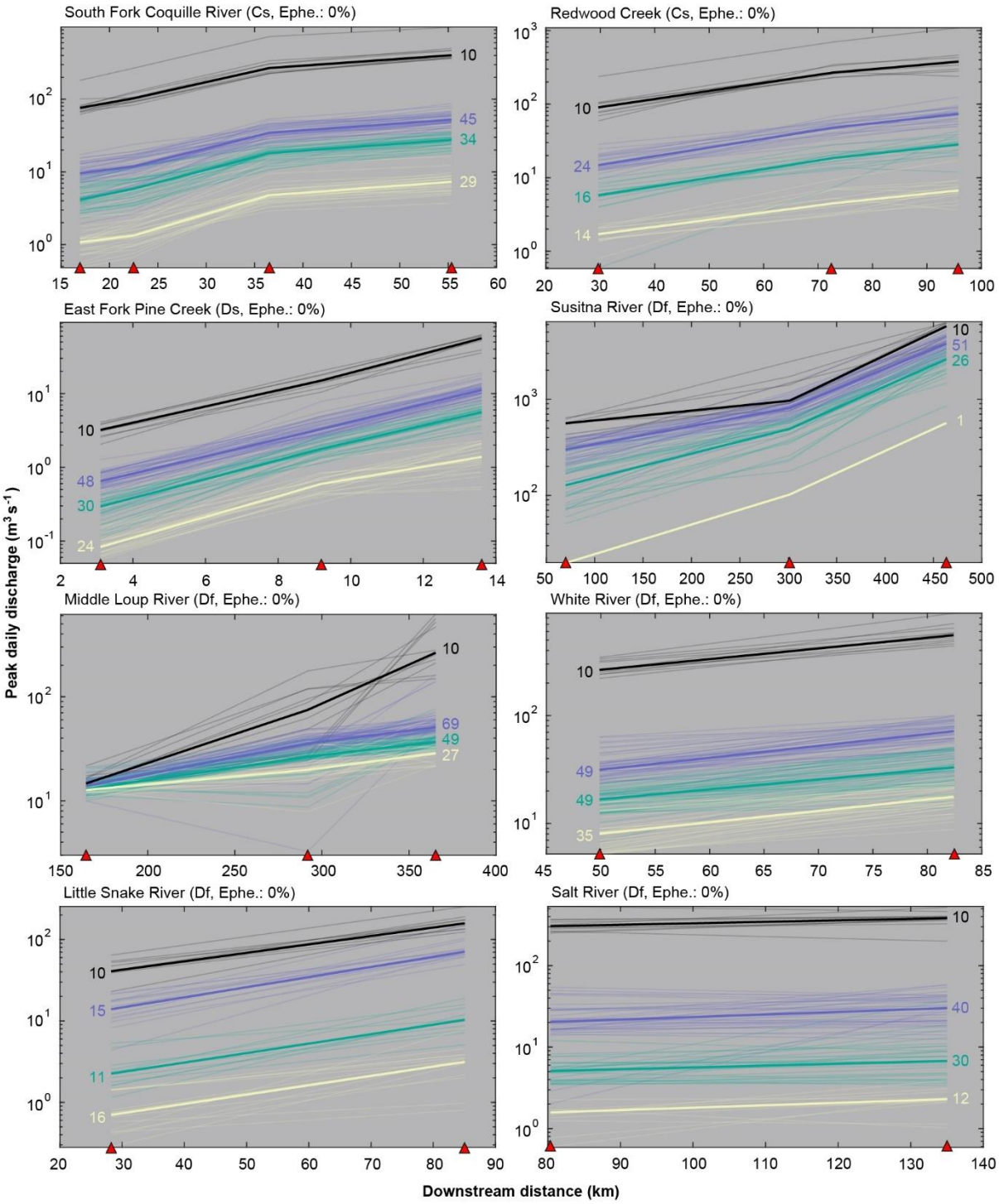
South Fork Coquille River (Cs, Ephe.: 0%)
Redwood Creek (Cs, Ephe.: 0%)
East Fork Pine Creek (Ds, Ephe.: 0%)
Susitna River (Df, Ephe.: 0%)
Middle Loup River (Df, Ephe.: 0%)
White River (Df, Ephe.: 0%)
Little Snake River (Df, Ephe.: 0%)
Salt River (Df, Ephe.: 0%)
Peak daily discharge (m3 s-1)
Downstream distance (km)

Continued.

Appendix C. Information of manually-extracted rivers for long profile analyses

K–G climate zone	Region/Country	River name	River length (km)	Interval of measurement (km)	NCI
Af	Puerto Rico	Rio Grande de Manatí	74.1	0.5	-0.33
	Colombia	Rio Andagueda	124.7	0.5	-0.42
	Dem. Rep. Congo	Tshuapa River	971.0	5.0	-0.14
	Malaysia	Pahang River	476.0	2.0	-0.42
		Sungai Ketial	16.2	0.2	-0.28
	Indonesia	Unknown (Tributary of Sungai Tariku)	28.4	0.2	-0.25
		Sungai Mamberamo	726.0	2.0	-0.47
Am	Honduras	Rio Sico	172.1	1.0	-0.42
	Nicaragua	Rio Ulang	133.4	0.5	-0.26
	Brazil	Abacaxis River	655.9	5.0	-0.26
	Nigeria	Cross River	567.3	2.0	-0.46
	Madagascar	Androranga	169.4	1.0	-0.24
		Unknown (Tributary of Androranga)	20.7	0.2	-0.21
	Myanmar	Unknown (Tributary of Dalet River)	72.2	0.5	-0.42
Aw	Brazil	Rio Mearim	1068.6	5.0	-0.32
	Cuba	Agabama River	114.3	0.5	-0.29
	Mexico	Rio Ometepec	137.8	0.5	-0.38
	Venezuela	Rio Zuata	181.0	1.0	-0.15
	Benin	Oueme River	595.5	2.0	-0.13
	Gabon	Ogooue River	1060.4	5.0	-0.15
		Ngounie River	450.0	2.0	-0.13
	Central African Republic	Mbari River	403.3	2.0	-0.28
	Thailand	Hanuman River	106.4	0.5	-0.13
	Vietnam	Unknown (Binh Thuan Province)	30.4	0.2	-0.39
	Timor-Leste	Rib Carablum	66.9	0.5	-0.20
		Unknown (in Loidahar)	9.1	0.1	-0.16
	Northern Territory, Australia	Roper River	528.9	2.0	-0.31
BWh	California, US	Unknown (Fort Sage Mountains)	5.9	0.1	0.00
	Mexico	Rio Sonoyta	313.4	1.0	-0.01
	Peru	Unknown (near Quilca Sumbilca)	14.35	0.1	-0.23
	Israel	Nahal Yael	1.7	0.1	0.07
		Nahal Netafim	10.6	0.2	-0.07
	Saudi Arabia	Unknown (near Riyadh)	33.2	0.5	-0.11
	Yemen	Wadi Amaqin	151.5	0.5	-0.10
	Pakistan	Winder River	114.1	0.5	-0.17

K–G climate zone	Region/Country	River name	River length (km)	Interval of measurement (km)	NCI
	Algeria	Unknown (in Bechar Province)	176.4	1.0	-0.25
	Somalia	Undaima River	430.5	2.0	-0.19
	Namibia	Gaub River	148.5	0.5	-0.08
		Kuiseb River	486.0	2.0	-0.08
	Northern Territory, Australia	Finke River	589.0	2.0	-0.11
	South Australia	Alberga River	660.7	5.0	-0.17
		Margare Creek	210.5	1.0	-0.20
	Western Australia	Unknown (Tributary of De Grey River)	58.7	0.5	-0.12
BWk	Nevada, US	Unknown (near Muller Mountain)	4.4	0.1	-0.18
	Chile	Rio Salado	197.2	1.0	-0.04
	Argentina	Arroyo Salado	239.7	1.0	-0.18
	South Africa	Renosterrivier	175.7	1.0	-0.26
		Unknown (Tributary of Renosterrivier)	36.3	0.5	-0.26
	Xinjiang, China	49 Hotien River	864.1	5.0	-0.24
	Qilian Shan, China	Danghe River	369.0	1.0	-0.01
BSh	Mexico	Unknown (Tributary of Rio Grande)	153.0	1.0	-0.33
	Brazil	Riacho da Vargem	156.0	1.0	-0.17
	Ethiopia	Gobele River	279.8	1.0	-0.28
	Botswana	Mosetse River	142.6	1.0	-0.12
	India	Shingoda	24.7	0.5	-0.13
	Western Australia	Fitzroy River	625.2	5.0	-0.28
	Queensland, Australia	Nicholson River	395.3	2.0	-0.10
BSk	Utah, US	Fisher Creek	22.8	0.2	-0.03
	Arizona, US	Walnut Gulch	35.1	0.2	-0.04
	Argentina	Unknown (near San Rafael)	108.9	0.5	-0.09
	Spain	Rambla de Nogalte	32.8	0.2	-0.03
	South Africa	Vetrivier River	273.6	2.0	-0.30
	Iran	Unknown (near Ghasem Abad)	171.8	1.0	-0.20
	Mongolia	Unknown (tributary of Ayrag Lake)	205.2	1.0	-0.04
	Western Australia	Hamersley River	80.6	0.5	-0.09
Cs	Oregon, US	Siuslaw River	175.1	1.0	-0.18
	California, US	Mill Creek	28.2	0.2	-0.14
	Chile	Rio Italta	244.8	1.0	-0.37
	Morocco	Oued Ghis	73.8	0.5	-0.16
	Albania	Viosa	224.9	1.0	-0.42
	Turkey	Boga Cayi	50.7	0.5	-0.30
	Iran	Cheshmeh Kileh	68.4	0.5	-0.25
Cw	Mexico	Unknown (tributary of Grande de Santiago River)	82.9	0.5	0.00
	Peru	Unknown (tributary of Rio Madre De Dios)	212.0	1.0	-0.37

K–G climate zone	Region/Country	River name	River length (km)	Interval of measurement (km)	NCI
	Angola	Longa River	533.7	2.0	-0.08
	Zambia	Unknown (tributary of Lunsemfwa River)	74.9	0.5	-0.15
	Nepal	Badhighat River	98.8	0.5	-0.31
	India	Siyom River	184.1	1.0	-0.37
	Vietnam	Sg. Bac Giang	137.1	0.5	-0.35
Cf	Florida, US	Suwannee River	385.7	2.0	-0.20
	Uruguay	Rio Arapey Grande	219.8	1.0	-0.27
	UK	River Tyne	121.6	0.5	-0.36
	France	Maine River	312.6	2.0	-0.18
	Jiangxi, China	Chenshan River	103.7	1.0	-0.39
	Taiwan	Lanyang River	73.3	0.5	-0.33
	Victoria, Australia	Delegate River	138.4	1.0	-0.08
	New Zealand	Karangarua River	41.9	0.5	-0.42
Ds	British Columbia, Canada	Unknown (tributary of Stikine River)	146.4	1.0	-0.31
	Idaho, US	Sheep Creek	12.6	0.1	-0.02
	Iceland	Unknown (near Dalvik)	38.7	0.2	-0.40
	Turkey	Koy Deresi	18.7	0.2	-0.17
		Bayram Cayi	120.5	1.0	-0.19
	Tajikistan	Obikhingou River	236	1.0	-0.35
	Kyrgyzstan	Unknown (tributary of Naryn River)	66.6	0.5	-0.24
Dw	Alaska, US	Robertson River	71.1	0.5	-0.36
	Tibet, China	Unknown (tributary of Cam Co)	92.1	0.5	-0.30
	Gansu, China	Unknown (in Gannan Autonomous Prefecture)	98.8	0.5	-0.22
	Inner Mongolia, China	Nuomin River	456.6	2.0	-0.29
	North Korea	Unknown (in North Hamgyong)	9.0	0.1	-0.21
	Amur, Russia	Selemdzha River	648.8	5.0	-0.32
	Sakha Republic, Russia	River Tyry	335.5	2.0	-0.28
Df	New Mexico, US	Rio Puerco	145.6	0.5	-0.10
	Idaho, US	Horse Creek	41.6	0.2	-0.05
	Nebraska, US	Dismal River	179.0	1.0	-0.06
	Alaska, US	Kuskokwim River	1285.0	5.0	-0.45
		Susitna River	267.6	1.0	-0.40
	Yukon, Canada	Peel River	715.4	5.0	-0.35
		Wind River	235.6	1.0	-0.19
	British Columbia, Canada	Prophet River	289.5	1.0	-0.29
	Alberta, Canada	Yates River	320.5	1.0	-0.16
	Ontario, Canada	Severn River	983.7	5.0	0.12
		Albany River	903.0	5.0	0.00

K–G climate zone	Region/Country	River name	River length (km)	Interval of measurement (km)	NCI
	Iceland	Unknown (near Eyja-og Miklaholtshreppur)	9.47	0.1	-0.22
	Norway	Malselva River	118.1	0.5	-0.37
	Sweden / Finland	Konkamaalven River	560.6	2.0	-0.22
	Hungary	Sajo River	213.9	1.0	-0.42
	Poland	Parseta River	151.3	1.0	-0.24
	Lithuania	Minija River	225.3	1.0	-0.22
	Ukraine	Cheremosh River	176.4	1.0	-0.24
	Northwestern, Russia	Vychegda River	1038.8	5.0	-0.18
	Urals, Russia	Taz River	1420.5	5.0	-0.33
	Far Eastern, Russia	Makhra River	1190.1	5.0	-0.38
		Kamchatka River	758.8	5.0	-0.40
	Japan	Unknown (near Horinai)	48.1	0.2	-0.23

Appendix D. Long profiles of manually-extracted rivers

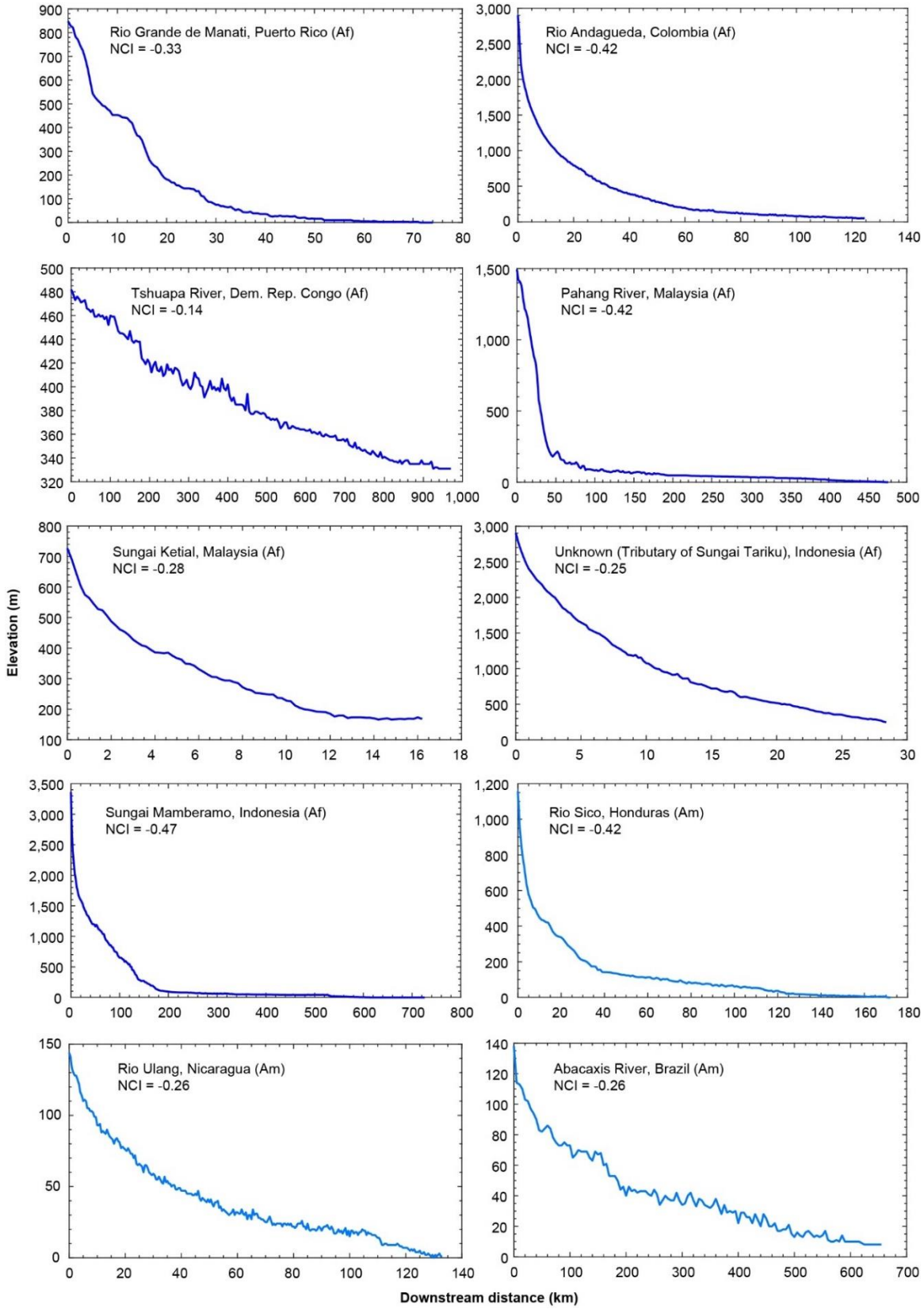

Long profiles of manually-extracted rivers. River name, country, K–G climate zone, and NCI value are shown in each plot. Profiles are colour coded by K–G climate zone.

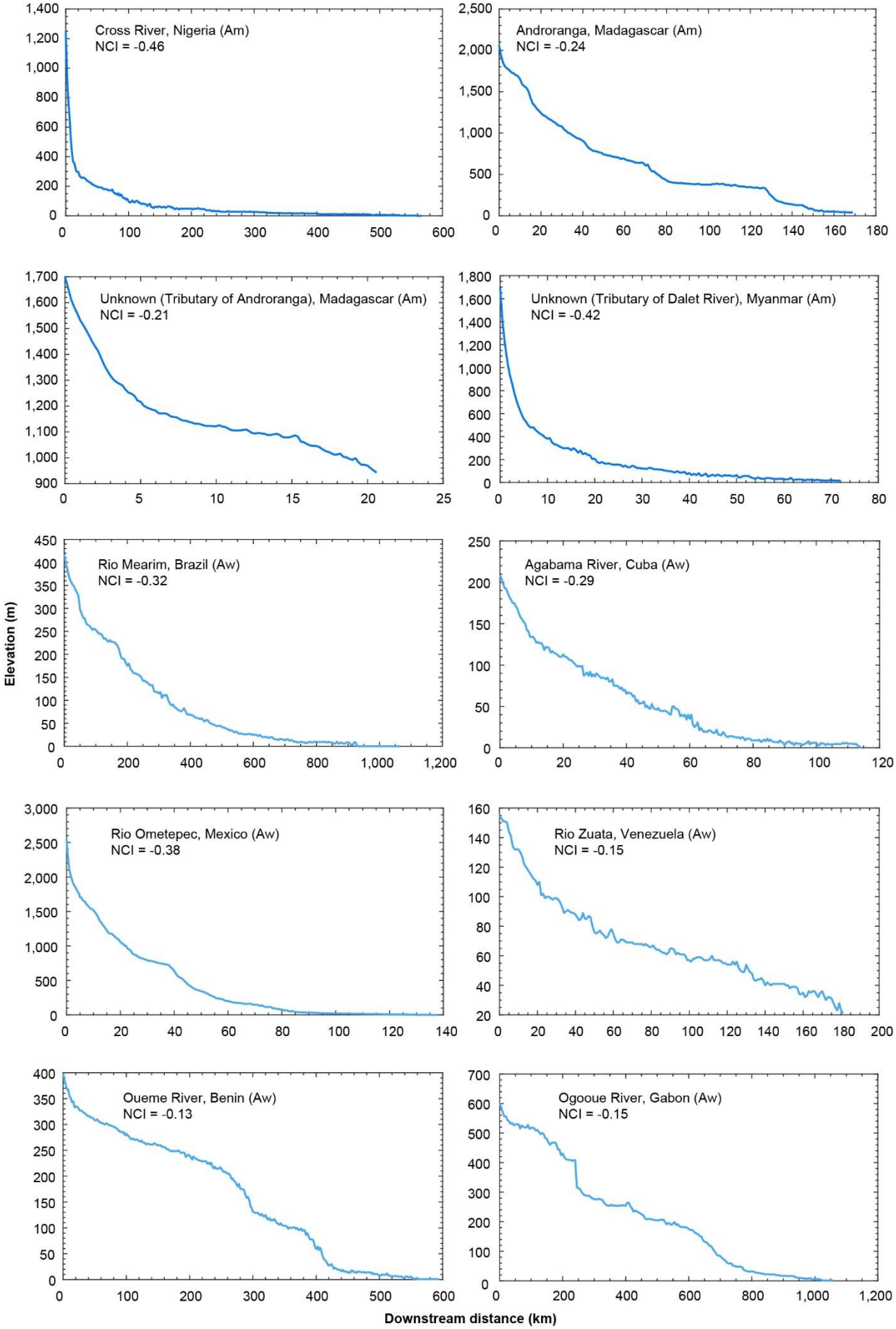
Cross River, Nigeria (Am)
NCI = -0.46
Androranga, Madagascar (Am)
NCI = -0.24
Unknown (Tributary of Androranga), Madagascar (Am)
NCI = -0.21
Unknown (Tributary of Dalet River), Myanmar (Am)
NCI = -0.42
Rio Mearim, Brazil (Aw)
NCI = -0.32
Agabama River, Cuba (Aw)
NCI = -0.29
Rio Ometepec, Mexico (Aw)
NCI = -0.38
Rio Zuata, Venezuela (Aw)
NCI = -0.15
Oueme River, Benin (Aw)
NCI = -0.13
Ogooue River, Gabon (Aw)
NCI = -0.15
Elevation (m)
Downstream distance (km)

Continued.

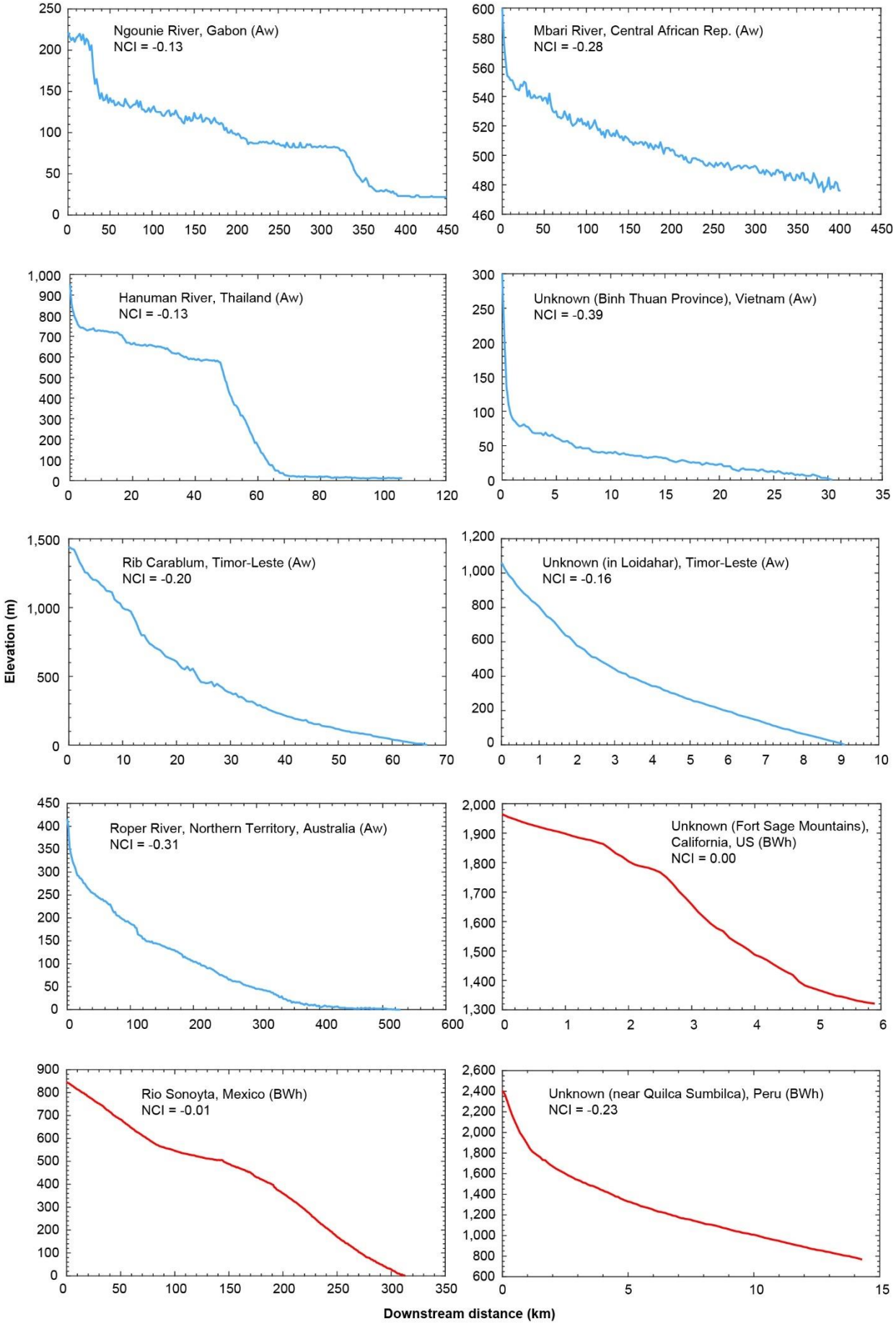
Ngounie River, Gabon (Aw)
NCI = -0.13
Mbari River, Central African Rep. (Aw)
NCI = -0.28
Hanuman River, Thailand (Aw)
NCI = -0.13
Unknown (Binh Thuan Province), Vietnam (Aw)
NCI = -0.39
Rib Carablum, Timor-Leste (Aw)
NCI = -0.20
Unknown (in Loidahar), Timor-Leste (Aw)
NCI = -0.16
Roper River, Northern Territory, Australia (Aw)
NCI = -0.31
Unknown (Fort Sage Mountains), California, US (BWh)
NCI = 0.00
Rio Sonoyta, Mexico (BWh)
NCI = -0.01
Unknown (near Quilca Sumbilca), Peru (BWh)
NCI = -0.23
Elevation (m)
Downstream distance (km)

Continued.

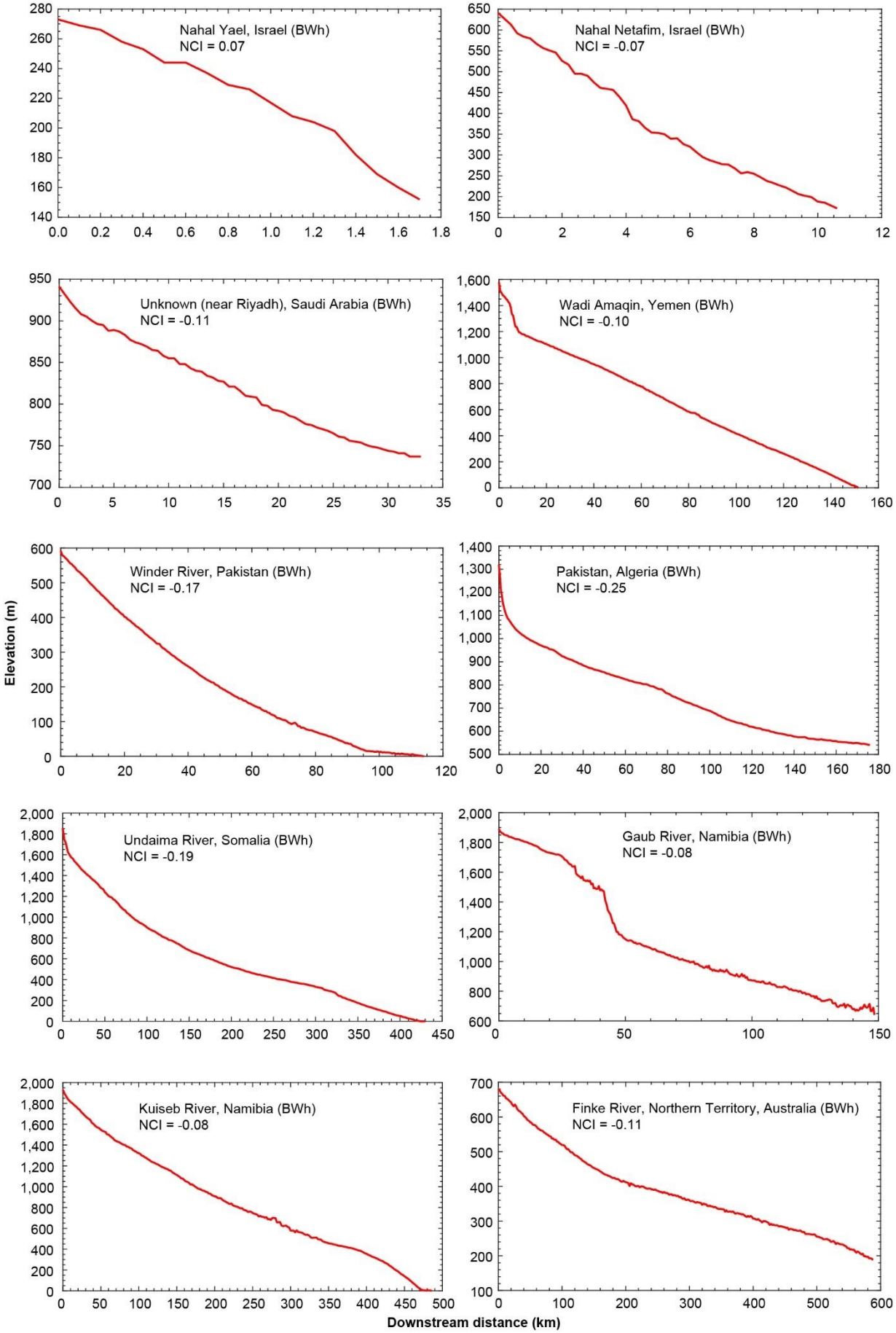
Nahal Yael, Israel (BWh)
NCI = 0.07
Nahal Netafim, Israel (BWh)
NCI = -0.07
Unknown (near Riyadh), Saudi Arabia (BWh)
NCI = -0.11
Wadi Amaqin, Yemen (BWh)
NCI = -0.10
Winder River, Pakistan (BWh)
NCI = -0.17
Pakistan, Algeria (BWh)
NCI = -0.25
Undaima River, Somalia (BWh)
NCI = -0.19
Gaub River, Namibia (BWh)
NCI = -0.08
Kuiseb River, Namibia (BWh)
NCI = -0.08
Finke River, Northern Territory, Australia (BWh)
NCI = -0.11
Elevation (m)
Downstream distance (km)

Continued.

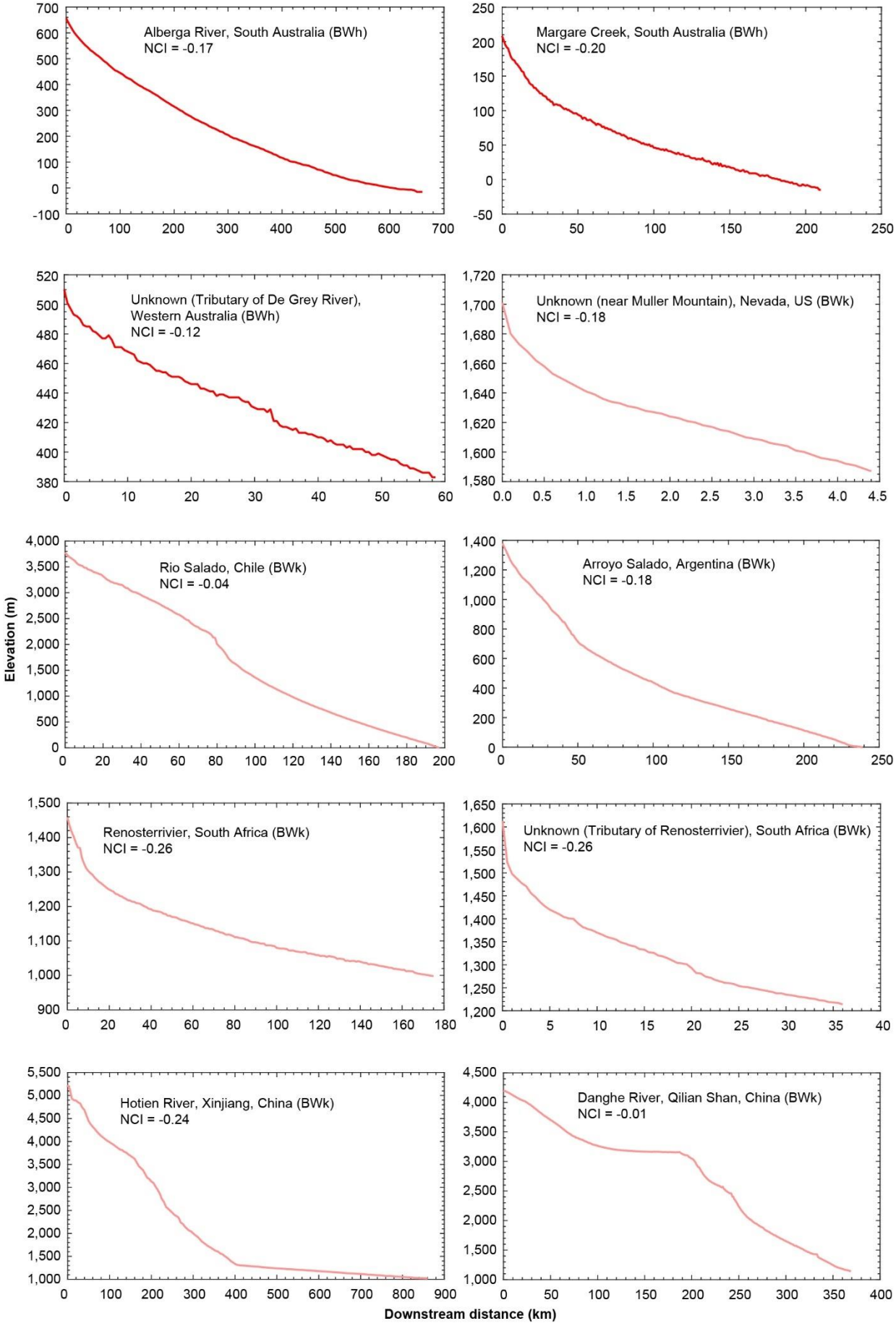
Alberga River, South Australia (BWh)
NCI = -0.17
Margare Creek, South Australia (BWh)
NCI = -0.20
Unknown (Tributary of De Grey River), Western Australia (BWh)
NCI = -0.12
Unknown (near Muller Mountain), Nevada, US (BWk)
NCI = -0.18
Rio Salado, Chile (BWk)
NCI = -0.04
Arroyo Salado, Argentina (BWk)
NCI = -0.18
Renosterrivier, South Africa (BWk)
NCI = -0.26
Unknown (Tributary of Renosterrivier), South Africa (BWk)
NCI = -0.26
Hotien River, Xinjiang, China (BWk)
NCI = -0.24
Danghe River, Qilian Shan, China (BWk)
NCI = -0.01
Elevation (m)
Downstream distance (km)

Continued.

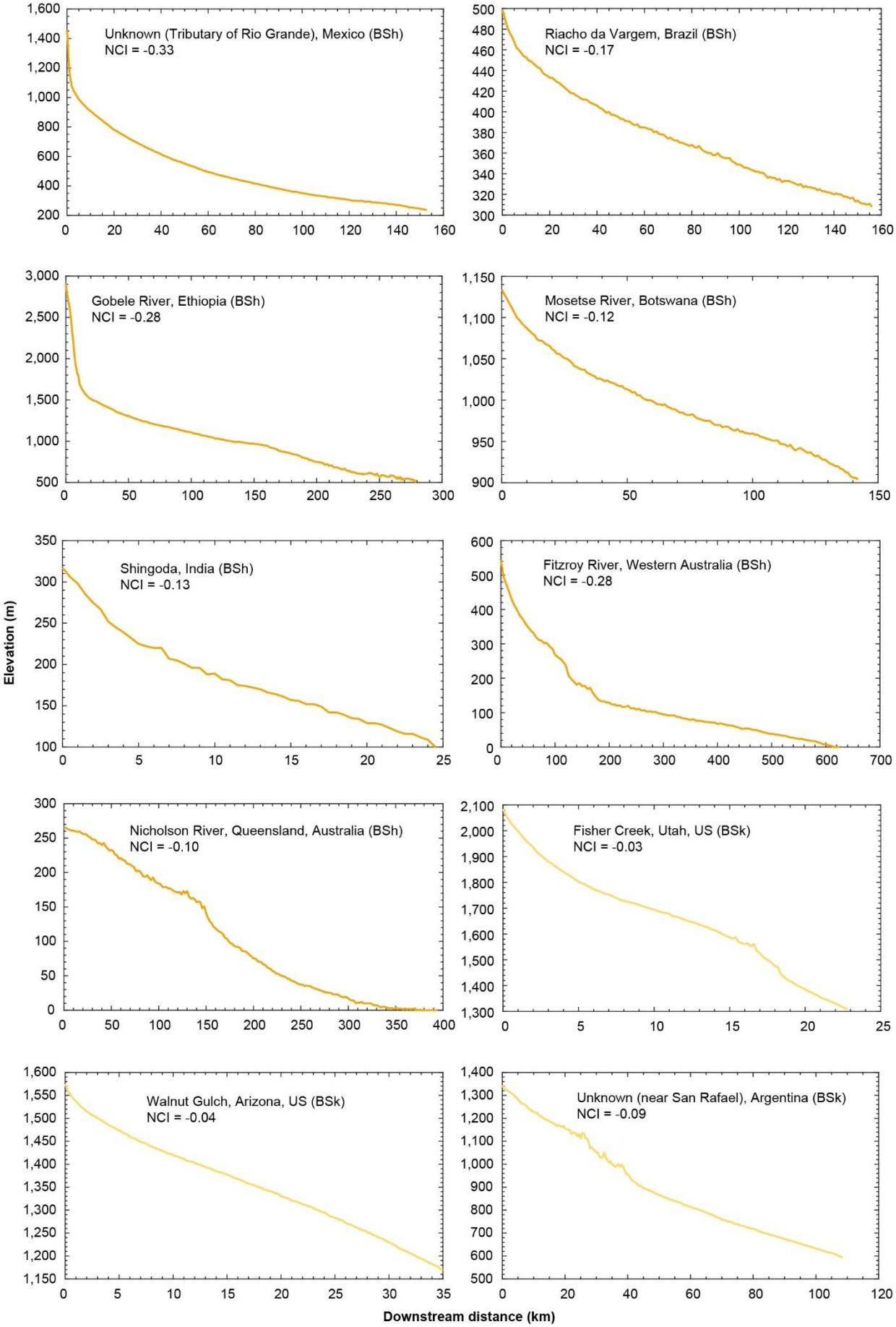
Unknown (Tributary of Rio Grande), Mexico (BSh)
NCI = -0.33
Riacho da Vargem, Brazil (BSh)
NCI = -0.17
Gobele River, Ethiopia (BSh)
NCI = -0.28
Mosetse River, Botswana (BSh)
NCI = -0.12
Shingoda, India (BSh)
NCI = -0.13
Fitzroy River, Western Australia (BSh)
NCI = -0.28
Nicholson River, Queensland, Australia (BSh)
NCI = -0.10
Fisher Creek, Utah, US (BSk)
NCI = -0.03
Walnut Gulch, Arizona, US (BSk)
NCI = -0.04
Unknown (near San Rafael), Argentina (BSk)
NCI = -0.09
Elevation (m)
Downstream distance (km)

Continued.

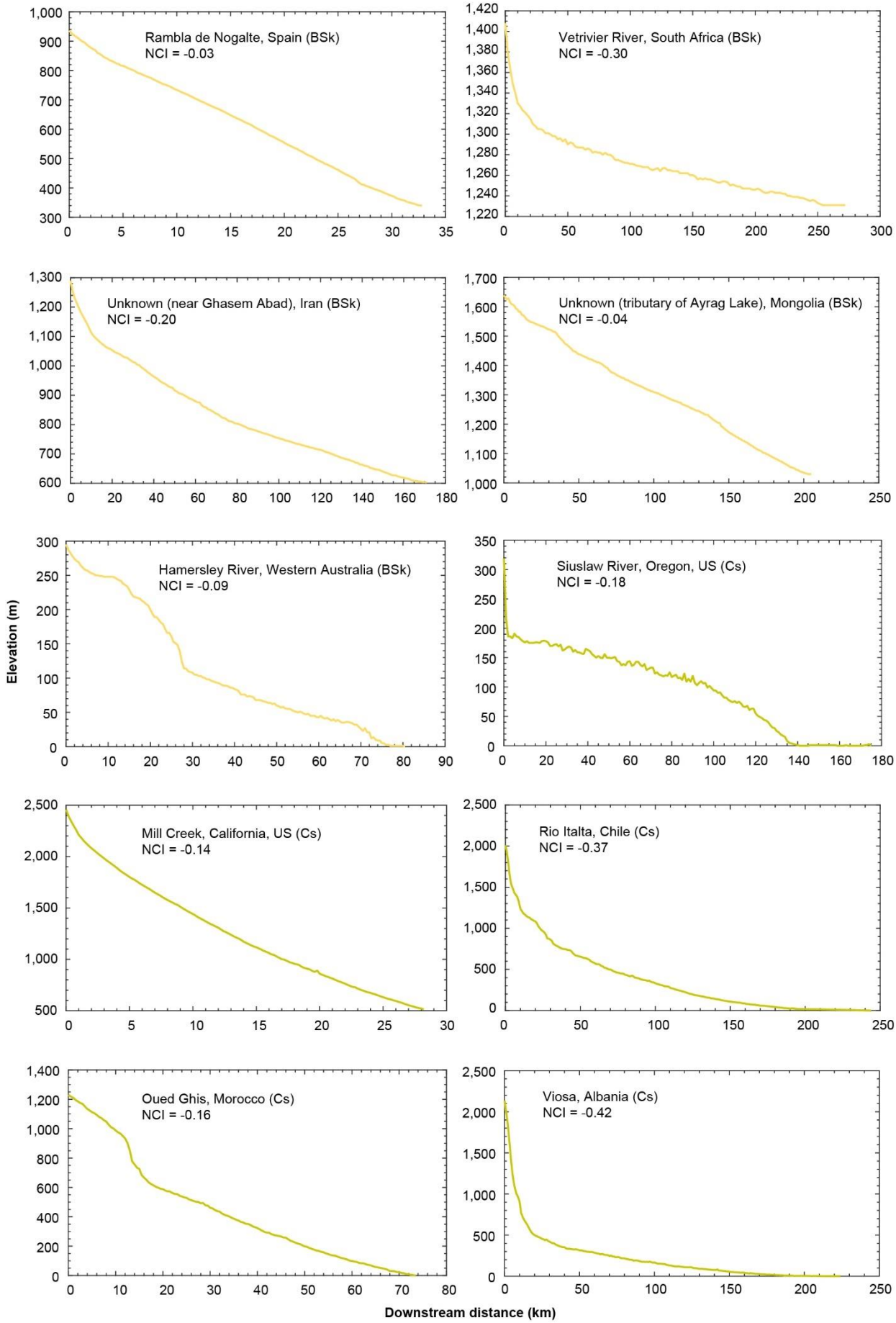
Rambla de Nogalte, Spain (BSk)
NCI = -0.03
Vetrivier River, South Africa (BSk)
NCI = -0.30
Unknown (near Ghasem Abad), Iran (BSk)
NCI = -0.20
Unknown (tributary of Ayrag Lake), Mongolia (BSk)
NCI = -0.04
Hamersley River, Western Australia (BSk)
NCI = -0.09
Siuslaw River, Oregon, US (Cs)
NCI = -0.18
Mill Creek, California, US (Cs)
NCI = -0.14
Rio Italta, Chile (Cs)
NCI = -0.37
Oued Ghis, Morocco (Cs)
NCI = -0.16
Viosa, Albania (Cs)
NCI = -0.42
Elevation (m)
Downstream distance (km)

Continued.

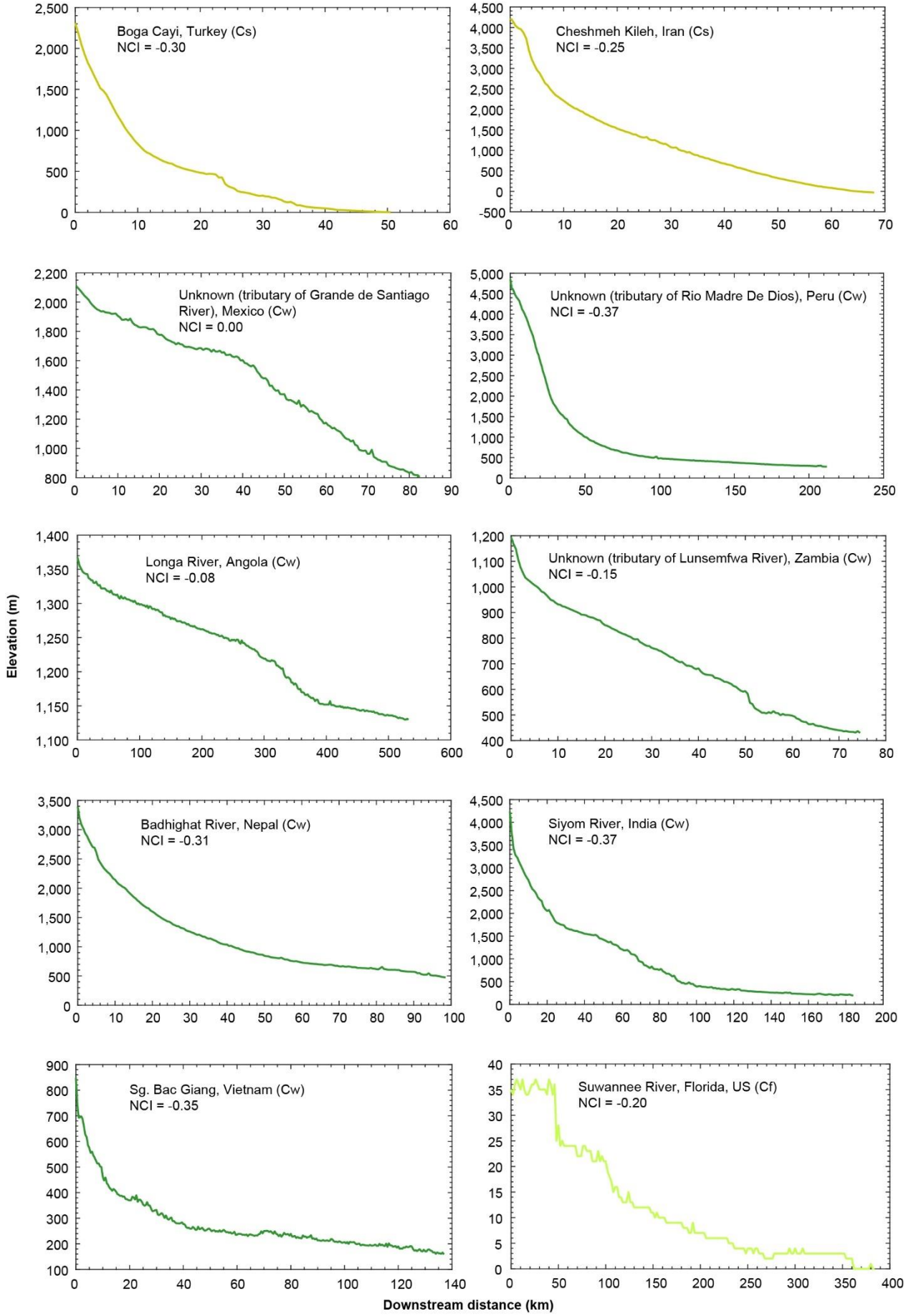
Boga Cayi, Turkey (Cs)
NCI = -0.30
Cheshmeh Kileh, Iran (Cs)
NCI = -0.25
Unknown (tributary of Grande de Santiago River), Mexico (Cw)
NCI = 0.00
Unknown (tributary of Rio Madre De Dios), Peru (Cw)
NCI = -0.37
Longa River, Angola (Cw)
NCI = -0.08
Unknown (tributary of Lunsemfwa River), Zambia (Cw)
NCI = -0.15
Badhighat River, Nepal (Cw)
NCI = -0.31
Siyom River, India (Cw)
NCI = -0.37
Sg. Bac Giang, Vietnam (Cw)
NCI = -0.35
Suwannee River, Florida, US (Cf)
NCI = -0.20
Elevation (m)
Downstream distance (km)

Continued.

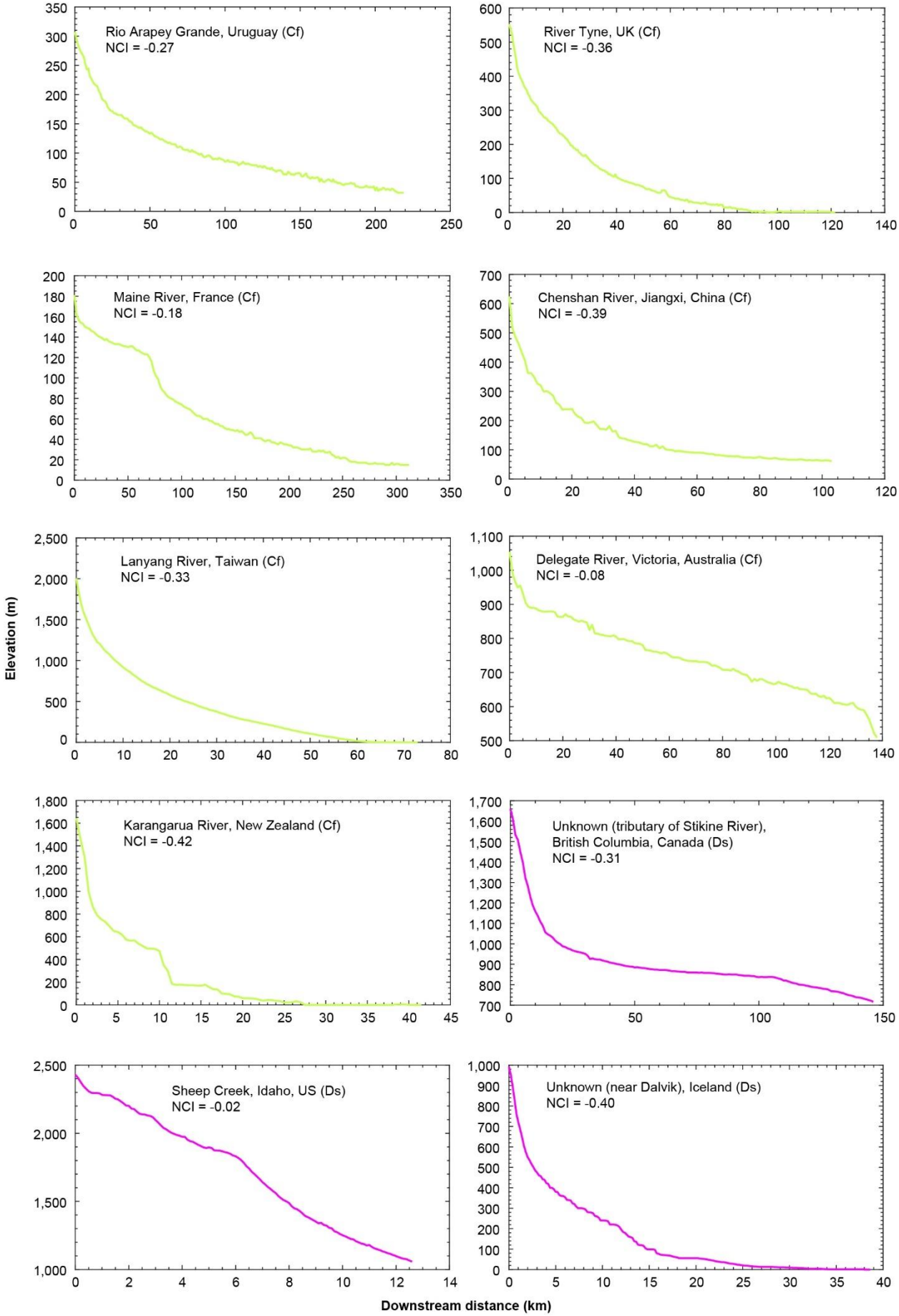
Rio Arapey Grande, Uruguay (Cf)
NCI = -0.27
River Tyne, UK (Cf)
NCI = -0.36
Maine River, France (Cf)
NCI = -0.18
Chenshan River, Jiangxi, China (Cf)
NCI = -0.39
Lanyang River, Taiwan (Cf)
NCI = -0.33
Delegate River, Victoria, Australia (Cf)
NCI = -0.08
Karangarua River, New Zealand (Cf)
NCI = -0.42
Unknown (tributary of Stikine River),
British Columbia, Canada (Ds)
NCI = -0.31
Sheep Creek, Idaho, US (Ds)
NCI = -0.02
Unknown (near Dalvik), Iceland (Ds)
NCI = -0.40
Elevation (m)
Downstream distance (km)

Continued.

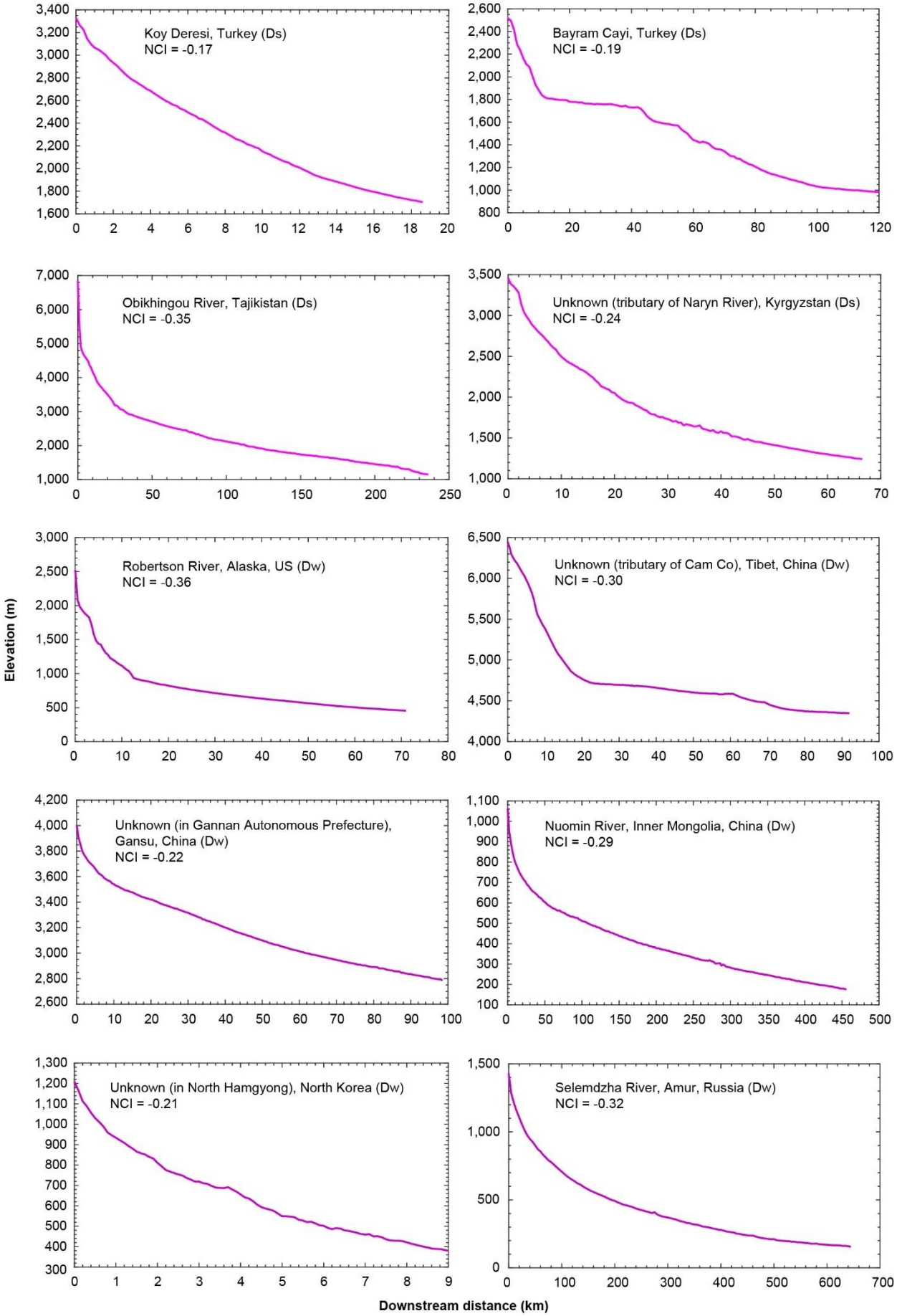
Koy Deresi, Turkey (Ds)
NCI = -0.17
Bayram Cayi, Turkey (Ds)
NCI = -0.19
Obikhingou River, Tajikistan (Ds)
NCI = -0.35
Unknown (tributary of Naryn River), Kyrgyzstan (Ds)
NCI = -0.24
Robertson River, Alaska, US (Dw)
NCI = -0.36
Unknown (tributary of Cam Co), Tibet, China (Dw)
NCI = -0.30
Unknown (in Gannan Autonomous Prefecture), Gansu, China (Dw)
NCI = -0.22
Nuomin River, Inner Mongolia, China (Dw)
NCI = -0.29
Unknown (in North Hamgyong), North Korea (Dw)
NCI = -0.21
Selemdzha River, Amur, Russia (Dw)
NCI = -0.32
Elevation (m)
Downstream distance (km)

Continued.

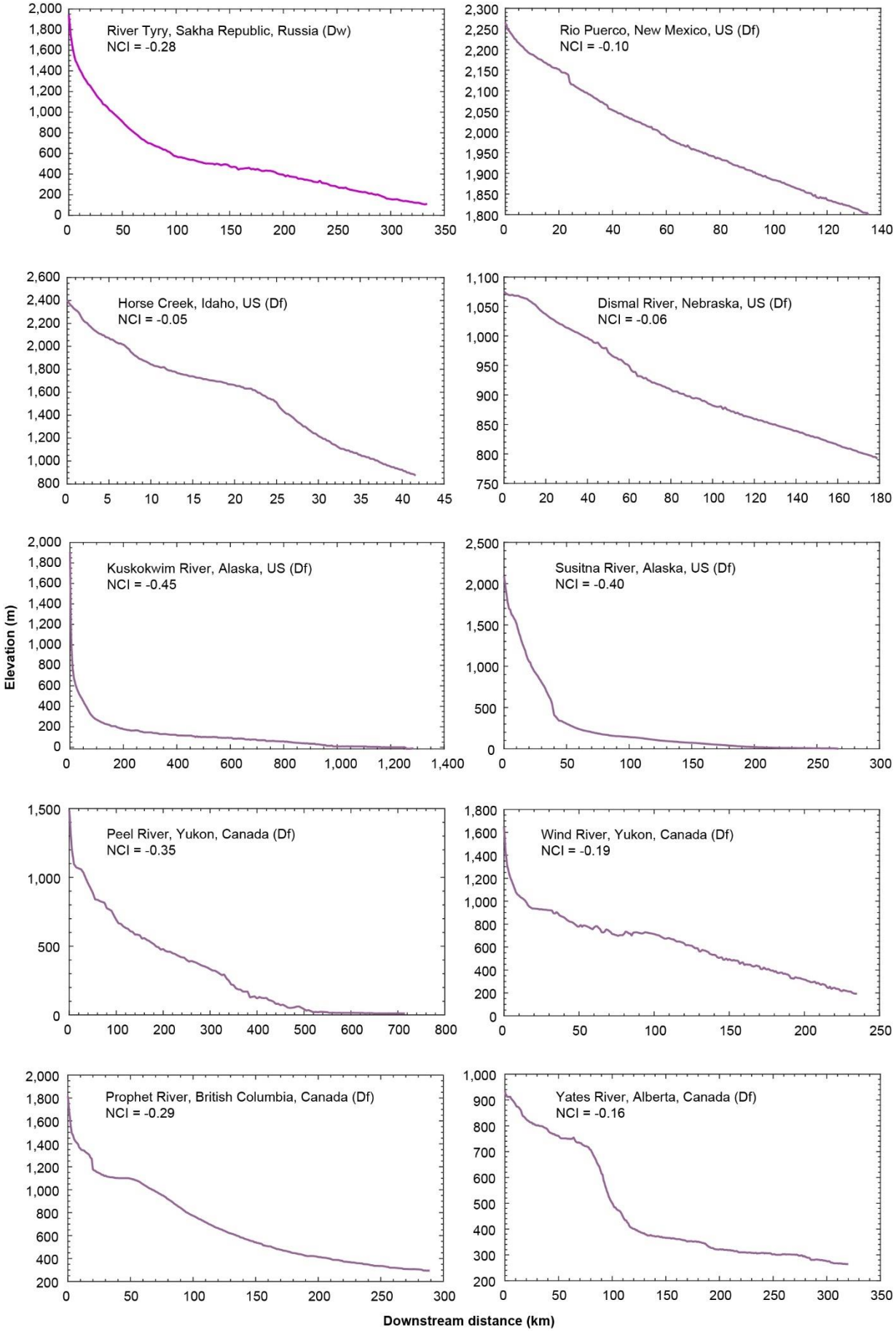
River Tyry, Sakha Republic, Russia (Dw)
NCI = -0.28
Rio Puerco, New Mexico, US (Df)
NCI = -0.10
Horse Creek, Idaho, US (Df)
NCI = -0.05
Dismal River, Nebraska, US (Df)
NCI = -0.06
Kuskokwim River, Alaska, US (Df)
NCI = -0.45
Susitna River, Alaska, US (Df)
NCI = -0.40
Peel River, Yukon, Canada (Df)
NCI = -0.35
Wind River, Yukon, Canada (Df)
NCI = -0.19
Prophet River, British Columbia, Canada (Df)
NCI = -0.29
Yates River, Alberta, Canada (Df)
NCI = -0.16
Elevation (m)
Downstream distance (km)

Continued.

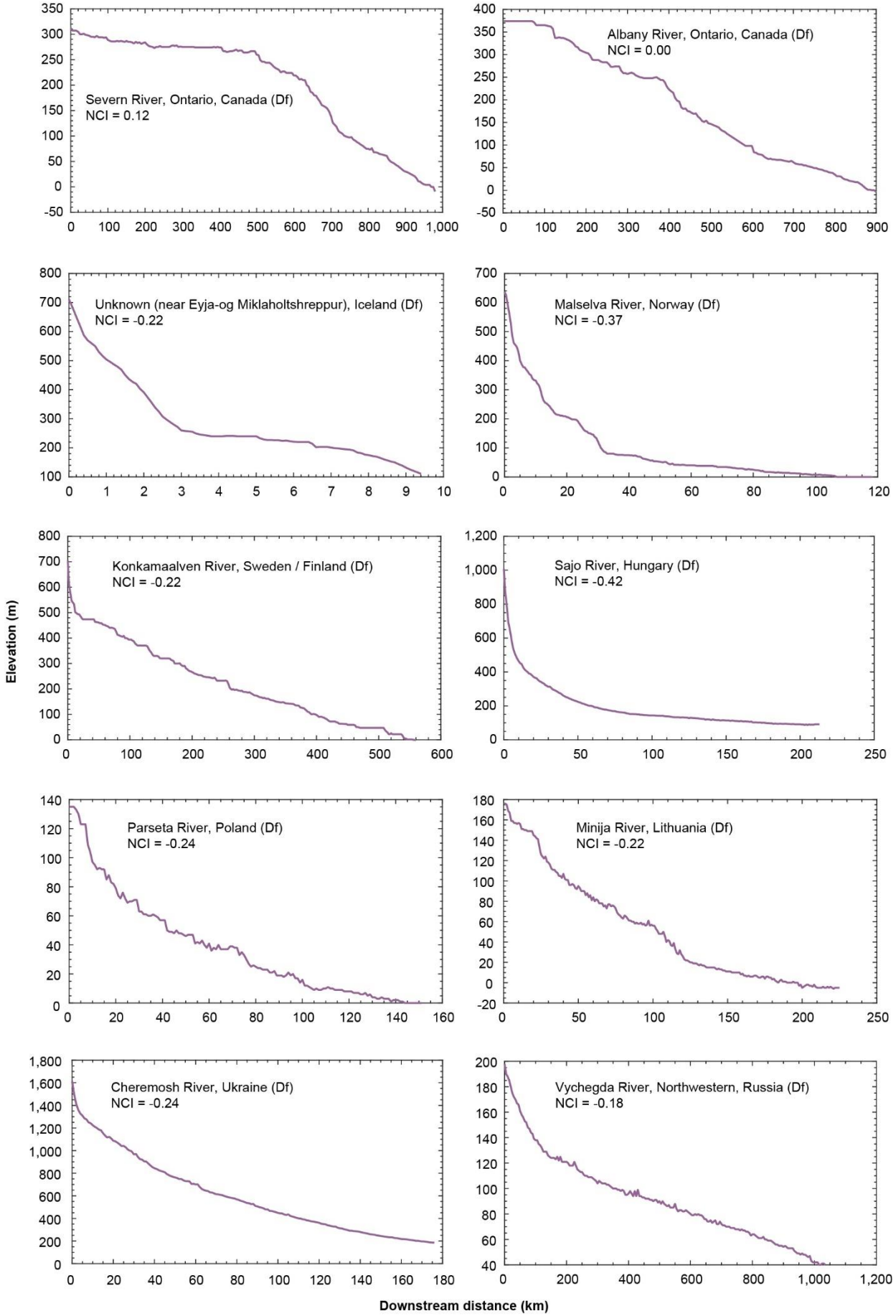
Severn River, Ontario, Canada (Df)
NCI = 0.12
Albany River, Ontario, Canada (Df)
NCI = 0.00
Unknown (near Eyja-og Miklaholtshreppur), Iceland (Df)
NCI = -0.22
Malselva River, Norway (Df)
NCI = -0.37
Konkamaalven River, Sweden / Finland (Df)
NCI = -0.22
Sajo River, Hungary (Df)
NCI = -0.42
Parseta River, Poland (Df)
NCI = -0.24
Minija River, Lithuania (Df)
NCI = -0.22
Cheremosh River, Ukraine (Df)
NCI = -0.24
Vychegda River, Northwestern, Russia (Df)
NCI = -0.18
Elevation (m)
Downstream distance (km)

Continued.

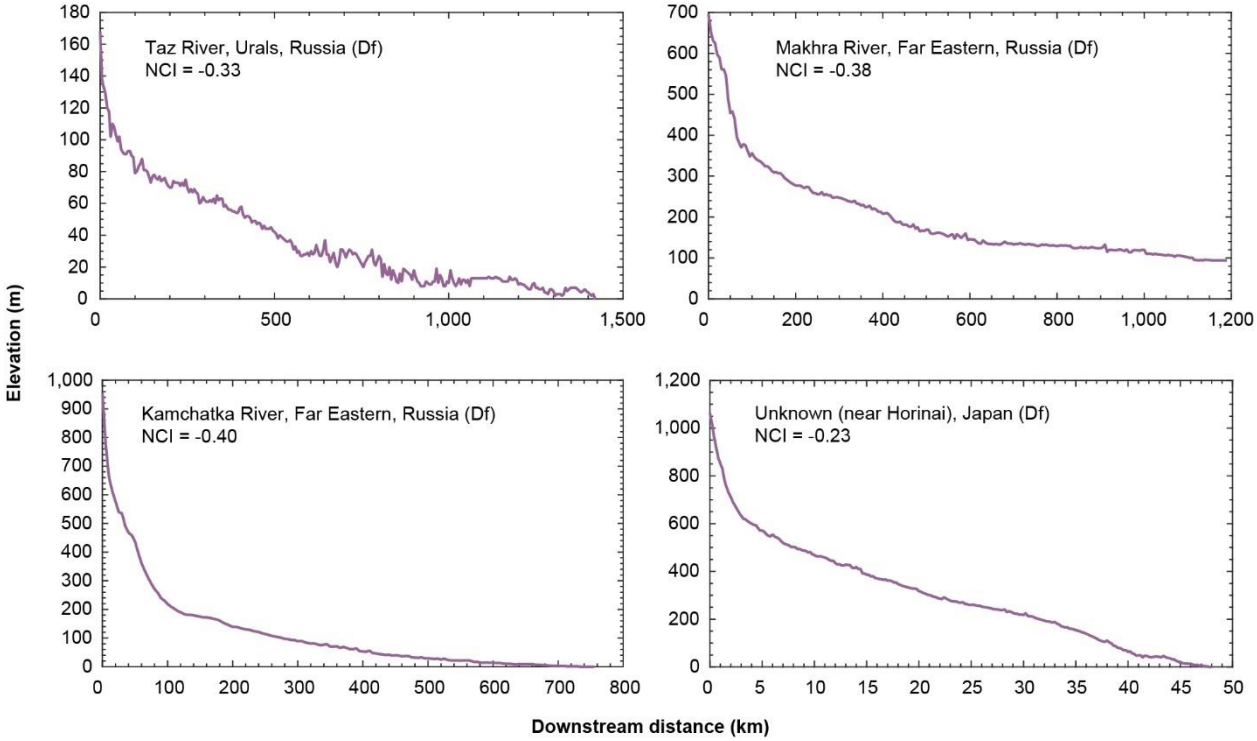
Taz River, Urals, Russia (Df)
NCI = -0.33
Makhra River, Far Eastern, Russia (Df)
NCI = -0.38
Kamchatka River, Far Eastern, Russia (Df)
NCI = -0.40
Unknown (near Horinai), Japan (Df)
NCI = -0.23
Elevation (m)
Downstream distance (km)

Continued.

Appendix E. Dataset of short-term drainage basin erosion rates

The following short-term erosion rates and relevant climate data are available at the University of Bristol data repository, data.bris, at https://doi.org/10.5523/bris.1pq50eh0902da25aps5nhc1ngv.

E.1 Compiled from literature

Country	Location	Erosion rate (mm kyr^{-1})	Basin area (km^2)	Latitude	Longitude	K–G climate zone	AI category	Reference*
Bolivia	SIR	2800.00	270.00	-16.45	-67.26	Cf	Semi-arid	1
Bolivia	TAM	950.00	950.00	-16.68	-67.09	Cf	Semi-arid	1
Bolivia	VBA	1550.00	1900.00	-17.03	-66.99	Cw	Humid	1
Bolivia	HUL	1530.00	17.00	-16.52	-67.86	Cw	Humid	1
Bolivia	ACH	2000.00	38.00	-16.44	-67.44	Cf	Humid	1
Bolivia	LUR	2980.00	810.00	-16.98	-67.66	Cw	Semi-arid	1
Bolivia	POR	1250.00	240.00	-16.91	-67.60	Cw	Semi-arid	1
Bolivia	VER	30.00	140.00	-16.86	-67.50	Cw	Dry sub-humid	1
Bolivia	MIG	50.00	360.00	-16.86	-67.53	Cw	Semi-arid	1
Bolivia	CAJ	6910.00	6500.00	-17.02	-66.70	Cw	Humid	1
Bolivia	COT	2730.00	5600.00	-16.82	-66.85	Cw	Humid	1
Bolivia	MIS	10.00	350.00	-16.97	-66.77	Cw	Semi-arid	1
Bolivia	VIN	20.00	50.00	-17.06	-66.72	Cw	Humid	1
Bolivia	LOC	1260.00	200.00	-17.33	-65.90	Cw	Humid	1
Bolivia	SPE	4130.00	320.00	-17.33	-65.86	Cw	Humid	1
Bolivia	ICO	1870.00	2300.00	-17.26	-65.90	Cw	Humid	1
Bolivia	BER	470.00	480.00	-18.18	-63.56	Aw	Dry sub-humid	1
Bolivia	ELV	180.00	64.00	-17.88	-63.34	Aw	Humid	1
Bolivia	EPS	780.00	203.00	-17.87	-63.30	Aw	Humid	1
Bolivia	AMO	5170.00	9200.00	-17.72	-66.23	BSk	Semi-arid	1
Bolivia	HUR	480.00	11200.00	-18.34	-65.47	Cw	Semi-arid	1
Bolivia	PNA	2500.00	31200.00	-18.46	-64.37	BSh	Semi-arid	1
Bolivia	MIZ	490.00	10800.00	-18.46	-64.36	BSh	Semi-arid	1
Bolivia	PAZ	190.00	4360.00	-20.09	-63.89	BSh	Semi-arid	1
Bolivia	SAN	980.00	7500.00	-20.34	-63.04	Aw	Semi-arid	1
Bolivia	AT	710.00	6340.00	-19.04	-65.40	Cw	Semi-arid	1
Bolivia	NU	260.00	1600.00	-19.27	-65.29	BSk	Semi-arid	1
Bolivia	VQ	630.00	13200.00	-19.36	-64.91	BSk	Semi-arid	1
Bolivia	SL	40.00	4200.00	-20.17	-65.88	BSk	Semi-arid	1
Bolivia	EP	50.00	20100.00	-21.15	-65.20	BSk	Semi-arid	1
Bolivia	CH	120.00	42900.00	-21.02	-64.97	BSk	Semi-arid	1
Bolivia	SJ	250.00	47500.00	-21.15	-64.21	Cw	Semi-arid	1
Bolivia	VI	330.00	81300.00	-21.29	-63.43	Cw	Semi-arid	1
Bolivia	CAB	80.00	230.00	-21.34	-64.60	Cw	Semi-arid	1
Bolivia	OB	160.00	920.00	-21.45	-64.64	Cw	Semi-arid	1
Bolivia	TO	1230.00	460.00	-21.48	-64.66	Cw	Semi-arid	1
Bolivia	SA	80.00	290.00	-21.58	-64.14	Cw	Semi-arid	1
Bolivia	PA	190.00	220.00	-21.56	-64.15	Cw	Semi-arid	1
Bolivia	AQM	1470.00	9400.00	-16.33	-67.56	Cf	Humid	1
Bolivia	SRC	570.00	4700.00	-16.73	-67.19	Cf	Humid	1

Bolivia	AIN	1430.00	29900.00	-16.70	-66.73	Cf	Humid	1
Bolivia	AB	1210.00	67500.00	-15.89	-66.85	Cf	Humid	1
Bolivia	LBE	300.00	2880.00	-17.73	-63.20	Aw	Humid	1
Nepal	Bhote Koshi	100.00	2308.00	27.75	85.26	Cw	Humid	2
Nepal	Upper Karnali	400.00	21121.00	28.95	81.44	Cw	Humid	2
Nepal	Karnali	900.00	45967.00	28.64	81.29	Cw	Humid	2
Nepal	Saradha	200.00	808.00	27.64	82.02	Cw	Humid	2
Nepal	Upper Rapti	1900.00	3648.00	27.90	82.85	Cw	Humid	2
Nepal	Rapti	1000.00	5197.00	27.95	82.23	Cw	Humid	2
Nepal	Kali-Gandaki	2800.00	7170.00	28.01	83.60	Cw	Humid	2
Nepal	Trishuli	300.00	4428.00	27.97	85.18	Cw	Humid	2
Nepal	Narayani	1500.00	32002.00	27.71	84.43	Cw	Humid	2
Nepal	Bagmati	600.00	2849.00	27.11	85.48	Cw	Humid	2
Nepal	Sapta-Koshi	900.00	54024.00	28.87	87.16	Cw	Semi-arid	2
Nepal	Kankai Mai	500.00	1172.00	26.70	87.88	Cw	Humid	2
US	Rio Puerco	405.63	1117.00	35.60	-107.17	Df	Arid	3
US	Rio Puerco	437.50	2220.00	35.59	-107.19	Df	Arid	3
US	Rio Puerco	151.25	16153.00	34.41	-106.85	BSk	Arid	3
US	Rio Puerco	290.63	14946.00	34.79	-106.99	BWk	Arid	3
US	Rio Puerco	42.50	7122.00	34.97	-107.19	BWk	Arid	3
US	Luquillo Forest	126.25	3.26	18.28	-65.79	Af	Humid	4
Israel	Nahal Yael	78.44	0.60	29.59	34.95	BWh	Hyper-arid	6
Taiwan	Fengshan	3004.81	208.00	24.83	121.07	Cf	Humid	7
Taiwan	Taan	6911.53	633.00	24.34	120.74	Cf	Humid	7
Taiwan	Tachia	1498.80	417.00	24.29	121.25	Cf	Humid	7
Taiwan	Choshui	11291.40	2989.00	23.84	120.40	Cf	Humid	7
Taiwan	Pachang	8503.40	441.00	23.33	120.25	Cf	Humid	7
Taiwan	Tsengwen	13504.75	1157.00	23.11	120.21	Cf	Humid	7
Taiwan	Peinan	34722.22	1584.00	22.79	121.15	Cf	Humid	7
Taiwan	Hsiukuluan	8934.37	1539.00	23.48	121.40	Cf	Humid	7
Taiwan	Hualien	12865.21	1506.00	23.92	121.60	Cf	Humid	7
Taiwan	Hoping	16952.98	553.00	24.32	121.74	Cf	Humid	7
Taiwan	Tanshui (1140H058)	742.28	842.00	25.08	121.69	Cf	Humid	7
Taiwan	Tanshui (1140H066)	1498.00	751.00	24.99	121.53	Cf	Humid	7
Taiwan	Tanshui (1140H067)	5208.33	204.00	24.94	121.35	Cf	Humid	7
Taiwan	Nankang	512.30	122.00	25.06	121.28	Cf	Humid	7
Taiwan	Touchien	1878.76	499.00	24.81	121.02	Cf	Humid	7
Taiwan	Chungkang	6060.61	165.00	24.64	120.96	Cf	Humid	7
Taiwan	Houlung	3840.04	472.00	24.59	120.83	Cf	Humid	7
Taiwan	Wu	3091.87	1981.00	24.11	120.58	Cf	Humid	7
Taiwan	Peikang	2303.18	597.00	23.56	120.30	Cf	Humid	7
Taiwan	Potzu	4541.52	289.00	23.47	120.23	Cf	Humid	7

Taiwan	Chishui	4955.95	227.00	23.30	120.31	Cf	Humid	7
Taiwan	Yenshui	4708.90	146.00	23.06	120.28	Cf	Humid	7
Taiwan	Kaoping	9956.11	3076.00	22.65	120.44	Cf	Humid	7
Taiwan	Tungkang	1428.57	175.00	22.57	120.54	Cf	Humid	7
Taiwan	Linpien	6653.23	310.00	22.46	120.55	Cf	Humid	7
Taiwan	Chihpen	13554.22	166.00	22.69	121.02	Cf	Humid	7
Taiwan	Nanao	8823.53	170.00	24.46	121.79	Cf	Humid	7
US	Arroyo de los Frijoles Watershed	86.88	0.16	35.76	-106.03	Df	Semi-arid	8
US	Volcano Hill Wash	372.50	9.30	34.84	-107.37	BSk	Arid	9
US	Arroyo Chavez	748.13	2.11	35.65	-107.08	Df	Semi-arid	5; 9
Sri Lanka	Atabage oya, Upper Mahaweli catchment	224.38	44.00	7.13	80.60	Af	Humid	10
Sri Lanka	Nilambe oya, Upper Mahaweli catchment	83.75	62.00	7.19	80.63	Af	Humid	10
Sri Lanka	Huluganga, Upper Mahaweli catchment	140.00	123.00	7.33	80.74	Am	Humid	10
Sri Lanka	Maha oya, Upper Mahaweli catchment	246.88	107.00	7.19	80.77	Am	Humid	10
Sri Lanka	Belihul oya, Upper Mahaweli catchment	345.63	146.00	7.17	80.84	Cf	Humid	10
Sri Lanka	Uma oya (1), Upper Mahaweli catchment	1325.00	740.00	7.19	80.95	Am	Humid	10
Sri Lanka	Uma oya (2), Upper Mahaweli catchment	1007.50	98.00	6.91	80.91	Cf	Humid	10
Sri Lanka	Peradeniya, Upper Mahaweli catchment	279.38	565.00	7.26	80.59	Af	Humid	10
Sri Lanka	Polgolla, Upper Mahaweli catchment	253.13	721.00	7.32	80.65	Am	Humid	10
Sri Lanka	Victoria, Upper Mahaweli catchment	318.75	16.00	7.24	80.79	Am	Humid	10
India	Ganga, Ganga basin	11643.84	32650.00	26.61	80.28	Cw	Dry sub-humid	10
India	Karnali, Ganga basin	624.71	72010.00	25.78	84.63	Cw	Dry sub-humid	10
India	Narayani/Gandak, Ganga basin	1172.26	34450.00	25.68	85.19	Cw	Dry sub-humid	10
India	Kosi, Ganga basin	864.00	56210.00	25.54	86.73	Cw	Humid	10
India	Ganga Bangladesh, Ganga basin	651.52	220150.00	24.05	89.03	Cw	Humid	10
Germany	Iller, Kempten	108.06	953.00	47.73	10.32	Cf	Humid	11
Germany	Tiroler Ache, Marquartstein	154.00	945.00	47.76	12.46	Df	Humid	11
Germany	Inn, Reisach	159.25	9756.00	47.66	12.18	Df	Humid	11
Italy	Sarca, Ponte Pià	75.38	575.00	46.05	10.82	Df	Humid	11
Germany	Ammer, Weilheim	71.00	-	47.85	11.14	Df	Humid	12
Germany	Iller, Krugzell	123.00	-	47.80	10.27	Df	Humid	12
Germany	Iller, Wiblingen	25.00	-	48.37	9.99	Cf	Humid	12
Germany	Isar, Sylvenstein	72.00	1100.00	47.59	11.55	Df	Humid	12
Germany	Isar, München	18.00	-	48.15	11.60	Df	Humid	12
Germany	Isar, Plattling	12.00	-	48.77	12.88	Df	Humid	12

Germany	Kotlaine	1022.00	-	47.68	11.45	Df	Humid	12
Germany	Lainbach	327.00	-	47.70	11.43	Df	Humid	12
Germany	Lech, Feldheim	17.00	-	48.73	10.92	Cf	Humid	12
Germany	Loisach, Schlehdorf	41.00	-	47.67	11.32	Df	Humid	12
Germany	Saalach, Unterjettenburg	186.00	-	47.68	12.82	Df	Humid	12
Germany	Tiroler Achen, Staudach	113.00	-	47.78	12.47	Df	Humid	12
Germany	Traun, Altenmarkt/Stein	46.00	-	47.99	12.54	Df	Humid	12
Germany	Weissach, Tegernsee	50.00	-	47.69	11.75	Df	Humid	12
Germany	Wertach, Türkheim	22.00	-	48.06	10.65	Cf	Humid	12
Germany	Wertach, Schwabmünchen	63.00	-	48.18	10.73	Cf	Humid	12
Germany	Inn, Kufstein	92.00	-	47.58	12.17	Df	Humid	12
Germany	Inn, Oberaudorf	74.00	-	47.65	12.19	Df	Humid	12
Germany	Inn, Rosenheim	84.00	-	47.85	12.14	Df	Humid	12
Germany	Inn, Wasserburg	96.00	-	48.06	12.23	Df	Humid	12
Germany	Inn, Neuötting	102.00	-	48.25	12.69	Df	Humid	12
Germany	Inn, Passau	64.00	-	48.57	13.47	Df	Humid	12
Germany	Salzach, Laufen	118.00	-	47.94	12.93	Df	Humid	12
Germany	Salzach, Burghausen	131.00	-	48.16	12.83	Df	Humid	12
Switzerland	Emme, Wiler	21.00	-	47.18	7.56	Df	Humid	12
Switzerland	Thur, Halden	81.00	-	47.51	9.21	Df	Humid	12
Switzerland	L'Arve, Gèneve	179.00	-	46.18	6.16	Df	Humid	12
Switzerland	Dongia, Valle di Blenio	20.00	-	46.43	8.97	Df	Humid	12
Switzerland	Val Roseg, Pontresina	184.00	-	46.49	9.91	Df	Humid	12
Switzerland	Ticino, Bellinzona	102.00	1515.00	46.19	9.01	Df	Humid	12
Switzerland	Maggia, Locarno	82.00	-	46.17	8.77	Df	Humid	12
Switzerland	Moesa, Lumino	35.00	-	46.22	9.06	Df	Humid	12
Austria	Drau, Rosegg	76.00	-	46.58	14.04	Df	Humid	12
Austria	Enns, Liezen	48.00	-	47.55	14.25	Df	Humid	12
Austria	Enns, Großreifling	43.00	-	47.67	14.71	Df	Humid	12
Austria	Gail, Gailitz	90.00	-	46.57	13.72	Df	Humid	12
Austria	Steyr, Steyrdurchbruch	46.00	-	47.86	14.20	Df	Humid	12
France	Rhone, mouth, Mediterranean	136.00	-	43.42	4.74	Cs	Dry sub-humid	12
France	Durance, Mirabeau	440.00	-	43.69	5.67	Cs	Humid	12
France	Isère	128.00	-	45.20	5.73	Df	Humid	12
France	Asse	254.00	-	43.88	5.90	Cs	Humid	12
France	Bléone	244.00	-	44.04	6.04	Cs	Humid	12
France	Ferrand	137.00	-	45.05	6.14	Df	Humid	12
France	Romanche	226.00	-	45.04	6.18	Df	Humid	12
Italy	Adda, Tirano	103.00	-	46.21	10.17	Df	Humid	12
Italy	Adda, Pizzighettone	68.00	-	45.19	9.80	Cf	Humid	12

Italy	Dora Baltea, Tavagnasco	301.00	-	45.55	7.83	Df	Humid	12
Italy	Oglio, Marcaria	18.00	-	45.11	10.53	Cf	Humid	12
Italy	Po, Casale Monferrato	20.00	-	45.14	8.45	Cf	Humid	12
Italy	Po, Becca	43.00	-	45.14	9.22	Cf	Humid	12
Italy	Sesia, Vercelli	40.00	-	45.33	8.44	Cf	Humid	12
Italy	Brenta, Bassano	25.00	-	45.76	11.73	Cf	Humid	12
Italy	Cismon, Cismon	213.00	-	45.93	11.74	Cf	Humid	12
Italy	Etsch/Adige, Trento	91.00	-	46.07	11.12	Df	Humid	12
Italy	Rio Cordon, Dolomites	59.00	-	46.45	12.10	Df	Humid	12
Italy	Sauglio, Turin	63.00	-	44.99	7.75	Cf	Humid	12
Italy	Sextenbach, Dolomites	129.00	-	46.71	12.32	Df	Humid	12
Italy	Tanaro, Nucetto	82.00	375.00	44.34	8.06	Cs	Humid	12
Italy	Tanaro, Clavesana	112.00	-	44.48	7.90	Cf	Humid	12
Italy	Tanaro, Farigliano	87.00	1522.00	44.51	7.91	Cf	Humid	12
Italy	Tanaro, Alessandria	74.00	-	44.92	8.61	Cf	Humid	12
Italy	Tanaro, Montecastello	120.00	7985.00	44.95	8.68	Cf	Humid	12
US	West Fork Horse Creek	3.13	17.00	45.41	-114.72	Df	Semi-arid	13
US	East Fork Horse Creek	1.56	14.00	45.99	-115.33	Df	Humid	13
US	Tailholt Creek	8.75	6.60	45.04	-115.68	Ds	Dry sub-humid	13
US	Circle End Creek	4.06	3.80	45.05	-115.67	Ds	Dry sub-humid	13
US	Trapper Creek	6.13	20.00	42.18	-113.94	BSk	Semi-arid	13
US	South Fork Red River	5.00	98.00	45.71	-115.34	Df	Humid	13
US	Johns Creek	4.75	293.00	45.82	-115.89	Df	Dry sub-humid	13
US	Johns Creek	4.75	2149.00	46.15	-115.98	Ds	Dry sub-humid	13
US	Lochsa River	16.44	3055.00	46.14	-115.60	Ds	Dry sub-humid	13
US	Selway River	15.31	4945.00	46.14	-115.60	Ds	Dry sub-humid	13
US	Salmon River	8.56	35079.00	45.86	-116.79	Df	Semi-arid	13
India	Yamuna, Ganga basin	3446.15	7620.00	30.44	77.67	Cw	Humid	14
US	Bryson City, Tuckasegee River	65.00	1700.00	35.43	-83.45	Cf	Humid	15
US	Little River	21.00	490.00	35.76	-83.85	Cf	Humid	15
Canada	Annapolis, Wilmott	4.59	546.00	45.60	-64.70	Df	Humid	16
Canada	Chaudiere, St Lambert	35.36	5805.00	46.83	-71.17	Df	Humid	16
Canada	Liard, River mouth	82.58	275000.00	61.70	-121.20	Df	Dry sub-humid	16
Canada	Peace, Peace River	198.01	186000.00	56.25	-117.32	Df	Dry sub-humid	16
Canada	Peace, Peace Point	76.19	293000.00	59.10	-112.40	Df	Dry sub-humid	16
Canada	Red Deer, Red Deer	18.93	11570.00	52.17	-113.67	Df	Dry sub-humid	16
Canada	South Saskatchewan, Lemsford	50.19	179000.00	51.02	-109.12	Df	Semi-arid	16
Canada	South Saskatchewan, Saskatoon	10.36	141000.00	52.10	-106.60	Df	Semi-arid	16
US	Chena, Fairbanks	34.22	5125.00	64.83	-147.83	Df	Dry sub-humid	16
US	Elm Fork Red, Magnum	438.00	1940.00	34.90	-99.52	Cf	Semi-arid	16

US	Little Colorado, Cameron	110.41	70600.00	35.25	-111.42	Ds	Semi-arid	16
US	Pecos, Santa Rosa	54.07	7490.00	34.93	-104.70	BSk	Semi-arid	16
US	Salt Fork Red, Mangum	47.91	3150.00	34.90	-99.52	Cf	Semi-arid	16
US	Walla Walla, Touchet	515.56	4279.00	46.08	-118.30	Cs	Semi-arid	16
Bolivia	Piray, Taruma	542.94	1590.00	-18.11	-63.46	Aw	Humid	16
France	Grand Morin, Villier	9.58	1200.00	48.87	3.00	Cf	Humid	16
France	Lot, Clairac	46.31	11500.00	44.40	-0.60	Cf	Humid	16
France	Marne, Noisiel	5.70	12500.00	48.85	2.62	Cf	Humid	16
France	Melarchez, Melarchez	9.13	7.00	48.82	3.08	Cf	Humid	16
Thailand	Nam Mae Pai, Sop Mae Samat	31.03	5530.00	19.23	97.93	Aw	Humid	16
Thailand	Nam Mae Pai, Ban Na Chalong	52.24	369.00	19.40	98.45	Aw	Humid	16
Thailand	Huai Mae Ya, Sop Huai Mae Ya	62.28	84.80	19.73	98.48	Aw	Humid	16
Thailand	Khlong Mala, Hat Som Paem	116.34	188.00	10.68	98.05	Am	Humid	16
Thailand	Khlong Sok, Ban Cheo Sai	75.05	892.00	8.82	98.83	Am	Humid	16
Mali	Bani, Douna	2.42	102000.00	14.73	-1.63	BSh	Arid	16
Algeria	El Abid	999.19	2635.00	32.25	6.33	BWh	Hyper-arid	16
Ivory Coast	Nzi, Zienoa	3.35	33150.00	6.08	-4.75	Aw	Humid	16
France	Somme	2.97	5560.00	50.19	1.62	Cf	Humid	16
France	Adour	1140.63	7830.00	43.53	-1.52	Cf	Humid	16
Canada	St. Lewis	3.13	2000.00	52.33	-55.82	Df	Humid	17
Canada	Saguenay	2.84	88000.00	48.13	-69.70	Df	Humid	17
Canada	Severn	1.38	100000.00	56.07	-87.56	Df	Humid	17
US	Alsea	116.28	860.00	44.42	-124.08	Cs	Humid	17
US	Androscoggin	12.07	8800.00	43.98	-69.86	Df	Humid	17
US	Calleguas	744.05	840.00	34.10	-119.09	Cs	Semi-arid	17
US	Connecticut	5.58	28000.00	41.28	-72.34	Df	Humid	17
US	Coos	74.22	1600.00	43.38	-124.18	Cs	Humid	17
US	Coquille	67.13	2700.00	43.12	-124.43	Cs	Humid	17
US	Duwamish	125.00	1200.00	47.58	-122.36	Cs	Humid	17
US	Edisto	1.67	7500.00	32.50	-80.35	Cf	Humid	17
US	Guadalupe	7.21	26000.00	28.41	-96.78	Cf	Humid	17
US	Gualala	187.50	900.00	38.77	-123.53	Cs	Humid	17
US	Hoh	692.31	650.00	47.75	-124.44	Cf	Humid	17
US	Housatonic	74.40	4200.00	41.17	-73.11	Df	Humid	17
US	James	23.81	21000.00	36.99	-76.28	Cf	Humid	17
US	Kennebeck	25.39	16000.00	43.75	-69.78	Df	Humid	17
US	Los Angeles	71.43	2100.00	33.76	-118.19	Cs	Semi-arid	17
US	Matolle	750.00	1000.00	40.30	-124.35	Cs	Humid	17
US	Merrimack	10.42	12000.00	42.82	-70.81	Df	Humid	17

US	Mobile	25.57	110000.00	30.67	-88.03	Cf	Humid	17
US	Navarro	187.50	800.00	39.19	-123.76	Cs	Humid	17
US	Neches	13.50	25000.00	29.97	-93.86	Cf	Humid	17
US	Nehalem	62.50	2200.00	45.66	-123.94	Cs	Humid	17
US	Nooksak	500.00	2000.00	48.77	-122.58	Cs	Humid	17
US	Nueces	10.32	43000.00	27.84	-97.49	Cf	Dry sub-humid	17
US	Pajaro	60.48	3100.00	36.85	-121.81	Cs	Semi-arid	17
US	Pascagoula	35.00	25000.00	30.36	-88.60	Cf	Humid	17
US	Passaic	9.87	1900.00	40.72	-74.12	Df	Humid	17
US	Patuxent	10.42	2400.00	38.31	-76.42	Cf	Humid	17
US	Penobscot	28.68	17000.00	44.50	-68.80	Df	Humid	17
US	Rogue	102.68	14000.00	42.42	-124.43	Cs	Humid	17
US	Sacramento	19.97	72000.00	38.06	-121.79	Cs	Semi-arid	17
US	St. John's	19.40	8700.00	30.40	-81.40	Cf	Humid	17
US	Salinas	130.68	11000.00	36.75	-121.80	Cs	Semi-arid	17
US	San Diego	14.20	1100.00	32.76	-117.25	BSk	Semi-arid	17
US	San Dieguito	10.42	900.00	32.98	-117.27	Cs	Semi-arid	17
US	San Joaquin	2.64	83000.00	38.03	-121.78	Cs	Semi-arid	17
US	Santa Ana	15.87	6300.00	33.63	-117.96	BSk	Semi-arid	17
US	Santa Margarita	39.47	1900.00	33.23	-117.42	BSk	Semi-arid	17
US	Santa Maria	129.17	4500.00	34.97	-120.65	Cs	Semi-arid	17
US	Santa Ynez	625.00	2000.00	34.69	-120.60	Cs	Semi-arid	17
US	Siletz	72.12	520.00	44.93	-124.02	Cs	Humid	17
US	Siuslaw	39.17	1500.00	44.02	-124.14	Cs	Humid	17
US	Sixes	812.50	300.00	42.85	-124.54	Cs	Humid	17
US	Smith	3333.33	300.00	41.94	-124.20	Cs	Humid	17
US	Snohomish	36.86	3900.00	48.02	-122.21	Cs	Humid	17
US	Tijuana	65.28	4500.00	32.55	-117.13	BSk	Arid	17
US	Tillamook	81.97	610.00	45.49	-123.90	Cs	Humid	17
US	Umpqua	72.92	12000.00	43.67	-124.21	Cs	Humid	17
US	York	4.60	6800.00	37.24	-76.40	Cf	Humid	17
US	Chilkat	789.47	1900.00	59.24	-135.54	Ds	Humid	17
US	Knik	1465.52	2900.00	61.48	-149.26	Ds	Humid	17
US	Matanuska	707.55	5300.00	61.49	-149.27	Ds	Humid	17
US	Speel	2586.21	580.00	58.01	-133.76	Df	Humid	17
US	Wailuku	19.23	650.00	19.73	-155.09	Af	Humid	17
Fiji	Rewa	1293.10	2900.00	-18.13	178.53	Af	Humid	17
Mexico	Actopán	550.00	2500.00	19.42	-96.32	Am	Humid	17
Mexico	Ameca	218.75	12000.00	20.67	-105.28	Aw	Humid	17
Mexico	Antigua	132.58	3300.00	19.31	-96.28	Am	Humid	17
Mexico	Balsas	57.29	120000.00	17.95	-102.13	Aw	Dry sub-humid	17
Mexico	Coahuayana	383.33	7500.00	18.68	-103.74	BSh	Dry sub-humid	17

Mexico	Culiacan	55.56	18000.00	24.49	-107.73	BSh	Semi-arid	17
Mexico	Diego	50.00	1000.00	15.56	-93.30	Aw	Humid	17
Mexico	Grijalva	16.25	50000.00	18.60	-92.69	Aw	Humid	17
Mexico	Jamapa	75.76	3300.00	19.10	-96.10	Aw	Humid	17
Mexico	La Unión	26.79	1400.00	17.91	-101.86	Aw	Dry sub-humid	17
Mexico	Maraquelia	110.29	1700.00	16.56	-98.81	Aw	Dry sub-humid	17
Mexico	Mayo	41.96	14000.00	26.73	-109.79	BWh	Arid	17
Mexico	Misantia	275.74	680.00	19.89	-96.50	Cf	Humid	17
Mexico	Mocorito	107.14	2800.00	25.08	-108.07	BSh	Semi-arid	17
Mexico	Panuco	48.53	85000.00	22.26	-97.79	Aw	Humid	17
Mexico	Papaloapán	93.75	46000.00	18.75	-95.75	Aw	Humid	17
Mexico	Piaxtla	227.27	11000.00	23.71	-106.81	BSh	Semi-arid	17
Mexico	San Fernando	125.00	18000.00	24.97	-97.75	BSh	Semi-arid	17
Mexico	San Lorenzo	150.00	10000.00	24.25	-107.42	BSh	Semi-arid	17
Mexico	Suchiate	173.61	1800.00	14.53	-92.23	BWh	Dry sub-humid	17
Mexico	Tehuantepec	261.36	11000.00	16.19	-95.15	Aw	Dry sub-humid	17
Mexico	Usumacinta	75.98	51000.00	18.65	-92.47	Aw	Humid	17
Mexico	Verde	266.45	19000.00	15.99	-97.79	BSh	Humid	17
Guatemala	Motagua	312.50	15000.00	15.74	-88.27	Af	Humid	17
El Salvador	Lempa	243.06	18000.00	13.26	-88.82	Am	Humid	17
Honduras	Coco	150.46	27000.00	15.00	-83.14	Am	Humid	17
Nicaragua	Escondido	244.79	12000.00	12.05	-83.74	Af	Humid	17
Nicaragua	Grande de Matagalpa	164.06	20000.00	12.91	-83.51	Af	Humid	17
Nicaragua	Prinza Polka	204.55	11000.00	13.41	-83.56	Af	Humid	17
Nicaragua	San Juan	78.53	39000.00	10.94	-83.70	Af	Humid	17
Costa Rica	Grande de Terraba	247.40	4800.00	8.96	-83.62	Am	Humid	17
US	Guanajibo	90.73	310.00	18.17	-67.18	Af	Humid	17
Colombia	Ancho	34.72	540.00	11.26	-73.49	BSh	Humid	17
Colombia	Atrato	190.97	36000.00	8.20	-76.92	Af	Humid	17
Colombia	Don Diego	27.64	520.00	11.26	-73.70	BSh	Humid	17
Colombia	Leon	729.17	1200.00	7.94	-76.75	Af	Humid	17
Colombia	Mira	638.16	9500.00	1.64	-79.00	Cf	Humid	17
Colombia	Mulatos	131.25	1000.00	8.65	-76.73	Af	Humid	17
Colombia	Patia	546.88	24000.00	2.64	-78.32	Cf	Humid	17
Colombia	Rancheria	28.41	2200.00	11.55	-72.90	BWh	Semi-arid	17
Colombia	San Juan	625.00	16000.00	4.12	-77.52	Af	Humid	17
Colombia	Sinú	175.00	15000.00	9.44	-75.95	Aw	Humid	17
Colombia	Turbo	285.16	160.00	8.12	-76.76	Af	Humid	17
Chile	Aconcagua	148.81	2100.00	-32.91	-71.51	Cs	Semi-arid	17
Argentina	Chubut	9.38	40000.00	-43.34	-65.06	BWk	Arid	17
Argentina	Coig	4.17	15000.00	-50.94	-69.17	BSk	Semi-arid	17
Argentina	Deseado	22.32	14000.00	-47.76	-65.87	BSk	Semi-arid	17

Argentina	Gallegos	12.25	5100.00	-51.60	-68.97	BSk	Semi-arid	17
Argentina	Santa Cruz	18.23	24000.00	-50.13	-68.35	BSk	Semi-arid	17
Brazil	Araguari	7.27	43000.00	1.24	-49.90	Aw	Humid	17
Brazil	Contas	1.12	56000.00	-14.27	-38.99	Af	Humid	17
Brazil	Doce	82.24	76000.00	-19.64	-39.81	Am	Humid	17
Brazil	Gurupi	156.25	40000.00	-1.10	-46.05	Am	Humid	17
Brazil	Itajai-Ácu	31.67	15000.00	-26.91	-48.64	Cf	Humid	17
Brazil	Itapicuru	0.15	43000.00	-2.77	-44.16	Af	Humid	17
Brazil	Jaguaribe	0.46	81000.00	-4.42	-37.77	Af	Humid	17
Brazil	Jequitinhonha	45.96	68000.00	-15.84	-38.86	Af	Humid	17
Brazil	Mearim	4.38	100000.00	-2.41	-44.33	Af	Humid	17
Brazil	Mucuri	104.17	15000.00	-18.10	-39.55	Af	Humid	17
Brazil	Paraguaçu	2.08	60000.00	-12.83	-38.80	Af	Humid	17
Brazil	Paraiba do Sul	43.86	57000.00	-21.62	-41.02	Af	Humid	17
Brazil	Parnaiba	5.51	340000.00	-2.74	-41.79	Af	Humid	17
Brazil	Tocantins	61.68	760000.00	-0.47	-48.23	Am	Humid	17
FG**	Approuague	11.36	11000.00	4.68	-51.96	Am	Humid	17
FG	Mana	5.21	12000.00	5.73	-53.84	Af	Humid	17
FG	Marowijne	13.26	66000.00	5.74	-53.97	Af	Humid	17
FG	Oyapoc	10.42	30000.00	4.47	-51.64	Am	Humid	17
Suriname	Coppename	12.50	20000.00	5.83	-55.95	Af	Humid	17
Suriname	Nickerie	12.89	9700.00	5.97	-57.02	Af	Humid	17
Suriname	Saramacca	7.81	16000.00	5.84	-55.93	Af	Humid	17
Suriname	Suriname	11.72	16000.00	5.93	-55.16	Af	Humid	17
Guyana	Berbice	11.36	11000.00	6.30	-57.53	Af	Humid	17
Guyana	Corantijn	9.55	72000.00	6.02	-57.08	Af	Humid	17
Guyana	Essequibo	41.98	67000.00	6.98	-58.40	Af	Humid	17
Turkey	Asi	9.78	23000.00	36.05	35.96	Cs	Humid	17
Turkey	Büyük Menderes	24.38	20000.00	37.54	27.17	Cs	Dry sub-humid	17
Turkey	Devrekani	102.27	1100.00	41.88	32.94	Cf	Humid	17
Turkey	Gediz	45.14	18000.00	38.59	26.82	Cs	Dry sub-humid	17
Turkey	Harsit	125.00	2600.00	41.01	38.84	Cf	Humid	17
Turkey	Iyidere	133.93	840.00	40.99	40.33	Cf	Humid	17
Turkey	Karasu	8.62	2900.00	41.88	35.12	Cf	Humid	17
Turkey	Küçük Menderes	104.17	3600.00	37.96	27.26	Cs	Dry sub-humid	17
Turkey	Melet	168.75	1000.00	40.98	37.93	Cf	Humid	17
Georgia	Bzybi	200.00	1500.00	43.19	40.28	Cf	Humid	17
Georgia	Chorokhi	232.95	22000.00	41.60	41.57	Cf	Humid	17
Georgia	Inguri	19.82	4100.00	42.39	41.56	Cf	Humid	17
Georgia	Khobi	216.35	1300.00	42.28	41.63	Cf	Humid	17
Georgia	Kodori	256.25	2000.00	42.82	41.13	Cf	Humid	17
Georgia	Supsa	142.05	1100.00	42.02	41.75	Cf	Humid	17

Yemen	Wadi Siham	357.14	4900.00	14.81	43.15	BWh	Arid	17
Yemen	Wadi Tuban	288.46	6500.00	12.83	44.94	BWh	Hyper-arid	17
Algeria	Agrioun	4545.45	660.00	36.64	5.34	Cs	Humid	17
Algeria	Kebir	125.00	1100.00	36.87	6.08	Cs	Humid	17
Algeria	Mazafran	986.84	1900.00	36.70	2.80	Cs	Humid	17
Algeria	Sebaou	300.00	2500.00	36.91	3.86	Cs	Humid	17
Algeria	Seybousse	136.36	5500.00	36.87	7.77	Cs	Dry sub-humid	17
Algeria	Soumman	301.47	8500.00	36.73	5.08	Cs	Humid	17
Algeria	Tafna	71.02	8800.00	35.30	-1.47	Cs	Semi-arid	17
Morroco	Bou Regreg	299.74	9800.00	34.04	-6.83	Cs	Semi-arid	17
Morroco	Draa	76.75	114000.00	28.68	-11.12	BWh	Arid	17
Morroco	Loukos	625.00	1800.00	35.20	-6.15	Cs	Dry sub-humid	17
Morroco	Massa	263.16	3800.00	30.08	-9.67	BSh	Arid	17
Morroco	Mellah	347.22	1800.00	33.70	-7.41	Cs	Semi-arid	17
Morroco	Mharhar	729.17	180.00	35.57	-5.99	Cs	Dry sub-humid	17
Morroco	Nekor	2215.19	790.00	35.20	-3.82	Cs	Semi-arid	17
Morroco	Oum Er Rbia	137.50	30000.00	33.32	-8.34	Cs	Semi-arid	17
Tunisia	Majardah	267.05	22000.00	37.01	10.19	Cs	Semi-arid	17
Tunisia	Miliane	281.25	2000.00	36.76	10.30	Cs	Semi-arid	17
Gambia	Gambia	1.62	77000.00	13.56	-16.60	Aw	Semi-arid	17
Guinea	Konkoure	14.84	16000.00	9.81	-13.75	Am	Humid	17
Liberia	Cavally	118.30	28000.00	4.36	-7.53	Af	Humid	17
Ivory Coast	Agneby	105.34	8900.00	5.30	-4.33	Aw	Humid	17
Ivory Coast	Bandama	7.73	97000.00	5.14	-4.96	Aw	Humid	17
Ivory Coast	Comoe	72.12	78000.00	5.19	-3.72	Am	Humid	17
Ivory Coast	Sassandra	22.94	79000.00	4.96	-6.08	Aw	Humid	17
Ghana	Ankobra	181.45	6200.00	4.90	-2.27	Am	Humid	17
Ghana	Ayensu	55.15	1700.00	5.36	-0.59	Aw	Humid	17
Ghana	Pra	39.47	38000.00	5.02	-1.63	Aw	Humid	17
Benin	Mono	34.48	29000.00	6.28	1.84	Aw	Dry sub-humid	17
Benin	Oueme	30.00	50000.00	6.45	2.53	Aw	Humid	17
Nigeria	Cross	78.13	60000.00	4.76	8.34	Am	Humid	17
Nigeria	Ogun	14.63	47000.00	6.59	3.46	Aw	Humid	17
Cameroon	Nyong	2.23	28000.00	3.26	9.91	Af	Humid	17
South Africa	Keurbooms	113.64	1100.00	-34.02	23.40	Cf	Humid	17
South Africa	Kromme	125.00	900.00	-34.14	24.84	Cf	Humid	17
South Africa	Matigulu	137.50	1000.00	-29.11	31.62	Cf	Humid	17
South Africa	Tugela	189.66	29000.00	-29.23	31.50	Cf	Humid	17
South Africa	Umfolozi	150.00	10000.00	-28.66	32.26	Cf	Humid	17
South Africa	Umgeni	241.48	4400.00	-29.81	31.04	Cf	Humid	17
South Africa	Umhlantuzi	185.81	3700.00	-28.81	32.09	Cf	Humid	17
South Africa	Umkomazi	232.56	4300.00	-30.20	30.80	Cf	Humid	17

South Africa	Umtamvuna	179.17	1500.00	-31.08	30.20	Cf	Humid	17
South Africa	Umvoti	180.80	2800.00	-29.39	31.34	Cf	Humid	17
South Africa	Umzimvubu	85.94	16000.00	-31.62	29.55	Cf	Humid	17
Madagascar	Ikopa	312.50	30000.00	-15.71	46.28	Aw	Humid	17
Madagascar	Mangoky	105.93	59000.00	-21.44	43.46	BSh	Semi-arid	17
Madagascar	Tsiribihina	166.67	45000.00	-19.64	44.42	BSh	Dry sub-humid	17
Philippines	Pasig	62.50	600.00	14.60	120.96	Aw	Humid	17
Philippines	Tagum	201.61	3100.00	7.34	125.78	Af	Humid	17
Indonesia	Seraju	1520.27	3700.00	-7.69	109.11	Af	Humid	17
Indonesia	Serang	822.37	5700.00	-6.66	111.19	Am	Humid	17
Papua New Guinea	Jaba	35326.09	460.00	-6.40	155.20	Af	Humid	17
Australia	Adelaide	41.12	7600.00	-12.22	131.23	Aw	Humid	17
Australia	Baffle Creek	64.10	3900.00	-24.52	152.06	Cf	Humid	17
Australia	Black	113.64	1100.00	-19.18	146.65	Aw	Humid	17
Australia	Boyne	75.00	2500.00	-23.94	151.36	Cf	Dry sub-humid	17
Australia	Brisbane	12.95	14000.00	-27.40	153.15	Cf	Humid	17
Australia	Burnett	13.26	33000.00	-24.76	152.40	Cf	Humid	17
Australia	Burrum	56.82	3300.00	-25.18	152.61	Cf	Humid	17
Australia	Calliope	54.35	2300.00	-23.82	151.22	Cf	Dry sub-humid	17
Australia	Daintree	357.14	2100.00	-16.28	145.45	Am	Humid	17
Australia	Derwent	7.47	9200.00	-42.91	147.38	Cf	Humid	17
Australia	East Fitzroy	13.39	140000.00	-23.52	150.87	Cf	Dry sub-humid	17
Australia	Endeavour	213.07	2200.00	-15.46	145.25	Aw	Humid	17
Australia	Finniss	395.83	9000.00	-12.88	130.34	Aw	Humid	17
Australia	Flinders	52.84	110000.00	-17.60	140.60	Aw	Semi-arid	17
Australia	Haughton	69.44	3600.00	-19.41	147.13	Aw	Humid	17
Australia	Hawkesbury	42.61	22000.00	-33.56	151.31	Cf	Humid	17
Australia	Herbert	100.00	10000.00	-18.51	146.28	Am	Humid	17
Australia	Hunter	312.50	22000.00	-32.92	151.79	Cf	Humid	17
Australia	Jardine	143.94	3300.00	-10.92	142.21	Aw	Humid	17
Australia	Jeannie	164.47	3800.00	-14.66	144.92	Aw	Humid	17
Australia	Johnson	516.30	2300.00	-17.51	146.07	Af	Humid	17
Australia	Kolan	62.50	3000.00	-24.65	152.18	Cf	Humid	17
Australia	Lockhart	133.93	2800.00	-12.88	143.38	Aw	Humid	17
Australia	Macleay	5.68	11000.00	-30.87	153.02	Cf	Humid	17
Australia	Mary	58.59	9600.00	-25.43	152.93	Cf	Humid	17
Australia	Mitchell	3.73	72000.00	-15.20	141.59	Aw	Humid	17
Australia	Normanby	120.54	14000.00	-14.40	144.14	Aw	Humid	17
Australia	Pascoe	174.42	4300.00	-12.50	143.27	Am	Humid	17
Australia	Plane Creek	127.31	2700.00	-21.40	149.28	Cw	Humid	17
Australia	Prosperpine	25.00	2500.00	-20.48	148.72	Aw	Humid	17

Australia	Ross	104.17	1800.00	-19.27	146.84	Aw	Humid	17
Australia	Shoalhaven	72.66	8000.00	-34.88	150.74	Cf	Humid	17
Australia	Shoalwater Creek	50.68	3700.00	-23.23	150.80	Cf	Humid	17
Australia	South Alligator	2.60	12000.00	-12.19	132.39	Aw	Humid	17
Australia	Stewart	111.61	2800.00	-14.07	143.69	Aw	Humid	17
Australia	Styx	60.48	3100.00	-22.38	149.78	Cf	Humid	17
Australia	Tamar	7.29	12000.00	-41.08	146.78	Cf	Humid	17
Australia	Tully	441.18	1700.00	-18.03	146.05	Am	Humid	17
Australia	Water Park Creek	98.68	1900.00	-22.93	150.74	Cf	Humid	17
Australia	Wildman	39.06	4800.00	-12.30	132.07	Aw	Humid	17
Australia	Yarra	22.87	4100.00	-37.85	144.91	Cf	Dry sub-humid	17
NZ**	Hutt	188.95	430.00	-41.24	174.90	Cf	Humid	17
NZ	Kaituna	20.83	1200.00	-37.75	176.42	Cf	Humid	17
NZ	Manawatu	395.83	6000.00	-40.48	175.21	Cf	Humid	17
NZ	Mokau	275.00	1500.00	-38.71	174.62	Cf	Humid	17
NZ	Otaki	81.73	1300.00	-40.76	175.10	Cf	Humid	17
NZ	Pahaoa	474.14	580.00	-41.40	175.72	Cf	Humid	17
NZ	Patea	193.75	1000.00	-39.77	174.49	Cf	Humid	17
NZ	Piako	14.58	1500.00	-37.19	175.50	Cf	Humid	17
NZ	Porangahau	305.06	840.00	-40.25	176.70	Cf	Humid	17
NZ	Rangitaiki	21.74	2300.00	-37.91	176.88	Cf	Humid	17
NZ	Rangitikei	176.28	3900.00	-40.30	175.22	Cf	Humid	17
NZ	Tarawera	39.77	1100.00	-37.89	176.79	Cf	Humid	17
NZ	Turakina	193.30	970.00	-40.07	175.13	Cf	Humid	17
NZ	Uawa	5681.82	550.00	-38.38	178.31	Cf	Humid	17
NZ	Waihou	50.00	2000.00	-37.17	175.54	Cf	Humid	17
NZ	Waikato	16.52	14000.00	-37.36	174.70	Cf	Humid	17
NZ	Wairoa	793.92	3700.00	-39.06	177.42	Cf	Humid	17
NZ	Wairua	190.97	3600.00	-36.18	174.06	Cf	Humid	17
NZ	Waitara	551.14	1100.00	-38.99	174.23	Cf	Humid	17
NZ	Waitotara	250.00	1200.00	-39.85	174.68	Cf	Humid	17
NZ	Whangaehu	226.97	1900.00	-40.04	175.10	Cf	Humid	17
NZ	Whareama	1046.88	400.00	-41.02	176.11	Cf	Humid	17
NZ	Aparima	35.16	1600.00	-46.33	168.02	Cf	Humid	17
NZ	Arawata	4838.71	930.00	-43.99	168.67	Cf	Humid	17
NZ	Ashburton	113.97	1700.00	-44.05	171.81	Cf	Humid	17
NZ	Ashley	43.27	1300.00	-43.28	172.72	Cf	Humid	17
NZ	Awatere	82.03	1600.00	-41.61	174.17	Cf	Humid	17
NZ	Clarence	123.11	3300.00	-42.17	173.94	Cf	Humid	17
NZ	Clutha	11.61	21000.00	-46.34	169.82	Cf	Humid	17
NZ	Grey	336.54	3900.00	-42.44	171.19	Cf	Humid	17
NZ	Hurunui	447.64	740.00	-42.90	173.29	Cf	Humid	17

NZ	Kakanui	77.25	890.00	-45.19	170.90	Cf	Humid	17
NZ	Mataura	79.86	5400.00	-46.58	168.80	Cf	Humid	17
NZ	Mokihinui	241.67	750.00	-41.52	171.94	Cf	Humid	17
NZ	Motueka	128.68	1700.00	-41.08	173.02	Cf	Humid	17
NZ	Opihi	41.67	2400.00	-44.28	171.35	Cf	Humid	17
NZ	Orari	46.88	800.00	-44.24	171.41	Cf	Humid	17
NZ	Oreti	46.43	3500.00	-46.46	168.30	Cf	Humid	17
NZ	Taieri	35.09	5700.00	-45.99	170.15	Cf	Humid	17
NZ	Takaka	168.27	260.00	-40.82	172.80	Cf	Humid	17
NZ	Taramakau	1375.00	1000.00	-42.56	171.13	Cf	Humid	17
NZ	Waiho	7327.59	290.00	-43.29	170.05	Cf	Humid	17
NZ	Waipara	50.68	740.00	-43.15	172.80	Cf	Humid	17
NZ	Wairau	125.00	4200.00	-41.51	174.06	Cf	Humid	17
NZ	Waitaha	5468.75	320.00	-42.96	170.66	Cf	Humid	17
NZ	Waitaki	17.71	12000.00	-44.94	171.14	Cf	Humid	17
NZ	Whataroa	5084.75	590.00	-43.12	170.25	Cf	Humid	17
Iceland	Austari-Vestari	131.58	1900.00	65.75	-19.41	Ds	Humid	17
Iceland	Blanda	183.82	1700.00	65.66	-20.30	Ds	Humid	17
Iceland	Hvita	71.02	2200.00	64.58	-21.76	Df	Humid	17
Iceland	Olfusa	92.21	6100.00	63.88	-21.21	Df	Humid	17
Iceland	Skjalfandafljot	47.35	3300.00	65.98	-17.59	Ds	Humid	17
Norway	Drammenselva	66.18	17000.00	59.73	10.24	Df	Humid	17
Norway	Glomma	223.21	42000.00	59.18	10.95	Df	Humid	17
Norway	Mandalselva	0.37	1700.00	58.02	7.46	Cf	Humid	17
Norway	Skiensvassdraget	93.75	10000.00	59.02	9.78	Df	Humid	17
Sweden	Angerman	1.17	32000.00	62.79	17.94	Df	Humid	17
Sweden	Dalälven	0.65	29000.00	60.64	17.45	Df	Humid	17
Sweden	Göta alv	1.63	50000.00	57.68	11.85	Df	Humid	17
Sweden	Indalsälven	3.25	25000.00	62.51	17.45	Df	Humid	17
Sweden	Kalixälven	1.39	18000.00	65.81	23.21	Df	Humid	17
Sweden	Ljungan	0.48	13000.00	62.34	17.39	Df	Humid	17
Sweden	Lule	1.00	25000.00	65.56	22.19	Df	Humid	17
Sweden	Ore	6.25	3000.00	63.52	19.74	Df	Humid	17
Sweden	Pite	2.27	11000.00	65.23	21.53	Df	Humid	17
Sweden	Rane	0.30	4100.00	65.83	22.35	Df	Humid	17
Sweden	Skellefte	0.47	12000.00	64.68	21.20	Df	Humid	17
Sweden	Torne	1.56	40000.00	65.81	24.15	Df	Humid	17
Finland	Ahtavanjoki	3.13	2000.00	63.67	22.82	Df	Humid	17
Finland	Iijoki	0.63	14000.00	65.34	25.26	Df	Humid	17
Finland	Kalajoki	5.95	4200.00	64.29	23.91	Df	Humid	17
Finland	Karjaanjoki	0.63	2000.00	60.09	23.56	Df	Humid	17
Finland	Kemijoki	0.86	51000.00	65.77	24.44	Df	Humid	17

Finland	Kiiminkijoki	1.64	3800.00	65.20	25.28	Df	Humid	17
Finland	Kokemänjoki	1.39	27000.00	61.57	21.66	Df	Humid	17
Finland	Kyronjoki	6.38	4900.00	63.19	21.97	Df	Humid	17
Finland	Lapuanjoki	4.57	4100.00	63.57	22.48	Df	Humid	17
Finland	Oulujoki	0.60	25000.00	65.00	25.40	Df	Humid	17
Finland	Paimionjoki	51.14	1100.00	60.40	22.64	Df	Humid	17
Finland	Perhonjoki	2.31	2700.00	63.89	23.14	Df	Humid	17
Finland	Pyhajoki	27.03	3700.00	64.49	24.22	Df	Humid	17
Finland	Siikajoki	0.28	4400.00	64.86	24.69	Df	Humid	17
Finland	Simojoki	1.37	3200.00	65.62	25.05	Df	Humid	17
Estonia	Narva	6.25	56000.00	59.47	28.04	Df	Humid	17
Latvia	Daugava	3.34	88000.00	57.06	24.03	Df	Humid	17
Latvia	Venta	4.52	8300.00	57.40	21.54	Df	Humid	17
Lithuania	Nemanus	4.21	98000.00	55.34	21.25	Df	Humid	17
Poland	Parsenta	2.50	3000.00	54.19	15.55	Df	Humid	17
Poland	Rega	3.85	2600.00	54.16	15.39	Df	Humid	17
Poland	Slupa	5.80	1400.00	54.59	16.85	Df	Humid	17
Netherlands	Maas	12.15	36000.00	51.87	4.01	Cf	Humid	17
Netherlands	Rhine	0.20	220000.00	51.98	4.09	Cf	Humid	17
UK	Conon	3.91	960.00	57.60	-4.39	Cf	Humid	17
UK	Dee	10.42	1800.00	53.24	-3.10	Cf	Humid	17
UK	Deveron	6.58	950.00	57.66	-2.51	Cf	Humid	17
UK	Don	14.42	1300.00	57.18	-2.08	Cf	Humid	17
UK	Earn	48.08	780.00	56.35	-3.30	Cf	Humid	17
UK	Findhorn	32.05	780.00	57.66	-3.63	Cf	Humid	17
UK	Ness	6.94	1800.00	57.49	-4.24	Cf	Humid	17
UK	Ouse	7.72	8900.00	53.56	0.13	Cf	Humid	17
UK	Thames	1.67	15000.00	51.49	0.75	Cf	Humid	17
UK	Trent	5.26	9500.00	53.70	-0.70	Cf	Humid	17
Ireland	Barrow	1.98	12000.00	52.24	-6.95	Cf	Humid	17
Ireland	Blackwater	3.79	3300.00	51.94	-7.84	Cf	Humid	17
Ireland	Boyne	2.08	3300.00	53.72	-6.25	Cf	Humid	17
Ireland	Erne	2.45	5100.00	54.51	-8.25	Cf	Humid	17
Ireland	Lee	5.21	1200.00	51.80	-8.27	Cf	Humid	17
Ireland	Liffey	1.79	1400.00	53.34	-6.19	Cf	Humid	17
Ireland	Moy	2.98	2100.00	54.18	-9.14	Cf	Humid	17
Ireland	Shannon	17.39	23000.00	52.68	-8.75	Cf	Humid	17
Ireland	Slaney	2.08	1800.00	52.34	-6.46	Cf	Humid	17
France	Argens	7.21	2600.00	43.41	6.74	Cs	Humid	17
France	Aude	7.42	5900.00	43.21	3.24	Cs	Dry sub-humid	17
France	Charente	13.74	9100.00	45.95	-1.08	Cf	Humid	17
France	Herault	19.40	2900.00	43.28	3.44	Cs	Dry sub-humid	17

France	Orb	17.36	1800.00	43.25	3.30	Cs	Dry sub-humid	17
France	Tet	195.31	1600.00	42.72	3.04	Cs	Dry sub-humid	17
France	Var	2232.14	2800.00	43.66	7.20	Cs	Humid	17
France	Vilaine	11.36	11000.00	47.50	-2.45	Cf	Humid	17
France	Golo	1.39	900.00	42.52	9.53	Cs	Humid	17
Spain	Adra	125.00	750.00	36.74	-2.98	BSk	Semi-arid	17
Spain	Andarax	51.14	2200.00	36.81	-2.43	BWk	Semi-arid	17
Spain	Besaya	62.50	1000.00	43.44	-4.03	Cf	Humid	17
Spain	Bidasoa	132.04	710.00	43.38	-1.79	Cf	Humid	17
Spain	Deba	37.50	500.00	43.30	-2.36	Cf	Humid	17
Spain	Deva	67.71	1200.00	43.39	-4.51	Cf	Humid	17
Spain	Guadalfeo	38.46	1300.00	36.72	-3.58	Cs	Semi-arid	17
Spain	Guadalhorce	17.58	3200.00	36.67	-4.45	Cs	Semi-arid	17
Spain	Guadiaro	16.67	1500.00	36.28	-5.28	Cs	Humid	17
Spain	Jucar	22.73	22000.00	39.15	-0.24	Cs	Semi-arid	17
Spain	Llobregat	8.41	5200.00	41.30	2.14	Cs	Humid	17
Spain	Narcea	48.47	4900.00	43.56	-6.08	Cf	Humid	17
Spain	Navia	31.25	2600.00	43.56	-6.73	Cf	Humid	17
Spain	Nervion	26.79	1400.00	43.33	-3.02	Cf	Humid	17
Spain	Oria	50.87	860.00	43.29	-2.13	Cf	Humid	17
Spain	Segura	36.18	19000.00	38.11	-0.64	BSk	Semi-arid	17
Spain	Sella	14.42	1300.00	43.47	-5.07	Cf	Humid	17
Portugal	Douro	11.48	98000.00	41.15	-8.67	Cs	Humid	17
Portugal	Guadiana	0.61	72000.00	37.17	-7.40	Cs	Semi-arid	17
Portugal	Tagus	3.13	80000.00	38.67	-9.28	Cs	Humid	17
Italy	Agri	156.25	280.00	40.22	16.74	Cs	Dry sub-humid	17
Italy	Crati	312.50	2400.00	39.72	16.53	Cs	Humid	17
Italy	Fortore	852.27	1100.00	41.92	15.29	Cf	Dry sub-humid	17
Italy	Magra	260.42	1200.00	44.05	9.99	Cs	Humid	17
Italy	Marecchia	1666.67	600.00	44.08	12.56	Cf	Humid	17
Italy	Ofanto	208.33	2700.00	41.36	16.20	Cf	Semi-arid	17
Italy	Ombrone	371.09	3200.00	42.66	11.01	Cs	Dry sub-humid	17
Italy	Potenza	273.44	800.00	43.42	13.67	Cs	Humid	17
Italy	Sinni	1420.45	1100.00	40.15	16.69	Cs	Dry sub-humid	17
Italy	Tavo	100.00	250.00	42.53	14.15	Cf	Humid	17
Italy	Trigno	218.75	1200.00	42.06	14.80	Cf	Humid	17
Italy	Volturno	477.27	5500.00	41.02	13.93	Cs	Humid	17
Italy	Gela	338.54	240.00	37.06	14.26	Cs	Semi-arid	17
Italy	Gornalunga	81.52	230.00	37.39	15.09	Cs	Semi-arid	17
Albania	Mat	706.52	2300.00	41.64	19.57	Cs	Humid	17
Albania	Vijose	762.87	6800.00	40.64	19.32	Cs	Humid	17
Croatia	Neretva	673.08	13000.00	43.02	17.45	Cf	Humid	17

Greece	Acheloos	381.94	5400.00	38.34	21.11	Cs	Humid	17
Greece	Alfios	506.76	3700.00	37.61	21.45	Cs	Humid	17
Greece	Aliakmon	289.47	9500.00	40.47	22.65	BSk	Semi-arid	17
Greece	Arachthos	2401.32	1900.00	39.02	21.05	Cs	Humid	17
Greece	Axiós	122.40	24000.00	40.50	22.72	BSk	Semi-arid	17
Greece	Évros	151.79	35000.00	40.74	26.03	Cs	Dry sub-humid	17
Greece	Gallikos	2.78	900.00	40.63	22.84	Cf	Semi-arid	17
Greece	Kalamas	659.72	1800.00	39.53	20.14	Cs	Humid	17
Greece	Louros	625.00	800.00	39.05	20.78	Cs	Humid	17
Greece	Néstos	100.81	6200.00	40.85	24.80	Cs	Dry sub-humid	17
Greece	Pinios	250.00	11000.00	39.94	22.72	BSk	Semi-arid	17
Greece	Sperchios	486.11	1800.00	38.87	22.56	Cs	Dry sub-humid	17
Greece	Strimonas	147.06	17000.00	40.79	23.85	Cs	Semi-arid	17
Russia	Anabar	2.50	100000.00	73.54	113.47	Df	Humid	17
Russia	Anadyr	11.25	200000.00	64.50	178.34	Ds	Humid	17
Russia	Gizhiga	17.19	12000.00	61.94	160.38	Df	Humid	17
Russia	Kamchatka	34.60	56000.00	56.21	162.49	Df	Humid	17
Russia	Kem	1.56	28000.00	64.96	34.68	Df	Humid	17
Russia	Khatanga	2.95	360000.00	73.24	106.74	Df	Humid	17
Russia	Mezen	7.21	78000.00	66.19	43.96	Df	Humid	17
Russia	Mzymta	187.50	1000.00	43.42	39.92	Cf	Humid	17
Russia	Nadym	6.84	64000.00	66.23	72.10	Df	Humid	17
Russia	Neva	4.22	74000.00	59.96	30.22	Df	Humid	17
Russia	Niva	33.65	13000.00	67.13	32.42	Df	Humid	17
Russia	Olenyok	3.13	220000.00	73.02	119.75	Df	Dry sub-humid	17
Russia	Onega	2.74	57000.00	63.93	37.99	Df	Humid	17
Russia	Penzhina	8.56	73000.00	62.47	165.11	Df	Humid	17
Russia	Pyr	3.98	110000.00	67.56	77.78	Df	Humid	17
Russia	Tauyo	12.00	25000.00	59.63	149.10	Dw	Humid	17
Russia	Taz	2.50	150000.00	67.56	78.58	Df	Humid	17
Russia	Tugur	7.81	12000.00	53.76	136.78	Df	Humid	17
Russia	Uda	9.53	61000.00	54.72	135.29	Df	Humid	17
India	Achenkovil	24.17	1500.00	9.31	76.38	Am	Humid	17
India	Bharathpuzha	21.17	6200.00	10.79	75.91	Am	Humid	17
India	Brahmani	84.13	52000.00	20.71	87.00	Aw	Humid	17
India	Cauweri	2.84	88000.00	11.36	79.83	Aw	Humid	17
India	Chalakudi	25.74	1700.00	10.18	76.16	Am	Humid	17
India	Chaliyar	105.60	2900.00	11.16	75.80	Am	Humid	17
India	Gundlakamma	7.35	8500.00	15.54	80.23	Aw	Semi-arid	17
India	Kadalundi	340.91	1100.00	11.12	75.83	Am	Humid	17
India	Kalinadi	84.13	5200.00	14.84	74.12	Am	Humid	17
India	Kallada	33.09	1700.00	8.93	76.54	Am	Humid	17

India	Mahi	35.71	35000.00	22.21	72.77	BSh	Semi-arid	17
India	Muvatupuzha	15.42	1500.00	9.83	76.38	Am	Humid	17
India	Nagavali	66.49	9400.00	18.21	83.94	Aw	Humid	17
India	Netravati	208.33	4200.00	12.84	74.83	Am	Humid	17
India	Pamba	71.02	2200.00	9.52	76.38	Am	Humid	17
India	Penner	20.45	55000.00	14.58	80.19	Aw	Dry sub-humid	17
India	Periyar	28.94	5400.00	10.18	76.16	Am	Humid	17
India	Ponnaiyar	2.73	16000.00	11.77	79.79	Aw	Humid	17
India	Rushikulya	97.40	7700.00	19.38	85.08	Aw	Humid	17
India	Sabarmati	5.95	21000.00	22.35	72.41	BSh	Semi-arid	17
India	Shetrunji	68.18	5500.00	21.30	72.11	BSh	Semi-arid	17
India	Subarnarekha	98.68	19000.00	21.56	87.38	Aw	Humid	17
India	Tamraparni	104.17	6000.00	8.65	78.13	Aw	Semi-arid	17
India	Tapti	192.31	65000.00	21.10	72.70	Aw	Humid	17
India	Valapattanam	85.53	1900.00	11.94	75.30	Am	Humid	17
India	Vamsadhara	386.36	11000.00	18.34	84.13	Aw	Humid	17
Myanmar	Salween	416.67	270000.00	16.15	97.56	Am	Humid	17
Malaysia	Kelantan	130.21	12000.00	6.22	102.24	Am	Humid	17
Malaysia	Langat	150.00	2500.00	2.80	101.41	Af	Humid	17
Malaysia	Muda	7.60	7400.00	5.58	100.34	Af	Humid	17
Malaysia	Muar	13.67	3200.00	2.05	102.55	Af	Humid	17
Malaysia	Pahang	98.68	19000.00	3.53	103.47	Af	Humid	17
Malaysia	Perak	43.27	13000.00	4.00	100.75	Af	Humid	17
Malaysia	Selangor	17.58	3200.00	3.34	101.23	Af	Humid	17
Malaysia	Terengganu	109.85	3300.00	5.34	103.15	Af	Humid	17
Malaysia	Rajang	367.65	51000.00	2.42	111.30	Af	Humid	17
Thailand	Khlong Phum Duang	25.00	3000.00	13.49	100.81	Aw	Humid	17
Thailand	Mae Klong	163.31	31000.00	13.36	100.01	Aw	Humid	17
Thailand	Pattani	54.69	4000.00	6.90	101.25	Am	Humid	17
Vietnam	Ba	44.64	14000.00	13.09	109.33	Aw	Humid	17
Vietnam	Ca	92.59	27000.00	18.77	105.77	Am	Humid	17
Vietnam	Ma	66.96	28000.00	19.79	105.93	Cw	Humid	17
Vietnam	Sai Gon	42.61	44000.00	10.41	106.80	Aw	Humid	17
Vietnam	Thai Binh	41.67	15000.00	20.67	106.71	Cw	Humid	17
Vietnam	Thu Bon	125.00	10000.00	15.87	108.39	Aw	Humid	17
Brunei	Tutong	67.93	2300.00	4.77	114.60	Af	Humid	17
China	Guanhe	68.36	6400.00	34.47	119.79	Cw	Humid	17
China	Hanjiang	150.00	30000.00	23.45	116.87	Cf	Humid	17
China	Jianjiang	98.68	9500.00	21.24	110.65	Cw	Humid	17
China	Jinjiang	136.36	11000.00	24.85	118.65	Cf	Humid	17
China	Jiulongjiang	129.17	15000.00	24.42	117.93	Cf	Humid	17
China	Luanhe	266.20	54000.00	39.43	119.30	Dw	Dry sub-humid	17

China	Majiahe	5.03	8700.00	38.20	117.97	Dw	Dry sub-humid	17
China	Minjiang	24.59	61000.00	26.07	119.68	Cf	Humid	17
China	Moyangjiang	81.97	6100.00	21.78	112.04	Cw	Humid	17
China	Nanliujiang	104.17	6600.00	21.60	109.08	Cw	Humid	17
China	Oujiang	93.75	18000.00	27.95	120.92	Cf	Humid	17
China	Qiantangjiang	65.48	42000.00	30.47	121.88	Cf	Humid	17
China	Tuhaihe	16.45	19000.00	38.16	118.08	Dw	Dry sub-humid	17
China	Yalujiang	46.88	64000.00	39.91	124.30	Dw	Humid	17
China	Changhuajiang	9.80	5100.00	19.30	108.66	Aw	Humid	17
China	Nandujiang	104.17	6600.00	20.08	110.38	Cw	Humid	17
Japan	Agano	73.05	7700.00	37.96	139.13	Cf	Humid	17
Japan	Goumo	8.49	3900.00	35.02	132.23	Cf	Humid	17
Japan	Iwaki	140.00	2500.00	41.01	140.36	Df	Humid	17
Japan	Jintsu	5.56	2700.00	36.76	137.22	Cf	Humid	17
Japan	Kiso	150.00	5000.00	35.03	136.75	Cf	Humid	17
Japan	Kitakami	68.75	10000.00	38.57	141.46	Df	Humid	17
Japan	Kumano	338.54	2400.00	33.73	136.01	Cf	Humid	17
Japan	Kurobe	220.59	680.00	36.92	137.43	Cf	Humid	17
Japan	Kuzuryo	8.41	2900.00	36.22	136.13	Cf	Humid	17
Japan	Mogami	285.71	7000.00	38.92	139.81	Cf	Humid	17
Japan	Omono	9.44	4700.00	39.69	140.06	Df	Humid	17
Japan	Ooi	913.46	1300.00	34.77	138.29	Cf	Humid	17
Japan	Shinano	83.33	12000.00	37.67	138.77	Cf	Humid	17
Japan	Shou	572.92	1200.00	36.79	137.08	Cf	Humid	17
Japan	Tenryu	612.75	5100.00	34.65	137.80	Cf	Humid	17
Japan	Yura	3.95	1900.00	35.52	135.29	Cf	Humid	17
Japan	Chikugo	387.93	2900.00	33.14	130.34	Cf	Humid	17
South Korea	Mankyong	250.00	1600.00	35.79	126.76	Df	Humid	17
South Korea	Sapgyo	47.79	1700.00	36.88	126.84	Dw	Humid	17
South Korea	Seumjin	255.10	4900.00	34.94	127.77	Cw	Humid	17
South Korea	Yeongsan	156.25	2800.00	34.78	126.38	Cf	Humid	17
US	Hudson	31.25	20000.00	40.61	-74.05	Df	Humid	18
US	Brazos	90.91	110000.00	28.94	-95.30	Cf	Humid	18
US	Eel	1093.75	8000.00	40.65	-124.31	Cs	Humid	18
US	Copper	729.17	60000.00	60.31	-145.00	Df	Humid	18
US	Susitna	312.50	50000.00	61.28	-150.58	Df	Humid	18
Canada	Fraser	56.82	220000.00	49.12	-123.19	Cs	Humid	18
Peru	Chira	1250.00	20000.00	-4.90	-81.15	BWh	Hyper-arid	18
Colombia	Magdalena	572.92	240000.00	11.05	-74.83	BSh	Dry sub-humid	18
Argentina	Negro	81.25	100000.00	-41.03	-62.79	BSk	Semi-arid	18
Albania	Drini	937.50	10000.00	41.85	19.37	Cs	Humid	18
Russia	Severnay Dvina	8.04	350000.00	64.70	40.24	Df	Humid	18

China	Liaohe	150.74	170000.00	40.86	121.81	Dw	Humid	18
China	Daling	1125.00	20000.00	40.86	121.56	Dw	Humid	18
China	Haihe	1012.50	50000.00	38.96	117.80	Dw	Dry sub-humid	18
China	Huaihe	33.65	260000.00	33.20	118.62	Cw	Humid	18
China	Pearl (Zhu Jiang)	98.01	440000.00	22.66	113.72	Cw	Humid	18
Myanmar	Irrawaddy	385.17	430000.00	15.79	95.07	Am	Humid	18
India	Mahanadi	9.62	130000.00	20.29	86.71	Aw	Humid	18
India	Damodar	875.00	20000.00	22.22	88.04	Aw	Humid	18
India	Godavari	193.55	310000.00	16.72	82.33	Aw	Humid	18
Mozambique	Limpopo	50.30	410000.00	-25.21	33.52	Aw	Dry sub-humid	18
Tanzania	Rufiji	59.03	180000.00	-7.76	39.32	Aw	Humid	18
Kenya	Tana	625.00	32000.00	-2.53	40.52	Aw	Humid	18
NZ	Haast	8125.00	1000.00	-43.84	169.03	Cf	Humid	18
PNG**	Fly	307.38	61000.00	-8.48	143.49	Af	Humid	18
PNG	Purari	1612.90	31000.00	-7.83	145.03	Af	Humid	18
PNG	Aure	6875.00	4500.00	-7.07	145.31	Af	Humid	19
NZ	Cleddau	8125.00	150.00	-44.68	167.92	Cf	Humid	19
NZ	Hokitika	10625.00	350.00	-42.72	170.95	Cf	Humid	19
Indonesia	Cijolang	1187.50	380.00	-6.91	107.94	Am	Humid	19
Philippines	Angat	5000.00	570.00	14.77	120.75	Am	Humid	19
Indonesia	Cimuntur	1875.00	580.00	-6.32	108.14	Aw	Humid	19
Indonesia	Cilutung	7500.00	600.00	-6.81	108.16	Am	Humid	19
Philippines	Agno	2718.75	1200.00	16.04	120.20	Am	Humid	19
Indonesia	Citanduy	2312.50	2500.00	-7.67	108.80	Af	Humid	19
NZ	Waiau	812.50	2000.00	-42.78	173.37	Cf	Humid	19
NZ	Rakaia	1000.00	2600.00	-43.90	172.21	Cf	Humid	19
NZ	Waimakariri	1062.50	3200.00	-43.39	172.71	Cf	Humid	19
Indonesia	Cimanuk	4875.00	3200.00	-6.75	108.15	Am	Humid	19
Indonesia	Kali Brantas	600.00	8500.00	-7.56	112.87	Aw	Humid	19
Indonesia	Porong	1062.50	12000.00	-7.56	112.87	Aw	Humid	19
Indonesia	Solo	750.00	16000.00	-6.85	112.58	Aw	Humid	19
India	Narmada	875.00	89000.00	21.62	72.58	BSh	Semi-arid	19
Vietnam	Hungho	687.50	120000.00	20.27	106.57	Cw	Humid	19
Thailand	Chao Phraya	42.50	160000.00	13.53	100.60	Aw	Humid	19
India	Krishna	162.50	250000.00	15.73	80.93	Aw	Humid	19
Italy	Aso	375.00	280.00	43.10	13.84	Cs	Humid	19
Algeria	Djer	1062.50	390.00	36.59	2.74	Cs	Dry sub-humid	19
Algeria	El Harrach	1000.00	390.00	36.74	3.13	Cs	Dry sub-humid	19
Italy	Tenna	562.50	490.00	43.29	13.73	Cs	Humid	19
Italy	Lamone	1500.00	520.00	44.53	12.28	Cf	Humid	19
Italy	Savio	1187.50	600.00	44.32	12.34	Cf	Humid	19
US	Carmel	396.88	630.00	36.54	-121.93	Cs	Dry sub-humid	19

Italy	Foglia	750.00	700.00	43.92	12.90	Cf	Humid	19
US	Redwood Creek	1062.50	730.00	41.29	-124.09	Cs	Humid	19
Japan	Hii	612.50	920.00	33.60	130.36	Cf	Humid	19
US	Mad	1250.00	1200.00	40.97	-124.12	Cs	Humid	19
Italy	Tronto	562.50	1200.00	42.89	13.92	Cf	Humid	19
Italy	Esino	500.00	1200.00	43.64	13.37	Cs	Humid	19
Italy	Biferno	1062.50	1300.00	41.98	15.03	Cf	Humid	19
Italy	Metauro	543.75	1400.00	43.83	13.05	Cs	Humid	19
Turkey	Tarsus	58.13	1400.00	36.79	34.83	Cs	Dry sub-humid	19
Italy	Simeto	1250.00	1800.00	37.40	15.09	Cs	Semi-arid	19
Albania	Shkumbini	2250.00	1900.00	41.04	19.44	Cs	Humid	19
Japan	Nagara	131.25	2000.00	35.03	136.73	Cf	Humid	19
Albania	Osumi	1750.00	2000.00	40.81	19.86	Cs	Humid	19
Morocco	Bou Sellem	62.50	2300.00	34.04	-6.83	Cs	Semi-arid	19
Venezuela	Maticora	1375.00	2500.00	11.01	-71.17	BSh	Semi-arid	19
Italy	Bradano	625.00	2700.00	40.39	16.86	BSk	Semi-arid	19
Italy	Pescara	184.38	3100.00	42.47	14.23	Cf	Humid	19
Italy	Reno	500.00	3400.00	44.59	12.28	Cf	Humid	19
Canada	Squamish	362.50	3600.00	49.69	-123.18	Df	Humid	19
Algeria	Isser	1062.50	3600.00	36.84	3.67	Cs	Humid	19
US	Santa Clara	875.00	4200.00	34.23	-119.26	Cs	Semi-arid	19
Madagascar	Morondava	1000.00	4200.00	-20.30	44.26	BSh	Semi-arid	19
Australia	Ord	393.75	46000.00	-15.04	128.15	BSh	Semi-arid	19
Albania	Semani	2625.00	5200.00	40.82	19.37	Cs	Humid	19
Canada	Homathko	468.75	5700.00	50.93	-124.86	Ds	Humid	19
Canada	Kliniklim	481.25	6500.00	51.09	-125.63	Ds	Humid	19
Venezuela	Tuy	1125.00	6600.00	10.24	-66.65	Aw	Humid	19
Italy	Arno	168.75	8100.00	43.68	10.28	Cs	Humid	19
South Korea	Kuem	350.00	10000.00	36.00	126.67	Df	Humid	19
Turkey	Goksu	156.25	10000.00	36.30	34.05	Cs	Dry sub-humid	19
Japan	Ishikari	93.75	13000.00	43.27	141.37	Df	Humid	19
Georgia	Rioni	393.75	13000.00	42.20	41.64	Cf	Humid	19
Turkey	Filyos	200.00	13000.00	41.58	32.05	Cf	Humid	19
Italy	Tiber	218.75	16000.00	41.74	12.23	Cs	Humid	19
Morocco	Sous	162.50	16000.00	30.36	-9.60	BSh	Arid	19
US	Stikine	687.50	18000.00	56.63	-132.38	Df	Humid	19
Turkey	Seyhan	168.75	19000.00	36.73	34.91	Cs	Dry sub-humid	19
Turkey	Ceyhan	171.88	20000.00	36.57	35.56	Cs	Humid	19
Turkey	Coruh	250.00	20000.00	41.60	41.57	Cf	Humid	19
Algeria	Cheliff	87.50	22000.00	36.04	0.13	Cs	Semi-arid	19
US	Klamath	100.00	22000.00	41.54	-124.07	Cs	Humid	19
Argentina	Colorado	187.50	23000.00	-39.69	-62.09	Cf	Semi-arid	19

South Korea	Nakdong	250.00	24000.00	35.09	128.93	Cw	Humid	19
South Korea	Han	250.00	26000.00	37.76	126.19	Dw	Humid	19
US	San Juan	100.00	31000.00	37.18	-110.90	BWk	Arid	19
US	Russian	425.00	36000.00	38.45	-123.13	Cs	Humid	19
Turkey	Yesil-Irmak	350.00	34000.00	41.38	36.66	Cf	Humid	19
Morocco	Sebou	581.25	40000.00	34.26	-6.67	Cs	Semi-arid	19
Canada	Skeena	162.50	42000.00	54.13	-130.09	Df	Humid	19
Turkey	Sakarya	125.00	46000.00	41.13	30.65	Cs	Humid	19
Russia	Kuban	100.00	48000.00	45.35	37.40	Cf	Humid	19
Morocco	Moulouya	81.25	51000.00	35.12	-2.34	Cs	Semi-arid	19
Turkey	Kizil-Irmak	193.75	74000.00	41.73	35.96	Cf	Humid	19
Spain	Ebro	131.25	85000.00	40.72	0.87	Cs	Dry sub-humid	19
Azerbaijan	Kura	125.00	180000.00	39.33	49.36	BSk	Semi-arid	19
France	Ardour	11.25	16000.00	46.11	1.43	Cf	Humid	19
Canada	Babbage	43.75	50000.00	69.21	-138.39	Ds	Dry sub-humid	19
France	Garonne	27.50	55000.00	45.59	-1.06	Cf	Humid	19
US	Kuskokwim	62.50	80000.00	60.19	-162.43	Df	Humid	19
Italy	Arzilla	812.50	100.00	43.85	13.01	Cf	Humid	19
Italy	Tesino	687.50	110.00	42.98	13.88	Cs	Humid	19
US	Gurabo	1062.50	160.00	18.27	-66.01	Af	Humid	19
Italy	Ete Vivo	1000.00	180.00	43.16	13.81	Cs	Humid	19
US	Grande	1125.00	230.00	18.44	-65.88	Af	Humid	19
NZ	Esk	687.50	250.00	-39.40	176.89	Cf	Humid	19
Italy	Misa	812.50	380.00	43.72	13.22	Cs	Humid	19
NZ	Waioeka	368.75	640.00	-37.99	177.27	Cf	Humid	19
NZ	Ruamahanga	225.00	640.00	-41.37	175.14	Cf	Humid	19
Italy	Musone	1062.50	640.00	43.47	13.64	Cs	Humid	19
Philippines	Pampanga	812.50	830.00	14.78	120.66	Aw	Humid	19
NZ	Tutaekuri	262.50	790.00	-39.57	176.91	Cf	Humid	19
UK	Usk	28.75	910.00	51.55	-2.98	Cf	Humid	19
Venezuela	Neveri	187.50	980.00	10.17	-64.71	BSh	Semi-arid	19
NZ	Karamea	200.00	1200.00	-41.25	172.10	Cf	Humid	19
Italy	Chienti	625.00	1300.00	43.29	13.74	Cs	Humid	19
NZ	Motu	1250.00	1400.00	-37.85	177.59	Cf	Humid	19
NZ	Waiapu	12500.00	1400.00	-37.78	178.48	Cf	Humid	19
NZ	Waipaoa	3625.00	1600.00	-38.71	177.94	Cf	Humid	19
NZ	Whakatane	1500.00	1600.00	-37.94	177.01	Cf	Humid	19
NZ	Ngaruroro	293.75	1900.00	-39.57	176.93	Cf	Humid	19
US	Skykomish	68.75	2200.00	47.82	-122.03	Cs	Humid	19
NZ	Tukituki	275.00	2400.00	-39.60	176.94	Cf	Humid	19
NZ	Mohaka	231.25	2400.00	-39.13	177.19	Cf	Humid	19
NZ	Buller	168.75	6300.00	-41.73	171.59	Cf	Humid	19

NZ	Whanganui	206.25	6600.00	-43.04	170.42	Cf	Humid	19
Japan	Yodo	168.75	7100.00	34.68	135.41	Cf	Humid	19
US	Sabine	36.25	13000.00	29.99	-93.79	Cf	Humid	19
Canada	Romaine	6.88	14000.00	50.30	-63.80	Df	Humid	19
Japan	Tone	156.25	12000.00	35.74	140.85	Cf	Humid	19
Canada	Saguanay	3.13	78000.00	48.13	-69.71	Df	Humid	19
US	Skagit	25.63	80000.00	48.31	-122.39	Cs	Humid	19
Sweden	Muonio Alv	9.38	24000.00	67.18	23.56	Df	Humid	19
US	Savannah	68.75	25000.00	32.03	-80.88	Cf	Humid	19
Ukraine	Dnester	25.00	62000.00	46.32	30.32	Df	Dry sub-humid	19
Poland	Oder	0.75	110000.00	53.67	14.53	Df	Humid	19
Australia	Burdekin	14.38	130000.00	-19.69	147.58	Aw	Dry sub-humid	19
Germany	Elbe	3.75	130000.00	53.91	8.86	Cf	Humid	19
Poland	Vistula	8.13	200000.00	54.35	18.95	Df	Humid	19
Uruguay	Uruguay	28.13	240000.00	-34.02	-58.33	Cf	Humid	19
Russia	Pechora	15.63	250000.00	68.27	54.06	Df	Humid	19
Russia	Indigirka	24.38	360000.00	66.44	143.15	Df	Dry sub-humid	19
Ghana	Volta	30.00	400000.00	5.78	0.67	Aw	Dry sub-humid	19
Russia	Don	11.25	420000.00	47.09	39.28	Df	Dry sub-humid	19
Russia	Volga	9.38	1400000.00	45.94	48.80	BSk	Arid	19
Taiwan	Erhjen	22500.00	350.00	22.91	120.18	Cf	Humid	19
UK	Ystwyth	102.50	170.00	52.41	-4.09	Cf	Humid	19
NZ	Rangitaiki	51.88	230.00	-37.91	176.88	Cf	Humid	19
UK	Avon	100.63	260.00	51.98	-2.18	Cf	Humid	19
UK	Esk	36.25	310.00	54.49	-0.61	Cf	Humid	19
Venezuela	Manzanares	156.25	830.00	10.47	-64.19	Aw	Humid	19
UK	Clyde	37.50	1900.00	55.93	-4.52	Cf	Humid	19
UK	Tyne	38.13	2200.00	55.01	-1.42	Cf	Humid	19
Ivory Coast	San Pedro	13.75	3300.00	4.76	-6.60	Aw	Humid	19
US	Chehalis	21.25	3400.00	46.96	-123.84	Cs	Humid	19
UK	Wye	31.88	4000.00	51.62	-2.66	Cf	Humid	19
Canada	St. Jean	30.00	5600.00	50.28	-64.34	Df	Humid	19
UK	Severn	40.63	6800.00	51.55	-2.73	Cf	Humid	19
US	Cape Fear	13.13	13000.00	33.89	-78.01	Cf	Humid	19
US	Rappahannock	35.00	1600.00	37.60	-76.36	Cf	Humid	19
Ghana	Tano	13.75	16000.00	5.10	-2.94	Am	Humid	19
US	Delaware	24.38	17000.00	38.87	-75.03	Cf	Humid	19
US	Pearl	28.75	17000.00	30.19	-89.53	Cf	Humid	19
Belgium	Scheldt	28.13	22000.00	51.39	4.21	Cf	Humid	19
Canada	Abitibi	3.75	24000.00	51.06	-80.91	Df	Humid	19
US	Potomac	17.50	25000.00	38.02	-76.37	Cf	Humid	19
US	Roanoke	50.00	25000.00	35.94	-76.69	Cf	Humid	19

US	Santee	23.13	27000.00	33.14	-79.26	Cf	Humid	19
US	Altamaha	44.38	35000.00	31.32	-81.29	Cf	Humid	19
Canada	Attawapiskat	3.75	36000.00	52.97	-82.26	Df	Humid	19
Germany	Weser	5.00	38000.00	53.53	8.56	Cf	Humid	19
Cameroon	Mbam	53.13	42000.00	4.40	11.27	Aw	Humid	19
US	Tombigbee	28.13	50000.00	31.14	-87.94	Cf	Humid	19
Poland	Y. Bug	9.38	34000.00	52.51	21.08	Df	Humid	19
US	Alabama	25.00	57000.00	31.14	-87.94	Cf	Humid	19
US	Susquehanna	18.13	62000.00	39.55	-76.08	Cf	Humid	19
Canada	Moose	4.38	60000.00	51.35	-80.40	Df	Humid	19
France	Seine	11.25	65000.00	49.44	0.17	Cf	Humid	19
Canada	Nottaway	9.38	66000.00	51.43	-78.93	Df	Humid	19
Cameroon	Sanaga	12.50	130000.00	3.57	9.65	Am	Humid	19
Senegal	Senegal	5.00	270000.00	15.98	-16.50	BWh	Arid	19
UK	Creedy	33.13	260.00	50.75	-3.55	Cf	Humid	19
UK	Welland	8.75	530.00	52.93	0.08	Cf	Humid	19
UK	Exe	15.00	600.00	50.61	-3.42	Cf	Humid	19
UK	Bristol Avon	16.88	670.00	51.50	-2.72	Cf	Humid	19
UK	Swale	15.00	1400.00	54.09	-1.34	Cf	Humid	19
UK	Nene	6.88	1500.00	52.83	0.22	Cf	Humid	19
UK	Ely Ouse	5.00	3600.00	52.81	0.36	Cf	Humid	19
US	Neuse	7.50	6900.00	35.06	-76.54	Cf	Humid	19
US	Ogeechee	5.63	6700.00	31.84	-81.05	Cf	Humid	19
US	Pamlico	11.88	11000.00	35.33	-76.45	Cf	Humid	19
US	Peedee	10.63	23000.00	33.36	-79.27	Cf	Humid	19
Finland	Kymijoki	0.25	37000.00	60.48	26.89	Df	Humid	19
US	Apalachicola	2.50	44000.00	29.72	-84.98	Cf	Humid	19
US	Tar	1.25	57000.00	35.55	-77.08	Cf	Humid	19
US	Lucky Hills (102), Walnut Gulch	144.38	0.01	31.74	-110.05	BSk	Semi-arid	20
US	Lucky Hills (105), Walnut Gulch	46.88	0.00	31.74	-110.05	BSk	Semi-arid	20
US	Lucky Hills (106), Walnut Gulch	50.00	0.00	31.74	-110.05	BSk	Semi-arid	20
US	Lucky Hills (121), Walnut Gulch	91.25	0.05	31.73	-110.04	BSk	Semi-arid	20
Panama	Upper Rió Chagres (CChC)	107.00	409.00	9.27	-79.51	Am	Humid	21
China	Danghewan, Qilian Shan	20.00	13762.00	39.65	94.88	BWk	Arid	22
China	Changmabao, Qilian Shan	120.00	10910.00	39.65	96.85	BWk	Semi-arid	22
China	Binggou, Qilian Shan	50.00	6896.00	39.60	98.00	BWk	Arid	22
China	Xindi, Qilian Shan	200.00	1582.00	39.65	98.82	BWk	Arid	22
China	Liyuanbao, Qilian Shan	90.00	2231.00	38.97	100.00	BWk	Arid	22

China	Zhamashike, Qilian Shan	120.00	4585.00	38.22	99.98	BSk	Semi-arid	22
China	Qilian, Qilian Shan	90.00	2413.00	38.20	100.22	BSk	Semi-arid	22
China	Yingluoxia, Qilian Shan	110.00	10003.00	38.23	100.18	BSk	Semi-arid	22
China	Jiutiaoling, Qilian Shan	90.00	1082.00	37.87	102.05	BSk	Semi-arid	22
China	Zamusi, Qilian Shan	110.00	842.00	37.70	102.57	BSk	Semi-arid	22
China	Shajintai, Qilian Shan	120.00	455.00	37.47	102.60	Dw	Semi-arid	22
US	Lucky Hills (103), Walnut Gulch	377.00	0.04	31.74	-110.05	BSk	Semi-arid	23
US	Lucky Hills (104), Walnut Gulch	91.00	0.05	31.74	-110.05	BSk	Semi-arid	23
US	Kendall (112), Walnut Gulch	5.00	0.02	31.74	-109.94	BSk	Semi-arid	23
Germany	Regenstauf, Regen	7.00	2658.00	49.13	12.13	Df	Humid	24
Germany	Deizisau, Neckar	25.00	4010.00	48.72	9.38	Cf	Humid	24
Germany	Poppenweiler, Neckar	27.00	5005.00	48.91	9.26	Cf	Humid	24
Germany	Lauffen, Neckar	23.00	7916.00	49.07	9.16	Cf	Humid	24
Germany	Rockenau, Neckar	27.00	12676.00	49.45	9.00	Cf	Humid	24
Germany	Mannheim, Neckar	26.00	13966.00	49.49	8.45	Cf	Humid	24
Belgium	Tailfer, Meuse	18.00	12484.00	50.40	4.88	Cf	Humid	24
Belgium	Nameche, Meuse	18.00	15328.00	50.47	4.99	Cf	Humid	24
Belgium	Liege, Meuse	17.00	21254.00	50.64	5.58	Cf	Humid	24
Netherlands	Eijsden, Meuse	17.00	21649.00	50.78	5.69	Cf	Humid	24
Netherlands	Heusden, Meuse	13.00	32711.00	51.74	5.14	Cf	Humid	24
Netherlands	Keizersveer, Meuse	11.00	33580.00	51.72	4.89	Cf	Humid	24
France	Goudet, Loire	3.00	432.00	44.89	3.92	Df	Humid	24
France	Bas, Loire	5.00	3234.00	45.31	4.13	Cf	Humid	24
France	Feurs, Loire	5.00	4960.00	45.74	4.21	Cf	Humid	24
France	Villerest, Loire	4.00	6584.00	46.00	4.05	Cf	Humid	24
France	Decize, Loire	5.00	16519.00	46.83	3.46	Cf	Humid	24
France	Nevers, Loire	7.00	18208.00	46.98	3.16	Cf	Humid	24
France	Gien, Loire	10.00	35500.00	47.68	2.63	Cf	Humid	24
France	Orleans, Loire	8.00	36966.00	47.90	1.90	Cf	Humid	24
France	Chaumont, Loire	10.00	40600.00	47.49	1.19	Cf	Humid	24
France	Langogne, Allier	3.00	324.00	44.73	3.86	Df	Humid	24
France	Langeac, Allier	4.00	1781.00	45.10	3.50	Df	Humid	24
France	Chatel, Allier	6.00	12430.00	46.40	3.32	Cf	Humid	24
France	Villeneuve, Allier	8.00	13348.00	46.66	3.23	Cf	Humid	24
France	Cuffy, Allier	8.00	14320.00	46.95	3.07	Cf	Humid	24
Taiwan	Lanyang River (H001)	4500.00	446.70	24.64	121.57	Cf	Humid	25
Taiwan	Lanyang River (H006)	10450.00	820.69	24.71	121.77	Cf	Humid	25
Taiwan	Lanyang River (H019)	4100.00	101.35	24.76	121.74	Cf	Humid	25
Brazil	Amazon	82.00	5980000.00	0.38	-50.03	Aw	Humid	26
Brazil	São Francisco	4.00	620000.00	-10.50	-36.39	Aw	Humid	26

Argentina	La Plata (Parana)	11.00	2860000.00	-35.24	-56.71	Cf	Humid	26
Venezuela	Orinoco	66.00	920000.00	8.84	-60.76	Af	Humid	26
Mexico	Colorado	89.00	700000.00	31.70	-114.71	BWh	Arid	26
US	Columbia	18.00	670000.00	46.26	-124.02	Cs	Humid	26
US	Mississippi	70.00	3200000.00	29.43	-89.60	Cf	Humid	26
US	Rio Grande	18.00	630000.00	25.95	-97.15	Cf	Dry sub-humid	26
US	Yukon	35.00	840000.00	62.60	-164.82	Df	Humid	26
Canada	Mackenzie	23.00	1770000.00	69.32	-133.98	Df	Semi-arid	26
Canada	St. Lawrence	1.00	1050000.00	49.39	-66.73	Df	Humid	26
Russia	Amur	10.00	2040000.00	52.96	141.13	Df	Humid	26
Russia	Lena	3.00	2450000.00	72.32	126.58	Df	Humid	26
Romania	Danube	35.00	790000.00	45.23	29.72	Df	Semi-arid	26
Ukraine	Dnieper	1.00	540000.00	46.50	32.30	Df	Dry sub-humid	26
Iraq	Shatt-Al-Arab	21.00	890000.00	29.93	48.61	BWh	Arid	26
Bangladesh	Brahmaputra	670.00	640000.00	23.80	89.77	Cw	Humid	26
Bangladesh	Ganges	257.00	980000.00	22.39	91.00	Am	Humid	26
China	Chiang Jiang (Yangtze River)	104.00	1730000.00	31.43	121.86	Cf	Humid	26
China	Huang He (Yellow River)	47.00	790000.00	37.76	119.16	Dw	Dry sub-humid	26
Pakistan	Indus	120.00	930000.00	24.02	67.47	BWh	Arid	26
Vietnam	Mekong	86.00	760000.00	9.78	106.48	Am	Humid	26
Egypt	Nile	10.00	3630000.00	31.45	30.38	BWh	Arid	26
DRC**	Zaire	5.00	3630000.00	-6.07	12.44	Aw	Dry sub-humid	26
Mozambique	Zambezi	13.00	1410000.00	-18.85	36.30	Aw	Humid	26
South Africa	Orange	24.00	890000.00	-28.63	16.45	BWk	Arid	26
Nigeria	Niger	7.00	2160000.00	5.14	5.38	Am	Humid	26
Australia	Murray	11.00	1140000.00	-35.36	139.36	BSk	Semi-arid	26
Ecuador	Gordeleg Catchment	93.75	1.00	-2.95	-78.89	Aw	Humid	27
Ecuador	Quingeo Catchment	4737.50	0.10	-3.04	-78.95	Aw	Dry sub-humid	27
Ecuador	Quingeo Catchment	2906.25	0.80	-2.95	-78.93	Aw	Dry sub-humid	27
Ecuador	Quingeo Catchment	131.25	12.00	-3.02	-78.91	Aw	Dry sub-humid	27
Ecuador	Quingeo Catchment	43.75	5.00	-3.01	-78.93	Aw	Dry sub-humid	27
Ecuador	Quingeo Catchment	212.50	7.00	-3.03	-78.92	Aw	Dry sub-humid	27
Ecuador	Quingeo Catchment	406.25	4.00	-3.03	-78.91	Aw	Dry sub-humid	27
Ecuador	Quingeo Catchment	181.25	1.00	-3.02	-78.91	Aw	Dry sub-humid	27
Ecuador	Quingeo Catchment	406.25	0.60	-2.96	-78.93	Aw	Dry sub-humid	27
Ecuador	Quingeo Catchment	2412.50	0.30	-2.94	-78.93	Aw	Dry sub-humid	27
Ecuador	Quingeo Catchment	1281.25	0.20	-2.95	-78.93	Aw	Dry sub-humid	27
Ecuador	Jadan Catchment	1375.00	0.10	-2.87	-78.88	Aw	Dry sub-humid	27
Ecuador	Jadan Catchment	1362.50	0.10	-2.87	-78.88	Aw	Dry sub-humid	27
Ecuador	Jadan Catchment	87.50	9.00	-2.87	-78.88	Aw	Dry sub-humid	27
Ecuador	Jadan Catchment	3625.00	0.30	-2.87	-78.88	Aw	Dry sub-humid	27

Ecuador	Jadan Catchment	418.75	3.00	-2.92	-78.87	Aw	Dry sub-humid	27
Ecuador	Jadan Catchment	16.25	0.10	-2.87	-78.84	Aw	Dry sub-humid	27
Ecuador	Deleg Catchment	637.50	1.00	-2.79	-78.93	Aw	Dry sub-humid	27
Ecuador	Deleg Catchment	937.50	2.00	-2.80	-78.93	Aw	Dry sub-humid	27
Ecuador	Deleg Catchment	543.75	3.00	-2.81	-78.92	Aw	Dry sub-humid	27
Ecuador	Deleg Catchment	9437.50	1.00	-2.81	-78.91	Aw	Dry sub-humid	27
Ecuador	Deleg Catchment	1137.50	0.10	-2.80	-78.90	Aw	Dry sub-humid	27
Ecuador	Deleg Catchment	931.25	0.10	-2.80	-78.90	Aw	Dry sub-humid	27
Ecuador	Burgay Catchment	8562.50	0.10	-2.82	-78.88	Aw	Dry sub-humid	27
Ecuador	Burgay Catchment	931.25	0.30	-2.72	-78.89	Aw	Dry sub-humid	27
Ecuador	Burgay Catchment	637.50	2.00	-2.71	-78.89	Aw	Dry sub-humid	27
Ecuador	Burgay Catchment	1056.25	3.00	-2.71	-78.89	Aw	Dry sub-humid	27
Ecuador	Burgay Catchment	1112.50	3.00	-2.71	-78.89	Aw	Dry sub-humid	27
Ecuador	Burgay Catchment	1137.50	6.00	-2.71	-78.89	Aw	Dry sub-humid	27
Ecuador	Gualaceo Catchment	52.50	2.00	-2.99	-78.81	Aw	Dry sub-humid	27
Ecuador	Gualaceo Catchment	268.75	3.00	-2.94	-78.80	Aw	Dry sub-humid	27
Ecuador	Gualaceo Catchment	2000.00	0.10	-3.00	-78.81	Aw	Dry sub-humid	27
Ecuador	Gualaceo Catchment	87.50	7.00	-2.93	-78.79	Aw	Dry sub-humid	27
Ecuador	Gualaceo Catchment	381.25	0.60	-2.93	-78.80	Aw	Dry sub-humid	27
Ecuador	Gualaceo Catchment	100.00	16.00	-2.94	-78.79	Aw	Dry sub-humid	27
Ecuador	Gualaceo Catchment	68.75	2.00	-3.00	-78.85	Aw	Humid	27
Ecuador	Gualaceo Catchment	850.00	0.20	-2.95	-78.82	Aw	Dry sub-humid	27
Bolivia	Beni at Rurrenabaque	1180.00	68000.00	-14.53	-67.50	Af	Humid	28
Bolivia	Beni at Riberalta	390.00	119000.00	-11.21	-66.25	Aw	Humid	28
Bolivia	Madre de Dios at Miraflores	230.00	124000.00	-11.11	-66.42	Aw	Humid	28
Bolivia	Orthón at Caracoles	30.00	32000.00	-10.82	-66.11	Aw	Humid	28
Bolivia	Beni at Cachuela Esperanza	260.00	283000.00	-10.55	-65.60	Aw	Humid	28
Bolivia	Grande at Puente Arce	2120.00	24000.00	-18.61	-65.16	Cw	Semi-arid	28
Bolivia	Pirai at Angostura	770.00	1400.00	-18.08	-63.46	Aw	Humid	28
Bolivia	Paracti at Paracti	4050.00	300.00	-17.22	-65.82	Cw	Humid	28
Bolivia	Grande at Abapo	890.00	60000.00	-18.91	-63.41	Aw	Semi-arid	28
Bolivia	Ichilo at Puerto Villarroel	470.00	7600.00	-16.84	-64.79	Am	Humid	28
Bolivia	Mamoré at Puerto Ganadero	160.00	159000.00	-14.86	-64.99	Am	Humid	28
Bolivia	Mamoré at Puerto Siles	90.00	216000.00	-12.80	-65.00	Aw	Humid	28
Bolivia	Mamoré at Guayaramerin	50.00	599000.00	-10.81	-65.35	Aw	Humid	28
Brazil	Madeira at Porto Velho	90.00	954000.00	-8.77	-63.91	Am	Humid	28
Peru	Requena	210.00	360000.00	-5.06	-73.86	Af	Humid	29
Peru	Tamshiyacu	210.00	733000.00	-4.01	-73.17	Af	Humid	29
Peru	Bellavista	170.00	101000.00	-3.70	-73.23	Af	Humid	29
Brazil	Manacapuru	110.00	2270000.00	-3.34	-60.68	Am	Humid	29

Brazil	Paricatuba	6.00	832000.00	-3.02	-60.48	Am	Humid	29
Brazil	Confluence	10.00	213000.00	-1.36	-61.87	Am	Humid	29
Brazil	Amatari	110.00	3154000.00	-3.29	-58.88	Am	Humid	29
Brazil	Fazenda Vista Allegre	130.00	1336000.00	-3.91	-59.16	Am	Humid	29
Brazil	Itenez	5.00	354000.00	-12.46	-64.33	Aw	Humid	29
Brazil	Óbidos	80.00	5088000.00	-1.92	-55.53	Am	Humid	29
Brazil	Itaituba	6.00	598000.00	-4.28	-55.97	Am	Humid	29

* References:

1. Aalto, R., Dunne, T., Guyot, J. L., 2006. Geomorphic controls on Andean denudation rates. The Journal of Geology, 114, 85–99.
2. Andermann, C., Crave, A., Gloaguen, R., Davy, P., Bonnet, S., 2012. Connecting source and transport: Suspended sediments in the Nepal Himalayas. Earth and Planetary Science Letters, 351, 158–170.
3. Bierman, P. R., Reuter, J. M., Pavich, M., Gellis, A. C., Caffee, M. W., Larsen, J., 2005. Using cosmogenic nuclides to contrast rates of erosion and sediment yield in a semi-arid, arroyo-dominated landscape, Rio Puerco Basin, New Mexico. Earth Surface Processes and Landforms, 30, 935–953.
4. Brown, E. T., Stallard, R. F., Larsen, M. C., Raisbeck, G. M., Yiou, F., 1995. Denudation rates determined from the accumulation of in situ-produced ^{10}Be in the Luquillo Experimental Forest, Puerto Rico. Earth and Planetary Science Letters, 129, 193–202.
5. Clapp, E. M., Bierman, P. R., Nichols, K. K., Pavich, M., Caffee, M., 2001. Rates of sediment supply to arroyos from upland erosion determined using in situ produced cosmogenic ^{10}Be and ^{26}Al. Quaternary Research, 55, 235–245.
6. Clapp, E. M., Bierman, P. R., Schick, A. P., Lekach, J., Enzel, Y., Caffee, M., 2000. Sediment yield exceeds sediment production in arid region drainage basins. Geology, 28, 995–998.
7. Dadson, S., Hovius, N., Pegg, S., Dade, W. B., Horng, M. J., Chen, H., 2005. Hyperpycnal river flows from an active mountain belt. Journal of Geophysical Research: Earth Surface, 110, F4046.
8. Gellis, A. C., Emmett, W. W., Leopold, L. B., 2005. Channel and hillslope processes revisited in the Arroyo de los Frijoles watershed near Santa Fe, New Mexico. US Geological Survey Professional Paper, 1704.
9. Gellis, A. C., Pavich, M. J., Ellwein, A. L., Aby, S., Clark, I., Wieczorek, M. E., Viger, R., 2012. Erosion, storage, and transport of sediment in two subbasins of the Rio Puerco, New Mexico. Geological Society of America Bulletin, 124, 817–841.
10. Hewawasam, T., von Blanckenburg, F., Schaller, M., Kubik, P., 2003. Increase of human over natural erosion rates in tropical highlands constrained by cosmogenic nuclides. Geology, 31, 597–600.
11. Hinderer, M., 2001. Late Quaternary denudation of the Alps, valley and lake fillings and modern river loads. Geodinamica Acta, 14, 231–263.
12. Hinderer, M., Kastowski, M., Kamelger, A., Bartolini, C., Schlunegger, F., 2013. River loads and modern denudation of the Alps—A review. Earth-Science Reviews, 118, 11–44.
13. Kirchner, J. W., Finkel, R. C., Riebe, C. S., Granger, D. E., Clayton, J. L., King, J. G., Megahan, W. F., 2001. Mountain erosion over 10 yr, 10 k.y., and 10 m.y. time scales. Geology, 29, 591–594.
14. Lupker, M., Blard, P.-H., Lavé, J., France-Lanord, C., Leanni, L., Puchol, N., Charreau, J., Bourlès, D., 2012. ^{10}Be-derived Himalayan denudation rates and sediment budgets in the Ganga basin. Earth and Planetary Science Letters, 333, 146–156.
15. Matmon, A., Bierman, P. R., Larsen, J., Southworth, S., Pavich, M., Caffee, M., 2003. Temporally and spatially uniform rates of erosion in the southern Appalachian Great Smoky Mountains. Geology, 31, 155–158.
16. Meybeck, M., Laroche, L., Dürr, H. H., Syvitski, J. P. M., 2003. Global variability of daily total suspended solids and their fluxes in rivers. Global and Planetary Change, 39, 65–93.
17. Milliman, J. D., Farnsworth, K. L., 2011. River Discharge to the Coastal Ocean: A Global Synthesis. Cambridge University Press, Cambridge.
18. Milliman, J. D., Meade, R. H., 1983. World-wide delivery of river sediment to the oceans. The Journal of Geology, 91, 1–21.
19. Milliman, J. D., Syvitski, J. P. M., 1992. Geomorphic/tectonic control of sediment discharge to the ocean: The importance of small mountainous rivers. The journal of Geology, 100, 525–544.
20. Nearing, M. A., Nichols, M. H., Stone, J. J., Renard, K. G., Simanton, J. R., 2007. Sediment yields from unit-source semiarid watersheds at Walnut Gulch. Water Resources Research, 43, W06426.
21. Nichols, K. K., Bierman, P. R., Finkel, R., Larsen, J., 2004. Long-term (10 to 20 kyr) sediment generation rates for the Upper Río Chagres Basin based on cosmogenic ^{10}Be, The Río Chagres: A Multidisciplinary Profile of a Tropical Watershed. Kluwer Academic Publishers, Amsterdam, 297–313.
22. Pan, B.-T., Geng, H.-P., Hu, X.-F., Sun, R.-H., Wang, C., 2010. The topographic controls on the decadal-scale erosion rates in Qilian Shan Mountains, N.W. China. Earth and Planetary Science Letters, 292, 148–157.
23. Pelletier, J. D., Nichols, M. H., Nearing, M. A., 2016. The influence of Holocene vegetation changes on topography and erosion rates: A case study at Walnut Gulch Experimental Watershed, Arizona. Earth Surface Dynamics, 4, 471–488.
24. Schaller, M., von Blanckenburg, F., Hovius, N., Kubik, P. W., 2001. Large-scale erosion rates from in situ-produced cosmogenic nuclides in European river sediments. Earth and Planetary Science Letters, 188, 441–458.
25. Siame, L. L., Angelier, J., Chen, R.-F., Godard, V., Derrieux, F., Bourlès, D. L., Braucher, R., Chang, K.-J., Chu, H.-T., Lee, J.-C., 2011. Erosion rates in an active orogen (NE-Taiwan): A confrontation of cosmogenic measurements with river suspended loads. Quaternary Geochronology, 6, 246–260.

26. Summerfield, M. A., Hulton, N. J., 1994. Natural controls of fluvial denudation rates in major world drainage basins. Journal of Geophysical Research: Solid Earth, 99, 13871–13883.
27. Vanacker, V., von Blanckenburg, F., Govers, G., Molina, A., Poesen, J., Deckers, J., Kubik, P., 2007. Restoring dense vegetation can slow mountain erosion to near natural benchmark levels. Geology, 35, 303–306.
28. Wittmann, H., von Blanckenburg, F., Guyot, J. L., Maurice, L., Kubik, P. W., 2009. From source to sink: Preserving the cosmogenic ^{10}Be-derived denudation rate signal of the Bolivian Andes in sediment of the Beni and Mamoré foreland basins. Earth and Planetary Science Letters, 288, 463–474.
29. Wittmann, H., von Blanckenburg, F., Maurice, L., Guyot, J.-L., Filizola, N., Kubik, P. W., 2011. Sediment production and delivery in the Amazon River basin quantified by in situ–produced cosmogenic nuclides and recent river loads. Bulletin, 123, 934–950.

** DRC: Democratic Republic of the Congo; FG: French Guiana; NZ: New Zealand; PNG: Papua New Guinea.

E.2 Compiled from USGS

Station ID	Location	Erosion rate (mm kyr^{-1})	Basin area (km^2)	Latitude	Longitude	K–G climate zone	AI category
1127500	YANTIC RIVER AT YANTIC, CT	9.60	231.29	41.56	-72.12	Df	Humid
1192883	COGINCHAUG RIVER AT MIDDLEFIELD, CT	5.70	77.18	41.52	-72.71	Df	Humid
1193500	SALMON RIVER NEAR EAST HAMPTON, CT	41.16	259.00	41.55	-72.45	Df	Humid
1379500	Passaic River near Chatham NJ	13.89	259.00	40.73	-74.39	Df	Humid
1400932	Baldwins Creek at Baldwin Lake nr Pennington NJ	10.76	6.53	40.34	-74.78	Df	Humid
1411000	Great Egg Harbor River at Folsom NJ	1.70	147.89	39.59	-74.85	Df	Humid
1464500	Crosswicks Creek at Extonville NJ	13.04	211.08	40.14	-74.60	Df	Humid
1467470	Schuylkill River at Port Carbon, PA	141.51	70.19	40.69	-76.16	Df	Humid
1470500	Schuylkill River at Berne, PA	48.04	919.45	40.52	-76.00	Df	Humid
1472157	French Creek near Phoenixville, PA	15.96	153.07	40.15	-75.60	Df	Humid
1473000	Perkiomen Creek at Graterford, PA	42.99	722.61	40.23	-75.45	Df	Humid
1473169	Valley Creek at PA Turnpike Br near Valley Forge	22.12	53.87	40.08	-75.46	Df	Humid
1480300	West Branch Brandywine Creek near Honey Brook, PA	36.90	48.43	40.07	-75.86	Df	Humid
1480617	West Branch Brandywine Creek at Modena, PA	23.43	142.45	39.96	-75.80	Df	Humid
1480870	East Branch Brandywine Creek below Downingtown, PA	21.65	232.84	39.97	-75.67	Df	Humid
1481000	Brandywine Creek at Chadds Ford, PA	39.59	743.33	39.87	-75.59	Df	Humid
1481500	BRANDYWINE CREEK AT WILMINGTON, DE	41.92	813.26	39.77	-75.58	Df	Humid
1491000	CHOPTANK RIVER NEAR GREENSBORO, MD	3.89	292.67	39.00	-75.79	Cf	Humid
1516500	Corey Creek near Mainesburg, PA	23.57	31.60	41.79	-77.01	Df	Humid
1517000	Elk Run near Mainesburg, PA	30.48	26.42	41.82	-76.96	Df	Humid
1549100	Blockhouse Creek Tributary at Liberty, PA	64.18	2.80	41.57	-77.10	Df	Humid
1549300	Blockhouse Creek at Buttonwood, PA	50.93	71.48	41.50	-77.15	Df	Humid
1549350	Steam Valley Run at Buttonwood, PA	28.70	13.83	41.49	-77.15	Df	Humid
1549500	Blockhouse Creek near English Center, PA	59.56	97.64	41.47	-77.23	Df	Humid
1570100	Conodoguinet Creek Trib No. 1 near Enola, PA	37.75	1.99	40.29	-76.99	Df	Humid
1570300	Conodoguinet Creek Trib No. 3 near Enola, PA	85.44	0.98	40.30	-76.95	Df	Humid
1589000	PATAPSCO RIVER AT HOLLOFIELD, MD	46.12	738.15	39.31	-76.79	Cf	Humid
1589025	PATAPSCO RIVER NEAR CATONSVILLE, MD	69.65	779.59	39.25	-76.76	Cf	Humid
1589035	PATAPSCO RIVER NEAR ELKRIDGE,	68.53	808.08	39.23	-76.72	Cf	Humid

	MD						
1594440	PATUXENT RIVER NEAR BOWIE, MD	14.19	901.32	38.96	-76.69	Cf	Humid
1603000	NORTH BRANCH POTOMAC RIVER NEAR CUMBERLAND, MD	37.75	2271.42	39.62	-78.77	Df	Humid
1614500	CONOCOCHEAGUE CREEK AT FAIRVIEW, MD	28.72	1279.45	39.72	-77.82	Df	Humid
1643020	MONOCACY R AT REICHS FORD BRIDGE NR FREDERICK,MD	43.84	2116.02	39.39	-77.38	Df	Humid
1645784	SNAKEDEN BRANCH AT RESTON, VA	250.24	2.05	38.93	-77.35	Cf	Humid
1647740	NORTH BRANCH ROCK CREEK NEAR ROCKVILLE, MD	10.54	32.37	39.10	-77.12	Cf	Humid
1650500	NORTHWEST BRANCH ANACOSTIA RIVER NR COLESVILLE, MD	154.47	54.39	39.07	-77.03	Cf	Humid
1658500	S F QUANTICO CREEK NEAR INDEPENDENT HILL, VA	19.86	19.74	38.59	-77.43	Cf	Humid
1659000	N BRANCH CHOPAWAMSIC CR NR INDEPENDENT HILL, VA	14.16	14.74	38.57	-77.43	Cf	Humid
1664000	RAPPAHANNOCK RIVER AT REMINGTON, VA	34.96	1603.20	38.53	-77.81	Cf	Humid
1667500	RAPIDAN RIVER NEAR CULPEPER, VA	34.96	1212.11	38.35	-77.98	Cf	Humid
2084160	CHICOD CR AT SR1760 NEAR SIMPSON, NC	12.62	116.55	35.56	-77.23	Cf	Humid
2118000	SOUTH YADKIN RIVER NEAR MOCKSVILLE, NC	50.40	792.54	35.85	-80.66	Cf	Humid
2119400	THIRD CREEK NR STONY POINT, NC	20.53	12.54	35.87	-81.07	Cf	Humid
3068600	SHAVERS FORK ABOVE BOWDEN, WV	21.87	357.42	38.90	-79.69	Df	Humid
3068610	TAYLOR RUN AT BOWDEN, WV	16.89	13.11	38.91	-79.70	Df	Humid
3068800	SHAVERS FORK BELOW BOWDEN, WV	31.23	391.09	38.91	-79.77	Df	Humid
3070420	Stony Fork Tributary near Gibbon Glade, PA	65.29	2.41	39.76	-79.59	Df	Humid
3070455	Stony Fork near Elliottsville, PA	51.63	19.27	39.77	-79.61	Df	Humid
3111548	Wheeling Creek below Blaine OH	72.92	253.04	40.07	-80.81	Df	Humid
3111585	Enlow Fork near West Finley, PA	83.09	98.68	39.97	-80.45	Df	Humid
3139000	Killbuck Creek at Killbuck OH	38.88	1201.75	40.48	-81.99	Df	Humid
3159500	Hocking River at Athens OH	42.40	2442.36	39.33	-82.09	Df	Humid
3198550	BIG COAL RIVER NEAR ALUM CREEK, WV	122.79	1152.54	38.25	-81.80	Cf	Humid
3199000	LITTLE COAL RIVER AT DANVILLE, WV	134.10	696.71	38.08	-81.84	Cf	Humid
3199400	LITTLE COAL RIVER AT JULIAN, WV	134.37	823.62	38.15	-81.85	Cf	Humid
3199700	COAL RIVER AT ALUM CREEK, WV	130.90	2167.82	38.29	-81.81	Cf	Humid
3200500	COAL RIVER AT TORNADO, WV	109.87	2232.57	38.34	-81.84	Cf	Humid
3202400	GUYANDOTTE RIVER NEAR BAILEYSVILLE, WV	91.99	792.54	37.60	-81.65	Cf	Humid
3207800	LEVISA FORK AT BIG ROCK, VA	327.45	769.23	37.35	-82.20	Cf	Humid
3207962	DICKS FORK AT PHYLLIS, KY	65.38	2.12	37.45	-82.34	Cf	Humid
3207965	GRAPEVINE CREEK NEAR PHYLLIS, KY	305.93	16.06	37.43	-82.35	Cf	Humid
3210000	JOHNS CREEK NEAR META, KY	258.74	145.82	37.57	-82.46	Cf	Humid
3217000	TYGARTS CREEK NEAR GREENUP, KY	58.26	626.78	38.56	-82.95	Cf	Humid
3230310	Little Darby Creek at West Jefferson OH	28.36	419.58	39.95	-83.27	Df	Humid
3230450	Hellbranch Run near Harrisburg OH	32.34	92.72	39.85	-83.16	Df	Humid
3230500	Big Darby Creek at Darbyville OH	44.77	1383.05	39.70	-83.11	Df	Humid
3234000	Paint Creek near Bourneville OH	78.17	2090.12	39.26	-83.17	Df	Humid
3239000	Little Miami River near Selma OH	20.59	126.65	39.81	-83.74	Df	Humid
3239500	North Fork Little Miami River near Pitchin OH	9.11	74.85	39.83	-83.78	Df	Humid
3240000	Little Miami River near Oldtown OH	21.13	334.11	39.75	-83.93	Df	Humid

3241500	Massies Creek at Wilberforce OH	32.45	163.69	39.72	-83.88	Df	Humid
3244000	Todd Fork near Roachester OH	121.65	567.21	39.34	-84.09	Df	Humid
3249500	LICKING RIVER AT FARMERS, KY	48.78	2141.92	38.12	-83.54	Cf	Humid
3261500	Great Miami River at Sidney OH	36.41	1401.18	40.29	-84.15	Df	Humid
3261950	Loramie Creek near Newport OH	39.08	393.68	40.31	-84.38	Df	Humid
3265000	Stillwater River at Pleasant Hill OH	37.18	1302.76	40.06	-84.36	Df	Humid
3280600	MIDDLE FORK KENTUCKY RIVER NEAR HYDEN, KY	105.14	523.18	37.15	-83.38	Cf	Humid
3291500	EAGLE CREEK AT GLENCOE, KY	191.68	1131.82	38.71	-84.82	Df	Humid
3297500	PLUM CREEK AT WATERFORD, KY	319.71	82.36	38.05	-85.43	Cf	Humid
3328500	EEL RIVER NEAR LOGANSPORT, IN	40.04	2043.50	40.78	-86.26	Df	Humid
3340800	BIG RACCOON CREEK NEAR FINCASTLE, IN	419.07	360.01	39.81	-86.95	Df	Humid
3383000	TRADEWATER RIVER AT OLNEY, KY	13.90	637.14	37.22	-87.78	Cf	Humid
3400990	CLOVER FORK AT HARLAN, KY	130.17	574.98	36.85	-83.33	Cf	Humid
3402000	YELLOW CREEK NEAR MIDDLESBORO, KY	256.71	156.95	36.67	-83.69	Cf	Humid
3403000	CUMBERLAND RIVER NEAR PINEVILLE, KY	19.23	2095.30	36.81	-83.77	Cf	Humid
3403500	CUMBERLAND RIVER AT BARBOURVILLE, KY	112.20	2486.39	36.86	-83.89	Cf	Humid
3407100	CANE BRANCH NEAR PARKERS LAKE, KY	327.80	1.74	36.87	-84.45	Cf	Humid
3407876	SMOKY CREEK AT HEMBREE, TN	517.17	44.55	36.24	-84.41	Cf	Humid
3410500	SOUTH FORK CUMBERLAND RIVER NEAR STEARNS, KY	62.69	2470.85	36.63	-84.53	Cf	Humid
3465500	NOLICHUCKY RIVER AT EMBREEVILLE, TN	165.80	2084.94	36.18	-82.46	Cf	Humid
3532000	POWELL RIVER NEAR ARTHUR, TN	64.52	1774.14	36.54	-83.63	Cf	Humid
3540500	EMORY RIVER AT OAKDALE, TN	42.66	1978.75	35.98	-84.56	Cf	Humid
3571000	SEQUATCHIE RIVER NEAR WHITWELL, TN	57.73	994.56	35.21	-85.50	Cf	Humid
4062400	MICHIGAMME RIVER NEAR WITCH LAKE, MI	5.05	818.44	46.25	-88.01	Df	Humid
4073466	SILVER CREEK AT SPAULDING ROAD NEAR GREEN LAKE, WI	4.73	116.81	43.84	-88.91	Df	Humid
4087120	MENOMONEE RIVER AT WAUWATOSA, WI	16.81	318.57	43.05	-88.00	Df	Humid
4151500	CASS RIVER AT FRANKENMUTH, MI	8.57	2178.18	43.33	-83.75	Df	Humid
4177810	FISH CREEK NEAR ARTIC, IN	8.67	253.82	41.47	-84.81	Df	Humid
4188496	Eagle Creek above Findlay OH	55.32	132.09	40.98	-83.65	Df	Humid
4195500	Portage River at Woodville OH	46.13	1108.51	41.45	-83.36	Df	Humid
4201500	Rocky River near Berea OH	60.24	691.53	41.41	-81.88	Df	Humid
4206000	Cuyahoga River at Old Portage OH	20.52	1046.36	41.14	-81.55	Df	Humid
4207200	Tinkers Creek at Bedford OH	88.23	217.30	41.38	-81.53	Df	Humid
4208000	Cuyahoga River at Independence OH	72.27	1831.12	41.40	-81.63	Df	Humid
4209000	Chagrin River at Willoughby OH	174.64	637.14	41.63	-81.40	Df	Humid
4212100	Grand River near Painesville OH	50.67	1774.14	41.72	-81.23	Df	Humid
4233286	SIXMILE CREEK AT BROOKTONDALE NY	87.10	69.93	42.38	-76.39	Df	Humid
4233300	SIXMILE CREEK AT BETHEL GROVE NY	99.65	101.01	42.40	-76.44	Df	Humid
5291000	WHETSTONE RIVER NEAR BIG STONE CITY, SD	6.06	1030.82	45.29	-96.49	Df	Dry sub-humid
5293000	YELLOW BANK RIVER NEAR ODESSA, MN	6.94	1188.80	45.23	-96.35	Df	Dry sub-humid
5341752	WILLOW RIVER @ WILLOW R STATE	10.17	756.28	45.01	-92.71	Df	Humid

	PARK NR BURKHARDT,WI						
5376800	WHITEWATER RIVER NEAR BEAVER, MN	75.69	701.89	44.15	-92.00	Df	Humid
5385500	SOUTH FORK ROOT RIVER NEAR HOUSTON, MN	92.66	712.25	43.74	-91.56	Df	Humid
5387500	Upper Iowa River at Decorah, IA	77.21	1323.48	43.30	-91.80	Df	Humid
5388250	Upper Iowa River near Dorchester, IA	96.24	1994.29	43.42	-91.51	Df	Humid
5389400	Bloody Run Creek near Marquette, IA	27.64	88.40	43.04	-91.21	Df	Humid
5403700	DELL CREEK NEAR LAKE DELTON, WI	3.77	116.29	43.55	-89.87	Df	Humid
5406470	BREWERY CREEK AT CROSS PLAINS, WI	24.68	19.94	43.12	-89.64	Df	Humid
5406491	GARFOOT CREEK NEAR CROSS PLAINS, WI	21.54	13.96	43.11	-89.68	Df	Humid
5406500	BLACK EARTH CREEK AT BLACK EARTH, WI	16.15	110.85	43.13	-89.73	Df	Humid
5408000	KICKAPOO RIVER AT LA FARGE, WI	34.57	688.94	43.57	-90.64	Df	Humid
5411400	Sny Magill Creek near Clayton, IA	36.55	71.48	42.95	-91.19	Df	Humid
5413500	GRANT RIVER AT BURTON, WI	58.15	696.71	42.72	-90.82	Df	Humid
5427718	YAHARA RIVER AT WINDSOR, WI	7.50	95.83	43.21	-89.35	Df	Humid
5427850	YAHARA RIVER AT STATE HIGHWAY 113 AT MADISON, WI	4.87	200.47	43.15	-89.40	Df	Humid
5427943	PHEASANT BRANCH AT AIRPORT ROAD NEAR MIDDLETON, WI	14.80	25.12	43.11	-89.54	Df	Humid
5427948	PHEASANT BRANCH AT MIDDLETON, WI	23.66	44.24	43.10	-89.51	Df	Humid
5427970	WILLOW CREEK AT MADISON, WI	47.25	8.16	43.07	-89.42	Df	Humid
5432695	RIDGEWAY BRANCH NEAR HOLLANDALE, WI	16.11	49.21	42.94	-89.92	Df	Humid
5432927	PLEASANT VALLEY CREEK @ CTH H NR BLANCHARDVILLE,WI	13.55	49.99	42.87	-89.80	Df	Humid
5436000	MOUNT VERNON CREEK NEAR MOUNT VERNON, WI	22.71	42.48	42.92	-89.62	Df	Humid
5436500	SUGAR RIVER NEAR BRODHEAD, WI	9.84	1354.56	42.61	-89.40	Df	Humid
5449500	Iowa River near Rowan, IA	5.64	1111.10	42.76	-93.62	Df	Humid
5455000	Ralston Creek at Iowa City, IA	264.35	7.80	41.66	-91.51	Df	Humid
5464130	Fourmile Creek near Lincoln, IA	144.68	35.69	42.23	-92.61	Df	Humid
5464133	Halfmile Creek near Gladbrook, IA	43.14	3.44	42.21	-92.61	Df	Humid
5464137	Fourmile Creek near Traer, IA	94.83	50.53	42.20	-92.56	Df	Humid
5471040	Squaw Creek near Colfax, IA	92.70	47.66	41.66	-93.27	Df	Humid
5471050	South Skunk River at Colfax, IA	107.21	2079.76	41.68	-93.25	Df	Humid
5483000	East Fork Hardin Creek near Churdan, IA	7.68	62.16	42.11	-94.37	Df	Humid
5483450	Middle Raccoon River near Bayard, IA	164.52	971.25	41.78	-94.49	Df	Humid
5483600	Middle Raccoon River at Panora, IA	10.48	1139.59	41.69	-94.37	Df	Humid
5486490	Middle River near Indianola, IA	367.82	1267.54	41.42	-93.59	Df	Humid
5487540	Walnut Creek near Prairie City, IA	40.83	17.56	41.60	-93.30	Df	Humid
5487550	Walnut Creek near Vandalia, IA	96.17	52.58	41.54	-93.26	Df	Humid
5487980	White Breast Creek near Dallas, IA	283.74	862.47	41.25	-93.29	Df	Humid
5498000	Middle Fabius River near Monticello, MO	262.55	1017.87	40.09	-91.74	Df	Humid
5502500	North Fork Salt River near Shelbina, MO	109.70	1245.78	39.74	-92.04	Df	Humid
5506500	Middle Fork Salt River at Paris, MO	99.56	922.04	39.48	-92.01	Df	Humid
5525000	IROQUOIS RIVER AT IROQUOIS, IL	18.09	1776.73	40.82	-87.58	Df	Humid
5527900	NORTH MILL CREEK AT HICKORY CORNERS, IL	22.65	52.32	42.47	-88.01	Df	Humid
5527905	HASTINGS CREEK NEAR LINDENHURST, IL	65.77	12.15	42.45	-88.02	Df	Humid
5527910	NORTH MILL CREEK NEAR MILBURN, IL	29.79	73.56	42.44	-88.00	Df	Humid

5532500	DES PLAINES RIVER AT RIVERSIDE, IL	18.50	1631.69	41.82	-87.82	Df	Humid
5544385	MUSKEGO (BIG MUSKEGO) LAKE OUTLET NR WIND LAKE, WI	2.47	87.80	42.85	-88.13	Df	Humid
5548105	NIPPERSINK CREEK ABOVE WONDER LAKE, IL	22.30	218.85	42.39	-88.37	Df	Humid
5559700	SENACHWINE CREEK AT CHILLICOTHE, IL	209.68	218.85	40.94	-89.50	Df	Humid
5570350	BIG CREEK AT ST. DAVID, IL	139.61	72.52	40.50	-90.05	Df	Humid
5570370	BIG CREEK NEAR BRYANT, IL	119.58	106.71	40.46	-90.13	Df	Humid
5570380	SLUG RUN NEAR BRYANT,IL	24.32	18.44	40.47	-90.14	Df	Humid
5579610	KICKAPOO CREEK AT 2100E ROAD NEAR BLOOMINGTON, IL	45.40	18.91	40.47	-88.86	Df	Humid
5579620	KICKAPOO CREEK TRIBUTARY NEAR BLOOMINGTON, IL	136.78	9.84	40.47	-88.88	Df	Humid
5579630	KICKAPOO CREEK NEAR BLOOMINGTON, IL	86.14	38.33	40.46	-88.88	Df	Humid
5585830	MCKEE CREEK AT CHAMBERSBURG, IL	127.24	883.19	39.82	-90.65	Df	Humid
5587480	PIASA CREEK NEAR MELVILLE, IL	578.02	265.58	38.96	-90.27	Df	Humid
5588720	JUDYS BRANCH AT RTE 157 AT GLEN CARBON, IL	570.40	21.57	38.74	-90.00	Df	Humid
5591200	KASKASKIA RIVER AT COOKS MILLS, IL	22.34	1225.06	39.58	-88.41	Df	Humid
6071100	L Prickly Pear C at Sieben Rnch nr Wolf Cr MT	5.63	701.89	46.89	-112.13	BSk	Semi-arid
6088300	Muddy Creek near Vaughn MT	86.77	580.16	47.63	-111.64	BSk	Semi-arid
6088500	Muddy Creek at Vaughn MT	203.09	663.04	47.56	-111.54	BSk	Semi-arid
6207800	Bluewater Creek near Bridger MT	23.07	72.78	45.33	-108.80	Df	Semi-arid
6207850	Bluewater C at Sanford Ranch nr Bridger MT	58.49	113.70	45.34	-108.84	Df	Semi-arid
6207870	Bluewater Creek near Fromberg MT	58.35	120.69	45.37	-108.87	Df	Semi-arid
6244500	FIVEMILE CREEK AB WYOMING CANAL, NR PAVILLION, WY	48.54	305.62	43.30	-108.70	BSk	Semi-arid
6250000	FIVEMILE CREEK NEAR RIVERTON, WY	364.57	922.04	43.20	-108.40	BWk	Arid
6253000	FIVEMILE CREEK NEAR SHOSHONI, WY	441.70	1082.61	43.22	-108.22	BWk	Arid
6256650	BADWATER C AT LYSITE, WY	143.99	1074.85	43.26	-107.70	BWk	Semi-arid
6256800	BRIDGER CREEK NEAR LYSITE, WYO.	58.32	471.38	43.29	-107.72	BWk	Semi-arid
6257000	BADWATER CREEK AT BONNEVILLE, WY	181.86	2092.71	43.27	-108.08	BWk	Arid
6257500	MUDDY CREEK NEAR PAVILLION, WY	109.44	691.53	43.36	-108.60	BWk	Semi-arid
6258000	MUDDY CREEK NEAR SHOSHONI, WY	180.72	859.88	43.29	-108.28	BWk	Arid
6268500	FIFTEEN MILE CREEK NEAR WORLAND, WY	285.57	1341.61	44.02	-108.01	BWk	Arid
6279795	CROW CREEK AT MOUTH, AT PAHASKA, WY	18.95	49.47	44.51	-109.97	Df	Dry sub-humid
6309500	MIDDLE FORK POWDER RIVER ABOVE KAYCEE, WY	66.81	1165.49	43.65	-106.81	Df	Semi-arid
6425720	BELLE FOURCHE R BL RATTLESNAKE C, NR PINEY, WY	0.54	1282.04	43.98	-105.39	BSk	Semi-arid
6425780	BELLE FOURCHE R AB DRY C NR PINEY WY	3.77	1538.45	44.03	-105.33	BSk	Semi-arid
6441110	PLUM CREEK BELOW HAYES, SD	204.64	766.64	44.21	-100.73	BSk	Semi-arid
6600500	Floyd River at James, IA	99.81	2294.73	42.58	-96.31	Df	Humid
6602020	West Fork Ditch at Hornick, IA	209.29	1043.77	42.23	-96.08	Df	Humid
6602400	Monona-Harrison Ditch near Turin, IA	924.37	2330.99	41.96	-95.99	Df	Humid
6607200	Maple River at Mapleton, IA	626.24	1732.70	42.16	-95.81	Df	Humid
6608500	Soldier River at Pisgah, IA	2495.63	1054.13	41.83	-95.93	Df	Humid

6609200	Steer Creek near Magnolia, IA	342.28	23.98	41.75	-95.93	Df	Humid
6609280	Boyer River at Deloit, IA	463.55	751.10	42.09	-95.31	Df	Humid
6609350	East Boyer River at Denison, IA	689.74	336.70	42.01	-95.37	Df	Humid
6609500	Boyer River at Logan, IA	1873.64	2255.88	41.64	-95.78	Df	Humid
6609590	Thompson Creek near Woodbine, IA	433.81	18.05	41.74	-95.81	Df	Humid
6610732	Big Papillion Creek at Fort Street at Omaha, Nebr.	483.13	334.11	41.31	-96.10	Df	Humid
6610750	Little Papillion Creek at Irvington, Nebr.	351.50	82.88	41.31	-96.05	Df	Humid
6637910	ROCK CREEK AT ATLANTIC CITY, WYO	27.33	55.17	42.51	-108.75	Df	Semi-arid
6712000	CHERRY CREEK NEAR FRANKTOWN, CO	16.57	437.71	39.36	-104.76	BSk	Semi-arid
6712500	CHERRY CREEK NEAR MELVIN, CO	16.60	932.40	39.61	-104.82	BSk	Semi-arid
6758200	KIOWA CREEK AT KIOWA, CO	142.10	287.49	39.34	-104.48	BSk	Semi-arid
6795250	SHELL CR .5 MI SW OF PLATTE CENTER, NE	87.59	590.52	41.53	-97.50	Df	Dry sub-humid
6808000	Mule Creek near Malvern, IA	365.37	27.45	40.94	-95.60	Df	Humid
6809000	Davids Creek near Hamlin, IA	350.95	67.34	41.67	-94.81	Df	Humid
6809500	East Nishnabotna River at Red Oak, IA	562.06	2315.45	41.01	-95.24	Df	Humid
6810900	BROWNELL C SUBWATERSHED 1A NR SYRACUSE NEBR	103.99	0.49	40.67	-96.13	Df	Humid
6811000	BROWNELL C SUBWATERSHED 1 NR SYRACUSE NEBR	27.43	1.99	40.67	-96.13	Df	Humid
6814000	TURKEY C NR SENECA, KS	904.86	714.84	39.95	-96.11	Df	Humid
6817000	Nodaway River at Clarinda, IA	655.54	1973.57	40.74	-95.01	Df	Humid
6821150	Little Platte River at Smithville, MO	226.15	606.06	39.39	-94.58	Df	Humid
6839000	MEDICINE CREEK AT MAYWOOD, NEBR.	30.05	598.29	40.66	-100.61	Df	Semi-arid
6839500	BRUSHY CREEK NEAR MAYWOOD, NEBR.	133.62	336.70	40.63	-100.63	Df	Semi-arid
6840000	FOX CREEK AT CURTIS, NEBR.	228.46	192.95	40.63	-100.49	Df	Semi-arid
6841000	MEDICINE CREEK ABOVE HARRY STRUNK LAKE, NE	264.51	1372.69	40.50	-100.32	Df	Semi-arid
6843000	MEDICINE CREEK AT CAMBRIDGE, NEBR.	210.68	2354.30	40.30	-100.18	Df	Semi-arid
6848000	PRAIRIE DOG C AT NORTON, KS	106.99	1771.55	39.81	-99.92	Df	Semi-arid
6878500	LYON C NR WOODBINE, KS	247.33	595.70	38.88	-96.91	Df	Humid
6880000	LINCOLN CREEK NEAR SEWARD, NEBR.	16.50	1134.41	40.92	-97.15	Df	Humid
6888000	VERMILLION C NR WAMEGO, KS	334.39	629.37	39.35	-96.22	Df	Humid
6890100	DELAWARE R NR MUSCOTAH, KS	543.74	1116.28	39.52	-95.53	Df	Humid
6890500	DELAWARE R AT VALLEY FALLS, KS	853.41	2387.97	39.35	-95.45	Df	Humid
6891500	WAKARUSA R NR LAWRENCE, KS	197.68	1100.74	38.91	-95.26	Df	Humid
6892000	STRANGER C NR TONGANOXIE, KS	273.90	1051.54	39.12	-95.01	Df	Humid
6893500	Blue River at Kansas City, MO	265.62	486.92	38.96	-94.56	Df	Humid
6893790	LITTLE BLUE R. AT LONGVIEW ROAD IN KANS. CITY, M	228.02	122.77	38.91	-94.47	Df	Humid
6897000	East Fork Big Creek near Bethany, MO	7167.77	246.05	40.30	-94.03	Df	Humid
6898000	Thompson River at Davis City, IA	354.75	1815.58	40.64	-93.81	Df	Humid
6898100	Thompson River at Mount Moriah, MO	440.72	2307.68	40.34	-93.77	Df	Humid
6899000	Weldon River at Mill Grove, MO	742.21	1279.45	40.31	-93.59	Df	Humid
6899700	Shoal Creek near Braymer, MO	1051.66	1012.69	39.70	-93.80	Df	Humid
6901500	Locust Creek near Linneus, MO	307.45	1424.49	39.90	-93.24	Df	Humid
6902200	West Yellow Creek near Brookfield, MO	198.74	349.65	39.84	-93.03	Df	Humid
6903900	Chariton River near Rathbun, IA	29.79	1421.90	40.82	-92.89	Df	Humid
6904000	Chariton River near Centerville, IA	95.02	1833.71	40.74	-92.80	Df	Humid
6906000	Mussel Fork near Musselfork, MO	215.96	691.53	39.52	-92.95	Df	Humid

6906300	East Fork Little Chariton R. near Huntsville, MO	130.55	569.80	39.45	-92.57	Df	Humid
6910750	Moreau River near Jefferson City, MO	109.05	1452.98	38.53	-92.19	Df	Humid
6911000	MARAIS DES CYGNES R AT MELVERN, KS	157.38	909.09	38.52	-95.70	Df	Humid
6911900	DRAGOON C NR BURLINGAME, KS	182.62	295.26	38.71	-95.84	Df	Humid
6912500	HUNDRED AND TEN MILE C NR QUENEMO, KS	189.61	833.98	38.65	-95.56	Df	Humid
6914000	POTTAWATOMIE C NR GARNETT, KS	150.70	865.06	38.33	-95.25	Df	Humid
6915000	BIG BULL C NR HILLSDALE, KS	305.31	370.37	38.66	-94.90	Df	Humid
6917500	MARMATON R NR FORT SCOTT, KS	137.19	1004.92	37.85	-94.70	Cf	Humid
6918440	Sac River near Dadeville, MO	27.33	665.63	37.44	-93.68	Cf	Humid
6921000	Pomme de Terre River near Bolivar, MO	58.25	582.75	37.61	-93.31	Df	Humid
6921070	Pomme de Terre River near Polk, MO	5.58	714.84	37.68	-93.37	Df	Humid
7026370	NORTH REELFOOT CREEK AT HWY 22, NEAR CLAYTON, TN	283.30	145.82	36.46	-89.25	Cf	Humid
7036100	St. Francis River near Saco, MO	34.25	1719.75	37.38	-90.47	Cf	Humid
7047815	Cross County Ditch near Birdeye, AR	5848.41	81.33	35.36	-90.65	Cf	Humid
7047882	Straight Slough near Birdeye, AR	75.22	1186.21	35.36	-90.66	Cf	Humid
7047904	Clark Corner Cut-Off near Colt, AR	434.60	1424.49	35.15	-90.66	Cf	Humid
7068510	Little Black River below Fairdealing, MO	17.87	502.46	36.63	-90.58	Cf	Humid
7068600	Little Black River at Success, AR	16.73	999.74	36.46	-90.73	Cf	Humid
7093740	BADGER CREEK, UPPER STATION, NEAR HOWARD, CO	11.06	274.54	38.66	-105.81	Df	Semi-arid
7093775	BADGER CREEK, LOWER STATION, NEAR HOWARD, CO.	22.11	546.49	38.47	-105.86	Df	Semi-arid
7103970	MONUMENT CR ABV WOODMEN RD AT COLORADO SPRINGS, CO	46.33	466.20	38.93	-104.82	BSk	Semi-arid
7103990	COTTONWOOD CREEK AT MOUTH AT PIKEVIEW, CO	352.32	48.95	38.93	-104.81	BSk	Semi-arid
7104905	MONUMENT CREEK AT BIJOU ST. AT COLO. SPRINGS, CO	73.88	608.65	38.84	-104.83	BSk	Semi-arid
7105500	FOUNTAIN CREEK AT COLORADO SPRINGS, CO	128.09	1015.28	38.82	-104.82	BSk	Semi-arid
7105600	SAND CREEK ABOVE MOUTH AT COLORADO SPRINGS, CO	221.01	135.72	38.79	-104.77	BSk	Semi-arid
7105800	FOUNTAIN CREEK AT SECURITY, CO	146.41	1294.99	38.73	-104.73	BSk	Semi-arid
7106500	FOUNTAIN CREEK AT PUEBLO, CO.	120.17	2395.74	38.29	-104.60	BSk	Semi-arid
7124410	PURGATOIRE RIVER BELOW TRINIDAD LAKE, CO.	10.75	1743.06	37.14	-104.55	BSk	Semi-arid
7175000	Double Creek Sws 5 near Ramona, OK	12.90	6.19	36.51	-95.94	Cf	Humid
7252500	SIXMILE C SWS 6 NR CHISMVILLE ARK	15.32	10.96	35.21	-93.88	Cf	Humid
7273100	HOTOPHA CREEK NR BATESVILLE, MS	429.30	90.91	34.36	-89.88	Cf	Humid
7274252	OTOUCALOFA CREEK CANAL NR WATER VALLEY, MS	526.79	251.49	34.14	-89.65	Cf	Humid
7275530	PETERS (LONG) CREEK NR POPE, MS	693.71	205.13	34.21	-89.98	Cf	Humid
7277700	HICKAHALA CREEK NR SENATOBIA, MS	350.53	313.39	34.63	-89.92	Cf	Humid
7280460	NORTH FORK TILLATOBA CREEK NR TEASDALE, MS	926.63	79.77	34.06	-90.02	Cf	Humid
7281977	YALOBUSHA RIVER AT DERMA, MS	265.47	414.40	33.84	-89.28	Cf	Humid
7282090	TOPASHAW CREEK CANAL NR DERMA, MS	411.27	163.17	33.78	-89.25	Cf	Humid
7285400	BATUPAN BOGUE AT GRENADA, MS	446.25	621.60	33.77	-89.79	Cf	Humid
7287150	ABIACA CREEK NR SEVEN PINES, MS	216.37	246.57	33.34	-90.15	Cf	Humid
7287160	ABIACA CREEK AT CRUGER, MS	140.90	247.86	33.34	-90.24	Cf	Humid

7287404	HARLAND CREEK NR HOWARD, MS	692.41	160.84	33.10	-90.17	Cf	Humid
8044000	Big Sandy Ck nr Bridgeport, TX	17.15	862.47	33.23	-97.69	Cf	Dry sub-humid
8050300	Elm Fk Trinity Rv nr Muenster, TX	84.71	119.14	33.61	-97.38	Cf	Dry sub-humid
8051500	Clear Ck nr Sanger, TX	117.12	764.05	33.34	-97.18	Cf	Humid
8052650	Little Elm Ck nr Celina, TX	149.17	120.95	33.37	-96.82	Cf	Humid
8052700	Little Elm Ck nr Aubrey, TX	134.83	195.54	33.28	-96.89	Cf	Humid
8063200	Pin Oak Ck nr Hubbard, TX	235.30	45.58	31.80	-96.72	Cf	Dry sub-humid
8317950	GALISTEO CREEK BELOW GALISTEO DAM, NM	133.36	1543.63	35.46	-106.21	Cf	Semi-arid
8318000	GALISTEO C AT DOMINGO, NM	453.93	1657.59	35.51	-106.32	Cf	Arid
8334000	RIO PUERCO ABV ARROYO CHICO NR GUADALUPE, NM	386.68	1087.79	35.60	-107.17	Df	Arid
9049200	WEST TENMILE CREEK AT COPPER MOUNTAIN, CO.	29.31	54.39	39.50	-106.17	Df	Humid
9066050	BLACK GORE CREEK NEAR VAIL, CO.	17.83	50.76	39.62	-106.28	Df	Semi-arid
9066250	GORE CREEK AT VAIL, CO.	10.17	148.41	39.64	-106.35	Df	Semi-arid
9093500	PARACHUTE CREEK AT PARACHUTE, CO.	85.76	512.82	39.45	-108.06	Df	Semi-arid
9095000	ROAN CREEK NEAR DE BEQUE, CO.	107.40	831.39	39.45	-108.32	BSk	Semi-arid
9207700	DRY PINEY CREEK NEAR BIG PINEY, WYO.	8.49	173.53	42.39	-110.25	Df	Semi-arid
9234700	RED CREEK NEAR DUTCH JOHN, UTAH	129.64	362.60	40.97	-109.24	BSk	Semi-arid
9306022	STEWART GULCH AB WEST FORK NR RIO BLANCO, CO	0.78	113.96	39.81	-108.18	Df	Semi-arid
9306058	WILLOW CREEK NEAR RIO BLANCO, CO.	2.26	125.36	39.84	-108.24	Df	Semi-arid
9306061	PICEANCE CREEK AB HUNTER C, NEAR RIO BLANCO, CO.	44.81	800.31	39.85	-108.26	Df	Semi-arid
9306175	BLACK SULPHUR CREEK NEAR RIO BLANCO, CO.	8.02	266.77	39.87	-108.29	Df	Semi-arid
9306235	CORRAL GULCH BELOW WATER GULCH, NR RANGELY, CO.	10.53	22.30	39.91	-108.53	Df	Semi-arid
9308000	WILLOW CREEK NEAR OURAY, UTAH	47.27	2323.22	39.94	-109.65	BSk	Arid
9406000	VIRGIN RIVER AT VIRGIN, UT	313.19	2476.03	37.20	-113.18	BSk	Semi-arid
9410000	SANTA CLARA RIVER AB WINSOR DAM NR SANTA CLARA, UT	113.81	875.42	37.22	-113.78	BWk	Arid
10104700	LITTLE BEAR R BL DAVENPORT C NR AVON UT	15.95	159.54	41.51	-111.81	Ds	Semi-arid
10174500	SEVIER RIVER AT HATCH, UT	7.97	880.60	37.65	-112.43	Df	Semi-arid
10336610	UPPER TRUCKEE RV AT SOUTH LAKE TAHOE, CA	13.09	142.19	38.92	-119.99	Ds	Humid
10336645	GENERAL C NR MEEKS BAY CA	6.81	19.27	39.05	-120.12	Ds	Humid
10336660	BLACKWOOD C NR TAHOE CITY CA	42.38	29.01	39.00	-120.00	Ds	Dry sub-humid
10336676	WARD C AT HWY 89 NR TAHOE PINES CA	27.34	25.12	39.13	-120.16	Ds	Humid
10336689	SNOW C A TAHOE VISTA CA	2.96	11.47	39.24	-120.04	Ds	Dry sub-humid
10336698	THIRD CK NR CRYSTAL BAY, NV	23.94	15.67	39.24	-119.95	Ds	Semi-arid
10336759	EDGEWOOD C NR STATELINE NV CA	8.34	8.29	38.96	-119.92	Ds	Dry sub-humid
10336780	TROUT CK NR TAHOE VALLEY, CA	9.53	95.05	38.92	-119.97	Ds	Dry sub-humid
10336790	TROUT C A SOUTH LAKE TAHOE CA	3.55	104.64	38.93	-119.98	Ds	Dry sub-humid
11022500	SAN DIEGO R NR SANTEE CA	2.15	976.43	32.82	-117.05	Cs	Semi-arid
11042000	SAN LUIS REY R A OCEANSIDE CA	27.32	1442.62	33.22	-117.36	BSk	Semi-arid
11046000	SANTA MARGARITA R A YSIDORA CA	102.77	1872.56	33.31	-117.35	BSk	Semi-arid
11046550	SAN JUAN C AT SAN JUAN CAPISTRANO CA	236.93	303.03	33.49	-117.66	BSk	Semi-arid
11047300	ARROYO TRABUCO A SAN JUAN	44.08	140.12	33.50	-117.67	BSk	Semi-arid

	CAPISTRANO CA						
11048500	SAN DIEGO C AT CULVER DRIVE NR IRVINE CA	697.60	108.26	33.68	-117.81	BSk	Semi-arid
11051500	SANTA ANA R NR MENTONE CA	35.91	543.90	34.11	-117.10	Cs	Semi-arid
11105850	ARROYO SIMI NR SIMI CA	1168.25	182.85	34.27	-118.79	Cs	Semi-arid
11108500	SANTA CLARA RIVER AT L.A.-VENTURA CO. LINE CA	483.58	1618.74	34.40	-118.70	Cs	Semi-arid
11113000	SESPE C NR FILLMORE	1719.65	652.68	34.44	-118.93	Cs	Semi-arid
11118500	VENTURA R NR VENTURA	1217.70	486.92	34.35	-119.31	Cs	Semi-arid
11141280	LOPEZ C NR ARROYO GRANDE CA	177.79	54.13	35.24	-120.47	Cs	Semi-arid
11147040	SANTA RITA C TRIB NR TEMPLETON CA	553.08	7.64	35.53	-120.85	Cs	Semi-arid
11147070	SANTA RITA C NR TEMPLETON CA	270.48	47.14	35.52	-120.77	Cs	Semi-arid
11148800	NACIMIENTO R NR BRYSON CA	298.34	380.73	35.80	-121.11	Cs	Arid
11149900	SAN ANTONIO R NR LOCKWOOD CA	156.64	562.03	35.90	-121.09	Cs	Arid
11151870	ARROYO SECO NR GREENFIELD CA	437.57	292.67	36.24	-121.48	Cs	Semi-arid
11153900	UVAS C AB UVAS RES NR MORGAN HILL CA	116.69	54.39	37.09	-121.72	Cs	Semi-arid
11160500	SAN LORENZO R A BIG TREES CA	606.43	274.54	37.04	-122.07	Cs	Humid
11162720	COLMA C A SOUTH SAN FRANCISCO CA	964.18	27.97	37.65	-122.43	Cs	Dry sub-humid
11169025	GUADALUPE R ABV HWY 101 A SAN JOSE CA	24.04	414.40	37.37	-121.93	Cs	Semi-arid
11169800	COYOTE C NR GILROY CA	65.66	282.31	37.08	-121.49	Cs	Semi-arid
11172175	COYOTE C AB HWY 237 A MILPITAS CA	8.23	826.21	37.42	-121.93	Cs	Semi-arid
11173575	ALAMEDA C BL WELCH C NR SUNOL CA	31.38	385.91	37.54	-121.86	Cs	Semi-arid
11176400	ARROYO VALLE BL LANG CYN NR LIVERMORE CA	28.86	336.70	37.56	-121.68	Cs	Semi-arid
11176900	ARROYO DE LA LAGUNA A VERONA CA	43.45	1043.77	37.63	-121.88	Cs	Semi-arid
11179000	ALAMEDA C NR NILES CA	44.11	1639.46	37.59	-121.96	Cs	Semi-arid
11180825	SAN LORENZO C AB DON CASTRO RES NR CASTRO V CA	525.27	46.62	37.70	-122.04	Cs	Semi-arid
11180960	CULL C AB CULL C RES NR CASTRO VALLEY CA	1287.64	15.00	37.72	-122.05	Cs	Semi-arid
11181040	SAN LORENZO C A SAN LORENZO CA	227.56	115.51	37.68	-122.14	Cs	Semi-arid
11306000	SF CALAVERAS R NR SAN ANDREAS CA	8.34	305.62	38.14	-120.66	Cs	Semi-arid
11308000	NF CALAVERAS R NR SAN ANDREAS CA	7.29	220.67	38.22	-120.70	Cs	Semi-arid
11335000	COSUMNES R A MICHIGAN BAR CA	63.33	1388.23	38.50	-121.04	Cs	Semi-arid
11376000	COTTONWOOD C NR COTTONWOOD CA	229.56	2400.92	40.39	-122.24	Cs	Dry sub-humid
11382000	THOMES C A PASKENTA CA	1704.13	525.77	39.89	-122.53	Cs	Semi-arid
11418500	DEER C NR SMARTSVILLE CA	15.31	219.11	39.22	-121.27	Cs	Humid
11449010	HIGHLAND C BL HIGHLAND CREEK DAM CA	19.99	36.78	38.95	-122.90	Cs	Humid
11451760	CACHE C AB RUMSEY CA	227.44	2473.44	38.91	-122.27	Cs	Semi-arid
11460000	CORTE MADERA C A ROSS CA	190.45	46.88	37.96	-122.56	Cs	Humid
11465150	PENA C NR GEYSERVILLE CA	702.32	57.76	38.70	-122.97	Cs	Humid
11465200	DRY C NR GEYSERVILLE CA	673.45	419.58	38.70	-122.96	Cs	Humid
11472150	EEL R NR DOS RIOS CA	359.94	1367.51	39.62	-123.34	Cs	Humid
11472900	BLACK BUTTE R NR COVELO CA	995.81	419.58	39.82	-123.08	Cs	Humid
11473000	MF EEL R BL BLACK BUTTE R NR COVELO CA	1779.54	950.53	39.83	-123.09	Cs	Humid
11473900	MF EEL R NR DOS RIOS CA	1068.39	1929.54	39.71	-123.33	Cs	Humid
11475500	SF EEL R NR BRANSCOMB CA	646.44	113.70	39.72	-123.65	Cs	Humid
11481000	MAD R NR ARCATA CA	1291.28	1256.14	40.91	-124.06	Cs	Humid

11481500	REDWOOD C NR BLUE LAKE CA	607.61	175.34	40.91	-123.82	Cs	Humid
11482500	REDWOOD C A ORICK CA	803.88	717.43	41.30	-124.05	Cs	Humid
11525600	GRASS VALLEY C A FAWN LODGE NR LEWISTON CA	175.65	79.77	40.68	-122.83	Cs	Humid
11525655	TRINITY R BL LIMEKILN GULCH NR DOUGLAS CITY CA	12.46	2097.89	40.67	-122.92	Cs	Humid
11528700	SF TRINITY R BL HYAMPOM CA	428.49	1978.75	40.65	-123.49	Cs	Humid
11529000	SF TRINITY R NR SALYER CA	496.33	2325.81	40.84	-123.57	Cs	Humid
12302055	Fisher River near Libby MT	24.94	2180.77	48.36	-115.31	Df	Dry sub-humid
12355000	Flathead River at Flathead British Columbia	36.63	1111.10	49.00	-114.48	Df	Humid
13344500	TUCANNON RIVER NEAR STARBUCK, WA	303.60	1116.28	46.51	-118.07	Cs	Semi-arid
14013600	MILL CREEK BELOW BLUE CREEK NEAR WALLA WALLA, WA	123.24	235.69	46.08	-118.19	Cs	Dry sub-humid
14138870	FIR CREEK NEAR BRIGHTWOOD, OR	5.78	14.14	45.48	-122.02	Cs	Humid
14138900	NORTH FORK BULL RUN RIVER NEAR MULTNOMAH FALLS, OR	18.16	21.55	45.49	-122.03	Cs	Humid
14139800	SOUTH FORK BULL RUN RIVER NEAR BULL RUN, OR	8.99	40.66	45.44	-122.11	Cs	Humid
14240525	NF TOUTLE RIVER BELOW SRS NEAR KID VALLEY, WA	3526.52	378.14	46.37	-122.58	Cs	Humid
14241500	SOUTH FORK TOUTLE RIVER AT TOUTLE, WA	1469.06	310.80	46.32	-122.70	Cs	Humid
14242580	TOUTLE RIVER AT TOWER ROAD NEAR SILVER LAKE, WA	2609.57	1284.63	46.34	-122.84	Cs	Humid
14306700	NEEDLE BRANCH NEAR SALADO,OREG.	69.98	0.70	44.51	-123.86	Cs	Humid
14306800	FLYNN CREEK NEAR SALADO,OREG.	62.83	2.02	44.54	-123.85	Cs	Humid
14306810	DEER CREEK NEAR SALADO,OREG.	78.92	3.03	44.53	-123.88	Cs	Humid
14307620	SIUSLAW RIVER NEAR MAPLETON, OR	71.59	1522.91	44.06	-123.88	Cs	Humid
16103000	Hanalei River nr Hanalei, Kauai, HI	230.45	47.94	22.18	-159.47	Af	Humid
16210200	Kaukonahua Stream blw Wahiawa Reservoir, Oahu, HI	7.06	43.25	21.50	-158.05	Aw	Humid
16210500	Kaukonahua Str at Waialua, Oahu, HI	22.14	101.68	21.57	-158.12	Aw	Dry sub-humid
16212480	Honouliuli Stream Tributary near Waipahu, Oahu, HI	44.73	4.82	21.40	-158.07	Aw	Humid
16212800	Kipapa Str nr Wahiawa, Oahu, HI	219.41	11.01	21.47	-157.96	Aw	Humid
16213000	Waikele Str at Waipahu, Oahu, HI	149.44	116.91	21.38	-158.01	BSh	Semi-arid
16225800	N. Halawa Str nr Kaneohe, Oahu, HI	178.40	4.61	21.41	-157.87	Aw	Humid
16226200	N. Halawa Str nr Honolulu, Oahu, HI	201.33	10.41	21.38	-157.90	Aw	Humid
16226400	N. Halawa Str nr Quar. Stn. at Halawa, Oahu, HI	102.58	11.91	21.37	-157.91	Aw	Humid
16227500	Moanalua Stream nr Kaneohe, Oahu, HI	31.78	2.38	21.39	-157.85	Aw	Humid
16238000	Makiki Stream at King St. bridge, Oahu, HI	50.81	6.40	21.30	-157.84	Aw	Dry sub-humid
16244000	Pukele Stream near Honolulu, Oahu, HI	112.93	2.98	21.31	-157.79	Aw	Humid
16247100	Manoa-Palolo Drainage Canal at Moiliili, Oahu, HI	80.95	26.42	21.29	-157.82	Aw	Dry sub-humid
16265600	RB of Kamooalii Str nr Kaneohe, Oahu, HI	126.13	2.82	21.39	-157.79	Aw	Humid
16270900	Luluku Str at alt 220 ft nr Kaneohe, Oahu, HI	98.29	1.27	21.39	-157.81	Aw	Humid
16272200	Kamooalii Str blw Luluku Str nr Kaneohe, Oahu, HI	60.45	9.89	21.39	-157.80	Aw	Humid
16273950	SF Kapunahala Str at Kaneohe, Oahu, HI	87.81	1.09	21.40	-157.81	Aw	Humid
16275000	Heeia Stream at Haiku Valley nr Kaneohe, Oahu, HI	259.48	2.49	21.41	-157.82	Aw	Humid
16415600	Kawela Gulch near Moku, Molokai, HI	222.18	13.68	21.07	-156.95	Aw	Semi-arid

16713000	Wailuku River at Hilo, HI	19.77	635.79	19.73	-155.09	Af	Humid
16854500	Ugum River above Talofofo Falls, nr Talofofo, Guam	304.84	15.33	13.32	144.74	Am	Humid
40734644	SILVER CREEK AT SOUTH KORO ROAD NEAR RIPON, WI	4.93	93.76	43.86	-88.87	Df	Humid
40854592	FISHER CREEK AT HOWARDS GROVE, WI	15.05	27.97	43.83	-87.83	Df	Humid
40857005	OTTER CREEK AT WILLOW ROAD NEAR PLYMOUTH, WI	17.14	24.60	43.79	-87.92	Df	Humid
50020500	RIO GRANDE DE ARECIBO NR ADJUNTAS, PR	774.48	32.89	18.18	-66.74	Af	Humid
50021030	RIO PELLEJAS ABV CENTRAL PELLEJAS, PR	429.45	17.79	18.20	-66.70	Af	Humid
50021500	RIO PELLEJAS NR UTUADO, PR	1058.64	24.73	18.23	-66.72	Af	Humid
50023000	RIO VIVI NR CENTRAL PELLEJAS, PR	651.73	14.66	18.21	-66.67	Af	Humid
50024950	RIO GRANDE DE ARECIBO BLW UTUADO, PR	1427.91	169.90	18.30	-66.70	Af	Humid
50025155	RIO SALIENTE AT COABEY NR JAYUYA, PR	186.60	23.96	18.21	-66.56	Af	Humid
50025850	RIO JAUCA AT PASO PALMA, PR	408.15	17.85	18.21	-66.65	Af	Humid
50026025	RIO CAONILLAS AT PASO PALMA, PR	1611.25	98.37	18.23	-66.64	Af	Humid
50026400	RIO YUNES AT HWY 140 NR FLORIDA, PR	513.36	36.23	18.32	-66.59	Af	Humid
50027000	RIO LIMON ABV LAGO DOS BOCAS, PR	553.31	85.99	18.33	-66.62	Af	Humid
50027750	RIO GRANDE DE ARECIBO ABV ARECIBO, PR	74.97	453.25	18.42	-66.70	Af	Humid
50028000	RIO TANAMA NR UTUADO, PR	711.92	47.66	18.30	-66.78	Af	Humid
50031200	RIO GRANDE DE MANATI NR MOROVIS, PR	423.17	142.97	18.30	-66.41	Af	Humid
50035000	RIO GRANDE DE MANATI AT CIALES, PR	321.32	331.52	18.32	-66.46	Af	Humid
50043800	RIO DE LA PLATA AT COMERIO, PR	696.53	281.01	18.22	-66.22	Af	Humid
50044830	RIO GUADIANA AT GUADIANA, PR	886.49	23.80	18.30	-66.22	Af	Humid
50045010	RIO DE LA PLATA BLW LA PLATA DAMSITE, PR	517.80	448.07	18.35	-66.24	Af	Humid
50047560	RIO DE BAYAMON BLW LAGO DE CIDRA DAM, PR	304.55	21.55	18.20	-66.14	Af	Humid
50048770	RIO PIEDRAS AT EL SENORIAL, PR	3634.19	19.40	18.36	-66.07	Af	Humid
50049000	RIO PIEDRAS AT RIO PIEDRAS, PR	2426.49	32.37	18.40	-66.06	Af	Humid
50051150	QUEBRADA BLANCA AT EL JAGUAL, PR	736.91	8.42	18.16	-65.98	Af	Humid
50051180	QUEBRADA SALVATIERRA NR SAN LORENZO, PR	736.95	9.69	18.17	-65.98	Af	Humid
50051800	RIO GRANDE DE LOIZA AT HWY 183 SAN LORENZO, PR	442.36	106.42	18.19	-65.96	Af	Humid
50053025	RIO TURABO ABV BORINQUEN, PR	829.48	18.54	18.16	-66.04	Af	Humid
50055000	RIO GRANDE DE LOIZA AT CAGUAS, PR	652.66	232.58	18.24	-66.01	Af	Humid
50055100	RIO CAGUITAS NR AGUAS BUENAS, PR	366.09	13.73	18.25	-66.09	Af	Humid
50055170	RIO CAGUITAS NR CAGUAS, PR	465.25	21.42	18.23	-66.05	Af	Humid
50055225	RIO CAGUITAS AT VILLA BLANCA AT CAGUAS, PR	606.41	42.99	18.25	-66.03	Af	Humid
50055390	RIO BAIROA AT BAIROA, PR	432.74	13.16	18.26	-66.04	Af	Humid
50055750	RIO GURABO BLW EL MANGO, PR	335.61	57.76	18.23	-65.89	Af	Humid
50056400	RIO VALENCIANO NR JUNCOS, PR	1081.10	42.48	18.22	-65.93	Af	Humid
50057000	RIO GURABO AT GURABO, PR	685.95	155.92	18.26	-65.97	Af	Humid
50058350	RIO CANAS AT RIO CANAS, PR	930.47	19.50	18.29	-66.05	Af	Humid
50059050	RIO GRANDE DE LOIZA BLW LOIZA DAMSITE, PR	330.66	541.31	18.34	-66.01	Af	Humid

50061800	RIO CANOVANAS NR CAMPO RICO, PR	369.24	25.49	18.32	-65.89	Af	Humid
50065500	RIO MAMEYES NR SABANA, PR	175.57	17.82	18.33	-65.75	Af	Humid
50070500	RIO FAJARDO ABV FAJARDO, PR	202.28	9.56	18.27	-65.72	Af	Humid
50071000	RIO FAJARDO NR FAJARDO, PR	520.43	38.59	18.30	-65.69	Af	Humid
50075000	RIO ICACOS NR NAGUABO, PR	1350.03	3.26	18.28	-65.79	Af	Humid
50110900	RIO TOA VACA ABV LAGO TOA VACA, PR	489.35	36.78	18.13	-66.46	Af	Humid
50114900	RIO PORTUGUES NR TIBES, PR	1390.86	18.83	18.10	-66.64	Af	Humid
50115000	RIO PORTUGUES NR PONCE, PR	1692.43	22.84	18.08	-66.63	Af	Humid
50136400	RIO ROSARIO NR HORMIGUEROS, PR	549.00	47.40	18.16	-67.09	Af	Humid
54310157	JACKSON CREEK TRIBUTARY NEAR ELKHORN, WI	15.69	11.24	42.65	-88.55	Df	Humid